



HAL
open science

MODEL-BASED IMAGING APPROACH TO QUANTIFY TISSUE STRUCTURAL PROPERTIES IN OPTICAL COHERENCE TOMOGRAPHY

Cecilia Lantos

► **To cite this version:**

Cecilia Lantos. MODEL-BASED IMAGING APPROACH TO QUANTIFY TISSUE STRUCTURAL PROPERTIES IN OPTICAL COHERENCE TOMOGRAPHY. Life Sciences [q-bio]. Université Paris Diderot, 2014. English. NNT: . tel-01257509

HAL Id: tel-01257509

<https://theses.hal.science/tel-01257509>

Submitted on 23 Jan 2016

HAL is a multi-disciplinary open access archive for the deposit and dissemination of scientific research documents, whether they are published or not. The documents may come from teaching and research institutions in France or abroad, or from public or private research centers.

L'archive ouverte pluridisciplinaire **HAL**, est destinée au dépôt et à la diffusion de documents scientifiques de niveau recherche, publiés ou non, émanant des établissements d'enseignement et de recherche français ou étrangers, des laboratoires publics ou privés.

UNIVERSITY PARIS DIDEROT - PARIS VII
Laboratory of Matter and Complex Systems
UNIVERSITY OF HOUSTON
Department of Mechanical Engineering

GRADUATE SCHOOL FRONTIERS IN LIFE SCIENCES, PARIS

PhD THESIS
Biomedical Engineering

Cecília LANTOS

MODEL-BASED IMAGING APPROACH TO
QUANTIFY TISSUE STRUCTURAL PROPERTIES
IN OPTICAL COHERENCE TOMOGRAPHY

Thesis directed by Stéphane DOUADY / Matthew A. FRANCKEK
Defended the September 29, 2014.

COMMITTEE

Mr. A. Claude BOCCARA
Mr. Stephen WONG
Mr. Matthew A. FRANCKEK
Mr. Stéphane DOUADY
Mrs. Darine ABI-HAIDAR
Mr. Laurent LIMAT

Reviewer
Reviewer
Thesis Director
Thesis Director
Examiner
Chairman

UNIVERSITÉ PARIS DIDEROT - PARIS VII
Laboratoire Matière et Systèmes Complexes
UNIVERSITÉ DE HOUSTON
Département de l'Ingénierie Mécanique

ÉCOLE DOCTORALE FRONTIÈRES DU VIVANT, PARIS

THÈSE DE DOCTORAT
Ingénierie Biomédicale

Cecília LANTOS

QUANTIFICATION DE STRUCTURES
TISSULAIRES EN TOMOGRAPHIE PAR
COHÉRENCE OPTIQUE

Thèse dirigée par Stéphane DOUADY / Matthew A. FRANCKEK
Soutenue le 29 septembre 2014.

JURY

M. A. Claude BOCCARA
M. Stephen WONG
M. Matthew A. FRANCKEK
M. Stéphane DOUADY
Mme. Darine ABI-HAIDAR
M. Laurent LIMAT

Rapporteur
Rapporteur
Directeur de thèse
Directeur de thèse
Examinatrice
Directeur de jury

“For an image, since the reality after which it is modeled does not belong to it, and it exists ever as the fleeting shadow of some other, must be inferred to be in another [that is, in space], grasping existence in some way or other, or it could not be at all.”

(Plato)

Abstract

The dissertation presents a revolutionary method to tissue characterization. The optical scattering property of the tissue measured with Optical Coherence Tomography (OCT) reveals the subsurface structure at histological level. Our work developed a model based approach to process OCT data for accurate tissue characterization. This way the qualitative images are represented in a quantitative model independently from the measurement settings. Since a tumor is differentiated from healthy tissue based on morphological analysis, our parametric model is able to diagnose healthy versus cancerous tissue.

Résumé

Cette dissertation représente une méthode révolutionnaire pour la caractérisation du tissu. La propriété de diffusion optique du tissu mesurée en Tomographie par Cohérence Optique (OCT) révèle la structure tissulaire sous la surface à l'échelle histologique. Notre œuvre a développé une approche basée sur modèle pour traiter les données OCT pour la précise caractérisation du tissu. Ainsi les images qualitatives sont représentées dans un modèle quantitatif indépendamment de réglages de mesure. Etant donné qu'une tumeur est différenciée du tissu sain basé sur une analyse morphologique, notre modèle paramétrique est capable de diagnostiquer le tissu sain vs cancéreux.

Acknowledgement

I would like to thank my former academic advisors, Marc Durand and Patrice Flaud for giving me the opportunity to join their ranks at Paris Diderot University and start work on a highly interdisciplinary project in the Laboratory of Matter and Complex Systems. This, together with my integration in the laboratory and graduate school has given me the inspiration that allowed me to accomplish the project laid down in my PhD thesis. Many thanks also go out to the successive directors of the laboratory, Loïc Auvray and Jean-Marc di Meglio.

Next, I should like to express my to gratitude to François Taddéi, director of the Frontiers in Life Sciences International and Interdisciplinary Graduate School, for his scientific and personal support. This research report would not have been possible without his support, and that of his co-director, Samuel Bottani, who did all the administrative work required for the completion of my PhD work.

Many thanks are due to Stéphane Douady, my academic supervisor at Paris Diderot University, for supporting me in the new direction my thesis has taken within the scope of the international collaboration between the Laboratory of Matter and Complex systems and the University of Houston, where Matthew Franchek my academic mentor led me through the evolution of this work at the Mechanical Engineering Department. I am also grateful to the UH Mechanical Engineering chairman, Pradeep Sharma, for his wisdom and knowledge that helped me to achieve my PhD thesis.

Special thanks to Kirill Larin from the Department of Biomedical Engineering at the University of Houston who opened his laboratory to us to be able to work with Optical Coherence Tomography and to use their datasets measured on tissue samples supplied from collaboration with the MD Anderson Cancer Center.

I would like to thank the members of the research group I was involved when I began to work on my project. I could always rely on them for all kinds of support, from basic to elaborate. They helped me answer the many questions that arose while developing my ideas: Rafik Borji in System Identification and Control Engineering, then Narendran Sudheendran and Shang Wang in Optical Coherence Tomography.

This international collaboration could not have been realized without the support of the Hungarian-American Fulbright Committee, and the Department of Hydrodynamic Systems at the Budapest University of Technology and Economics. Beside the grant from the Paris Diderot University, and the Fulbright Committee, I obtained financial support from the University of Houston Foundation, the Frontiers in Life Sciences Graduate School, and Matthew Franchek's sponsorship at the University of Houston.

My deepest gratitude is also due to the members of the supervisory committee for their valuable feedback in the defense, Laurent Limat, Darine Abi Haidar, Matthew Franchek, Stéphane Douady, and especially to my reviewers: Claude Boccara and Stephen Wong.

In Paris, I acknowledge the scientific and personal discussion and support with my friends and colleagues, Florence Gazeau, Nebraska Zambrano, and Kees van der Beek, and with my tutors Darine Abi Haidar and Dirk Drasdo.

I would like to dedicate all this work to my closest friend, Kees van der Beek who supported me during all of these years. He was not only a friend, he was also an advisor by scientific discussions, in writing papers, and giving presentations.

Special thanks also to my family and all my friends who have always been there for me, either they are in Houston (Patty, Judit, Fatemeh), Paris (Malak, Cecilia, Li, Camille, Zsuzsa) or Budapest (Edina, Judit, Mariann, Anna).

Table of Contents

Introduction.....	20
I. Soft Tissue Diagnostics	21
I/1. Soft Tissue Tumors and Diagnosis	21
I/1/a. Soft Tissue Tumor (Sarcoma)	21
I/1/b. Symptoms and Diagnosis.....	22
I/1/c. Imaging Modalities for Soft Tissue Tumors	23
1. Structural Imaging Methods for Soft Tissue Tumors	23
2. Functional Imaging Methods for Soft Tissue Mass	26
I/2. Adipocytic Tumors and Diagnosis	27
I/2/a. Adipocytic Tumor (Liposarcoma).....	27
I/2/b. Objectives: Diagnosis of Liposarcoma	31
II. Fourier-Domain Optical Coherence Tomography	39
II/1. Comparison with other optical imaging modalities.....	39
II/2. Theory Optical Coherence Tomography	46
II/2/a. Wave-equation	46
II/2/b. Broadband Signal.....	50
II/2/c. Low-Coherence Interferometry	52
II/3. Review of Optical Coherence Tomography	56
II/3/a. Operation modes in OCT	56
II/3/b. Applications of OCT.....	61
II/3/c. Light sources and Axial Resolution.....	63
II/3/d. Lateral Resolution.....	69
II/3/e. Lateral Resolution using Gaussian Laser Beam	73
II/3/f. Sensitivity	77
II/4. Spectral-Domain Optical Coherence Tomography	80
II/4/a. Setup of the SD OCT system	80
II/4/b. Interference in the SD OCT system.....	81
II/4/c. Interpolation of the intensity range, light attenuation in tissue.....	83
II/4/d. Dispersion compensation by phase correction	86

II/4/e. Sensitivity roll-off.....	91
III. Quantifying tissue structural properties from OCT to diagnose cancer	95
III/1. Literature of quantifying imaging-based data	95
III/2. Data analysis, Results.....	116
III/2/a. Introduction	116
III/2/b. Steps of Data analysis.....	119
Step 1: First Steps towards quantitative tissue analysis.....	119
Step 2. Histograms characterize different tissue types	123
Step 3: Removing Tissue Surface Irregularity.....	124
Step 4: Compensate measurement settings and light attenuation effect	127
Step 5. Define Region of Interest (ROI) on the STD/MEAN curves	130
Step 6. Results of the STD/MEAN curves.....	137
Step 7. Define Region of Interest (ROI) on the mean normalized Intensity variations...	140
Step 8. Results of the mean normalized Intensity variation.....	145
Step 9. Discussion of the data analysis	148
III/3. Data Analysis applied on new measurements	154
III/3/a. Comparison of the Data.....	154
III/3/b. Error analysis.....	170
Conclusion	175
Bibliography	176
Appendix.....	187

List of Figures

Figure I.1.1. Soft Tissue Development. MSC: Mesenchymal Stem Cell [2].....	22
Figure I.2.1. a) Adipocyte b) Adipose tissue with fibrous septa (dividing wall) between clusters of adipocytes. CT- Connective Tissue [33, 34].....	28
Figure I.2.2. Normal fatty tissue with large fat cells. Histology (H&E – hematoxylin & eosin stain). Magnification: a) 4x, b) 10x.	28
Figure I.2.3 Adipose tissue in reactive states. Medium magnification [9].	29
Figure I.2.4. Atypical lipoma/lipoma-like WDLS M: 4-10x [11].	30
Figure I.2.5. Atypical adipocytes in atypical lipoma/lipoma-like WDLS [11].....	30
Figure I.2.6. Stromal sclerosis in Atypical lipoma/lipoma-like, WDLS [11].	30
Figure I.2.7. WDLS with myxoid features [11].	30
Figure I.2.8. DDLS subtypes: a. Myxofibrosarcoma b. Solitary fibrous tumor c. Fibrosarcoma d. Gastrointestinal stromal tumor [11].	31
Figure I.2.9. DDLS subtypes: a. Pleomorphic liposarcomatous component b. Mildly pleomorphic spindle cell sarcoma c. Pleomorphic component with large cells containing eosinophilic hyaline globules d. Osteosarcomatous differentiation [11].	31
Figure I.2.10. X-ray of the abdomen with soft tissue tumor findings [36].	32
Figure I.2.11. CT of LPS in the Retroperitoneum.	33
Figure I.2.12. a) T ₁ weighted- b) T ₂ weighted fat saturated axial MRI of a liposarcoma [7].	33
Figure I.2.13. Doppler ultrasound on LS [7, 38].....	34
Figure I.2.14. Moderately hypervascular tumor in the right upper thigh [16].	35
Figure I.2.15. Comparison of OCT image and Histology.....	35
Figure I.2.16. FDG-PET/CT image of high grade soft tissue sarcoma in the right thigh with high FDG uptake (SUVmax, 18.4). [29].....	36
Figure I.2.17. Luciferase-labeled human Liposarcoma cells injected subcutaneously in SCID mice. Left mouse with the non-angiogenic dormant tumor undetectable by gross examination. Right mouse with developed angiogenic tumor after 133 days. The tumor is palpable ~23 days after well detectable bioluminescence signal [42].....	37
Figure I.2.18. Fluorescence images of Normal Fat Tissue, WDLS and DDLS. FISH analysis (Fluorescence in situ hybridization) Fluorophores: Centromeric probe (green), MDM2 probe (red), Dapi nuclear stain (blue).....	37
Figure II.1.1. Electromagnetic spectrum [46].....	39
Figure II.1.2. Simplified model of biological medium with three layers. Each layer is associated with an absorption coefficient μ_a , a scattering coefficient μ_s , an anisotropic factor g , and a refractive index n [44].	40
Figure II.1.3. Scheme of Confocal Microscopy [51].	41
Figure II.1.4. Single- and Multi-photon excitation [49].	41
Figure II.1.5. Dual-function reporter genes. One single protein with two functional components/ or coding sequences can be combined to make a single mRNA that produces two proteins [49].	42
Figure II.1.6. Comparison of conventional imaging methods for diagnosis [69]. Ultrahigh Resolution OCT can achieve a resolution up to 1 μm	44

Figure II.2.1. Electro-magnetic wave propagation [81].....	47
Figure II.2.2. Solution of hyperbolic partial differential equation on space-time plane.....	48
Figure II.2.3. Left: Monochromatic light (coherence length is infinity). Right: Broadband signal: Sum of the different wavelengths yields a wavepacket (Short Coherence Length Light) [modified from 59].....	50
Figure II.2.4. Optical Spectrum and Coherence Function of the Laser source: <i>S840-B-I-20: 20 mW Benchtop Lightsource at 840 nm</i> . Left: Power Spectral Density in the function of wavenumber or wavelength ($k = 2\pi/\lambda$), and Right: corresponding Point Spread Function of the generated Laser Signal; Up: High-Power Mode, Down: Low-Power Mode.....	51
Figure II.2.5. Hilbert function of a single wavelength; Analytic signal represented in a 3D plot [87].	53
Figure II.2.6. Broadband signal. The real high frequency signal $a(t)$ is shown in black with the real envelope of its analytic signal $A(t)$ in red [88].....	54
Figure II.3.1. Michelson Interferometer. Wave constructive/destructive interference appears on the detector due to path-length difference ($2L2 - 2L1 = 2d$) from the two mirrors (point source). Interference fringe pattern appears in case of divergent laser source:	56
Figure II.3.2. Schematic of TD-OCT, $I_E - I_{Em} = LCI$ signal, A is the real envelope [modified from 59 & 85].	57
Figure II.3.3. Conventional OCT operation mode. Cross-sectional images (B-scan) are composed of adjacent A-lines [49].....	58
Figure II.3.4. Schematic of SD OCT with interference fringes detected on the camera array ($I(k)$) from one and two layers, with the backreflection ($F(z)$) after Fourier Transform [59, 85].	58
Figure II.3.5. Schematic of SS OCT with interference fringes detected in time, and backreflection after Fourier Transform [59].	59
Figure II.3.6. Scan planes of conventional OCT yielding cross-sections, and OCM yielding ‘en face’ images scanning laterally [89].	60
Figure II.3.7. Parallel OCT detection [85].....	60
Figure II.3.8. Standard fiber-optic Michelson interferometer with 2:2 fiber coupler [92].	61
Figure II.3.9. Free-space equivalent to the fiber-optic Michelson interferometer with a beamsplitter cube [92].....	61
Figure II.3.10. a-b) UHR OCT of macular hole in vivo c) Fundus photograph, white arrow shows central foveal region where OCT cross-section was recorded d) corresponding histology from similar postmortem eye [59].	62
Figure II.3.11. a-c) Stained Histology of diseased human coronary arteries obtained autopsy and d-f) corresponding OCT images [59].....	63
Figure II.3.12. Optical therapeutic window [99].	64
Figure II.3.13. OCT image penetration depth of human epiglottis ex vivo performed at 850-nm and 1300-nm central wavelengths penetrating deeper into the tissue, and corresponding histology; g – glandular structure, c – cartilage. Bar equals 500 μm [49].	64
Figure II.3.14. Free space OCT iso-resolution lines; Axial resolution vs. bandwidth of OCT light sources [100-102].	65
Figure II.3.15. Normalized Optical Power Spectrum and Coherence Function of our OCT system. Laser source: Supraluminescent Diode (SLD) S840-B-I-20: 20 mW Benchtop Lightsource at 840 nm; a) Power Spectral Density and b) corresponding Point Spread Function.	67

Figure II.3.16. Optical spectrum using femtosecond Ti:Al ₂ O ₃ laser with 260 nm linewidth and 1.5 μm axial resolution vs. a standard resolution SLD light source with 32 nm linewidth and 11.5 μm axial resolution [59].	68
Figure II.3.17. Comparison of different laser light sources representing the advantages of supercontinuum (SC) over amplified spontaneous emission (ASE), and superluminescent LED (SLD) [103, 108].	68
Figure II.3.18. Ideal optical geometry. Numerical Aperture defined by the half-angle θ of the light cone angle, focused to point source F , f – focal length, d – lens diameter, n – refractive index of the medium.	69
Figure II.3.19. Diffraction of light through an aperture with D diameter [111].	70
Figure II.3.20. Image formation of light with circular numerical aperture [112].	70
Figure II.3.21. The depth of field is an inverse function of the Numerical Aperture.	71
Figure II.3.22. Comparison of OCT operating at low NA and OCM operating at high NA with overlapped coherence and confocal gate enhancing resolution and image quality, but at limited depth [modified from 114].	72
Figure II.3.23. Gaussian beam intensity distribution [modified from: 122].	74
Figure II.3.24. The propagation of a Gaussian beam [modified from 111 & 123].	74
Figure II.3.25. Gaussian Laser beam profile, with parameters: beam waist ($2w_0$), focal length, Depth of focus (b), Divergence angle (θ) [modified from 124].	76
Figure II.4.1. SD-OCT measurement setup in the laboratory on a table against vibration.	80
Figure II.4.2. SD-OCT scheme [24].	80
Figure II.4.3. Fourier Transform of the Interferometer Exit.	83
Figure II.4.4. Interferometer Exit recorded on Normal Fat Tissue.	84
Figure II.4.5. Normal Fat Tissue. a) OCT A-line (1mm = 228 px) b) B-scan composed of 100 A-lines (white bar = 500 μm).	85
Figure II.4.6. a) Autocorrelation for a perfectly balanced detector b) Phase delay (zeroth order) c) Group delay (first order) d) GVD (second order) [128].	87
Figure II.4.7. Degradation of PSF (point spread function), peak broadening and intensity loss at increasing path-length differences without dispersion compensation (linear & logarithmic scale).	88
Figure II.4.8. Interferometer Exit; Spectrum from two interfered signals, one is delayed by a path-length-difference $l = 400 \mu\text{m}$; and chirped due to dispersion.	89
Figure II.4.9. a) Complex representation of the fringe signal b) Unwrapped phase.	90
Figure II.4.10. Point Spread Functions in function of path-length difference with dispersion compensation (linear & logarithmic scale).	90
Figure II.4.11. a) Simulated interferogram; Dotted line: light source spectrum $G(\zeta)$; Solid line: interferometric modulation; $\delta\zeta$: pixel width b) Fourier transform of the interferogram [136].	91
Figure II.4.12. Scattering process and wavefront dispersion affecting OCT images [104].	94
Figure III.1.1. Attenuation of backscattered light (red line) in tissue after averaging 500 A-lines. Tissue surface begins at around 1000 μm (Intensity on logarithmic scale).	95
Figure III.1.2. OCT image of the boundary between healthy tissue and DDLS. The left part of the image is the denser tumor area; the right part is the normal fat tissue containing adipose cells [26].	96
Figure III.1.3. Three curves show the backscattered intensity in time at three different positions in the sclera reduced from OCT measurements. The arrows show the diffusion starting point [143].	96
Figure III.1.4. Ovarian Tissue.	98

Figure III.1.5. Averaged OCT profile with numerical fit to three layers: Red-Intima, Blue-Media, Green-Adventitia, logarithmic scale [141].	99
Figure III.1.6. Averaged OCT A-scan (thin grey line), and the fitted signal using equation (III.1.7) (thick dark line) with the calculated attenuation coefficient μ_t (\pm 95% confidence interval) reduced from two layers; logarithmic scale [151].	99
Figure III.1.7. Involved (malignant) human axillary lymph node with diffuse involvement of the node tissue a) H&E histology b) parametric OCT image c) en face OCT image at a specific depth position; Scale bar = 1 mm [157].	100
Figure III.1.8. OCT signal with slope, and after subtracting the slope from the raw A-scan, logarithmic scale [159].	101
Figure III.1.9. Slope and standard deviation of Fat Tissue, WDLs, Smooth Muscle Connective Tissue and its cancerous version: Leiomyosarcoma. 40000 sample points per sample, and 1 sample per tissue type are represented with 95% confidence intervals [159].	101
Figure III.1.10. (A) Photograph (B) Schematic of the Biopsy guidance probe [161].	102
Figure III.1.11. OCT A-scan profiles of breast tissue specimens: (A) adipose; (B) fibroglandular tissue; and (C) adenocarcinoma recorded with Low-Coherence Interferometry. Insets are the histological sections [161].	102
Figure III.1.12. OCT A-line from adipose (left) and fibroglandular (right) human breast tissue with first-order fit (red line); Logarithmic scale [162].	103
Figure III.1.13. Averaged, area normalized power spectra on human adipose and fibroglandular tissue in breast, calculated from training set. Green window shows ROI [162].	103
Figure III.1.14. Adipose, fibroglandular and tumor tissue characteristics in breast. Parameters of Slope, Standard Deviation around slope and Spatial Frequency are calculated from a training set. The last two parameters show similar characteristics [162].	104
Figure III.1.15. OCT A-line a) Adipose tissue b) Inductive ductal carcinoma tumor tissue c) Stroma tissue; Logarithmic Scale [164].	105
Figure III.1.16. Fourier-Domain data normalized by area, and averaged from tumor (black), stroma (dark gray), and adipose (light gray) tissue A-lines [164].	106
Figure III.1.17. Histogram of the mean distance between high-intensity backreflections from 1 OCT A-line of human tumor (black), stroma (dark gray) and adipose (light gray) tissues [164].	106
Figure III.1.18. Steps of A-line processing: first column – adipose tissue; second column – fibrous and adipose tissue; third column – tumor tissue; 8 parameters are extracted [163].	108
Figure III.1.19. Scatter plot illustrating the clustering of the three main tissue types (adipose – green, fibrous – blue, tumor - red) and their projections on the x , y , and z planes for three parameters: Slope, Std, and PeakArea [163].	109
Figure III.1.20. H&E images of adipose with stromal regions (a), cancer with adipose cells (d), and stroma (e), their corresponding OCT B-scans [(b)(e)(h)], and fractal dimension distribution calculated from the A-lines of the B-scan [(c)(f)(i)] [165].	110
Figure III.1.21. a) A-scan profile selected from b) B-scan at porcine artery. Arrows show the approximative region of intima (image size: $1.5 \times 3 \text{ mm}^2$); Logarithmic scale [141].	111
Figure III.1.22. Example OCT images (after 4×4 local average filtering – better result) of mouse (a) skin, (b) fat, (c) normal lung and (d) abnormal lung. Image size: $1 \times 0.25 \text{ mm}$ [166].	112
Figure III.1.23. a. OCT B-scan of Stratum Corneum (up) and Epidermis (down) segmented manually. b. Different fitting distributions to the B-scan data of Stratum corneum and Epidermis [168].	113

Figure III.1.24. a) OCT image of chick embryo b) Spatial contrast computed from a 7x7 moving window [169].	114
Figure III.1.25. Original A-scan profile and similar A-scan at the end of the process recorded at two SD-OCT devices [172].	115
Figure III.2.1. Histological images.	116
Figure III.2.2. Tissue Cross-Sections. OCT Images (B-scans composed of 500 A-lines);	117
Figure III.2.3. OCT A-line of Normal Fat Tissue a) arbitrary unit b) dB scale.	118
Figure III.2.4. OCT A-line of WDLS a) arbitrary unit b) dB scale.	118
Figure III.2.5. OCT A-line of DDLS a) arbitrary unit b) dB scale.	118
Figure III.2.6. 5 A-line-plots $x = \text{pixel position of the A-line from the B-scans of Figure III.2.2, and the mean value of 400 A-lines. A) Normal Fat Tissue b) WDLS (Well-Differentiated Liposarcoma) c) DDLS (De-Differentiated Liposarcoma)}$	120
Figure III.2.7. Mean, standard deviation, and standard deviation over mean of 400 A-lines of the OCT images on Figure III.2.2.	120
Figure III.2.8. Intensity variation of 400 A-lines in a B-scan at specific depth positions z [pixel]. (1mm = 228 pixels).	121
Figure III.2.9. Reordered Intensity Values from Figure III.2.8 at specific depth positions z [pixel] (1mm = 228 pixels)	122
Figure III.2.10. Reordered Intensity Values of Normal Fat Tissue, WDLS, DDLS, normalized to the maximum value at a depth position z [pixel] close to surface.	122
Figure III.2.11. Histogram fitted to the Intensity Values at a depth position z [pixel] close to surface, normalized by area, with subtracted mean; red-Normal Fat Tissue, blue-WDLS and brown-DDLS.	123
Figure III.2.12. Edge detection. Black lines mark the Highest scattering maximum a) meat b) fat.	124
Figure III.2.13. Edge detection. Black lines mark the best correlation between adjacent A-lines a) meat b) fat.	124
Figure III.2.14. Edge detection. Absolute threshold at a given intensity value a) meat b) fat.	124
Figure III.2.15. Edge detection. Canny edge detector applied 3x a) meat b) fat.	125
Figure III.2.16. Canny edge binary images applied successively to obtain the surface of the tissue. White pixel value '1' showing edges, black pixel value '0' showing no edge. The border of the tissue becomes continuous only on the third image.	125
Figure III.2.17. Original image with the straightening line found after the algorithm.	126
Figure III.2.18. Step 1. 2D median filter applied on the raw image. The median filter is calculated from a moving 10x10 pixel box.	126
Figure III.2.19. Canny edge detector is applied 3x on the 2D filtered image, then the surface is straightened according to the first '1' value at each line of the binary image (red line). The obtained edge is median filtered. The median intensity value is calculated from 20 adjacent pixel points successively (green line).	126
Figure III.2.20. The original image is properly straightened applying the filtered edge.	126
Figure III.2.21. Saturation points affecting the images.	127
Figure III.2.22. Noise crossing the tissue.	127
Figure III.2.23. Straightened Tissue Surface, and mean+std at each depth position.	128
Figure III.2.24. Normalized Sensitivity roll-off.	129
Figure III.2.25. Mean, standard deviation, and standard deviation over mean of 400 A-lines after sensitivity curve correction.	130

Figure III.2.26. STD/MEAN ratio at each depth position in a B-scan on Normal Fat (red), WDLS (cyan), DDLS (black).....	131
Figure III.2.27. Mean intensity from each depth position (blue) and first derivative (red) of a B-scan..	132
Figure III.2.28. a) Windowing scheme on the normalized mean intensity signals from Figure III.2.27 and b) Standard Deviation over Mean at each depth position in the same region. Normal Fat (red-), WDLS (cyan-), DDLS (black line). The region shows 150 pixel - depth from the tissue surface.....	133
Figure III.2.29. GEV Distribution parameters after windowing process, green dots show the optimal window size, the largest separation on the μ - σ plane. One B-scan is analyzed here.	133
Figure III.2.30. Variation of a) μ and b) σ by incrementing window size beginning from the tissue surface, 200 B-scans on Normal Fat Tissue, 160 B-scans on WDLS and DDLS.....	134
Figure III.2.31. Variation of a) μ and b) σ by shifting a 40-pixel size window beginning from the tissue surface, 200 B-scans on Normal Fat Tissue, 160 B-scans on WDLS and DDLS.....	135
Figure III.2.32. GEV parameters, 200 B-scans for Normal Fat Tissue, 160 B-scans for WDLS and DDLS a) σ -, b) μ - variation of B-scans in a tissue volume.	136
Figure III.2.33. GEV parameters on the σ - μ plane. 200 B-scans for Healthy Fat 160 B-scans for WDLS and DDLS. Green point marks the Center of Gravity.....	137
Figure III.2.34. Histogram, GEV Distribution parameters (k, σ, μ) fitted to the STD/mean ratio of the intensity values in ROI; Mean+standard deviation on 200 B-scans of Normal Fat, and 160 B-scans of WDLS and DDLS.	138
Figure III.2.35. Comparison of the GEV Distribution parameters (k, σ, μ) represented at each axe of the 3D coordinate system calculated from the STD/mean ratio of the intensity values; Mean and standard deviation on 200 B-scans of Baseline Tissue and 160 B-scans of Deviation 1&2.	139
Figure III.2.36. Projection planes of the 3D coordinate system on Figure III.2.35. Comparison of the GEV Distribution parameters represented at each axe of the 3D coordinate system calculated from the STD/mean ratio of the intensity values; Mean and standard deviation on 200 B-scans of Baseline Tissue and 160 B-scans of Deviation 1&2.	140
Figure III.2.37. Scheme of the windowing process on the mean normalized B-scans, from a minimum window size of 20 pixels, incremented successively with 1 pixel, and shifted pixel by pixel up to 150 pixel depth.....	140
Figure III.2.38. GEV Distribution parameters (σ, μ) computed from windowing process; green dots show the Center of Gravity. Minimum window size of 20 pixels in a 1 pixel increment and shifted in depth.	141
Figure III.2.39. Variation of a) μ and b) σ computed from a window size of 20 beginning from the tissue surface, and incremented by 5-pixel-shift till 150 pixel depth. 200 B-scans on Normal Fat Tissue, 160 B-scans on WDLS and DDLS.	142
Figure III.2.40. Variation of a) μ and b) σ computed from a window size of 40 beginning from the tissue surface, shifted in depth by 5-pixel-shift till 150 pixel depth. 200 B-scans on Normal Fat Tissue, 160 B-scans on WDLS and DDLS.	143
Figure III.2.41. GEV Distribution parameters computed from ROI on 200 B-scans for Normal Fat Tissue, 160 B-scans for WDLS and DDLS a) σ -, b) μ - variation of B-scans.....	144
Figure III.2.42. GEV Distribution parameters on the σ - μ plane computed from ROI on 200 B-scans for Healthy Fat Tissue, 160 B-scans for WDLS and DDLS. Green point marks the Center of Gravity.	145
Figure III.2.43. Histogram, GEV Distribution parameters (k, σ, μ) calculated from the men normalized intensity values in ROI. Mean and standard deviation on 200 B-scans of Normal Fat Tissue and 160 B-scans of WDLS and DDLS are analyzed.	146

Figure III.2.44. Comparison of the GEV Distribution parameters (k , σ , μ) represented at each axe of the 3D coordinate system calculated from the mean normalized intensity values in ROI. Mean and standard deviation of 200 B-scans of Baseline Tissue and 160 B-scans of Deviation 1&2 are analyzed.....	147
Figure III.2.45. Projection planes of the 3D coordinate system on Figure III.2.44. Comparison of the GEV Distribution parameters represented at each axe of the 3D coordinate system calculated from the mean normalized intensity values at each depth position in ROI. Mean and standard deviation of 200 B-scans of Baseline Tissue and 160 B-scans of Deviation 1&2.	148
Figure III.2.46. Std/mean curves with and without sensitivity roll-off correction of Normal Fat Tissue, WDLS, DDLS on 1 B-scan shown on Figure III.2.2. Solid lines show the computation from the original image, dashed lines show the corrected version.	148
Figure III.2.47. PDF drawn from the GEV parameters of the std/mean curves shown on Figure III.2.46 with and without sensitivity roll-off correction of Normal Fat Tissue, WDLS, DDLS on 1 B-scan shown on Figure III.2.2. Solid lines show the computation from the original image, dashed lines show the corrected version.	149
Figure III.2.48. PDF drawn from the GEV parameters of the std/mean ratio calculated from 200 Normal Fat Tissue, 160 WDLS and DDLS B-scans. Mean+std are shown in black+green for the sensitivity corrected images, and blue+cyan for the original data.	150
Figure III.2.49. PDF drawn from the GEV parameters of the mean normalized intensity curves with and without sensitivity roll-off correction of Normal Fat Tissue, WDLS, DDLS on 1 B-scan shown on Figure III.2.2. Solid lines show the computation from the original image, dashed lines show the corrected version.....	151
Figure III.2.50. PDF drawn from the GEV parameters of the normalized intensity values calculated from 200 Normal Fat Tissue, 160 WDLS and DDLS B-scans. Mean+std are shown in black+green for the sensitivity corrected images, and blue+cyan for the original data.	152
Figure III.3.1. OCT images of Normal Fat Tissue excised from Abdomen/RetroPeritoneum,.....	154
Figure II.3.2. OCT A-line of Normal Fat Tissue (K37) a) arbitrary unit b) dB scale	155
Figure III.3.3. Histology of Normal Fat Tissue from A/RP. The corresponding OCT image is K28.	155
Figure III.3.4. K36 WDLS with mitotic change.....	156
Figure III.3.5. K25 Fibrous Atypical Lipomatous Tumor.....	157
Figure III.3.6. K47 Atypical Lipomatous Tumor/ WDLS with small mitotic change.	158
Figure III.3.7. K58 Lipomatous Tumor with mild cytological atypia.....	158
Figure III.3.8. K35 Highly fibrotic DDLS.	159
Figure III.3.9. K12 Spindle cell sarcoma (DDLS) with osteoid formation.	160
Figure III.3.10. K33 DDLS with extensive myxoid change.....	160
Figure III.3.11. K26b cellular pleomorphic fibromyxoid areas with mitotic figures.	161
Figure III.3.12. Scatterplot classifying Normal Fat Tissue, WDLS and DDLS. 4 tissue samples per tissue type are analyzed, 60 data points per sample are considered.....	162
Figure III.3.13. Scatterplot classifying Normal Fat Tissue, WDLS, DDLS on the projections planes of the 3d coordinate system shown on Figure III.3.12. 4 tissue samples per tissue type are analyzed, 60 data points per sample are considered;	163
Figure III.3.14. Scatterplot representing 12 tissue samples; 4 tissue samples per Normal Fat Tissue, WDLS and DDLS are analyzed, 60 data points per sample are considered.	163

Figure III.3.15. Scatterplot representing 12 tissue samples; 4 tissue samples per Normal Fat Tissue, WDLS and DDLS are analyzed on the projection planes of the 3d coordinate system shown on Figure III.3.14. 60 data points per sample are considered;.....	164
Figure III.3.16. GEV Distribution separating Normal Fat Tissue (red), WDLS (cyan) and DDLS (black); 4 samples per tissue type are presented.	166
Figure III.3.17. GEV Distribution separating 12 tissue samples; 4 tissue samples per Normal Fat Tissue, WDLS and DDLS are presented.	166
Figure III.3.18. Classification of Normal Fat Tissue, WDLS and DDLS. 4 tissue samples per tissue type are analyzed. Middle of the boxes represent the mean, the edges represent the standard deviation of the parameters k, σ, μ	167
Figure III.3.19. Classification of Normal Fat Tissue, WDLS, DDLS. 4 tissue samples per tissue type are analyzed. Mean is the center, standard deviation is the edges of the boxes;	167
Figure III.3.20. Classification of Normal Fat Tissue, WDLS and DDLS. 4 tissue samples per tissue type are represented separately. Middle of the boxes represent the mean, the edges represent the standard deviation of the parameters k, σ, μ	168
Figure III.3.21. Classification of Normal Fat Tissue, WDLS, DDLS. 4 tissue samples per tissue type are represented separately. Mean is the center, standard deviation is the edges of the boxes.	168
Figure III.3.22. Error analysis on the acquired images. a) Improperly straightened tissue surface b) Saturation points c) Tissue surface obliqueness.....	170
Figure III.3.23. a) Straightened Tissue Surface with marked edge b) The tissue surface edge is applied on the perturbed image at three positions.	171

List of Tables

Table I.1.1. General strategy of diagnosing Soft Tissue Tumors [3, 19].	25
Table I.1.2. Algorithm for Imagery evaluation of Soft Tissue Tumors [8].	26
Table I.2.1. WHO Classification of Soft Tissue Tumors (2006) [18].	27
Table I.2.2. WHO Classification of Adipocytic Tumors (2006) [18].	27
Table I.2.3. Retroperitoneal Liposarcoma (RPLS) diagnosis and treatment with CT [25].	32
Table II.1.1. Comparison of biomedical imaging modalities regarding their penetration level, resolution and cost; Optical imaging modalities are marked with yellow [44].	39
Table III.2.1. Coefficients of the exponential equations discriminating Normal Fat Tissue vs. WDLS and DDLS.	122
Table III.2.2. Coefficients of the Normalized Histograms at specific depth position discriminating Normal Fat Tissue vs. WDLS and DDLS.	123
Table III.2.3. GEV parameters calculated from the STD/MEAN ratio of the intensity in ROI, mean and standard deviation is calculated on 200 B-scans of Normal Fat Tissue, and 160 B-scans of WDLS and DDLS.	138
Table III.2.4. Comparison of the GEV Distribution parameters calculated from the STD/mean ratio at each depth position in ROI; mean and standard deviation on 200 B-scans of Baseline Tissue and 160 B-scans of Deviation 1&2 is calculated.	139
Table III.2.5. GEV parameters (k, σ, μ) from the mean-normalized intensity values in ROI. Mean and standard deviation calculated from 200 B-scans of Normal Fat, and 160 B-scans of WDLS and DDLS.	146
Table III.2.6. Comparison of the GEV parameters calculated from the mean-normalized intensity values in ROI. Mean and standard deviation on 200 B-scans of Baseline Tissue and 160 B-scans of Deviation 1&2.	147
Table III.2.7. GEV Distribution parameters, computed on the std/mean ratio at 1 B-scan of Normal Fat Tissue, WDLS and DDLS; left: no correction is applied (Solid line on Figure III.2.47), right: sensitivity-correction is applied (Dashed line on Figure III.2.47)	149
Table III.2.8. GEV parameters calculated from the std/mean ratio of the intensity values in ROI; mean and standard deviation on 200 B-scans of Normal Fat Tissue, and 160 B-scans of WDLS and DDLS are shown.	150
Table III.2.9. Comparison of the mean GEV parameters calculated from the std/mean ratio of the intensity values in ROI with and without correction on 200 B-scans of Normal Fat Tissue, and 160 B-scans of WDLS and DDLS.	150
Table III.2.10. GEV Distribution parameters computed on the mean normalized intensity values at 1 B-scan of Normal Fat Tissue, WDLS and DDLS; left: no correction is applied, right: sensitivity-correction is applied.	151
Table III.2.11. GEV parameters calculated from the mean-normalized intensity values in ROI; mean and standard deviation from 200 B-scans of Normal Fat Tissue, and 160 B-scans of WDLS and DDLS.	152
Table III.2.12. Comparison of the mean GEV parameters calculated from the mean-normalized intensity values in ROI with and without correction on 200 B-scans of Normal Fat Tissue, and 160 B-scans of WDLS and DDLS.	153

Table III.3.1. Mean, standard deviation, and standard deviation per mean of Generalized Extreme Value Distribution parameters (k , σ , μ) computed from 4 samples per Normal Fat Tissue, WDLS and DDLS. 165

Table III.3.2. Errors coming from not properly straightening the tissue surface..... 172

Table III.3.3. Errors coming from saturation and surface obliqueness..... 173

Introduction

Revealing structural property of biological material, the normal, inflammatory, benign or malignant state of the tissue can be established. In clinical practice, diagnosis of cancer from structural features is validated by histological analysis. Applying imaging modalities is the first step to complete a diagnosis. It reveals the tissue topology and cellular components without excising the tissue, and it gives a good direction for micro-biopsy.

Structural property of the tissue can be described by its optical scattering properties. The scattering property is measured using Optical Coherence Tomography (OCT). OCT is a noninvasive measurement technique based on the optical coherence theory of a broadband laser light or white light. It performs high resolution (1-15 μm) optical biopsy, scanning the internal microstructure under the surface. Optical Coherence Tomography has already been used for multiple types of cancer disease diagnostics in research and clinical applications.

The main purpose of our project is to develop fast and non-invasive OCT (Optical Coherence Tomography) based techniques for tissue diagnostics and monitoring. Our goal is to identify computational models that quantify tissue properties using Imaging-based data. Since a tumor is differentiated from healthy tissue based on morphological analysis, model-based approach to cancer diagnosis is developed.

Instead of subjective image analysis, we approach the diagnosis from mathematical point of view in order to quantify topological changes. A statistical model-based imaging method is created based on the images analyzing the scattering properties distinguishing various tissue types using the example of human Normal Fat Tissue vs. Well-Differentiated- (WD-), and De-Differentiated Liposarcoma (DDLs), but the idea can be broadened toward the analysis of other type of cancer since the diagnosis is based on morphology.

A set of image-based measurements will form the model. The outcome from these computations is the assignment of parameterized models to tissue type, grade of cancer detected from the scattered light wave. These parameters are paramount in the determination of the tissue optical and structural properties. The aim would be quantitatively characterizing different tissue types based on their scattering properties.

A new method is described here to quantify tissue properties in the structural features from OCT measurements distinguishing between tissue types. A model-based laser imaging technique is developed to enable prognosis. We use the adapted model coefficients to classify the tissue as healthy or cancerous. This model based imaging can become a clinical tool to provide a second opinion for physiologists. The results of this work would be the basis of a new cancer detector device.

I. Soft Tissue Diagnostics

I/1. Soft Tissue Tumors and Diagnosis

I/1/a. Soft Tissue Tumor (Sarcoma)

The origin of tumor comes from the disease of genes, which disturbs the cell mechanism, resulting to uncontrolled cell-division and growth. Benign tumors do not spread to other parts of the body, unlike malignant tumors, called cancer. Highly dangerous cancer metastasizes having the ability to travel toward other parts of the body through the lymphatic or vascular system.

Carcinoma is the most commonly diagnosed cancer (90%), it originates from the epithelium of the organs that covers the surface of the body and the internal organs. Sarcoma originates from the connective tissue (bone, muscle, fat, tendon, cartilage). Melanoma arises from the pigment cells of the skin, Lymphoma is the cancer of lymphocytes from bone marrow and lymph nodes (to fight infection), Leukemia is the white cells' cancer, Myeloma is the cancer of plasma cells in bone marrow. The 3 latter types is the disease of immune system to fight against infection. Nerve cell cancer comes from brain or spinal cord, germ cell cancer comes from reproductive cells [1].

We can classify cancer depending on which body cells they start in. The body cells are grouped according to their embryonic origin, where the germ layer is divided into 3 parts: ectoderm (skin and nervous system), mesoderm (supporting tissue) and endoderm (internal organs). [2]

Soft tissue is derived from the mesoderm layer of the embryonic stage. It is the supportive, connective or surrounding structure of the body (mesenchymal tissue) including muscle that supports bones, tendons and ligaments that connect muscles and bones, synovial tissue of joints (cartilage), fascia surrounding the musculoskeletal system, and supportive network providing systems of circulation, transport and defense, including nerves, blood vessels, lymphatics, bone marrow and fat [3].

Figure I.1.1 shows the development of the mesenchymal tissue types.

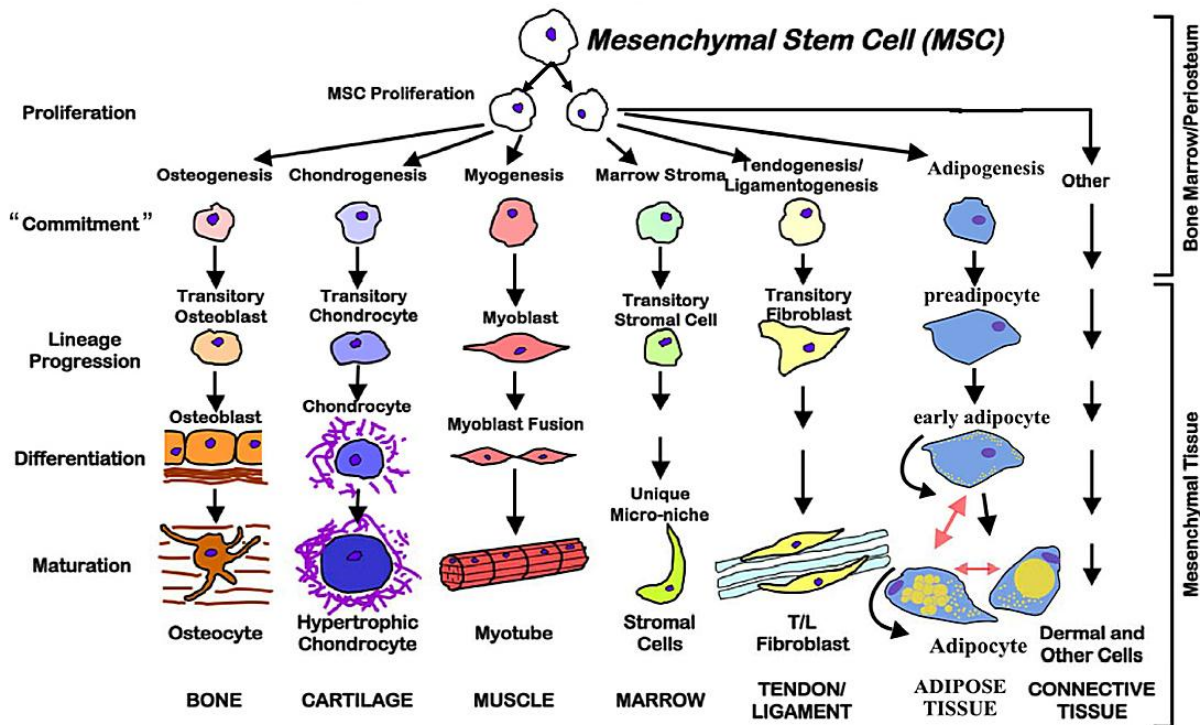


Figure I.1.1. Soft Tissue Development. MSC: Mesenchymal Stem Cell [2].

Soft tissue sarcomas are uncommon malignant tumours, 1% of all cancers, and the ratio of malignant (sarcoma) vs. benign (lipoma) soft tissue tumor is 1:100. Most occurs in adults, 15% in children and adolescents. Although there are various types of soft tissue sarcoma, they generally share similar characteristics, produce similar symptoms and are treated in similar ways [4, 5, 6].

Sarcomas are age and site specific, they can occur in extremities (skin, subcutis, trunk, head, neck) and deeply (beneath deep fascia, in skeletal muscle, abdomen/retroperitoneum, mesentery, omentum, mediastinum), some types are more common at certain age and site and gender. They can arise anywhere in body, including viscera, not only in specific organs. They can reach large sizes before symptoms [6].

I/1/b. Symptoms and Diagnosis

Most sarcomas present as painless, enlarging mass lesions without characteristic clinical symptoms. The findings are swelling, palpable mass, with possible tenderness or pain and loss of function in case there is compression of adjacent structures. [6] To detect the suspected lesion and establish a diagnosis and the staging of cancer, multidisciplinary analysis is required prior to biopsy including pathologist, surgeons, oncologists, radiologists [3]. Clinical features, the age of the patient, the size and location of the lesion, the tumor growth pattern are important factor in the diagnosis [7].

Screening in non-symptom patients or imaging after detecting a palpable mass is an essential step of disease diagnosis. Imaging can confirm the existence and type of tumor (lesion

detection and staging), whether it is benign or malignant and able to metastasize. It identifies a specific or differential diagnosis and guides therapy decisions. It gives direction for micro-biopsy for histology to establish the final diagnosis and a sampling strategy, and assess tumor behavior in response to treatment. Imaging methods, as Computed Tomography, Ultrasound and Optical Coherence Tomography guide deep-seated lesion sampling [3, 8, 9-12]

Histological excision should always confirm the imaging diagnosis. Soft tissue tumor is sampled with fine needle aspirates (FNA) and core needle biopsies (CNBs). FNA is a first-line diagnostic procedure performed under local anesthesia using a long, thin needle (diameter = 0,4-0,8mm) to draw out fluid and cells for analysis. CNB is used (diameter = 1,2-1,4mm) to draw a column of tissue out of a suspicious area [3].

Accurate diagnosis can be stated on the basis of morphology (imaging + histology) and a combination of ancillary techniques: immunocytochemistry (antibodies targeted on peptides or protein antigens labeling within cells), immunohistochemistry (antibodies targeted on peptides or protein antigens labeling within excised tissue), genetic techniques (Omics technologies, Genomics, Proteomics, Metabolomics) [3].

I/1/c. Imaging Modalities for Soft Tissue Tumors

Diagnoses of cancer in soft tissue tumors with the help of imaging modalities have two main branches depending on the type of information they produce. One group is the structural/ anatomical imaging (Ultrasound (US), X-ray, Computed Tomography (CT), Magnetic Resonance Imaging (MRI)), the other one is the metabolic/ functional/ chemical imaging (MRI with a spectroscopy option, single-photon emission CT, positron emission tomography (PET), fluorescence spectroscopy, diffuse imaging). [12, 13]

Despite the advantages of chemical imaging, the structural identification remains the main factor in cancer diagnosis [8]. Analyzing structural features (imaging & histology) is the most important tool to diagnose normal and cancerous fat tissue [14, 15]. Functional imaging is an additional tool to detect physiology and molecular mechanisms [12].

1. Structural Imaging Methods for Soft Tissue Tumors

Conventional radiography (X-ray) without contrast agents (plain film) is the first diagnostic tool for soft tissue revealing skeletal deformity, calcification, which can be suggestive of tumor. CT, MRI and US are 3D methods with superior contrast resolution compared to conventional radiograph [3,8].

US and MRI are the most valuable techniques evaluating soft tissue masses. US is better for superficial lesions and MRI for deep, large or diffuse lesions. CT is a complementary tool in detecting calcification and joint or bone involvement, differentiating lipomatous tumors, detecting tumor recurrence, and response to therapy [7, 16, 17].

MRI follows the radiographic analysis. It is the optimal imaging tool of soft tissue tumors regarding contrast resolution and multi-planar views acquisition. MRI and CT are able to detect tumor place, size and border and relationship to adjacent structure [3, 8, 10, 11, 18].

MR Imaging provides better tissue discrimination between normal and abnormal tissues than any other imaging modality, but MRI remains nonspecific to characterize benign or

malignant lesion, and having inability to detect calcification it should be evaluated in conjunction with radiograph or other imaging methods [8, 18].

MRI with contrast agents is used in specific cases but usually without increasing the sensitivity to detect soft tissue mass. MR spectroscopy is not used routinely in diagnosis, but can be helpful in differentiating soft tissue tumors [3, 8].

Ultrasonography is a low-cost, real-time, readily available, relatively inexpensive method of detecting soft tissue tumors without contrast agent and ionizing radiation. US does not specify soft tissue masses and diagnosis. It confirms the presence, shape, size and internal characteristics/echoes of suspected lesion, calcification, compressibility and vascularity. US guides percutaneous biopsy and monitors therapy. US with plain film diagnose some pseudotumors, benign tumors or malformations in clinically and radiologically suggestive cases [7, 8, 11].

US Doppler does not establish diagnosis, but confirms the vascular feature of a lesion, response to chemotherapy or radiotherapy, necrosis and decrease of lesion size. It is better for superficial lesion having a limited field of view, and less contrast [3, 8, 11].

Ultrasonography can be used for identification of recurrent tumor, but very operator dependent and less valuable in case of complex osseous anatomy, so MRI is more preferable. Table I.1.1 shows a general strategy of diagnosis. An algorithm for the imagery evaluation of a patient with a soft tissue mass is presented in Table I.1.2 from imaging suspicious area, through staging of lesion till performing biopsy [3, 19].

Angiography can reveal tumor size, extent, source, and degree of vascularity and malignancy. Histologic diagnosis cannot be based on angiographic imaging, but it guides surgical planning and therapy treatment [20-22].

Characteristics of tissue structural properties are studied non-invasively with these different imaging modalities [12, 13]. Each works at different scale based on different physical principles using specific frequency range of the electromagnetic spectrum. These techniques optimally are coupled for multidisciplinary analysis of soft tissue mass and for guidance of micro-biopsy [23].

They are used in clinical practice to evaluate Soft Tissue Tumors, but do not provide sufficient resolution in detecting tumor margins having large instrument footprints, and require long imaging time and occasional contrast agents. Optical Coherence Tomography (OCT) is another optional real-time imaging technology with higher spatial resolution [23-26].

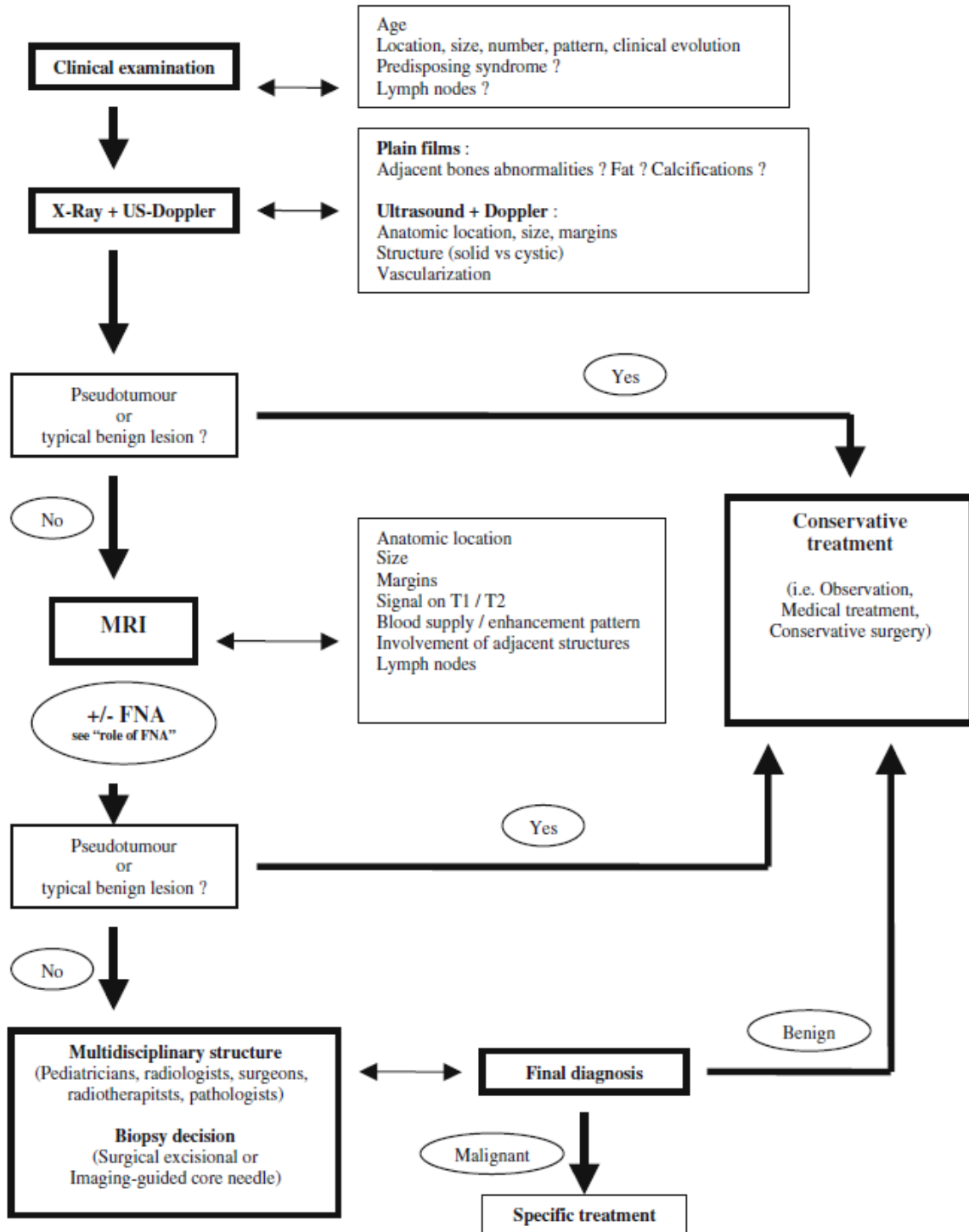


Table I.1.1. General strategy of diagnosing Soft Tissue Tumors [3, 19].

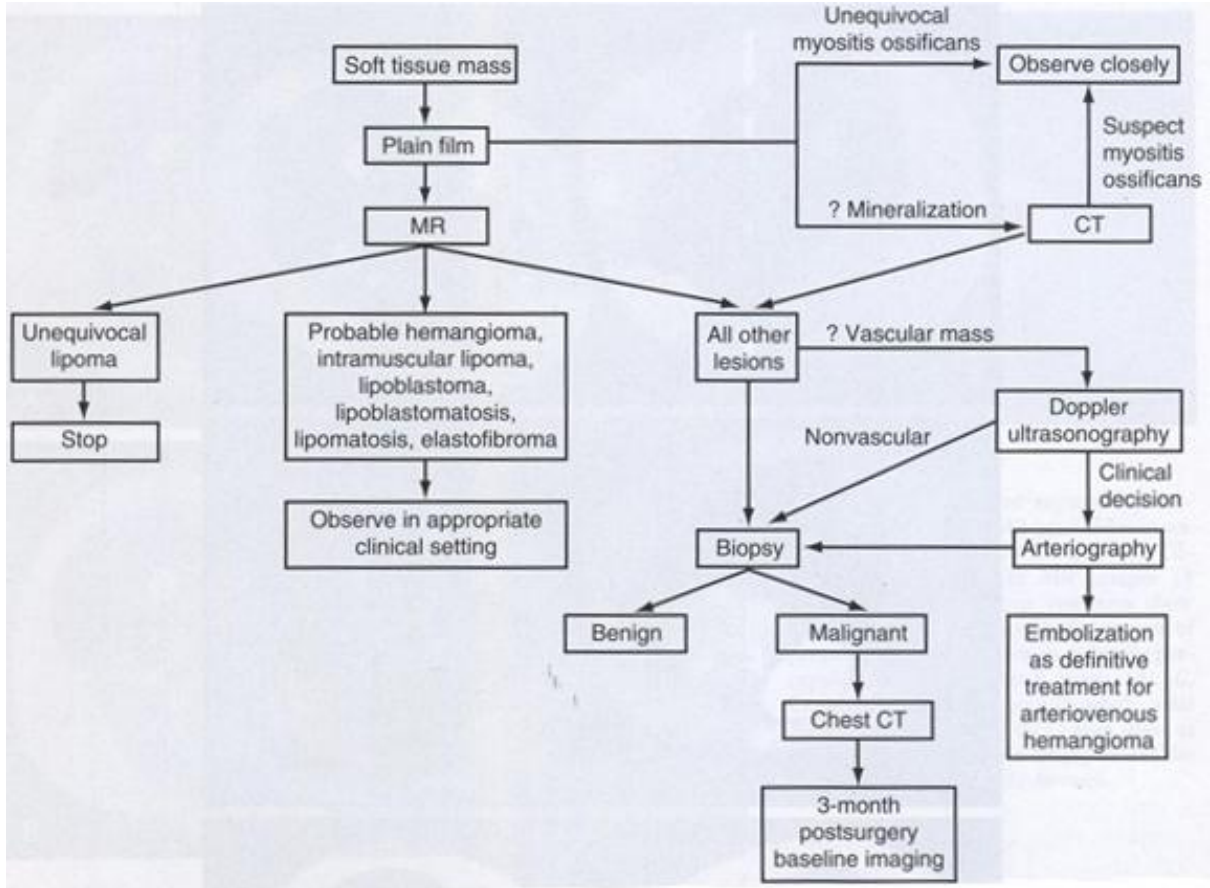


Table I.1.2. Algorithm for Imagery evaluation of Soft Tissue Tumors [8].

2. Functional Imaging Methods for Soft Tissue Mass

Functional or molecular and cytogenetic imaging can provide additional information to structural analysis giving enhanced or earlier tumor detection or more biological information to precise histological subtypes, to improve treatment decisions and predict response to therapy. [12, 27, 28].

Positron Emission Tomography (PET) is a recent technique in evaluating soft tissue tumors and further analyses are needed for diagnosis and staging [3]. The technique is selectively used for distinguishing benign tumors from high grade sarcomas, pretreatment grading of sarcomas, and evaluation of local recurrence [18]. FDG-PET (fluorodeoxyglucose-PET) can improve the anatomic details with CT and distinguish benign from malignant tumors [11]. Furthermore biopsies can be guided by FDG-PET towards the most malignant sections of tumors [29]. Scintigraphy has role in case of metastasis [8, 11].

I/2. Adipocytic Tumors and Diagnosis

I/2/a. Adipocytic Tumor (Liposarcoma)

Soft tissue tumors are relatively rare, and Liposarcomas (Cancerous Fat Tissue) are the most common soft tissue sarcomas (STS), they account 20% of all sarcomas in adults [14]. They are the most common primary retroperitoneal malignant tumors [30].

According to the WHO report on Soft tissue tumors, Liposarcoma is part of the Adipocytic Tumors (Tables I.2.1&2) [4, 18, 31]. Adipocytic tumor is the cancer of Fat Tissue.

Adipocytic tumors
Fibroblastic / Myofibroplastic tumors
So-called fibrohistiocytic tumors
Smooth muscle tumors
Pericytic (Perivascular) Tumors
Skeletal Muscle Tumors
Vascular Tumors
Chondro-osseus tumors
Tumors of uncertain differentiation

Table I.2.1. WHO Classification of Soft Tissue Tumors (2006) [18].

Benign	Lipoma
	Lipomatosis
	Lipomatosis of nerve
	Lipoblastoma/ Lipoblasomatosis
	Angiolipoma
	Myolipoma
	Chondroid Lipoma
	Extrarenal angiomyolipoma
	Extra-adrenal myelolipoma
	Spindle cell lipoma
	Pleomorphic lipoma
	Hibernoma
Intermediate (locally aggressive)	Atypical lipomatous tumor/ Well differentiated liposarcoma
Malignant	Dedifferentiated liposarcoma
	Myxoid liposarcoma
	Round cell liposarcoma
	Pleomorphic liposarcoma
	Mixed-type liposarcoma
	Liposarcoma, not otherwise specified

Table I.2.2. WHO Classification of Adipocytic Tumors (2006) [18].

Diagnosis of Liposarcoma and classification into subtypes is based on morphological features and cytogenetic aberrations. Analyzing structural features (histology) is the most important tool to diagnose normal and cancerous fat tissue [14, 15, 18].

The morphology of the Normal Fat Tissue is built up from clusters of large adipose cells (70-130 μm) often with thin capillaries [32]. The adipocyte (fat cell) contains a plenteous cytoplasm filled with lipid droplets, and small, dark, regular nuclei (Figures I.2.1&2) [9].

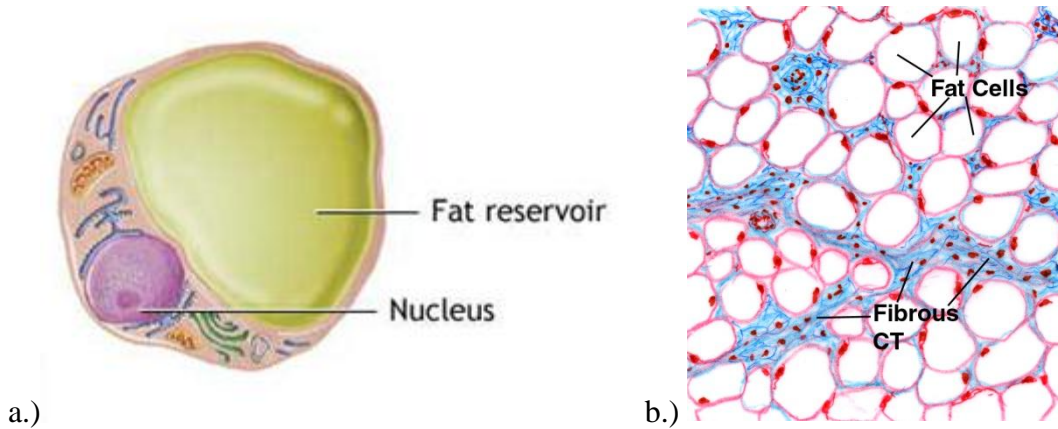


Figure I.2.1. a) Adipocyte b) Adipose tissue with fibrous septa (dividing wall) between clusters of adipocytes. CT- Connective Tissue [33, 34].

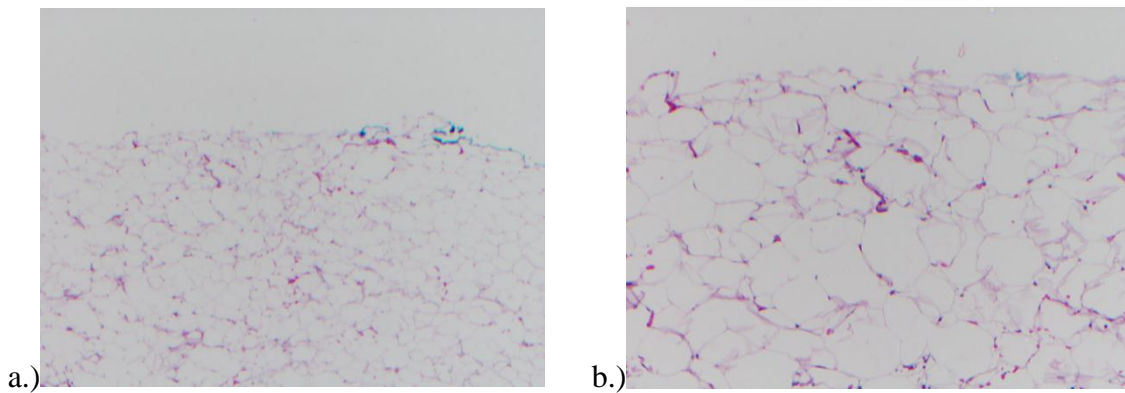


Figure I.2.2. Normal fatty tissue with large fat cells. Histology (H&E – Hematoxylin & Eosin stain). Magnification: a) 4x, b) 10x.

In reactive states, posttraumatic, inflammatory or in adipose tissue bordering various tumors, cellular changes can be seen in the adipose tissue: myxoid-like background [consisting of an amorphous mucoïd material] (Figure I.2.3a), enhanced capillary network, adipocytes varying in size (Figure I.2.3a&b) and more cellularity due to the presence of fibroblasts and histiocytes (Figure I.2.3b) [9].

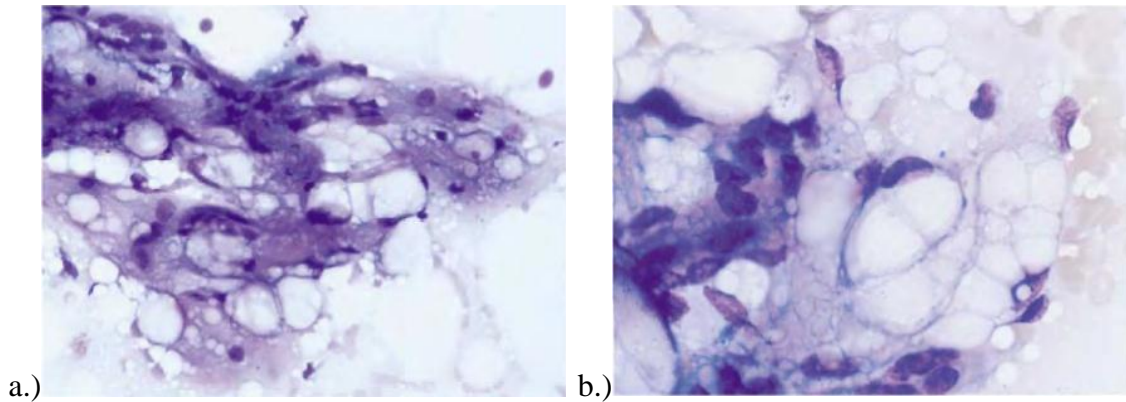


Figure I.2.3. Adipose tissue in reactive states. Medium magnification [9].

Liposarcoma is the group of histologically and genetically distinct sarcomas with fatty differentiation. It is one of the most common soft tissue sarcomas with a ratio of 20 % in adults. The majority is deep-seated, intra- or intermuscular tumors, the most common sites are the extremities, trunk and retroperitoneum [9, 11, 35].

The histological classification of Lipoma (benign) and Liposarcoma (malignant or intermediate) with histological subtypes, age and site occurrence, genetic changes on chromosome is described in **Appendix 1**.

In this study we differentiate Normal Fat Tissue from Intermediate (locally aggressive) tumor, so called Well-Differentiated Liposarcoma (WDLS) and from one type of Malignant tumor, called De-Differentiated Liposarcoma (DDL) [18].

Well-differentiated Liposarcoma is the most common variant of LS with 50 % ratio, it can occur mainly in late adult life in extremities and retroperitoneum. In this latter case there is more recurrence and hence higher mortality rate. It is a non-metastasizing low-grade tumor with the ability to dedifferentiate [4, 9, 35]. In this study the next WDLS subtypes will be analyzed:

Atypical lipoma/lipoma-like well-differentiated liposarcoma (Figure I.2.4) represents variation in adipocyte size, and focal nuclear atypia. Figure I.2.4a shows increased cellularity with histiocytic infiltration. Figure I.2.5 zooms to the atypical adipocytes in lipoma-like WDLS featuring enlarged nuclei, intranuclear vacuoles and hyperchromasia. Figure I.2.6 is lipoma-like WDLS with stromal sclerosis, with characteristics of expanded, hypercellular fibrous septa. Figure I.2.7 depicts WDLS with myxoid features mainly found in the retroperitoneum. On Figures I.2.7a&c multivacuolated lipoblasts are present focally, on Figures I.2.7c&d capillaries are enhanced [11].

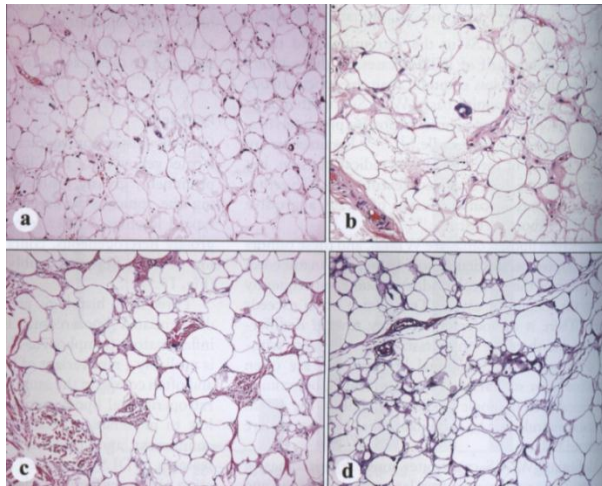


Figure I.2.4. Atypical lipoma/lipoma-like WDLs M: 4-10x [11].

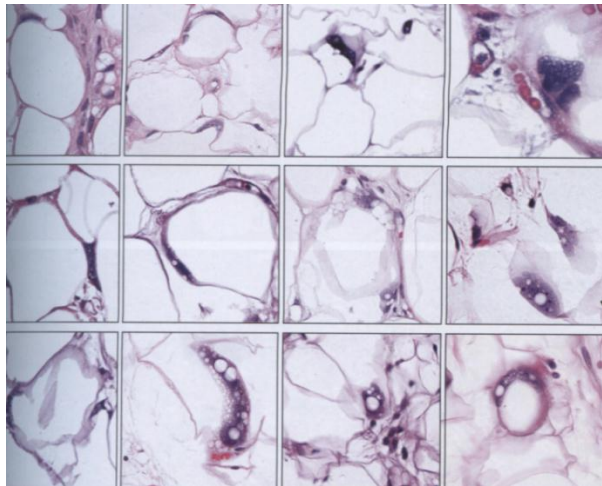


Figure I.2.5. Atypical adipocytes in atypical lipoma/lipoma-like WDLs [11].

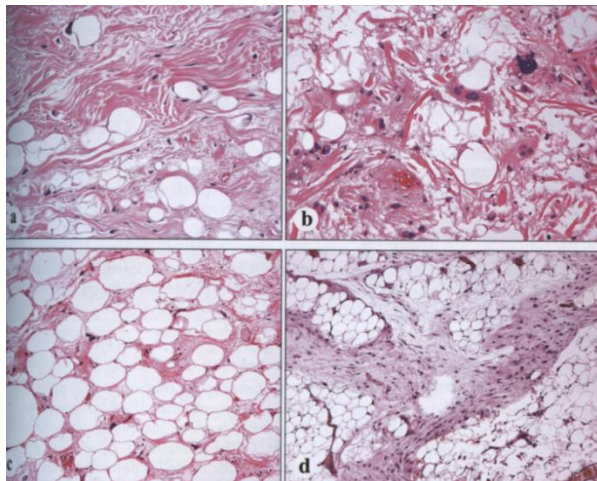


Figure I.2.6. Stromal sclerosis in Atypical lipoma/lipoma-like, WDLs [11].

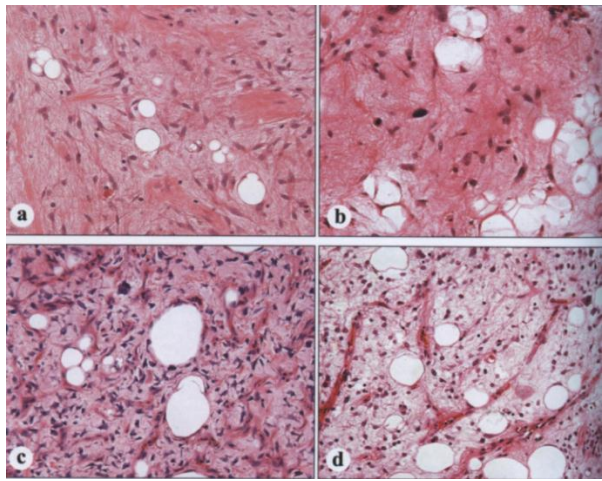


Figure I.2.7. WDLs with myxoid features [11].

De-differentiation occurs in approximately 10% of well differentiated liposarcomas of any subtype, especially in deep-seated tumours, such as those located in the retroperitoneum. The dedifferentiated components may present in the primary tumor or in a recurrence. They are fully malignant tumours, and have high risk for recurrence, metastasis and mortality. Dedifferentiated liposarcoma tends to recur locally in around 40% of cases. Approximately 15–20% of cases show distant metastases [4, 30, 35]. In this study DDLS subtypes with fibrotic, myxofibrotic and pleomorphic changes will be analyzed (Figures I.2.8&9):

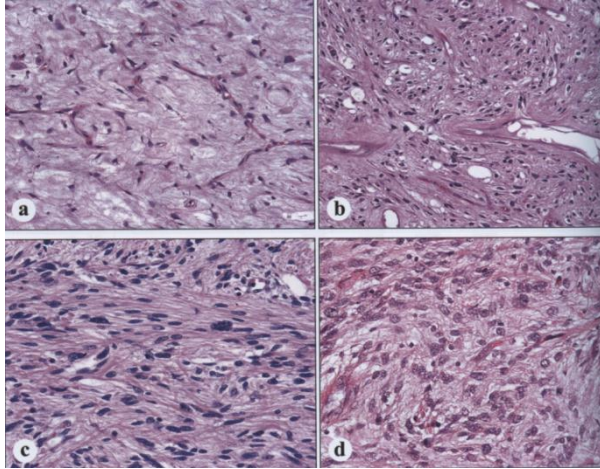


Figure I.2.8. DDLs subtypes: a. Myxofibrosarcoma b. Solitary fibrous tumor c. Fibrosarcoma d. Gastrointestinal stromal tumor [11].

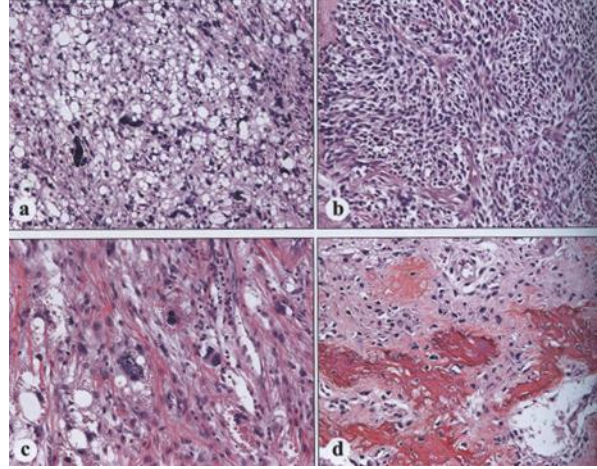


Figure I.2.9. DDLs subtypes: a. Pleomorphic liposarcomatous component b. Mildly pleomorphic spindle cell sarcoma c. Pleomorphic component with large cells containing eosinophilic hyaline globules d. Osteosarcomatous differentiation [11].

WD and DD could stem from different cellular clones, but it is also possible that DD evolves progressively from WD. Since, as opposed to WD, DD is liable to metastasize and therefore has a much worse prognosis, the treatment strategy to eliminate it is much different from that against WD. It is therefore very important to carefully diagnose the type of affliction, DD or WD, before any operative intervention is attempted [25].

I/2/b. Objectives: Diagnosis of Liposarcoma

Liposarcomas are the most radiosensitive soft-tissue tumors. Conventional plain radiography (X-ray) is nonspecific, not being able to differentiate malignant from benign and inflammatory states. It shows higher radiopacity in case of higher tumor grade, and reveals cancer in case of calcification. Figure I.2.10 shows an abdominal X-ray with soft tissue tumor in the retroperitoneum. The diagnosis is based on the colonic gas shadow and bowels displacement, effacing normal fat planes and focal calcifications in the left iliac fossa and lumbar region [7, 16, 36].



Figure I.2.10. X-ray of the abdomen with soft tissue tumor findings [36].

CT can distinguish WDLs based on the large fatty elements, but differentiate between malignant from benign variant and diagnose poorly differentiated tumors is cumbersome [16, 17].

Imaging Findings to classify Liposarcoma into Histologic Subtypes are: Median tumor size, Average fat content, Irregular margins, Tumor infiltration to an organ, Involved Major vessels, Heterogenous tumor (nonadipose elements detected), Focal nodular/water density area, Ground-glass opacities, Hypervascularity, Cystic degeneration/Necrosis, Septations and Calcifications [25].

Amongst those parameters the radiologic evaluation with CT is the most sensitive to the presence or absence of focal nodular/water density area as a marker of dedifferentiation diagnosing well DD, however some WDLs can be over-diagnosed to be DDLS (Table I.2.3) [25].

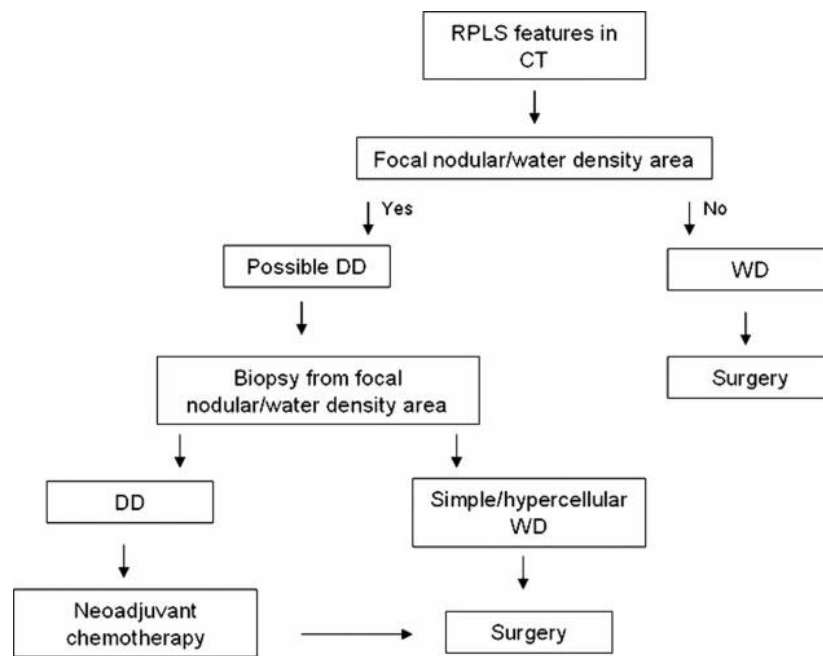


Table I.2.3. Retroperitoneal Liposarcoma (RPLS) diagnosis and treatment with CT [25].

Figure I.2.11a shows CT with large WDLS and smaller DDLS region. Figure I.2.11b is a different patient under biopsy taken from DDLS region.

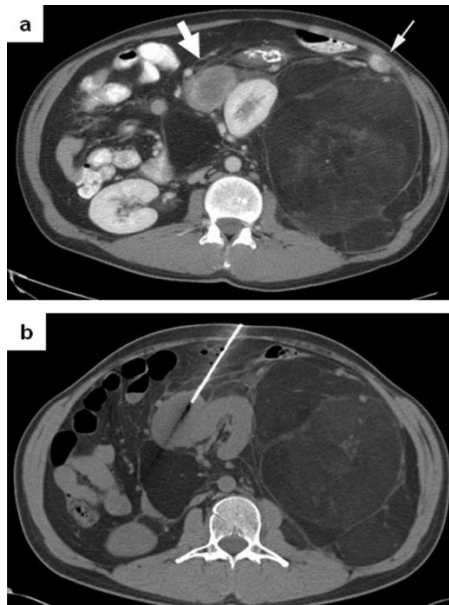


Figure I.2.11. CT of LPS in the Retroperitoneum.

- a. Large white arrow points to suggestive WDLS region (focal nodular/water density area), smaller white arrow points to DDLS region (focal nodular/water density area).
Cancer findings in this LPS:
calcification in a water density nodule anterior to displaced kidney,
ctypical fatty tissues,
thickened septa,
ground-glass opacities.
- b. Biopsy from confirmed DDLS [25].

An additional modality (radiologic/histologic) is needed for accurate diagnosis. MR is the useful technique as it can detect the varying proportions of fatty and non-fatty tumor and accurately document the relationship of the tumor to the surrounding structures [7, 16, 25].

On Figure I.2.12 fat suppression sequences confirm the presence of adipose tissue. It may look normal fat in case of WDLS also containing entirely adipose cells. Areas that disappear in the fat suppression sequences and show different enhancement levels on MR scan (e.g. thick fibrous septa) are consistent with a well-differentiate liposarcoma (white arrow). [7, 30].

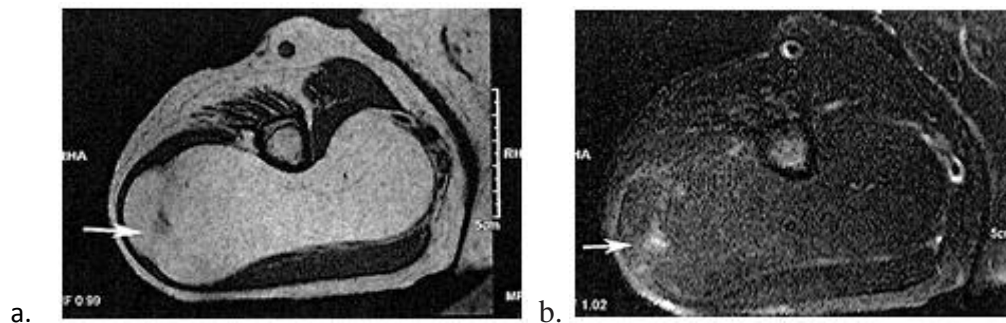


Figure I.2.12. a) T₁ weighted- b) T₂ weighted fat saturated axial MRI of a liposarcoma [7].

Enhancement following intravenous contrast material is seen in all liposarcomas, but also in some benign lesions. Both, CT and MRI identify adipose tissue, CT and MR images of well-differentiated liposarcoma and normal fat are similar and difficult to diagnose [30, 37].

The diagnosis of a dedifferentiated liposarcoma should be considered when an abdominal mass shows on CT and MR imaging intense enhancement, adjacent organs invasion, vascular infiltration, calcification or ossification, and areas of necrosis or haemorrhage [30, 37].

MR characterizes better fat-containing mass, CT detects better calcification or ossification revealing tumor in soft tissue, and CT is used in certain cases where MRI is not applicable, such as at air/tissue interface and during motion artifact (chest wall and anterior abdominal wall) [3, 8, 18].

Ultrasonography can confirm the presence of a tumorous mass. Poorly differentiated tumors are less reflective, so less distinguishable. On Figure I.2.13a WDLS on US is hyperechoic relative to adjacent muscle. On Figure I.2.13b Color Doppler US shows DDLS as hypoechoic tumor. In both cases vascularity is present within the lesion [7, 16, 38].

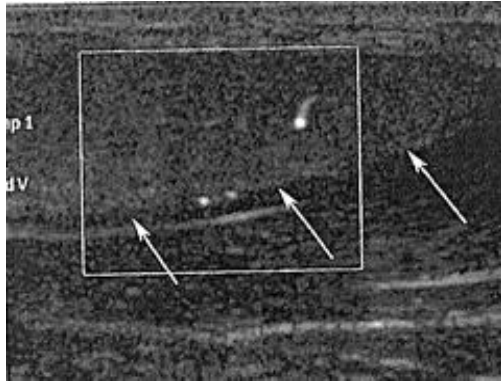


Figure I.2.13. Doppler ultrasound on LS [7, 38].
a) Doppler ultrasound of a WDLS [7].

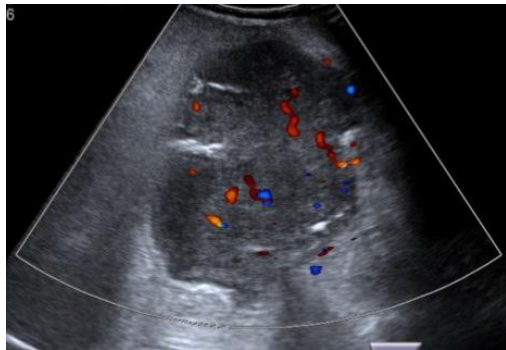


Figure I.2.13.b) Color Doppler ultrasonography of a DDLS [38].

Bening and malignant tumors can be also avascular. Liposarcoma usually has higher vascularity than lipoma. (Doppler) US or Angiography can reveal this feature. They are not able to differentiate tissue types but are useful to establish the location of tumorous mass due to the displacement of organs and major vessels except in case of very small tumors [16, 39].

Angiography is valuable for preoperative planning, intra-arterial infusion, and transcatheter embolization. Figure I.2.14 shows a moderately hypervascular liposarcoma with irregular, fine tumor vessels and tumor stain area [16].



Figure I.2.14. Moderately hypervascular tumor in the right upper thigh [16].

Furthermore Optical Coherence Tomography can provide higher spatial resolution. It screens subsurface structure giving images at the cellular scale (Figure I.2.15), so it has major value for surgical application in guiding micro-biopsy and detect tumor boundary. Due to the limited penetration depth (1-3 mm), for deep-seated tumors application of needle/catheter is needed [24].

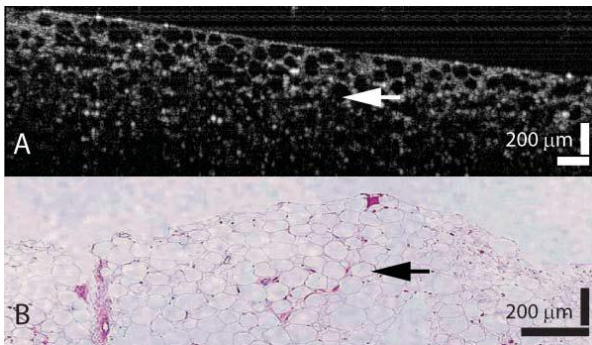


Figure I.2.15. Comparison of OCT image and Histology.

Figure I.2.15.a) Normal Fat Tissue A. OCT B. H&E histology; arrow: adipocyte [24].

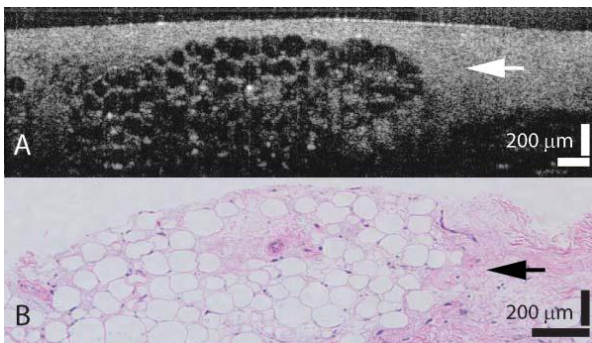


Figure I.2.15.b) WDLS A. OCT B. H&E histology; arrow: fibrous tissue. [24].

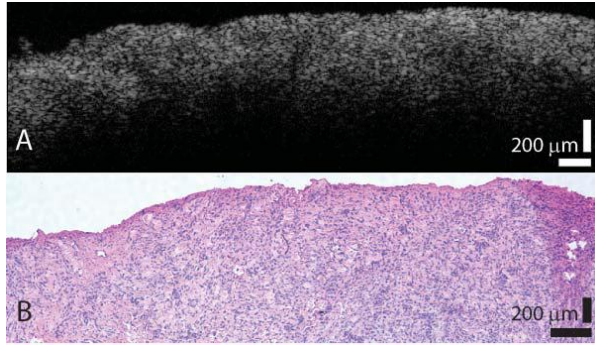


Figure I.2.15.c) DDLS A. OCT B. H&E histology [24].

Besides structural analysis, functional imaging methods applied on LPS should be also mentioned. Nuclear Imaging provides information in 2D (Scintigraphy) and 3D (Positron Emission Tomography). Scintigraphy ^{67}Ga scanning, thallium-201 (^{201}Tl) chloride, technetium-99m ($^{99\text{m}}\text{Tc}$) pertechnetate, $^{99\text{m}}\text{Tc}$ bleomycin and $^{99\text{m}}\text{Tc}$ pentavalent dimer-captosuccinic acid ($^{99\text{m}}\text{Tc}[\text{V}]\text{-DMSA}$) scanning have been proved in diagnosing liposarcoma [16].

The imaging with fluorine-18 fluorodeoxyglucose (^{18}F FDG) positron emission tomography (PET) scanning (FDG-PET) depicts the increased metabolism in abnormal tissues, enabling visualization and quantification in vivo. FDG-PET can discriminate between sarcomas and benign tumors and low and high grade sarcomas based on the mean SUV (standardized uptake value). [16, 29, 40]

PET/CT with FDG glucose is becoming the most important diagnostic imaging tool in oncology. Studies have shown the improved diagnosis of the incorporation of molecular PET and anatomical CT imaging over PET or CT solely [29] (Figure I.2.16).

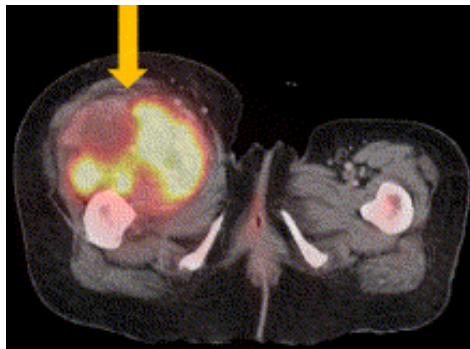


Figure I.2.16. FDG-PET/CT image of high grade soft tissue sarcoma in the right thigh with high FDG uptake (SUVmax, 18.4). [29].

In several cases the structural diagnosis is accompanied with molecular diagnosis having a particular importance in the classification of soft tissue tumors especially Liposarcomas [41].

Bioluminescence Imaging can detect tumor before gross examination (Figure I.2.17.)

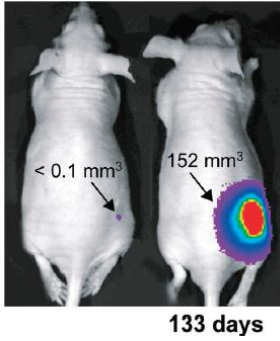


Figure I.2.17. Luciferase-labeled human Liposarcoma cells injected subcutaneously in SCID mice. Left mouse with the non-angiogenic dormant tumor undetectable by gross examination. Right mouse with developed angiogenic tumor after 133 days. The tumor is palpable ~23 days after well detectable bioluminescence signal [42].

Molecular analysis based on Fluorescence Images made on Normal Fat Tissue, WDLS and DDLS can be seen on Figure I.2.18.

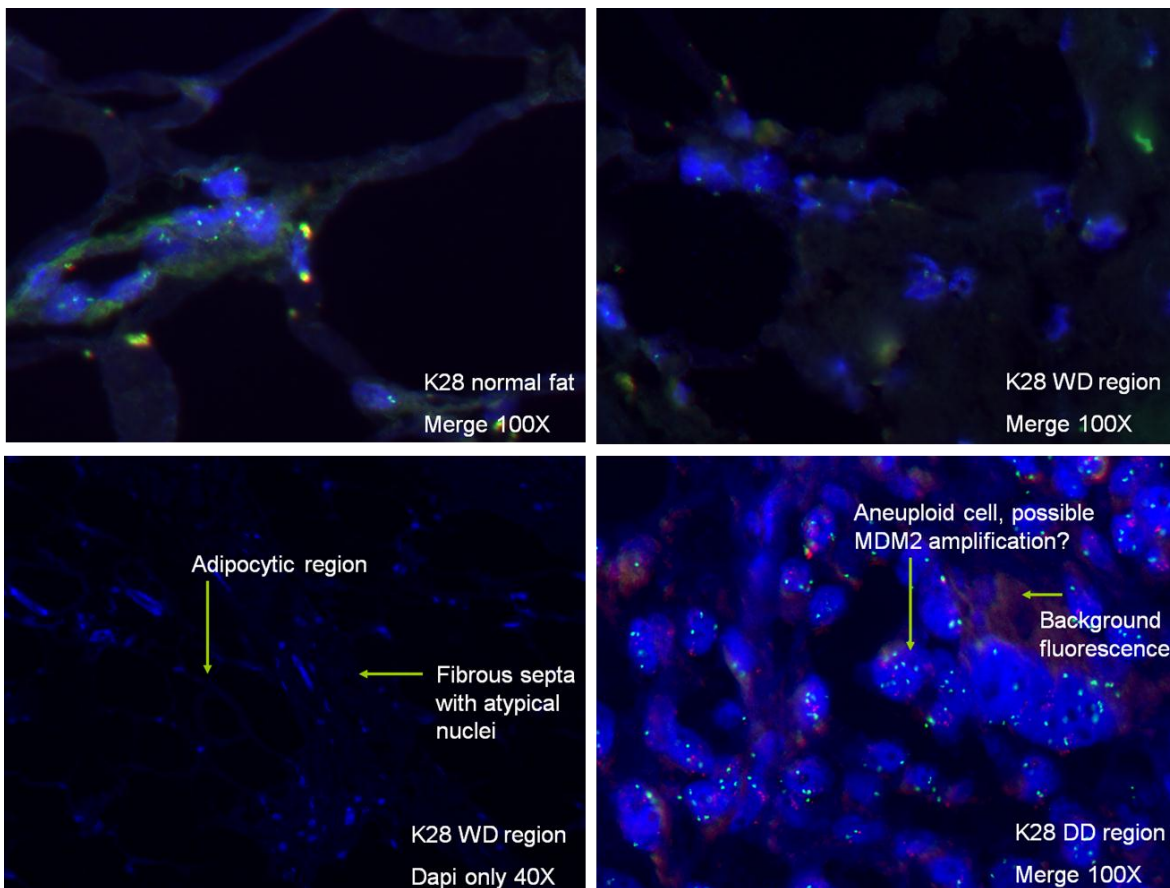


Figure I.2.18. Fluorescence images of Normal Fat Tissue, WDLS and DDLS. FISH analysis (Fluorescence in situ hybridization) Fluorophores: Centromeric probe (green), MDM2 probe (red), Dapi nuclear stain (blue).

Centromere is part of DNA in the middle of the chromosome. Amplification of MDM2 gene shows tumor, Dapi nuclear staining reveals the atypical nuclei in the fibrous region of WDLS, and the high density of nuclei in DDLS.

In significant cases, WDLS/DDLS show an amplification of chromosome 12q13-15, which holds the marker genes CDK4 (regulates cell cycle) and MDM2 (negatively regulates p53 stability) [43].

With the progress of molecular imaging methods, LPS classification into subtypes has been promoted and the differential diagnosis has been improved; moreover novel therapeutic targets can be screened, identified and healed [27].

However functional methods can reveal cancer, structural visualization remains the gold standard diagnostic technique in oncology, furthermore anatomical information about a cancer patient is crucial for the precise tumor treatment [12].

II. Fourier-Domain Optical Coherence Tomography

II/1. Comparison with other optical imaging modalities

Optical imaging modalities are those measurement techniques which use the wavelength range of the electromagnetic spectrum from the soft Ultraviolet (UV) (wavelength: $\lambda = 200 - 400$ nm) through the Visible Light (wavelength: $\lambda = 400 - 760$ nm) till the Near Infrared (NIR) (wavelength: $\lambda = 760 - 3000$ nm) (Figure II.1.1). Compared to other conventional imaging methods, optical imaging provides higher resolution. The penetration depth is limited due to the strong scattering of optical radiation in tissues, but it can be set up as endoscopy for inner surface study beside the microscopic use on outer parts (Table II.1.1) [44, 45].

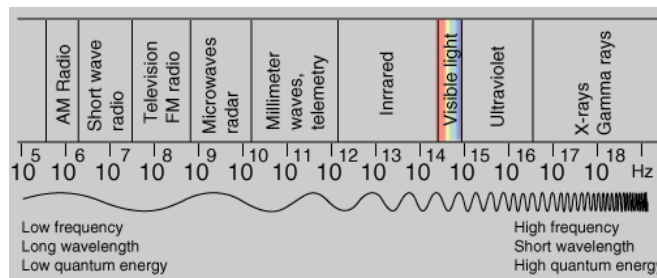


Figure II.1.1. Electromagnetic spectrum [46].

Optical imaging methods can provide either structural or molecular information real time in a non-invasive way, at low cost at different scale to study cells or whole organs. The distinction of these optical imaging modalities is based on which part of light they detect during light-matter interaction. The penetration depth and the resolution are enhanced improving optical instrumentation (implementing confocal settings or interferometry), applying mathematical modeling of light propagation in tissue (Monte Carlo simulation), and digital signal processing techniques (deconvolution) [44, 45, 47].

Medical Imaging Modality	Penetration Level	Resolution	Cost
X-ray Radiographs	Organ-Tissue	<mm	Low
X-Ray CT	Organ-Tissue	mm	Moderate
MRI	Organ-Tissue	mm	High
fMRI	Tissue-Cellular	mm	Very High
SPECT	Tissue-Cellular	mm	High
PET	Tissue-Cellular-Molecular	mm	Very High
Ultrasound	Organ-Tissue	<mm	Low
Optical Microscopy	Tissue-Cellular	micron	Low
Fluorescence Microscopy	Cellular-Molecular	micron	Low
Confocal Microscopy	Tissue-Cellular-Molecular	micron	Low-Moderate
Endoscopy	Tissue	micron	Low
Optical Coherence Tomography	Tissue-Cellular	micron	Moderate
Diffuse Reflectance	Cellular-Molecular	micron	Low

Table II.1.1. Comparison of biomedical imaging modalities regarding their penetration level, resolution and cost; Optical imaging modalities are marked with yellow [44].

The light penetrating to the tissue is divided into multiple parts (Figure II.1.2). Most of the photons are randomly scattered, this phenomenon is the Diffuse Reflectance due to multiple scattering (*Diffuse Reflectance Imaging*) or they are absorbed (Termination) then reflected at different energy level shifting the incident wavelength–range (*Fluorescence Microscopy*). *Photoacoustic Imaging* uses some part of absorption which transforms to heat and internal pressure wave. *Bioluminescence Imaging* detects spontaneous internal light emission [44].

A small portion of photons are reflected from the layers perfectly, this phenomena is the specular reflection due to single scattering, these photons are called ballistic photons, or snake photons in case of closely perfect scattering. *Optical Coherence Tomography* operates recording these photons' behavior at different layers of the media. A few photons go through the tissue (Transmittance) (*Transillumination Imaging*). Besides the methods based on the linear optical scattering (*Rayleigh scattering*), a different approach, *Raman Scattering* detects optical inelastic scattering properties of the material. Contrast agents can be used to extract further molecular information [44].

The scattering properties of tissue are related to tissue morphology, and the absorption properties are related to the tissue biochemistry. The coefficients μ of the proportions of the light fractions depend on the incident wavelength λ , angle of incidence and the tissue material properties (anisotropy g , refractive index n) [44, 45, 48, 49].

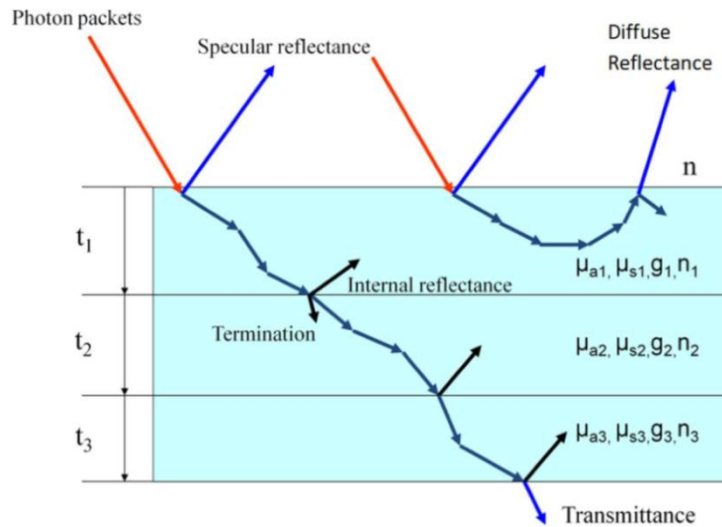


Figure II.1.2. Simplified model of biological medium with three layers. Each layer is associated with an absorption coefficient μ_a , a scattering coefficient μ_s , an anisotropic factor g , and a refractive index n [44].

Imaging systems are based on the extraction of these different coefficients in a unique way. *Conventional Microscopy* detects light from the entire illuminated field usually operating with white light. *Confocal Microscopy* detects light reflected from a specific layer (t_i) through changing focus position in axial direction and successively suppressing out-of-focus light using a pinhole (Figure II.1.3.) [44, 45, 49, 50].

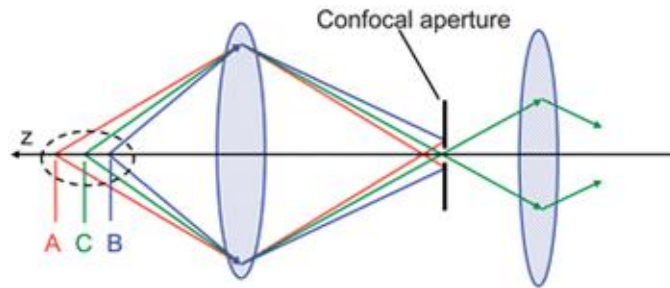


Figure II.1.3. Scheme of Confocal Microscopy [51].

Confocal Microscopy can operate in *diffuse reflectance* or *fluorescence imaging* mode using UV or visible light. Besides the wide-field setting, *Confocal Laser Scanning Microscopy (CLSM)* scans pixel by pixel, plane by plane to give 3d volume. The procedure is time consuming, so it does not give possibility for dynamic changes but the morphology of confocal microscopic images are comparable to histology [44, 49].

In NIR range *Multiphoton Microscopy* gives sliced axial view similar to Confocal Microscopy. As far as one photon illumination reveals information from all the focal volume, smearing the exact focal plane, multiple-photon illumination gives information from the exact focus position due to nonlinear dependence of the illumination (Figure II.1.4). The axial sectioning is time consuming, but NIR light penetrates deeper into tissue, and less scattered. To provide the same excitation energy level, as light with shorter wavelength range, more photons are needed, most commonly two photons, so the technique is mainly called two-photon microscopy [44, 49].

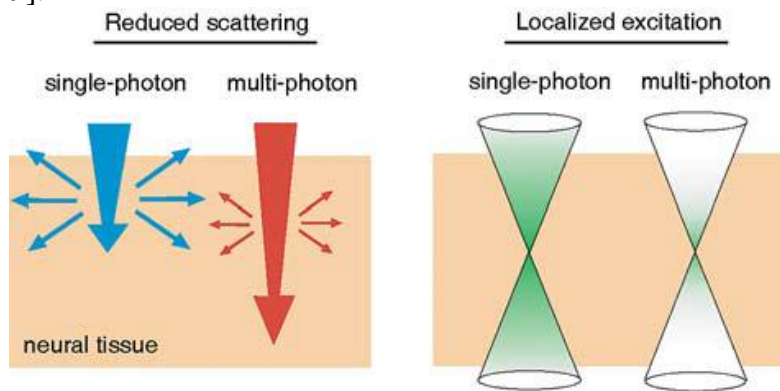


Figure II.1.4. Single- and Multi-photon excitation [49].

Higher penetration depth can be achieved in two-photon compared to Confocal Microscopy, but it usually achieves worse resolution than that of confocal microscopes because the focal spots widen as the illumination wavelength increases [52].

Multiphoton Microscopy operates in NIR fluorescence imaging mode, in addition to the UV or visible light fluorescence Confocal Microscopy. *Fluorescence Imaging* uses endogenous or exogenous molecules or materials (fluorophores) that emit light when activated by an external light source. The incident light is absorbed, and then scatters back at smaller energy state so as longer wavelength. Fluorescence microscopy can quantify molecular properties, gene expression, proteins and pathophysiology [44, 50, 52].

Using various excitation wavelengths the whole excitation-emission matrix can be recorded. *Three-dimensional Total Synchronous Luminescence Spectroscopy (3d-TSLS)* scans simultaneously the excitation and emission wavelengths. However these improvements give significantly better results, they require more time which gives them incompatible to use in vivo [53].

Fluorescence can be combined with Bioluminescence Imaging to detect molecular information (Figure II.1.5). *Bioluminescent Imaging (BLI)* records light-emitting proteins, and can measure gene expression, tumor growth and therapeutic monitoring or drug response [50, 54].

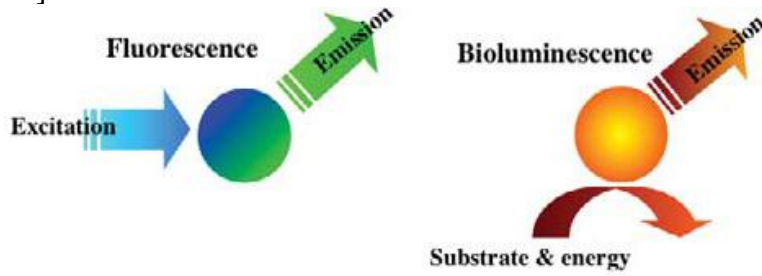


Figure II.1.5. Dual-function reporter genes. One single protein with two functional components/ or coding sequences can be combined to make a single mRNA that produces two proteins [49].

Diffuse Reflectance Images are formed by multiply backscattered diffused light. *Diffuse Optical Tomography (DOT)* reconstructs quantitative information about light absorption and scattering in 3D. The penetration depth is limited up to a few cm in tissue, in the NIR region, but the spatial resolution is in the millimeter range. The reconstruction of 3d absorption/scattering map is based on multispectral measurements and model-based reconstruction of light tissue interaction (backprojection methods based on diffusion theory, iterative image reconstruction, and forward models) [44, 55, 56].

DOT operates in Time-Domain mode using short laser pulses, Frequency-domain mode using sinusoidally intensity amplitude modulated light source and, continuous-wave mode. DOT is able to quantify blood oxygenation and hemoglobin content [50, 55, 56, 57].

Diffuse Optical Spectroscopy (DOS) uses multi-frequency intensity-modulated and continuous-wave NIR light to quantify tissue absorption and scattering properties. DOS quantifies tissue chromophore concentrations of oxyhemoglobin, deoxyhemoglobin, methemoglobin, water, and lipid [50].

Time-Domain and Frequency-Domain techniques measures dynamic changes in diffuse reflectance from chromophores, and fluorescence imaging from fluorophores (*Fluorescence Lifetime Imaging*) yielding cancer diagnosis [45, 57]. *Total Internal Reflection Fluorescence (TIRF)* provides selective visualization, giving the fluorescence behavior of a single molecule [49].

Diffuse reflectance signals are several orders of magnitude higher than endogenous fluorescence signals, it requires simpler experiments, cost-effective, it has a large volume interaction in the tissue detecting smaller tumors, but the detected spectra is an overlapped information from different site and component. Contrarily fluorescence imaging classifies tissue types with higher accuracy. The combination of both techniques and in addition including scattering properties in Trimodal Spectroscopy yields statistically acceptable results [45, 49, 53].

Diffuse Optical Imaging Methods collect multiply scattered light from the illuminated volume, and a bundle of fibers detects the light around the tissue. Optical Microscopy techniques, Conventional or Confocal Microscopy detect backscattered or fluorescent light from the focal volume [58].

Optical Coherence Tomography (OCT) also gives sliced axial view, instead of confocal solution, the operation is based on interference theory. The light source is usually continuous-wave, wavelength-broadband in the white light or NIR region. Scanning or Wide-field illumination also applies. The image formation is based on single scattered ballistic photon detection whose property is to keep their coherence during light-matter interaction so interference can occur when these photons interact after going through different path-length [49 58-60,].

The detected backscattered light from the tissue reveals subsurface morphology up to 1-3 mm, with 10-15 μm resolution. Beside the structure measured from backscattered intensity amplitude, OCT measures phase information from which it can reveal functional information, e.g. velocity measurements in veins (Doppler-OCT). Physiological variables can be extracted (total hemoglobin concentration, blood oxygen saturation...) from absorption spectra calculated from the attenuation of the backscattered intensity signal, and using spectroscopic methods (Spectroscopic-OCT). The development and application of ultrashort pulse (femtosecond) lasers in OCT provides higher speed and resolution [49, 59-65].

Optical Coherence Tomography is usually performed with back-scattered light. However, it can also be conducted with transmitted light using pulsed laser and time-gating imaging, which is based on the principle that ballistic photons go faster through the media, and then the light is detected after a certain picosecond, which is defined to get an optimal image quality [66].

Other transillumination methods use a toxic material for material clearing to reduce scattering effect and make it more transparent, so it can be used only on post-mortem samples. *Optical Projection Tomography (OPT)* is based on multiple projection illumination and backprojection calculation. The imaging depth is comparable to conventional microscopy. It can measure tissue fluorescence or absorption properties. *Selective Plane Illumination Microscopy (SPIM)* uses light sheets to illuminate slice by slice instead of the entire volume to remove more scattering effect. For larger scale, *Mesosopic Fluorescence Tomography (MFT)* operates in a similar manner as OPT, instead of using backprojection scheme, it is based on the forward modeling of photon propagation in tissue [52]. Optical clearing in OCT has been also studied [67, 68].

Figure II.1.6 compares the resolution and penetration depth of different conventional imaging methods [69]. Their comparison to perform dynamic changes is not applied here. In addition to the above mentioned methods, *Laser Speckle Imaging* has a main contribution to functional imaging and in OCT-elastography to analyze mechanical properties of the tissue [70, 71].

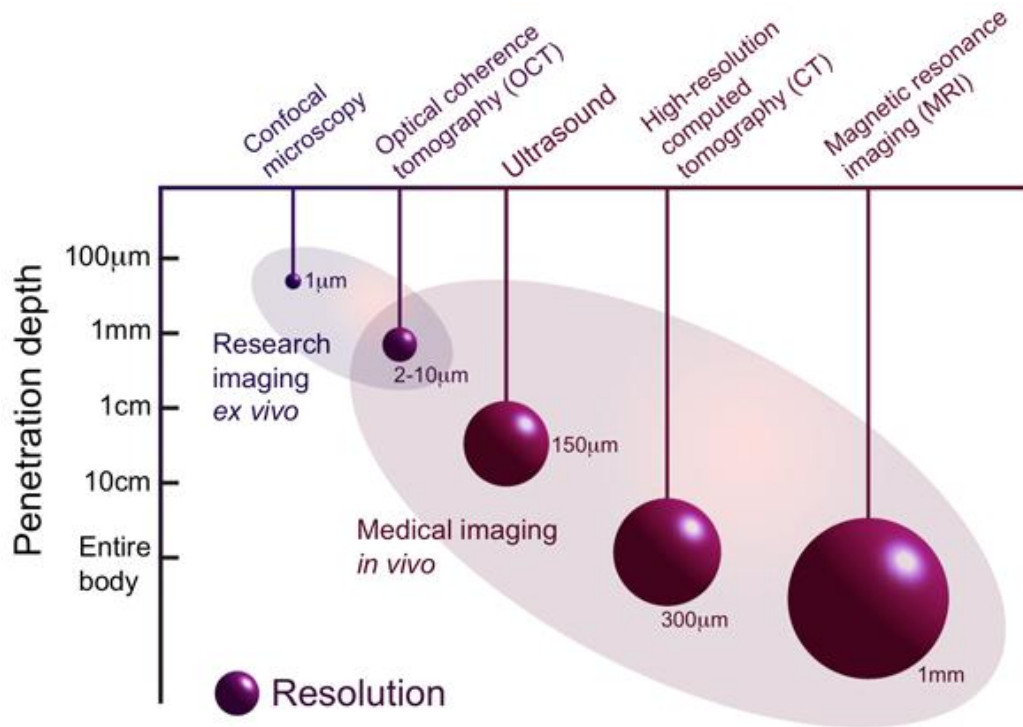


Figure II.1.6. Comparison of conventional imaging methods for diagnosis [69]. Ultrahigh Resolution OCT can achieve a resolution up to 1 μm .

The advantage of OCT compared to the other optical imaging methods is the accurate 3d structural information, which resolution is comparable to histological excision, to a higher penetration depth than spectroscopic/diffuse methods, and provides faster scanning operation yielding accurate dynamic changes over Confocal Microscopy. The most important application is detecting tumor boundaries for surgical resection, recording heterogeneous tissue, small metastasis, and guide biopsy in case a small area is chosen in the tissue. OCT can also be used in a fine gauge needle to be able to diagnose with a fiber-optic component through the lumen [45, 72].

On the contrary quantitative diagnosis from spectroscopic (fluorescence), diffuse reflectance and their combined methods has been developed, and provides information for objective diagnosis, while the structural information in OCT is based simply on grey-level images, and there is not a standardized description of these images. Currently one of the major research areas of OCT is to describe quantitatively the qualitative images it provides only for subjective analysis of the clinician's and pathologist's visual interpretation [44, 45, 72-75].

The focus of this work is the quantitative classification of tissue subsurface morphology. The main contribution will be to get a universal comparable imaging method to be able to use in clinical practice independently from the measurement settings.

These well-known and broadly used imaging methods are based on the phenomenon of elastic scattering of light on particles which does not change the matter quantum state. Alternative optical imaging method reduces information from the inelastic properties of the scattered light.

The inelastic scattered Raman signal is around 0.001 % of the incident light and it reveals chemical information. *Spontaneous Raman scattering* is very weak and requires complicated

process, measurement settings, and algorithms to discern from the Rayleigh scattering. There are ways to improve Raman signal (*Stimulated Raman, Coherent Anti-Stokes Raman (CARS), Resonance Raman* and *Surface-Enhanced Raman/Resonance Spectroscopy*). Other label-free optical imaging can also provide chemical information: *Coherent Nonlinear Optical Microscopy*, including *Nonlinear Dissipation Microscopy and Pump-Probe Microscopy* [45, 76, 77]. Compound application of label-free imaging modalities can differentiate cancerous lesion [78].

The optical imaging method's resolution theoretically is limited by the Abbe diffraction limit (d), calculated from the light wavelength (λ), refractive index of the matter (n) and the instrument numerical aperture ($NA = n \sin \theta$):

$$d = \frac{\lambda}{2(n \sin \theta)} \quad (II.1.1)$$

Instead of photons, electrons are used in the Electronic Microscopy (EM) techniques yielding a much better resolution based on the same physical principle, electrons having $\sim 100x$ smaller wavelength than photons. The gap between these two techniques is the nanoscopy or super-resolution microscopy, which breaks the diffraction barrier of the optical resolution up to (macro)molecular level. Axial resolution can be improved with 2 opposing lenses, new methods are developed in the near- and far-field region, and whether the subdiffraction resolution is based on a linear or nonlinear response of the sample to its locally illuminating 'exciting or depleting' irradiance [47, 49].

The energy transformation of light is studied in *Photoacoustic Tomography*. A short-pulsed laser beam is directed to the area. Some part of the absorbed light is converted to heat which initiates acoustic waves to be detected by transducers. Due to smaller ultrasonic scattering, it gives higher spatial resolution and penetration depth. It reveals tumor, pigmented lesion or blood vessels [44, 50].

Multispectral Optoacoustic Tomography (MSOT) uses acoustic and photon propagation mathematical models in tissue for 3D reconstruction. A similar method is developed, called *Spectral Photoacoustic Tomography (SPAT)* to detect only superficial events. For larger microscopic scale the *Mesosopic Optoacoustic Imaging (MSOT)* is applied using multi-projection illumination and multi-projection acoustic detection [52].

II/2. Theory Optical Coherence Tomography

II/2/a. Wave-equation

Light is the phenomenon of the electromagnetic (EM) radiation. The wave equation for electromagnetic waves is reduced from the Maxwell's equations. These 4 equations describe the varying electric and magnetic fields changing in time by four statements: Faraday Law for Induction, Ampere Law, Gauss Law for Electricity and Gauss Law for Magnetism. The wave equation will be reduced from these equations for charge- and current-free region, and in the absence of magnetic or polarizable media [60, 79, 80]. (Bold letters will represent vectors.)

The Gauss Law for Electricity: \mathbf{E} – electric field:

$$\nabla \cdot \mathbf{E} = 0 \quad (II.2.1)$$

The Gauss Law for Magnetism: \mathbf{B} – magnetic field:

$$\nabla \cdot \mathbf{B} = 0 \quad (II.2.2)$$

The Ampère Law of the Electric Field in 3D for vectorial form can be described as:

$$\nabla \times \mathbf{B} = \mu_0 \varepsilon_0 \frac{\partial \mathbf{E}}{\partial t} = \frac{1}{c^2} \frac{\partial \mathbf{E}}{\partial t} \quad (II.2.3)$$

where ε_0 = permittivity, μ_0 = permeability, c = speed of light.

Faraday Law of Induction describes:

$$\nabla \times \mathbf{E} = -\frac{\partial \mathbf{B}}{\partial t} \quad (II.2.4)$$

The EM wave is reduced according to the following steps: First the curl of the Faraday form is taken:

$$\nabla \times (\nabla \times \mathbf{E}) = -\frac{\partial (\nabla \times \mathbf{B})}{\partial t} \quad (II.2.5)$$

$$\nabla \times (\nabla \times \mathbf{E}) = \nabla (\nabla \cdot \mathbf{E}) - \nabla^2 \mathbf{E} \quad (II.2.6)$$

$$\nabla (\nabla \cdot \mathbf{E}) - \nabla^2 \mathbf{E} = -\frac{\partial (\nabla \times \mathbf{B})}{\partial t} \quad (II.2.7)$$

Then the Ampere Law is substituted to the curl of the Faraday Law:

$$\frac{\partial}{\partial t} (\nabla \times \mathbf{B}) = \mu_0 \varepsilon_0 \frac{\partial^2 \mathbf{E}}{\partial t^2} = \frac{1}{c^2} \frac{\partial^2 \mathbf{E}}{\partial t^2} \quad (II.2.8)$$

$$\nabla \times (\nabla \times \mathbf{E}) = \nabla (\nabla \cdot \mathbf{E}) - \nabla^2 \mathbf{E} = -\mu_0 \varepsilon_0 \frac{\partial^2 \mathbf{E}}{\partial t^2} = -\frac{1}{c^2} \frac{\partial^2 \mathbf{E}}{\partial t^2} \quad (II.2.9)$$

Based on Gauss Law ($\nabla \cdot \mathbf{E} = 0$), the EM wave is obtained:

$$\nabla^2 \mathbf{E} = \mu_0 \epsilon_0 \frac{\partial^2 \mathbf{E}}{\partial t^2} = \frac{1}{c^2} \frac{\partial^2 \mathbf{E}}{\partial t^2} \quad (II.2.10)$$

And equivalently for the perpendicular magnetic field:

$$\nabla^2 \mathbf{B} = \frac{1}{c^2} \frac{\partial^2 \mathbf{B}}{\partial t^2} \quad (II.2.11)$$

The magnetic field \mathbf{B} is perpendicular to the electric field \mathbf{E} in the orientation where the vector product $\mathbf{E} \times \mathbf{B}$ is in the direction of the propagation of the wave. The representation of the electromagnetic wave propagation is shown in Figure II.2.1:

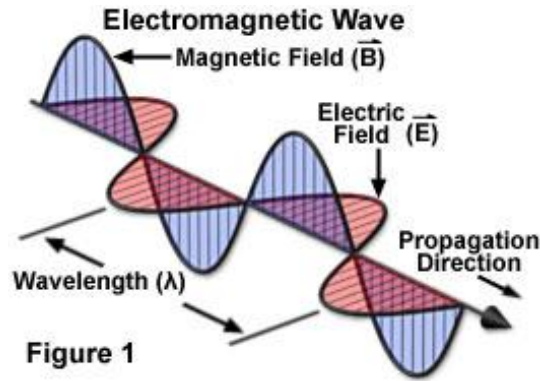


Figure II.2.1. Electro-magnetic wave propagation [81].

The wave-equation is described as a linear second order hyperbolic partial differential equation (PDE):

$$\frac{\partial^2 \mathbf{u}}{\partial t^2} = c^2 \nabla^2 \mathbf{u} \quad (II.2.12)$$

where u describes the alternating magnitude of an electromagnetic field, and the constant c is the phase velocity of the light wave. Substituting the Laplacien operator (∇^2) in rectangular coordinates in 3D :

$$\frac{\partial^2 \mathbf{u}}{\partial t^2} = c^2 \left(\frac{\partial^2 \mathbf{u}}{\partial x^2} + \frac{\partial^2 \mathbf{u}}{\partial y^2} + \frac{\partial^2 \mathbf{u}}{\partial z^2} \right) \quad (II.2.13)$$

In 1D, plane wave traveling in x direction:

$$\frac{\partial^2 \mathbf{u}}{\partial t^2} = c^2 \left(\frac{\partial^2 \mathbf{u}}{\partial x^2} \right) \quad \text{or} \quad u_{tt} = c^2 u_{xx} \quad (II.2.14)$$

The (quasi)linear, second-order PDEs can be classified as hyperbolic, parabolic or elliptic type. If PDE is hyperbolic, the solution can be drawn in the space-time plane (Figure II.2.2).

This shows, when there is a perturbation at point P, its effect propagates at a given region of the time-space plane defined by two characteristic curves (C^+ , C^-). The tangent of these characteristic curves defines the velocity of the propagation. The energy of the initial disturbance is conserved, so the velocity remains constant (no attenuation). Examples are the Maxwell equations in vacuum [60, 79, 80].

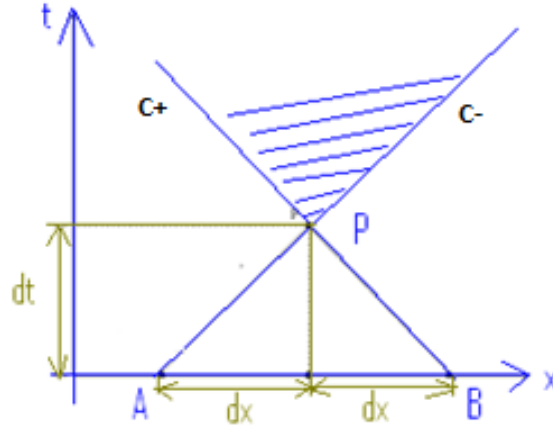


Figure II.2.2. Solution of hyperbolic partial differential equation on space-time plane.

On the contrary, in case of parabolic PDE, the perturbation at a certain point propagates infinitely fast, so it has effect immediately in all the half-space, not only at a given region, but it attenuates with distance exponentially from the perturbation point (e.g. diffusion, heat eq.). The characteristic direction is the boundary of the half-space. The elliptic PDE has no time-axis; it propagates uniformly in space x - y direction, there is no characteristic equation (e.g. Laplace, Poisson, Helmholtz eqs.).

The general solution (D'Alembert) of the wave equation is based by transforming the x , t independent variables to new continuously differentiable variables ξ and η (on the space-time plane: rotation/displacement of x , t coordinate axes to ξ , η : characteristics C^- , C^+).

$$\xi = \xi(x, t) = x - ct \quad \text{and} \quad \eta = \eta(x, t) = x + ct \quad (II.2.15)$$

The differential equation will have the general solution based on that the propagation of the disturbance along these characteristics is constant.

$$x - ct = \text{constant}, \quad x + ct = \text{constant} \quad (II.2.16)$$

$$u(x, t) = f_-(\xi) + f_+(\eta) = f_-(x - ct) + f_+(x + ct) \quad (II.2.17)$$

where f_- is right-, and f_+ is left traveling waves.

Harmonic wave with constant amplitude (A) and phase ($kx \pm \omega t$) with phase velocity (c):

$$f(x \pm ct) = A \cos k(x \pm ct) = A \cos(kx \pm \omega t) \quad (II.2.18)$$

The optical frequency ($1/k$) is related to the temporal frequency (ω) by the equations:

$$\lambda = \frac{2\pi}{k} = \frac{2\pi c}{\omega} = \frac{c}{f} \quad \text{or} \quad k = \frac{2\pi}{\lambda} = \frac{2\pi f}{c} = \frac{\omega}{c} \quad (II.2.19)$$

where k -wavenumber, λ -wavelength.

The signals propagate with velocity c in both directions. One wave varies sinusoidally in both space and time traveling through the characteristics in one direction can be described in a complex form:

$$u(x, t) = A \cos(kx - \omega t) + j A \sin(kx - \omega t) \quad (II.2.20)$$

and in Euler form:

$$u(x, t) = A e^{i(kx - \omega t)} \quad (II.2.21)$$

The electric field of the laser signal cannot be measured directly. Instead the intensity of the electric field is recorded. In this case, instead of the instantaneous intensity, the time-average values are recorded.

The intensity is the time average of the Poynting vector (S [W/m^2]) that represents the energy flux of an electromagnetic field, defined as the cross-product of the electric (\mathbf{E}) and the magnetic field (\mathbf{B}):

$$\mathbf{S}(\mathbf{r}, t) = \mathbf{E} \times \mathbf{B} \left[\frac{W}{m^2} \right] \quad (II.2.22)$$

The time average of the Poynting vector is proportional to the time average of the squared electric field, as explained below. EM plane wave propagating in the z direction is described by the EM pair:

$$\mathbf{E}(z, t) = E_x(z, t) \mathbf{x} \quad (II.2.23)$$

$$\mathbf{B}(z, t) = B_y(z, t) \mathbf{y} \quad (II.2.24)$$

where:

$$E_x(z, t) = E_1 \cos(\omega t - kz) \quad (II.2.25)$$

$$B_y(z, t) = \frac{E_x(z, t)}{c} = \frac{E_1}{c} \cos(\omega t - kz) \quad (II.2.26)$$

where c is the velocity of the propagating energy. The power density is:

$$\mathbf{S} = \mathbf{E} \times \mathbf{B} = E_x B_y \sin \frac{\pi}{2} \mathbf{z} = \frac{E_1^2}{c} \cos^2(\omega t - kz) \mathbf{z} \quad (II.2.27)$$

The time averaged power density is substituting $\cos^2(x) = \frac{1 + \cos 2x}{2}$, and calculating the average by integrating: $\int \frac{1 + \cos 2x}{2} = \frac{x}{2} + \frac{1}{4} \sin 2x$. The average will be $\frac{1}{2}$ for the interval from zero to any of multiple $\frac{\pi}{2}$:

$$\bar{\mathbf{S}} = \overline{|\mathbf{E} \times \mathbf{B}|} = \frac{E_1^2}{c} \overline{\cos^2(\omega t - kz)} = \frac{E_1^2}{c} \overline{\left(\frac{1}{2} + \frac{1}{2} \cos(2\omega t - 2kz) \right)} = \frac{1}{2} \frac{E_1^2}{c} W m^{-2} \quad (II.2.28)$$

Finally the intensity is defined from the time average of the Poynting vector or the squared electric field:

$$\bar{I} = \frac{1}{T} \int_0^T |\mathbf{S}(\mathbf{r}, dt)| dt = \frac{1}{T} \epsilon C \int_0^T E^2(t) dt \quad (II.2.29)$$

In the equation the constants ϵ and C are material properties. The intensity is defined from the time average of the squared electric field [60, 79, 80].

II/2/b. Broadband Signal

The broadband signal is composed of waves at different wavelengths and forms a wavepacket (Figure II.2.3).

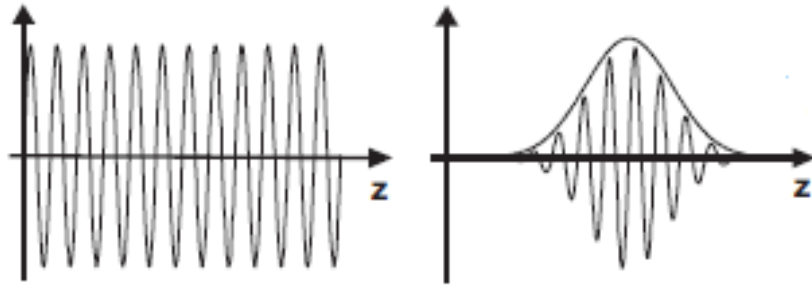


Figure II.2.3. Left: Monochromatic light (coherence length is infinity). Right: Broadband signal: Sum of the different wavelengths yields a wavepacket (Short Coherence Length Light) [modified from 59].

The equation of the wavepacket:

$$u(x, t) = \sum_i A_i \sin(k_i x - \omega_i t) \quad (II.2.30)$$

The distribution of the wavelengths should be continuous to get a localized wavepacket. It can be written in integral form:

$$u(x, t) = \int A(k) \sin(kx - \omega t) dk \quad (II.2.31)$$

Coherence length or Point Spread Function (PSF) is the auto-correlation of this broadband signal. The coherence length of the wavepacket defines the resolution of the system, and higher resolution requires wider broadband range, as explained below [60, 79, 80].

The auto-correlation (convolution) of a stationary, ergodic signal $x(t)$ is defined in time domain:

$$R_x(\tau) = E[x(t)^* x(t + \tau)] = \int_{-\infty}^{\infty} x(t)^* x(t + \tau) dt \quad (II.2.32)$$

For bounded interval:

$$R_x(\tau) = \lim_{T \rightarrow \infty} \frac{1}{T} \int_0^T x(t)^* x(t + \tau) dt \quad (II.2.33)$$

The Fourier Transform of the PSF function is the Power Spectral Density (PSD) (Wiener-Khinchin Theorem Figure II.2.4):

$$S_x(f) = FT[R_x(\tau)] = \int_{-\infty}^{\infty} R_x(\tau) e^{-i2\pi f t} d\tau \quad (II.2.34)$$

$$S_x(f) = X^*(f)X(f) = |X(f)|^2 \quad (II.2.35)$$

For bounded interval:

$$S_x(f) = FT[R_x(\tau)]_{-T}^T = \lim_{T \rightarrow \infty} \int_{-T}^T R_x(\tau) e^{-i2\pi f t} d\tau = \lim_{T \rightarrow \infty} \frac{1}{T} [|X_T(f)|^2] \quad (II.2.36)$$

Or inversely:

$$R_x(\tau) = IFT[S_x(f)] = \int_{-\infty}^{\infty} S_x(f) e^{i2\pi f t} df = \int_{-\infty}^{\infty} |X(f)|^2 e^{i2\pi f t} df \quad (II.2.37)$$

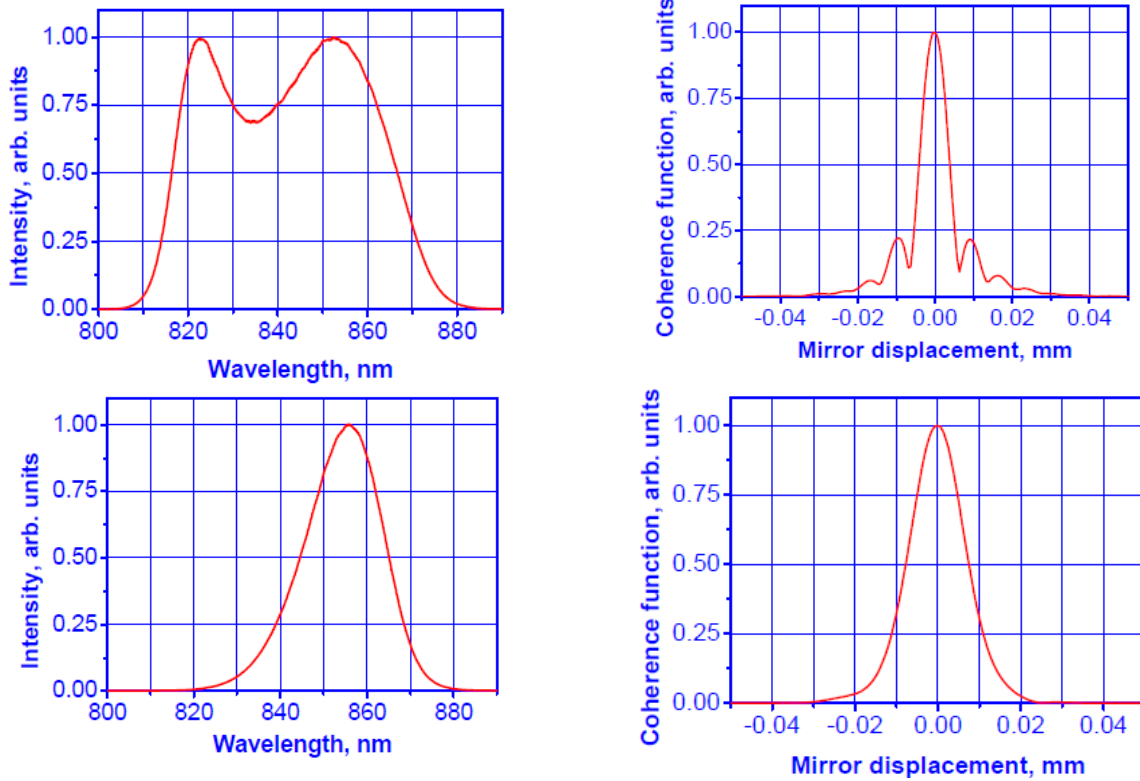


Figure II.2.4. Optical Spectrum and Coherence Function of the Laser source: *S840-B-I-20: 20 mW Benchtop Lightsource at 840 nm*. Left: Power Spectral Density in the function of wavenumber or wavelength ($k = 2\pi/\lambda$), and Right: corresponding Point Spread Function of the generated Laser Signal; Up: High-Power Mode, Down: Low-Power Mode.

The FWHM – Full Width Half Maximum of the PSF gives the resolution of the broadband source laser beam. Broader spectrum provides better resolution. (Figure II.2.4a – high power mode of OCT, Figure II.2.4b – low power mode of OCT).

There should be a requirement between broadband of the frequency components, and the coherence length. This is defined as Fourier Uncertainty Principle, similar in quantum mechanics, applied here to classical waves with conjugate variables of the signal in time- and frequency-domain.

$$\Delta\omega\Delta t \approx 1 \text{ or } \Delta k\Delta x \approx 1 \quad (II.2.38)$$

In Signal Processing this limit is called Heisenberg-Gabor limit. According to the principle the signal cannot be either bandlimited or timelimited. The function in time domain and its Fourier Transform in frequency domain cannot both have bounded [82, 83]. In addition the law of persistency for input signals requires continuously non-zero spectrum over some finite frequency range [84].

To summarize, the aim behind low-coherence source is to get a higher resolution due to the signal which is composed of multiple wavelengths. This low-coherence defined above from the limited large bandwidth is temporal coherence. The phase shift is lost and does not affect the autocorrelation, only the signal shape. It is important to mention that OCT still keeps his spatial coherence when laser source is used, which does not contain multiple sources, and is not spread like in the case of the candle, sun or tungsten light-bulbs filament. In these cases different points of the source emit light independently, and erases the spatial coherence. Spatial coherence of laser beams appears in speckle patterns, and diffraction fringes at shadow edges [60, 79, 80].

II/2/c. Low-Coherence Interferometry

Light wave will be represented as a scalar, stationary, ergodic, analytic signal. The analytic signal is the complex representation of the real valued signal, which imaginary part can be obtained from the real part with a Hilbert function (\mathcal{H}) (Figure II.2.5). Simply the Hilbert transform makes a phase shift on the real value signal to get the imaginary part [85, 86]. The analytic representation of the signal featured with one-sided spectra facilitates digital processing and mathematical modifications.

$$a_H(t) = \mathcal{H}\{a(t)\} \quad (II.2.39)$$

$$a_a(t) = a(t) + j a_H(t) \quad (II.2.40)$$

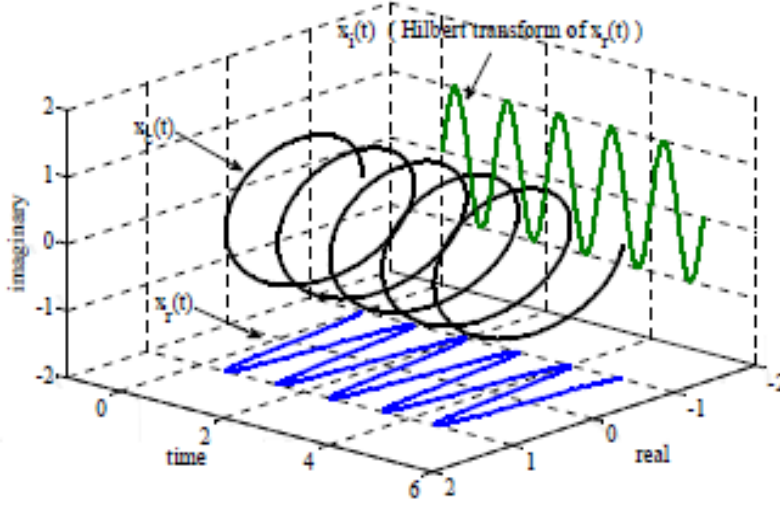


Figure II.2.5. Hilbert function of a single wavelength; Analytic signal represented in a 3D plot [87].

To digitally obtain the analytic signal, the next steps are required: Fourier transform of the Electric Field $E(t)$ reveals the frequency components of the time domain signal. The result for a Real-value signal is a both-sided spectra, negative and positive components are mirrored, so one part can be removed while keeping the information contained.

$$\hat{E}(f) = FT\{E(t)\} = \int_{-\infty}^{\infty} E(t) e^{-i2\pi ft} dt \quad (II.2.41)$$

The corresponding analytic signal of the Electric Field is obtained by inverse transforming the doubled one-sided spectra, since the complex signal has only positive frequency components:

$$E_a(t) = IFT\{2 \cdot \hat{E}(f)\}_0^{\infty} = \int_0^{\infty} 2\hat{E}(f)e^{j2\pi ft} df = A(t)e^{j[\Phi(t)-2\pi f_0 t]} \quad (II.2.42)$$

where $A(t)e^{j\Phi(t)}$ is the complex envelope of $E_a(t)$. $A(t) = |E_a(t)| = \sqrt{a^2 + a_H^2}$ is the real amplitude envelope, the instantaneous phase $\Phi(t) = \arg\{E_a(t)\}$ and f_0 is the mean frequency of the power spectrum of $E_a(t)$ (Figure II.2.6).

The amplitude of the analytic signal ($A(t)$) shows the slowly varying features of the signal, and the phase ($\Phi(t)$) contains the high frequency information [85].

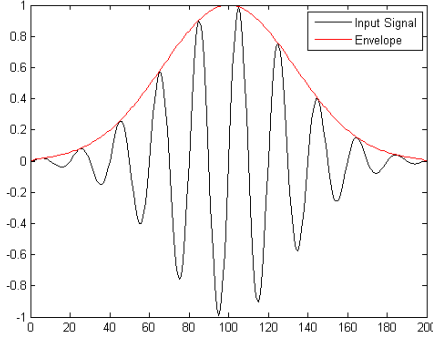


Figure II.2.6. Broadband signal. The real high frequency signal $a(t)$ is shown in black with the real envelope of its analytic signal $A(t)$ in red [88].

The instantaneous intensity is defined as:

$$I(t) = E_a^*(t)E_a(t) \quad (II.2.43)$$

Furthermore interference occurs upon interaction of two light waves containing the same frequency components. Let us call them reference- $E_{aR}(t)$ and sample signal $E_{aS}(t)$. The interference signal is the cross-correlation of the two analytic signals defined as mutual coherence function [85]:

$$\Gamma_{RS}(\tau) = \langle E_{aR}^*(t)E_{aS}(t + \tau) \rangle \quad (II.2.44)$$

Mutual coherence function is defined for two oscillatory signals at the same frequency components; and it expresses if they keep a constant phase difference in time. Interference signal is the sum of the reference signal and the sample signal with a time delay Δt .

$$E_E(t; \Delta t) = E_{aR}(t) + E_{aS}(t + \Delta t) \quad (II.2.45)$$

The averaged intensity is the coherence function $\Gamma(\tau)$, the auto-correlation of the analytic signal at $\tau = 0$:

$$\bar{I} = \langle E_a(t) \rangle = \langle E_a^*(t)E_a(t + \tau) \rangle|_{\tau=0} = \Gamma(\tau)|_{\tau=0} \quad (II.2.46)$$

The averaged intensity in frequency domain is the product of the electric field and his complex conjugate or the Euclidian norm of a complex number. It will give the amplitude of the squared electric field:

$$\bar{I} = \|\hat{E}(f)\|_2^2 = \hat{E}(f)\hat{E}^*(f) = Ee^{-i\omega t}Ee^{+i\omega t} = |\hat{E}(f)|^2 \quad (II.2.47)$$

The averaged intensity of the interference signal will give:

$$\begin{aligned} \bar{I}_E(\Delta t) &= \langle I_E(t; \Delta t) \rangle = \Gamma_{EE}(0; \Delta t) = \langle E_E^*(t; \Delta t)E_E(t; \Delta t) \rangle \\ \bar{I}_E(\Delta t) &= \langle (E_{aS}(t) + E_{aR}(t + \Delta t))(E_{aS}(t) + E_{aR}(t + \Delta t))^* \rangle \\ &= \langle E_{aR}^*(t)E_{aR}(t + \Delta t) \rangle + \langle E_{aS}^*(t)E_{aS}(t + \Delta t) \rangle \\ &\quad + \langle E_{aR}^*(t)E_{aS}(t + \Delta t) \rangle + \langle E_{aS}^*(t)E_{aR}(t + \Delta t) \rangle \\ \bar{I}_E(\Delta t) &= \langle I_R(t) \rangle + \langle I_S(t) \rangle + G_{RS}(\Delta t) \end{aligned} \quad (II.2.48)$$

where $G_{RS}(\Delta t)$ is called the interferogram, computed from twice the real part of the cross-correlation of the two interacting analytic signals:

$$G_{RS}(\Delta t) = 2\text{Re}[\langle E_{aR}^*(t)E_{aS}(t + \Delta t) \rangle] = 2\text{Re}[\Gamma_{RS}(\Delta t)] \quad (\text{II.2.49})$$

The normalized correlation function is called complex degree of coherence (γ). This value ($0 \dots 1$) is a measure of the mutual coherence, (the degree of linear dependence) between two interacting analytic signals indicating that the electric fields interacting at two distinct points or at the same point but with a time delay τ , are still coherent with each other. Expressing in frequency domain:

$$\gamma^2(f) = \frac{|\widehat{E}_{aR}(f)\widehat{E}_{aS}^*(f)|^2}{\widehat{E}_{aR}(f)E_{aR}^*(f)\widehat{E}_{aS}(f)E_{aS}^*(f)} \quad (\text{II.2.50})$$

or in time domain:

$$\gamma_{RS}(\tau) = \frac{\langle E_{aR}^*(t)E_{aS}(t + \tau) \rangle}{\sqrt{|E_{aR}(t)|^2}\sqrt{|E_{aS}(t)|^2}} = \frac{\Gamma_{RS}(\tau)}{\sqrt{\langle I_R(t) \rangle}\sqrt{\langle I_S(t) \rangle}} \quad (\text{II.2.51})$$

it gives:

$$G_{RS}(\Delta t) = 2\text{Re}[\Gamma_{RS}(\Delta t)] = 2\sqrt{\langle I_R(t) \rangle\langle I_S(t) \rangle}\text{Re}[\gamma_{RS}(\Delta t)] \quad (\text{II.2.52})$$

$$G_{RS}(\Delta t) = 2\text{Re}[\Gamma_{RS}(\Delta t)] = 2\sqrt{\langle I_R(t) \rangle\langle I_S(t) \rangle}|\gamma_{RS}(\Delta t)| \cos(\Phi_{SR} - 2\pi f_0 \Delta t)$$

where $|\gamma_{RS}(\Delta t)|$ is the degree of coherence of the two signals, Φ_{SR} is the constant phase between the wavepackets, f_0 is the central frequency and $2\pi f_0 \Delta t$ is the phase delay, $\Delta t = \Delta z/c$ is the time delay, Δz is the path difference between the two signals, and c is the light speed.

There is a corresponding spectral detection mode. The interferogram can be obtained from the power spectra applying the Wiener-Khinchin theorem. The light source auto-correlation function is obtained from its power spectra [85]:

$$S_{source}(f) = FT[\Gamma(\tau)] \quad (\text{II.2.53})$$

And similarly the cross-correlation of two waves is obtained from the cross-spectral density function of the sample and reference beam:

$$W_{SR}(f) = FT[\Gamma_{RS}(\tau)] \quad (\text{II.2.54})$$

The spectral interference detection with the interferometric time delay Δt :

$$S(f; \Delta t) = S_R(f) + S_S(f) + 2\text{Re}[W_{SR}(f)] \cos(2\pi f \Delta t) \quad (\text{II.2.55})$$

II/3. Review of Optical Coherence Tomography

II/3/a. Operation modes in OCT

Optical Coherence Tomography performs axial scanning based on Low-Coherence Interferometry (LCI). The core of OCT is the Michelson Interferometer developed in the 19th century (Figure II.3.1). A monochromatic source split into two arms, and then travelling different pathlengths ($2d$) will have a phase-shift between each other, which is dependent on the wavelength (λ). Upon interacting again they will produce an interference pattern (wave superposition). Constructive interference occurs if the waves from the two arms arrive in phase ($\alpha = 0$):

$$m\lambda = 2d \quad m = 0, 1, 2, \dots \quad (II.3.1)$$

and destructive interference occurs in case of a phase-shift ($\alpha = \pm\pi$):

$$\left(m + \frac{1}{2}\right)\lambda = 2d \quad m = 0, 1, 2, \dots \quad (II.3.2)$$

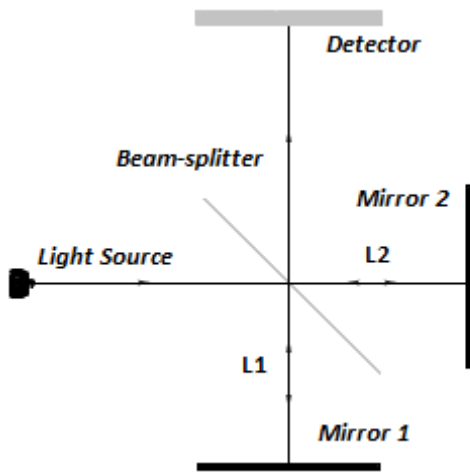


Figure II.3.1. Michelson Interferometer. Wave constructive/destructive interference appears on the detector due to path-length difference ($2L_2 - 2L_1 = 2d$) from the two mirrors (point source). Interference fringe pattern appears in case of divergent laser source:



If the point source is expanded by a lens, the laser beam will diverge, and a 2D detection will occur instead of a single point, and the path-length difference will be dependent on the beam angle, and a circular interference pattern will be produced on the screen over the angular range from the source. At one point on the 2D image constructive interference will occur if:

$$m\lambda = 2d \cos \theta \quad (II.3.3)$$

At different pathlength difference, the interference fringe pattern will change. In the equations above it is assumed that the light traverses the same medium in air ($n_{air} = 1$). The optical pathlength changes in other medium by multiplying the geometrical pathlength by the refractive index of the medium ($d_{opt} = nd_{geom}$) [79, 80].

When a low-coherence light source is placed in the Michelson Interferometer, the technique is called Low-Coherence Interferometry (LCI), which is the basic mechanism of OCT realized with a broadband source, and placing the sample in one arm. 50/50 beam-splitter and point-like detection is assumed.

Interference fringes occur where the (optical) path-length difference of the two arms ($2d$) is less than the coherence length of the light source (l_c), called ‘coherence gate’. In other words, the cross-correlation function of the interacting signals at nearly zero time delay will create the interferometric signal (I_E), which envelope (A) contains the scattering magnitude of the specific depth (z) of the sample [60].

Depth-scanning is solved by mechanically translating the reference mirror, so to position the coherence gate successively in depth at different position. This operation mode is called *Time-Domain (TD) OCT* (Figure II.3.2).

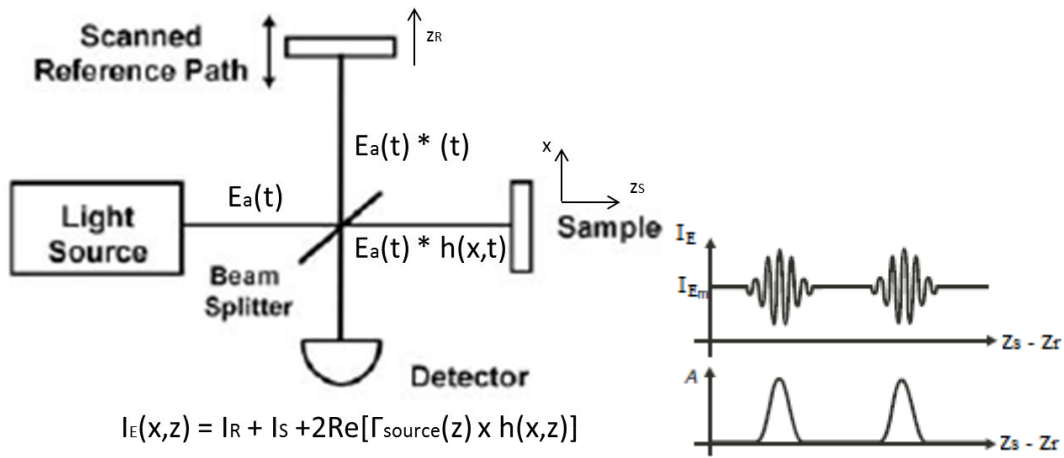


Figure II.3.2. Schematic of TD-OCT, $I_E - I_{Em} = \text{LCI signal}$, A is the real envelope [modified from 59 & 85].

The interferogram detected at the detector in case of two perfectly reflecting mirrors is twice the real part of the light source coherence function $\Gamma_{\text{source}}(\tau)$ [85]:

$$G_{SR}(\tau) = 2\text{Re}[\Gamma_{SR}(\tau)] = 2\text{Re}[\Gamma_{\text{source}}(\tau)] = G_{\text{source}}(\tau) \quad (\text{II.3.4})$$

When the sample is scanned, the interferogram is twice the real part of the convolution of the source coherence function $\Gamma_{\text{source}}(t)$ and the backscattered sample response function $h(t)$:

$$G_{SR}(\tau) = 2\text{Re}[\Gamma_{SR}(\tau)] = 2\text{Re}[\Gamma_{\text{source}}(\tau) * h(\tau)] \quad (\text{II.3.5})$$

Transforming to frequency domain the corresponding spectral interferogram is:

$$W_{SR}(f) = S_{\text{source}}(f)H(f) \quad (\text{II.3.6})$$

The intensity function in function of depth ($I(z)$) is called A-line. Besides the OCT depth-scanning by the reference mirror, a lateral scanning is performed by moving the sample or the

sample beam to obtain a cross-sectional image ($I(x,z)$), called B-scan then a 3d structure ($I(x,y,z)$), called C-scan (Figure II.3.3).

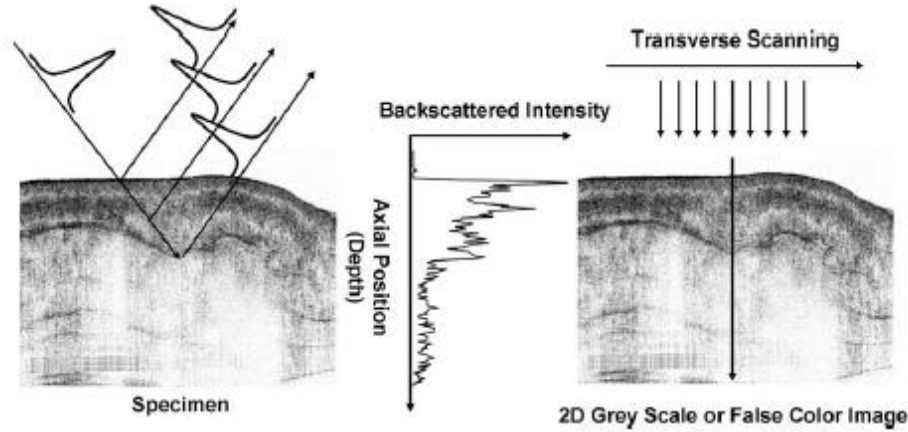


Figure II.3.3. Conventional OCT operation mode. Cross-sectional images (B-scan) are composed of adjacent A-lines [49].

The mechanical depth-scanning can be replaced by detecting separately the spectral components of the backscattered field amplitude $A_S(K)$, and to recover depth information by Fourier-transform based on the Wiener-Khinchin theorem [85].

$$F_S(z) \propto FT[A_S(K)] \quad (II.3.7)$$

By Fourier Transforming the detected cross-spectral intensity will result the interferogram detected in time domain. This operation mode is used in *Fourier-Domain (FD) OCT*, which has two detection processes, *Spectral-Domain (SD) OCT* and *Swept-Source (SS) OCT*. SD OCT detects the spectrum simultaneously through a spectrometer, and a photodiode array or CCD line scan camera (Figure II.3.4):

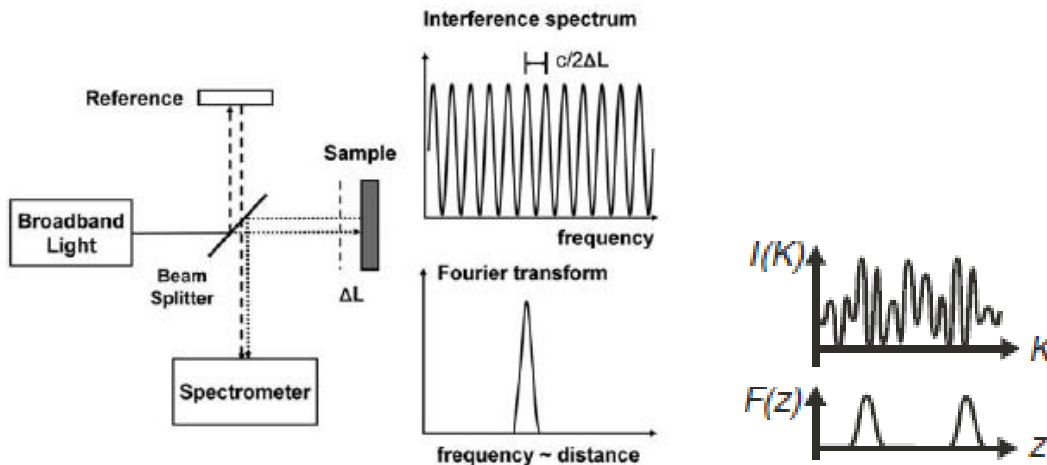


Figure II.3.4. Schematic of SD OCT with interference fringes detected on the camera array ($I(k)$) from one and two layers, with the backreflection ($F(z)$) after Fourier Transform [59, 85].

The spectrometer exit detects a periodic spectrum in function of wavelength, which frequency depends on the path-length difference, and the amplitude depends on the scattering potential of the specific layer. The sum of the periodic functions from different layers is detected. In case of two perfectly reflecting mirrors at a path-length difference z_S , the spectral interferogram is:

$$G_{SR}(K) = 2\sqrt{I_M(K)I_M(K)}\cos(Kz_S) \quad (II.3.8)$$

Placing the sample in the sample arm, the spectral intensity at the interferometer exit is:

$$I_{SR}(K) = I_R(K) + I_S(K) + 2\sqrt{I_S(K)I_R(K)}\text{Re}[\mu(K)e^{i[\phi_S(K)-\phi_R(K)]}]. \quad (II.3.9)$$

where $I_S(K) = |A_S(K)|^2$ is the sample beam power spectrum with $A_S(K) = a_S(K)e^{i\phi_S(K)}$ complex amplitude. $I_R(K)$ is the reference beam power spectrum, and $\mu(K)$ the spectral degree of coherence ($=1$, light launched in single-mode fiber). $\phi_S(K)$ is the spectral phase of the sample wave and $\phi_R(K)$ the spectral phase of the reference beam.

Fourier transforming the spectral interferometer exit will yield the scattering intensity of the tissue in depth ($I(z)$), the A-scan. Lateral scanning is performed similarly to TD-OCT to record B-scan, and C-scan [49, 59, 85].

SS-OCT records the spectral components $I_{SR}(K)$ sequentially in time with a spectrally sweeping source and detecting with a single detector. The frequency sweeps from the sample and reference arm are delayed due to path-length difference, which generate the interference signal with a beat frequency proportional to the delay. The Fourier transform of the detected beat signal reflected from different layer of the sample will provide the depth scattering information [49, 59, 85] (Figure II.3.5).

SS-OCT replaces the line-scan camera array by frequency sweeping to be able to detect with one photodiode making possible to use longer wavelengths (1000-1300 nm), and surmounting the limitation of silicon-based detectors sensitive only at shorter wavelength-range. Similarly to FD-OCT, the depth-resolved scattering properties is extracted without scanning reference mirror, only the lateral scan is required to reconstruct structural information.

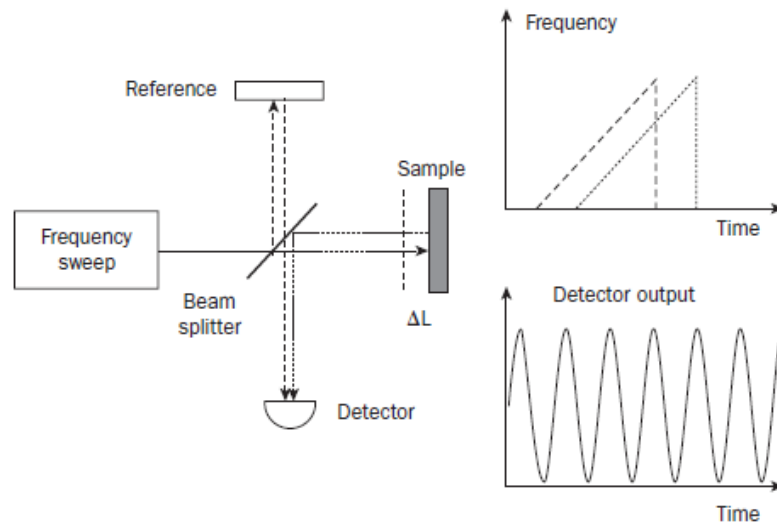


Figure II.3.5. Schematic of SS OCT with interference fringes detected in time, and backreflection after Fourier Transform [59].

The operation modes described above are the typical scanning mechanism in conventional OCT techniques. However, a lateral raster scanning (xy) can also be performed by moving the sample or probe beam to create ‘en face’ image, and the reference mirror is adjusted mechanically similarly to TDOCT to scan a new depth position and get 3d information (x,y,z). This method is preferred in *Optical Coherence Microscopy (OCM)* (Figure II.3.6).

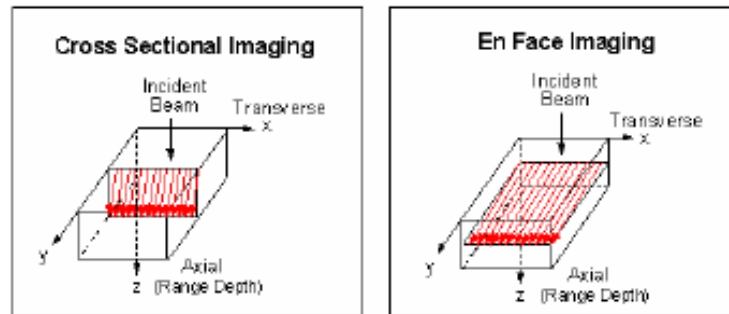


Figure II.3.6. Scan planes of conventional OCT yielding cross-sections, and OCM yielding ‘en face’ images scanning laterally [89].

‘En face’ scanning imaging is single-point detection technique. Higher performance can be obtained with parallel OCT operation modes and detecting with linear or 2D camera arrays to detect all the ‘en face’ image simultaneously. Figure II.3.7 is an example with a 2D CMOS detector with parallel pixel detection [59, 85, 90, 91].

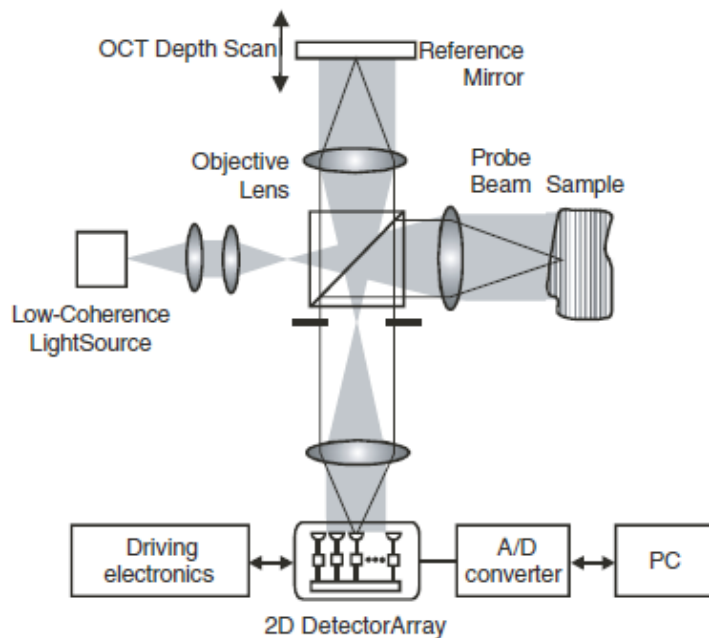


Figure II.3.7. Parallel OCT detection [85].

This parallel detection is performed in Full-Field (FF) OCT detection scheme implementing water-immersion microscope objectives into the two arms; this version is called

the Linnik interferometer. Full-field illumination is used with broadband white-light sources. In this setting phase-modulation is required to set in one arm of the interferometer by a dithered reference mirror or phase modulator [59, 85, 90, 91].

The OCT techniques described above have been realized in free-space systems, and fiber-optics implementation. The basic schemes are represented on Figures II.3.8&9 [85, 92].

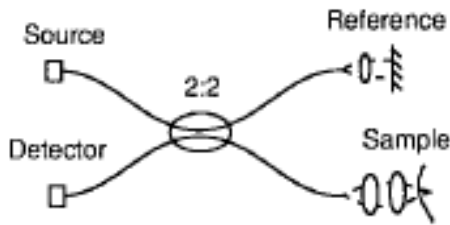


Figure II.3.8. Standard fiber-optic Michelson interferometer with 2:2 fiber coupler [92].

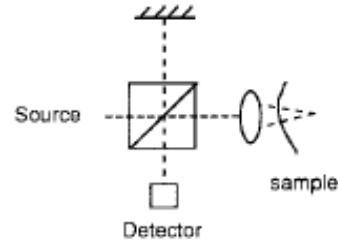


Figure II.3.9. Free-space equivalent to the fiber-optic Michelson interferometer with a beamsplitter cube [92].

II/3/b. Applications of OCT

The power of OCT is to yield gray-scale image revealing subsurface structure based on the scattering intensity properties from the tissue layers at different depth position at micrometer resolution. OCT can provide an image penetration depth up to 1-3 mm depending on tissue type and wavelength-range.

OCT was developed in the early 1990s for the noninvasive imaging of biological tissue, and has been translated from benchtop (research laboratories) to bedside (clinical practice) use [93]. The first application areas were in ophthalmology (Figure II.3.10). Furthermore applications are developed in dermatology, dentistry, gynecology, laryngology, pulmonary medicine and respiratory tract, in gastroenterology, urology, cardiology and vascular disease with the guidance of catheter, endoscope or laparoscope (Figure II.3.11). OCT beam adapted in optical fiber can reach lumen in the cardiovascular system or the gastrointestinal tract, and implementing the fiber in a needle can be inserted into tissue. Improved OCT techniques permit application in developmental biology resolving cellular structure and function [49, 59, 60, 85, 92, 94].

In biomedical application of OCT there is a special focus in tumor diagnostics, and biopsy guidance to reduce sampling errors from conventional biopsy, and to guide surgical intervention. OCT is useful in early cancer diagnosis since most cancer originates within the limited imaging depth on the external surfaces, and internal organs. Morphological alteration in tissue is the principle sign to differentiate malignant from normal tissue. This can be detected with OCT comparable to histology, but not at sufficient sensitivity. One major research area of OCT is to obtain images which can give accurate information for diagnosis without other imaging tools or without cutting the tissue through biopsy [49, 59, 60, 85, 92, 94].

Non-biological applications of OCT have also been reported, and are increasing in industrial and manufacturing process, e.g. non-destructive evaluation, estimation of porosity, fiber architecture and structure; in metrology, measurements of material thickness, surface roughness and volume loss; and operating in hazardous environment [49, 59, 60, 85, 92, 94].

OCT represents a wide variety of improvements. The imaging depth can be increased by decreasing the scattering coefficient of the sample by so called optical clearing [95], the contrast can be improved with Spectroscopic OCT computing Short-Fourier Transform to better differentiate structure [96], and extract absorption coefficients. Doppler OCT provides functional imaging by velocity measurements. Further improvements are the polarization OCT through birefringence of the electric field, OCT elastography to measure elasticity, quantum OCT, and magnetic OCT implementing additional elements [59, 60, 92, 97, 98].

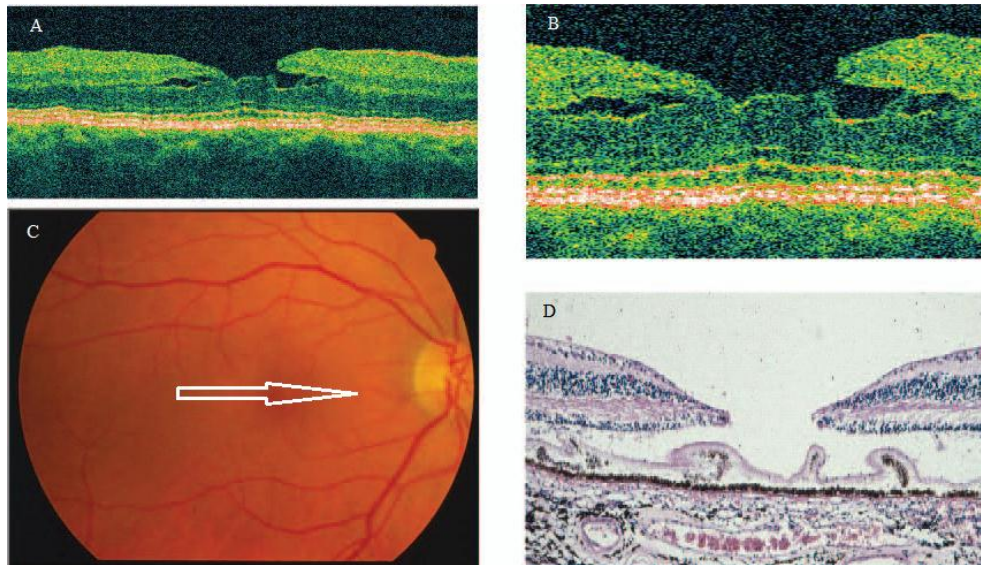


Figure II.3.10. a-b) UHR OCT of macular hole in vivo c) Fundus photograph, white arrow shows central foveal region where OCT cross-section was recorded d) corresponding histology from similar postmortem eye [59].

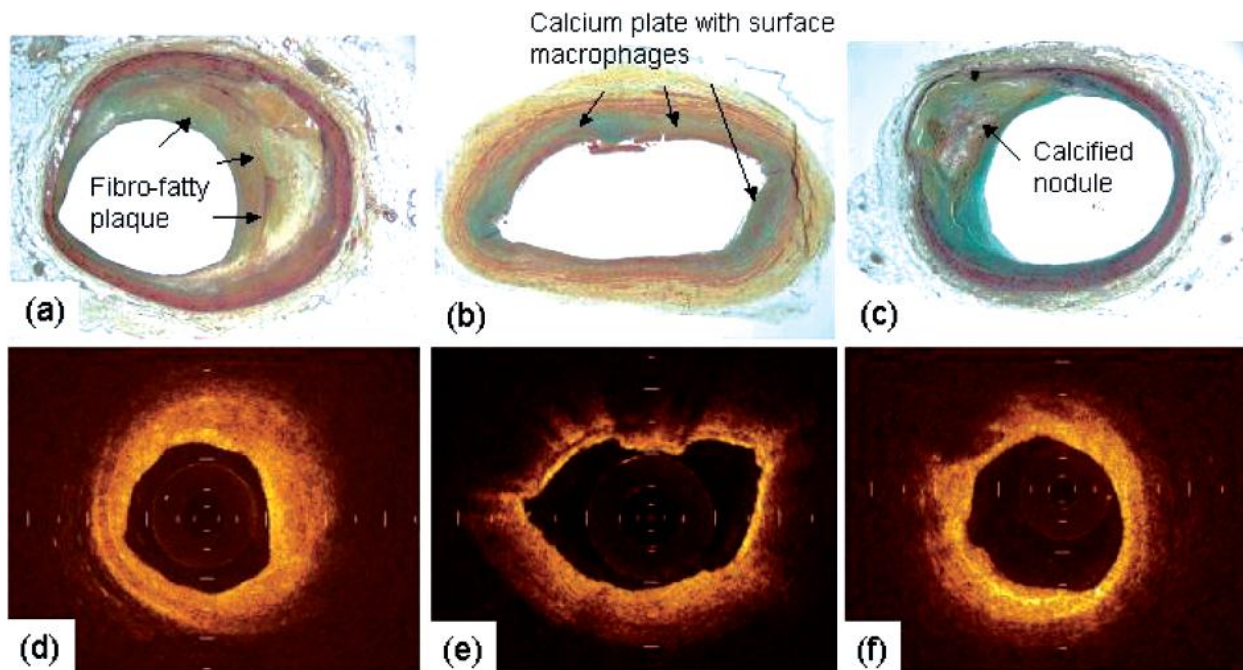


Figure II.3.11. a-c) Stained Histology of diseased human coronary arteries obtained autopsy and d-f) corresponding OCT images [59].

II/3/c. Light sources and Axial Resolution

Optical imaging methods use wavelength range from the ultraviolet through the visible light till the infrared wavelength range. UV (0-400 nm) under the wavelength of 200 nm destroys the biological function, and can be applied only to non-bio-materials. Optical Coherence Tomography is based on the backscattered proportion of the light. In biological materials scattering magnitude is higher in the near infrared region (700-1300 nm), and the absorption can be neglected, in contrary to visible (400-700) and UV light region (200-400 nm). In NIR more scattered light can be detected from the tissue, and having longer wavelengths it penetrates deeper into the tissue. Figure II.3.12 illustrates the optical/therapeutic window showing materials usually composing living tissue with the most sensitive absorbance (melanin, hemoglobin, water) [49].

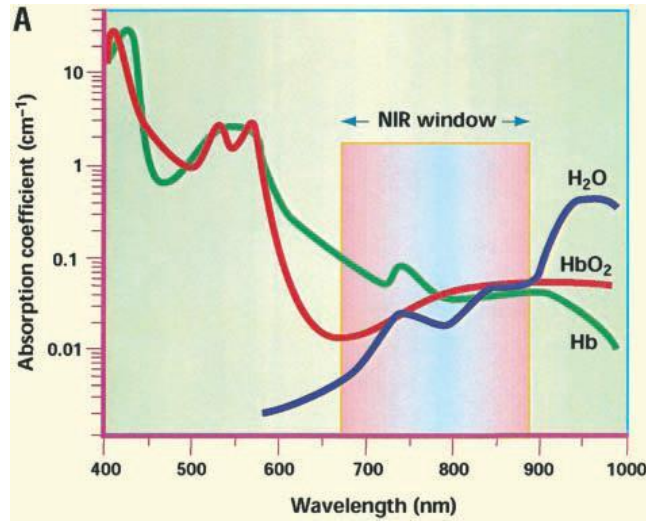


Figure II.3.12. Optical therapeutic window [99].

Conventional OCT light sources operate in the NIR region in continuous mode, with a wavelength-range chosen around 850 or 1300 nm for highly scattering media (Figure II.3.13.)

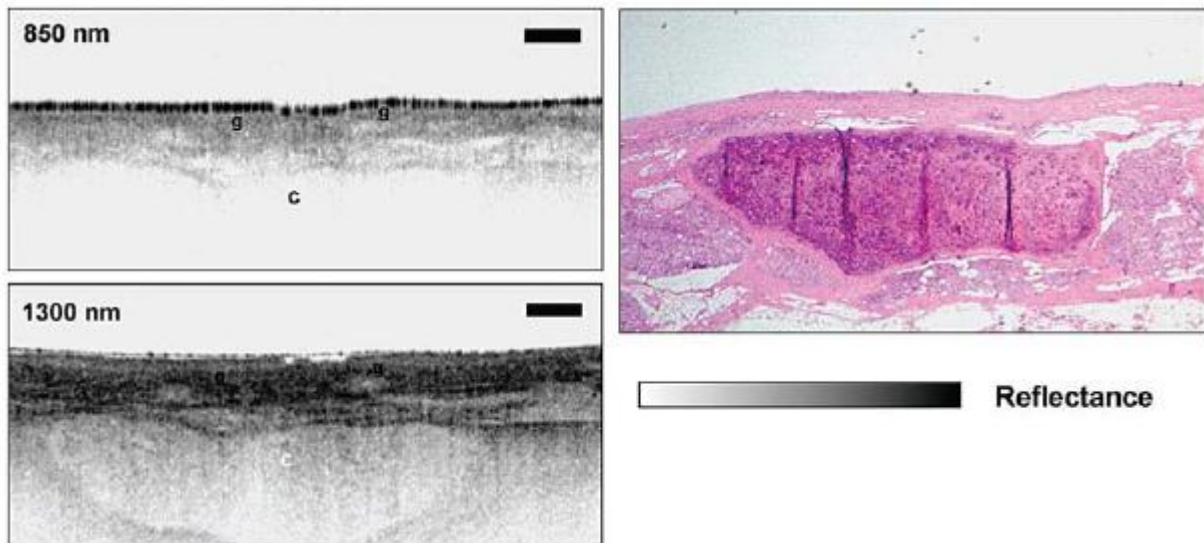


Figure II.3.13. OCT image penetration depth of human epiglottis ex vivo performed at 850-nm and 1300-nm central wavelengths penetrating deeper into the tissue, and corresponding histology; g – glandular structure, c – cartilage. Bar equals 500 μm [49].

Most biological tissues are highly scattering media, and so although longer wavelengths are advisable to enable deep imaging detection, longer central wavelength requires broader band to get the same axial resolution (Figure II.3.14). An optimal solution of wavelength range and light source should be found between the image penetration depth and axial resolution [59].

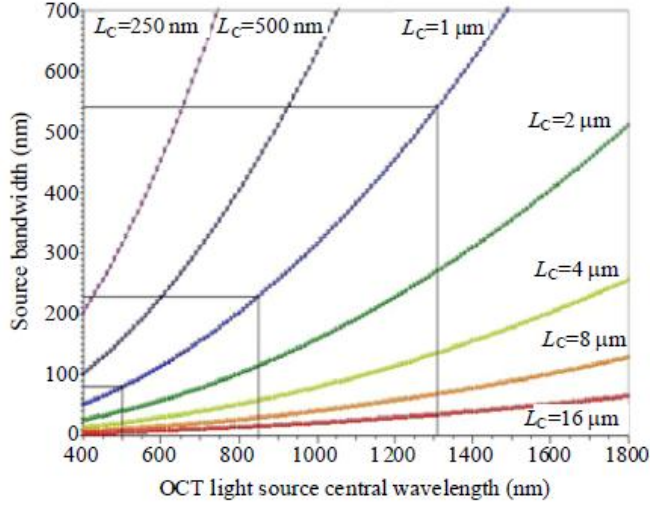


Figure II.3.14. Free space OCT iso-resolution lines; Axial resolution vs. bandwidth of OCT light sources [100-102].

In low-coherence interferometry the axial resolution is dependent only on the light source, and independent from the geometrical settings of the system (beam focusing, spot size) in contrary to conventional or confocal microscopy. Broadband light source is described by the center wavelength λ_c , (840 nm in our system) and broadband $\Delta\lambda$ defined as the full-width-at-half-maximum (FWHM) of the power spectrum (50 nm using high Power mode in the same system) (Figure II.3.15a).

The generated input signal Power Spectral Density is assumed to shape a Gaussian form with f_c (*central frequency component*) position- and f_σ (*frequency standard deviation*) scale parameter of the distribution function [103, 104]:

$$PSD(f, f_c, f_\sigma) = \frac{1}{f_\sigma \sqrt{2\pi}} e^{-\frac{(f-\lambda f_c)^2}{2f_\sigma^2}} \quad (II.3.10)$$

Substituting the standard deviation parameter f_σ by the FWHM of the power spectrum (Δf) yields:

$$\Delta f = 2\sqrt{2 \ln 2} f_\sigma \quad (II.3.11)$$

$$PSD = S_x(f) = \frac{2\sqrt{\ln 2}}{\Delta f \sqrt{\pi}} e^{-2\sqrt{\ln 2} \left(\frac{f-f_c}{\Delta f}\right)^2} \quad (II.3.12)$$

Applying the Wiener-Khinchin theorem:

$$R_x(\tau) = \int_{-\infty}^{\infty} S_x(f) e^{i2\pi f \tau} df \quad (II.3.13)$$

From the definition of the Fourier Transform of a Gaussian function (f_0 -position-, and f_σ -scale parameter) the integral is:

$$R_x(\tau) = e^{-\frac{1}{2}(\omega_\sigma \tau)^2} e^{i\omega_0 \tau} = e^{-\frac{1}{2}(2\pi f_\sigma \tau)^2} e^{i2\pi f_0 \tau} \quad (II.3.14)$$

Substituting the scale parameter with the FWHM of the power spectrum we obtain the complex analytic signal envelope (first term), and the high frequency component (interference fringes):

$$R_x(\tau) = e^{\left[-\frac{1}{2}\left(\frac{2\pi\Delta f\tau}{2\sqrt{\ln 2}}\right)^2\right]} e^{i2\pi f_0\tau} \quad (II.3.15)$$

$$R_x(\tau) = e^{\left[-\left(\frac{\pi\Delta f\tau}{2\sqrt{\ln 2}}\right)^2\right]} e^{i2\pi f_0\tau} \quad (II.3.16)$$

with Euler coordinates:

$$R_x(\tau) = e^{\left[-\left(\frac{\pi\Delta f\tau}{2\sqrt{\ln 2}}\right)^2\right]} [\cos(2\pi f_0\tau) + i \sin(2\pi f_0\tau)] \quad (II.3.17)$$

The detected intensity is twice the real part of the coherence function:

$$Re[R_x(\tau)] = e^{\left[-\left(\frac{\pi\Delta f\tau}{2\sqrt{\ln 2}}\right)^2\right]} \cos 2\pi f_0\tau \quad (II.3.18)$$

Substituting the detected intensity on the LCI (Low-Coherence Interferometry) equation:

$$I(\tau) = I_R + I_S + 2\sqrt{I_R I_S} Re[R_x(\tau)] \quad (II.3.19)$$

we obtain:

$$I(\tau) = I_R + I_S + 2\sqrt{I_R I_S} e^{\left[-\left(\frac{\pi\Delta f\tau}{2\sqrt{\ln 2}}\right)^2\right]} \cos 2\pi f_0\tau \quad (II.3.20)$$

Then substituting time with length and velocity ($\tau = z/c$), the axial resolution (Δz) is obtained at the FWHM of the coherence function envelope:

$$e^{\left[-\frac{\pi^2\Delta f^2\Delta z^2}{4\ln 2c^2}\right]} = \frac{1}{2} \quad (II.3.21)$$

$$\frac{\pi^2\Delta f^2\Delta z^2}{4\ln 2c^2} = \ln 2 \quad (II.3.22)$$

$$\Delta z = \frac{2\ln 2c}{\pi\Delta f} \quad (II.3.23)$$

Finally we should distinguish the axial resolution or coherence length in wavelength range quantities substituting $\Delta f/f_0 = \Delta\lambda/\lambda_c$, then $f_0 = c/\lambda_c$:

$$\Delta z = \frac{2\ln 2\lambda_c^2}{\pi\Delta\lambda} \quad (II.3.24)$$

The axial resolution Δz is defined at the full-width-at-half maximum of the autocorrelation function (12 μm in air) (Figure II.3.15b).

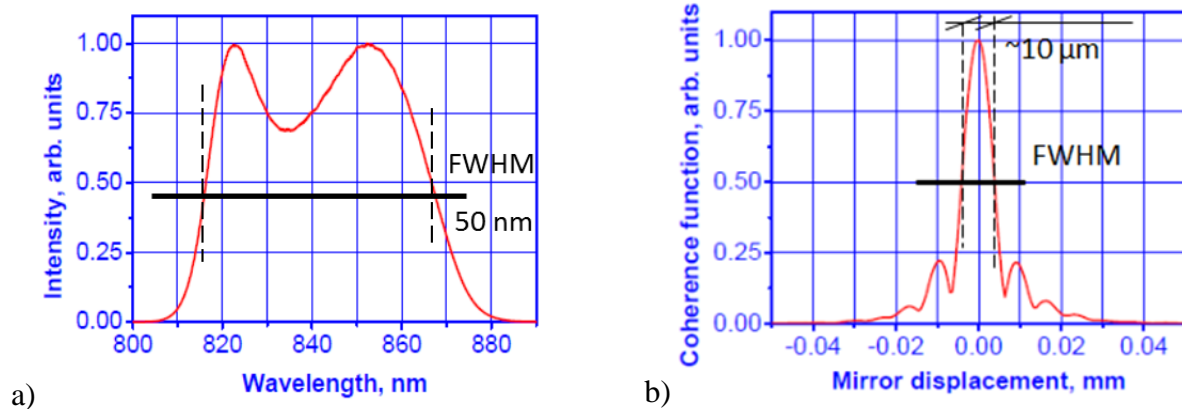


Figure II.3.15. Normalized Optical Power Spectrum and Coherence Function of our OCT system. Laser source: Supraluminescent Diode (SLD) S840-B-I-20: 20 mW Benchtop Lightsource at 840 nm; a) Power Spectral Density and b) corresponding Point Spread Function.

The coherence length was calculated assuming a Gaussian spectral spectrum which Fourier Transform is also a perfect Gaussian function without sidelobes. The shape of the broadband sources affects the axial resolution although possessing the same bandwidth and central wavelength. Approximating the PSD of our SLD which is an overlapped double-gaussian source, as a perfect Gaussian with the same bandwidth can result in an error in axial resolution. The spectral dip on the spectrum shape leads to sidelobes in the interferometric signal. In this case the level of the sidelobes in the coherence function does not affect the coherence length defined at the FWHM of the coherence function, but causes image artifacts and inaccurate layer detection [102, 105].

The Supraluminescent diode in Near Infrared region is the most commonly used laser source in Conventional OCT. SLDs are powerful and low-cost light sources with Gaussian power spectrum achieving 10-20 μm axial resolution operating between 800 and 1350 nm. Two or more spectrally shifted SLDs are joint to broaden the linewidth larger than 150 nm, and so to increase the coherence length till 3-5 μm , but leading to a Gaussian spectral shape with bumps degrading the depth-scanned information and at limited output power [102, 103].

Ultrahigh Resolution (UHR) OCT imaging has been developed in the NIR using ultra-broad bandwidth light source technology [106, 107]. Kerr-lens-mode-locked (KLM) Femtosecond lasers can achieve 1-3 μm axial resolution, Titanium:sapphire laser operates between 700-1100 nm, Ti:Al₂O₃ around 800 nm, Chromium:forsterite around 1300 nm, and Nd:Glass and Yb around 1000 nm center wavelength. Due to complex maintenance, bulkiness, especially around 1300 nm, and high price, they are limited in research applications [59, 60, 103]. Figure II.3.16 compares the standard SLD and Femtosecond laser bandwidth:

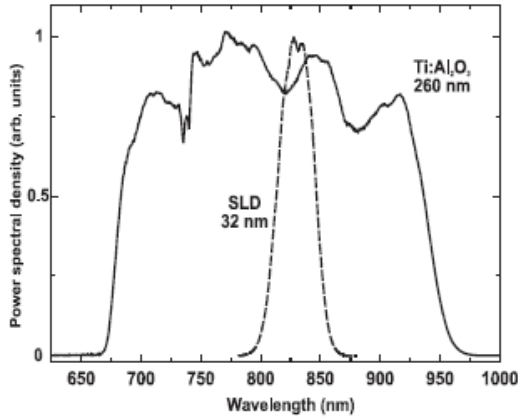


Figure II.3.16. Optical spectrum using femtosecond Ti:Al₂O₃ laser with 260 nm linewidth and 1.5 μm axial resolution vs. a standard resolution SLD light source with 32 nm linewidth and 11.5 μm axial resolution [59].

High axial resolution in the higher wavelength ranges can be produced with the Multiple quantum well (MQW) semiconductor optical amplifiers and Doped fiber based amplified spontaneous emission (ASE) sources, both operating between 1300-1600 nm.

A novel technique, the Supercontinuum (SC) laser with photonic crystal fibers (PCF) generates light source spanning the visible and NIR spectrum, with a broadband of 400-2000, 460-2400, or 500-1700 nm. Usually mode-locked pulsed laser sources are used to produce (ns, ps, fs) pulses and high peak power which lead to a nonlinear effect in the material and generate new frequency component to create the broadband. Figure II.3.17 compares some existing techniques [103]:

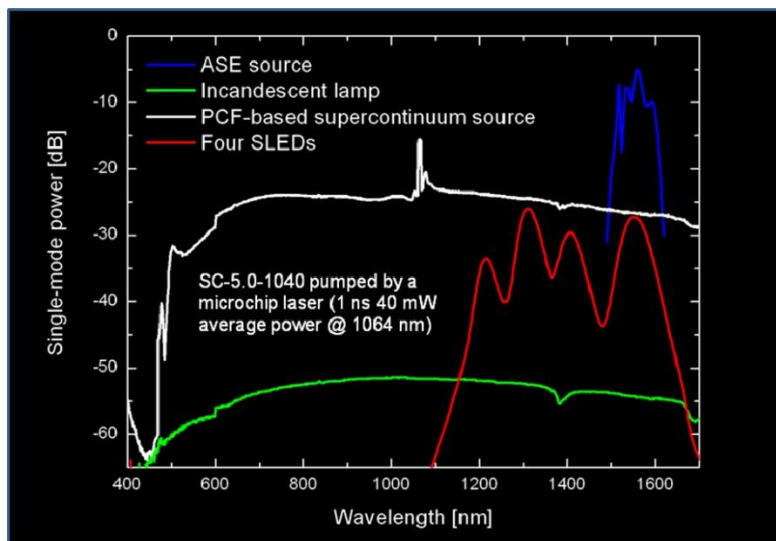


Figure II.3.17. Comparison of different laser light sources representing the advantages of supercontinuum (SC) over amplified spontaneous emission (ASE), and superluminescent LED (SLD) [103, 108].

In the visible spectrum, incandescent light sources including (xenon) halogen lamps are used. White-light interferometry was the first application in living tissue detection [109]. They are less powerful, but they feature a broad bandwidth, and furthermore no spatial coherence that suppress speckle noise. To visualize microscopic structure, and increase the power performance, the interferometer should be interfaced with microscope optics. The power limitation can be surmountable by multiple LCI channels/beams combined to one LCI beam. This was implemented with tungsten halogen lamp and xenon arc lamp [110]. The second method uses a Linnik-type interferometer. This is a Michelson-type interferometer with microscopes in the

sample arm to detect a 2D surface simultaneously with a CCD camera [85]. Interference in white-light interferometry at each pixel position occurs when the path-length difference between reference and sample arm closely matches.

II/3/d. Lateral Resolution

The axial and lateral resolution in OCT is decoupled. While the axial resolution is determined from the light source characteristics, and independently from the focusing geometry, the lateral resolution is obtained similarly to conventional and confocal microscopy since it is determined in function of the Numerical Aperture (NA) of the system:

$$NA = n \sin \theta \quad (II.3.25)$$

where n is the refractive index of the medium where the light beam is set to focus, and θ is the divergence angle of the light beam. In classical optics θ is defined from the geometrical properties, the focal length f , the d diameter of the focusing lens. The ratio gives the f -number (Figure II.3.18).

$$f_{\#} = \frac{f}{d} \quad (II.3.26)$$

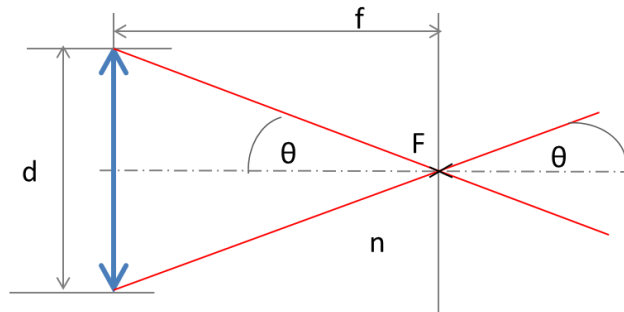


Figure II.3.18. Ideal optical geometry. Numerical Aperture defined by the half-angle θ of the light cone angle, focused to point source F , f – focal length, d – lens diameter, n – refractive index of the medium.

However the light beam has a finite spot size at the focus position, with diameter d , and so it spreads out as it propagates with the divergence angle θ , cone half-angle defined from the diffraction limit (Figure II.3.19) [111]:

$$\theta \sim \frac{\lambda}{D} \quad (II.3.27)$$

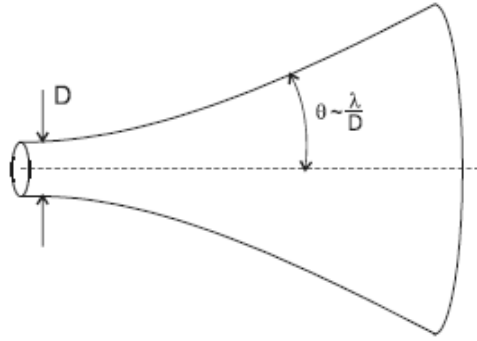


Figure II.3.19. Diffraction of light through an aperture with D diameter [111].

The angular proportionality depends on the light beam intensity distribution in the transverse direction, how sharp it will fall to zero, and how the cone edge is defined. In the case of white light microscopy, the light beam goes through a circular aperture then propagates in the z direction, and the light intensity decreases sharply in the transverse direction (x - y), and then undergoes oscillations yielding an Airy pattern, the result of Fraunhofer diffraction (Figure II.3.20). We assume a perfect optical system, the lens imperfection, and geometrical optics aberrations are not included here. The angular resolution is calculated from the Bessel function of the first kind [59]:

$$I_{conventional}(v) = \left(2 \frac{J_1(v)}{v}\right)^2 \quad (II.3.28)$$

The cone edge is defined at the position of the first dark ring, the first zero of the Bessel function (Rayleigh criterion):

$$\theta = 1.22 \frac{\lambda}{D} \quad (II.3.29)$$

with the corresponding lateral resolution (for small angles $\theta \approx \sin \theta$) is:

$$\Delta x = 1.22 \frac{f\lambda}{D} \approx 1.22 \frac{\lambda}{2NA} = 0.61 \frac{\lambda}{NA} \quad (II.3.30)$$

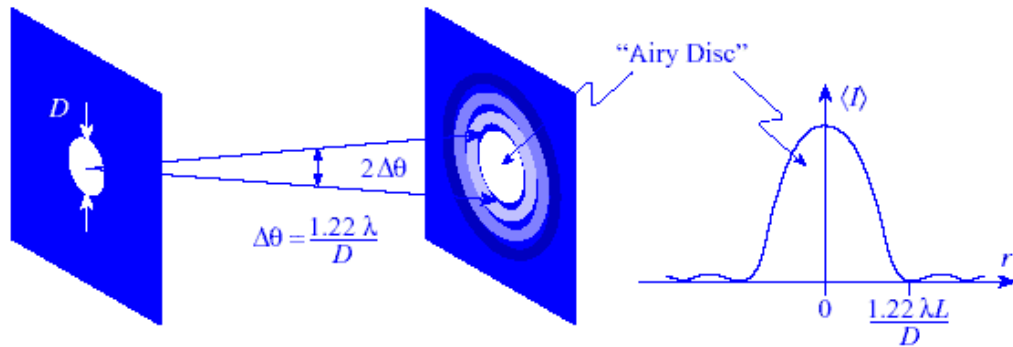


Figure II.3.20. Image formation of light with circular numerical aperture [112].

The Depth of Focus defines the limit where the image is considered sharp, and it is proposed to calculate from the square of the NA (Figure II.3.21):

$$DOF = 1.22n \frac{\lambda}{NA^2} \quad (II.3.31)$$

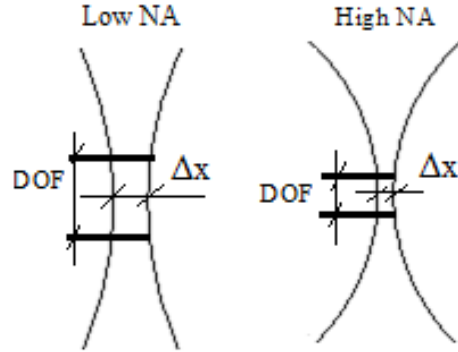


Figure II.3.21. The depth of field is an inverse function of the Numerical Aperture.

Resolution in the microscope is directly related to the FWHM dimensions of the microscope's point spread function, and it is common to measure this value experimentally in order to avoid the difficulty in attempting to identify intensity maxima in the Airy disk. Measurements of resolution utilizing the FWHM values of the PSF (from the Airy pattern, first order Bessel function) are somewhat smaller than those calculated employing the Rayleigh criterion [113]:

$$\Delta x = 0.51 \frac{\lambda}{NA} \quad (II.3.32)$$

However, it is more correct to treat the sample arm of an OCT system as a reflection-mode scanning confocal microscope. As in wide-field microscopy, resolution at the focal plane is determined by the diameter of the Airy disc, and therefore is said to be diffraction limited. Analytic expressions for intensity in the focal plane are defined from a first-order Bessel function of the first kind, and at the half-width of the intensities. We interpret the lateral point-spread function of an OCT system at the position of its focal plane (reduced in case of confocal function of lateral position) as:

$$I_{confocal}(v) = \left(2 \frac{J_1(v)}{v}\right)^4 \quad (II.3.33)$$

and defining the lateral resolution Δx as its full width at half maximum power, which calculates to

$$\Delta x = 0.37 \frac{\lambda}{NA} \quad (II.3.34)$$

The lateral field of view for an OCT system depends greatly upon the details of the lateral scanning system employed (θ_{max} – angle of sample arm rotation).

$$FOV_{lateral} = 2f\theta_{max} \quad (II.3.35)$$

It is important to mention the axial resolution defined in confocal microscopy, and related Axial Field of View or Depth of Focus. The intensity calculated along the optic axis (u) calculated from the Bessel functions is [59, 113]:

$$I_{confocal}(u) = \left(\frac{\sin(u/4)}{u/4} \right)^4 \quad (II.3.36)$$

and in conventional microscopy:

$$I_{conventional}(u) = \left(\frac{\sin(u/4)}{u/4} \right)^2 \quad (II.3.37)$$

OCT systems axial resolution is defined from the low-coherence interferometry (coherence gate), as explained earlier. OCT systems which axial resolution is comparable with the axial resolution defined from confocal sectioning (confocal gate), and both gates are aligned/overlapped, are called *Optical Coherence Microscopy (OCM)*, operating at high NA as confocal and conventional microscopy. It can provide better image rejecting out-of-focus light due to the coherence and confocal gate compared to OCT, or confocal microscopy, but it operates at limited Depth of Focus (Figure II.3.22).

Conventional OCT operates at low NA, yielding higher lateral resolution, and larger confocal length, (Axial Field of View, Depth of Focus) inversely proportional to the square of the NA. It is advisable that the coherence gate be scanned inside the focal depth defined at the FWHM of the confocal axial response function [59]:

$$DOF_{axial} = \frac{0,565\lambda}{\sin^2\left(\frac{\theta}{2}\right)} = \frac{0,565\lambda}{\sin^2\left[\frac{\sin^{-1}(NA)}{2}\right]} \quad (II.3.38)$$

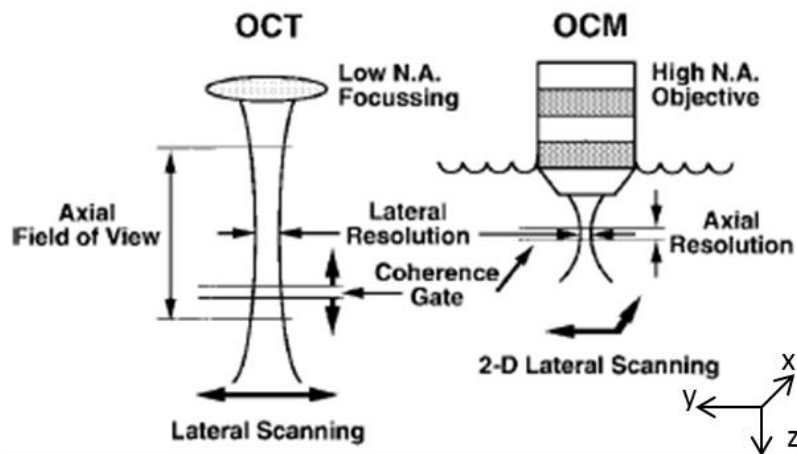


Figure II.3.22. Comparison of OCT operating at low NA and OCM operating at high NA with overlapped coherence and confocal gate enhancing resolution and image quality, but at limited depth [modified from 114].

OCM can achieve fine 1-2 μm lateral resolution, and scans laterally yielding “en face” images (x - y plane), then it repeats the scanning process at different depth. Full-Field OCT ($NA = 0.3$) provides en face images simultaneously without scanning mechanism using microscope objectives. It provides lateral resolution similar to OCM, and better axial resolution using low cost thermal light sources than can be provided from conventional OCT using ultrashort pulse laser source, but it can reach only a limited penetration depth (200 μm) in the sample [90, 91, 115].

The alignment of the coherence and focal gate in OCM and FF-OCT should be solved carefully. The refractive index of the tissue can deflect the focal plane of the objective from the theoretical one (and the coherence plane due to dispersion). Objective with water immersion can be used which refractive index is close to tissue, and so also to keep the optical path-lengths difference of both arms nearly zero. In addition water or oil immersion objectives (e.g. $n_{immersion_oil} (=1.52) > n_{water} (=1.33) > n_{air} \approx n_{vacuum} = 1$) can improve NA to obtain better image quality besides decreasing f-number with bigger lens [116, 117].

Conventional OCT with low NA provides larger depth of focus with less resolution, but the axial scanning range in OCT is still deeper than the confocal gate. In TD OCT the scanning range depth is defined from the mechanically translated mirror in the reference arm and system sensitivity, while in FD OCT the depth-scan Field of View is limited by the spectrometer resolution, the number of pixels, and the spectral bandwidth ΔK .

Since the scanned depth is deeper than the confocal depth of focus, the image quality can degrade in the out of focus regime. To overcome the focus depth limitation, several techniques have been developed which apply dynamic focus tracking, adaptive optics, axicon lens or correct the distortion digitally (deconvolution, inverse scattering, retrieving phase information, image fusion techniques) [85, 118-120].

II/3/e. Lateral Resolution using Gaussian Laser Beam

Conventional OCT systems operate in the Visible/Near Infrared region, and use radially symmetrical laser beams with transverse Gaussian intensity distribution. The electric field variation of a Gaussian beam defined radially and propagating in z direction is defined as [111, 121]:

$$E(r, z) = E_0 \frac{w_0}{w(z)} e^{-\frac{r^2}{w^2(z)}} \quad (II.3.39)$$

where r is the radial distance from the center of the beam (z axis), w_0 is the beam waist, the minimal radius at the focal plane, $z = 0$, where the electric field is E_0 , and z is the distance along the direction of propagation. The parameter $w(z)$ is the radius of the beam at the position z .

The intensity calculated from the complex conjugates of the electric field is also Gaussian. The intensity at given z position in lateral direction:

$$I(r, z) = I(0, z) e^{-\frac{2r^2}{w^2(z)}} \quad (II.3.40)$$

The intensity at the beam-axis propagating in z direction is the total beam power per effective unit area of the beam at position z :

$$I(0, z) = \frac{P}{\frac{1}{2}\pi w^2(z)} \quad (II.3.41)$$

The beam radius $w(z)$ of the Gaussian beam at any z position is defined from the Gaussian electric field or intensity distribution at the given z position. It is calculated from where the electric field or intensity is $1/e$ or $1/e^2$ of the peak value on the central axis (Figure II.3.23).

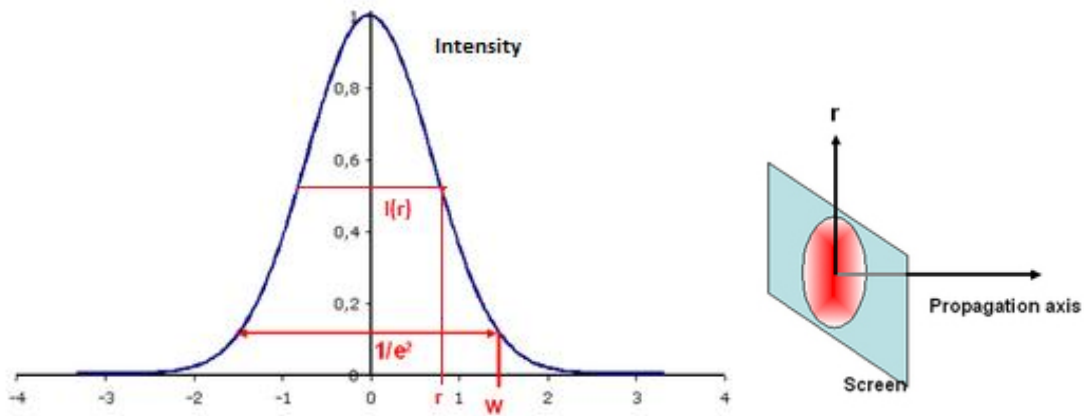


Figure II.3.23. Gaussian beam intensity distribution [modified from: 122].

The advantage of the Gaussian intensity source is that it keeps its transverse Gaussian shape with distance along the propagation axis, independently from the optical system. The intensity distribution is less sharp, and the oscillations detected in case of the Airy pattern disappear, so the divergence angle and lateral resolution is defined differently, as explained below. The equations assume a perfect optical system, with spherical optical surfaces, not large f-number and a waist $w_0 \geq 2\lambda/\pi$.

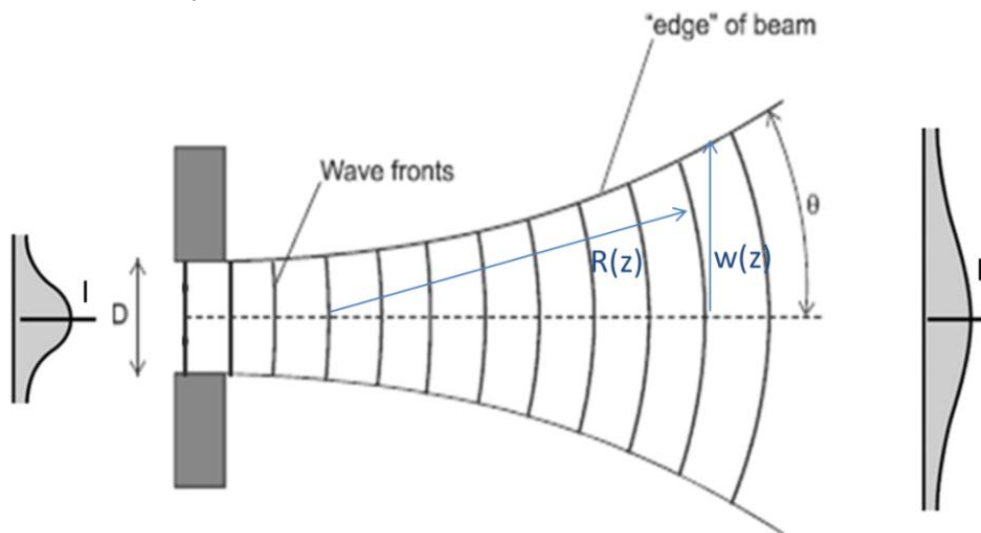


Figure II.3.24. The propagation of a Gaussian beam [modified from 111 & 123].

Two parameters, the beam radius ($w(z)$) and the radius of the curvature ($R(z)$) of the wave front describe the behavior of the beam (Figure II.3. 24).

$$w^2(z) = w_0^2 \left[1 + \left(\frac{z}{z_R} \right)^2 \right] \quad (II.3.42)$$

$$R(z) = z \left[1 + \left(\frac{z_R}{z} \right)^2 \right] \quad (II.3.43)$$

where w_0 is the radius of the beam waist, at $z = 0$, where the wave fronts are planar, $R(0) = \infty$, and the parameter z_R is the Rayleigh length. The Rayleigh length is the position of the propagation axis, where the wave front function $R(z)$ has its minimum value, $R'(z) = 0$, and is defined from the divergence angle of the asymptotic cone of the beam radius variation, and the beam waist radius (Figure II.3.25).

$$z_R = \frac{w_0}{\theta} \quad (II.3.44)$$

The characteristic of Gaussian beams is the asymptotic cone, along which the laser beam increases linearly farther from the waist ($z \gg z_R$), and its divergence angle is:

$$\theta = \frac{\lambda}{\pi w_0} \quad (II.3.45)$$

The Rayleigh length is defined as:

$$z_R = \frac{\pi w_0^2}{\lambda} \quad (II.3.46)$$

We can state from the equations above, that at $z = 0$ the spot size has its minimum value w_0 , and it increases to $w(z_R) = \sqrt{2}w_0$ at $z = z_R$, and so the area will be twice of the area at the focal plane:

$$Area(z = z_R) = w^2(z_R)\pi = 2w_0^2\pi \quad (II.3.47)$$

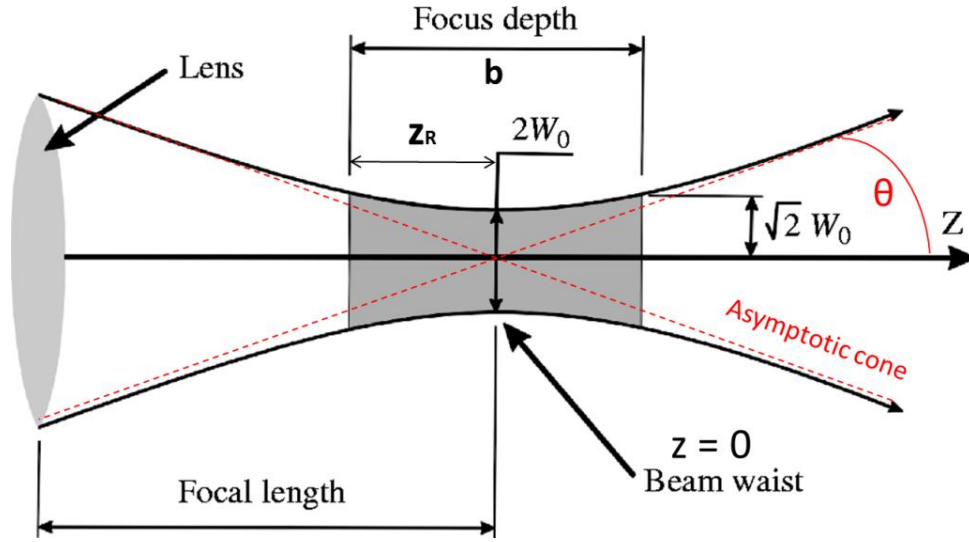


Figure II.3.25. Gaussian Laser beam profile, with parameters: beam waist ($2w_0$), focal length, Depth of focus (b), Divergence angle (θ) [modified from 124].

The angular divergence can be also defined from the equation of $w^2(z)$: If $z \gg z_R$, then

$$w(z) = w_0 \frac{z}{z_0} \quad (II.3.48)$$

$$\theta \approx \tan \theta = \frac{w(z)}{z} \approx \frac{w_0}{z_0} \quad (II.3.49)$$

The full angular width of the diverging beam is: $\Theta = 2\theta$:

$$\Theta = 2\theta = \frac{2\lambda}{\pi w_0} \quad (II.3.50)$$

The divergence angle, approximating the initial beam spot size as a point source, is calculated from geometrical optics as the diameter of the Gaussian beam on the lens, d , divided by the focal length of the lens:

$$\Theta = 2\theta = \frac{d}{f} = \frac{1}{f\#} \quad (II.3.51)$$

From the two equations expressing θ , the beam waist and the lateral resolution Δx is determined from the geometrical parameters as:

$$\Delta x = 2w_0 = \frac{4\lambda}{\pi} \left(\frac{f}{d} \right) \quad (II.3.52)$$

where λ is the central wavelengths, f is the focal length, and d is the diameter of the Gaussian beam at the objective lens. For small angles ($\theta \approx \sin \theta$):

$$z_R = \frac{\pi w_0^2}{\lambda} = \frac{w_0}{\theta} = \frac{w_0}{NA} \quad (II.3.53)$$

The NA is related to the initial beam radius, which expresses that small initial beam waist will spread out quickly (high NA), and bigger beam waist will increase slowly (low NA).

$$NA \approx \frac{\lambda}{\pi w_0} \quad (II.3.54)$$

Furthermore from the equation of $w^2(z)$ the depth of focus can be reduced, where the image is still considered sharp, and the lateral resolution is maintained. This is defined as two times the Rayleigh range.

$$2z_R = b = \frac{\pi \Delta x^2}{2\lambda} = \frac{\pi(2w_0)^2}{2\lambda} = \frac{8\lambda}{\pi} \left(\frac{f}{d}\right)^2 \quad (II.3.55)$$

These equations explained here conclude the same trade-off between the diffraction-limited fine lateral resolution versus Depth of Focus set by the NA similarly to optical microscopy [49, 59].

The assumption stating these formulas can also affect the real resolution of the system. The beam waist is usually defocused in contrary to geometric optics, and can move toward the lens when increasing the focal length. Furthermore an incorrect sampling rate can also limit the transversal resolution [121].

II/3/f. Sensitivity

The power of the LCI/OCT signal is defined from the detection process. The light incident to the detector generates photocurrent, which is converted to voltage. The measured photoelectric signal $U_G(t)$ of the interferogram G_{SR} is [85, 98, 103]:

$$U_G(t) \propto i_G(t) = \frac{\eta q_e}{\hbar \omega_0} \int_{Ar(\mathbf{r})} G_{SR}(\mathbf{r}, t) d^2\mathbf{r} \quad (II.3.56)$$

where $i_G(t)$ is the photoelectric current, η is the quantum efficiency of the detector, q_e is the electron charge, $\omega_0 = 2\pi f$ is the source center angular frequency, $\hbar = h/2\pi$ is the Planck's constant and $Ar(\mathbf{r})$ is the sensitive detector area. The photocurrent signal of the interference from the sample (P_S) and reference arm power P_R is:

$$\langle i_G \rangle = \frac{\eta q_e}{\hbar \omega_0} \sqrt{2P_S P_R} = \frac{\eta q_e}{h f_0} \sqrt{2P_S P_R} \quad (II.3.57)$$

The sensitivity is defined as the ratio of the mean signal power reflected from a mirror per the noise power of the system:

$$SNR = \frac{\langle i_G^2 \rangle}{\langle i_N^2 \rangle} \quad (II.3.58)$$

In case of an ideal Michelson interferometer splitting both arms power equally, and assuming perfectly reflecting sample, the detected photocurrent is proportional to the source power P :

$$\langle i_G^2 \rangle = \left(\frac{\eta q_e}{h f_0} \right)^2 P \quad (II.3.59)$$

In terms of reflectivity, proportionally to the signal power, the sensitivity is the ratio of the perfect mirror reflection (*Reflectivity* = 1) per the minimum detectable signal reflection equal to the system noise:

$$S = \frac{1}{R_{S,min}} \Big|_{SNR=1} \quad (II.3.60)$$

The all-in noise power of the system comes from the shot noise $\langle i_{sh}^2 \rangle$, the excess intensity noise $\langle i_{ex}^2 \rangle$, these two terms are the photocurrent noise of broadband light sources, and from the thermal noise of the receiver $\langle i_{re}^2 \rangle$:

$$\langle i_N^2 \rangle = \langle i_{sh}^2 \rangle + \langle i_{ex}^2 \rangle + \langle i_{re}^2 \rangle \quad (II.3.61)$$

OCT operates at a power in the shot-noise limited range, and the excess intensity and receiver noise can be neglected. The overall noise is expressed as:

$$\langle i_N \rangle = \langle i_{sh} \rangle = \sqrt{2q_e B \langle i_{DC} \rangle} \quad (II.3.62)$$

where B is the detection bandwidth (passband between the lowest and highest frequencies), and $\langle i_{DC} \rangle$ is the mean detector photo current determined from the reference arm power. In case of ideal 50:50 beam splitter it is equal half of the source power. Based on these assumptions, the noise power is:

$$\langle i_N \rangle = \sqrt{\frac{\eta q_e}{h f_0} 2q_e B \frac{P}{2}} \quad (II.3.63)$$

Then substituting $\langle i_G^2 \rangle$ and $\langle i_N^2 \rangle$ into SNR gives:

$$SNR = \frac{\eta P}{h f_0 B} \quad (II.3.64)$$

Usually expressing in dB scale:

$$SNR = 10 \log_{10} \left(\frac{\eta P}{h f_0 B} \right) \quad (II.3.65)$$

The signal-to-noise ratio in the shot-noise limited regime is proportional to the source power. This intermediate regime is the optimal for OCT. The limit regimes are when the thermal

or the excess noise would dominate. The thermal noise of the receiver is independent from the source power, and when OCT operates at lower power, this would be the dominating noise. At higher power, the excess noise would limit the sensitivity since it is proportional by the square of the source power [85, 98].

The signal-to-noise ratio defined here is inversely proportional to the electrical detection bandwidth. Using a single detector (Time-Domain (TD) OCT), the measurement bandwidth B is inversely proportional to the detector acquisition time $B = 1/\tau$. An optimal solution is required to set off the axial resolution vs. image acquisition speed while keeping the same source power and sensitivity [103].

Replacing the single detector of TD OCT, where all spectral components contribute in gross to the detected interferogram, with a multiple-detection camera array will improve the SNR ratio, where separately detecting the spectral components will reduce the cross shot-noise [125].

FD OCT operates with a 1D detector-array detecting each spectral component separately simultaneously (Spectral-domain OCT), or with a single detector, but detecting each channel successively in time (Swept-Source OCT). With M separate channels the SNR at the same power is $M/2$ -times higher due to M , the number of channels, but divided by two due to the Hermitian symmetry of Fourier-transform of real valued signals. This operation mode improves imaging speed, but the complex conjugate artifact and digital signal processing effects degrades the signal [59, 85, 125].

Parallel OCT detection SNR is further improved with a 2D camera by the number of pixels, but the CCD has limitation detecting the time average instead of alternating current. The sensitivity can be improved with phase-modulation or smart CMOS detectors. Furthermore FF OCT using spatial incoherent light source suppress speckle noise formation to improve image quality, but the low power featuring this light source limits the sensitivity [85, 90].

II/4. Spectral-Domain Optical Coherence Tomography

II/4/a. Setup of the SD OCT system

Fourier-Domain Optical Coherence Tomography, and the Spectral-Domain OCT version was used for the experiments. The measurement setup in the laboratory can be seen on Figure II.4.1 with the corresponding scheme on Figure II.4.2.

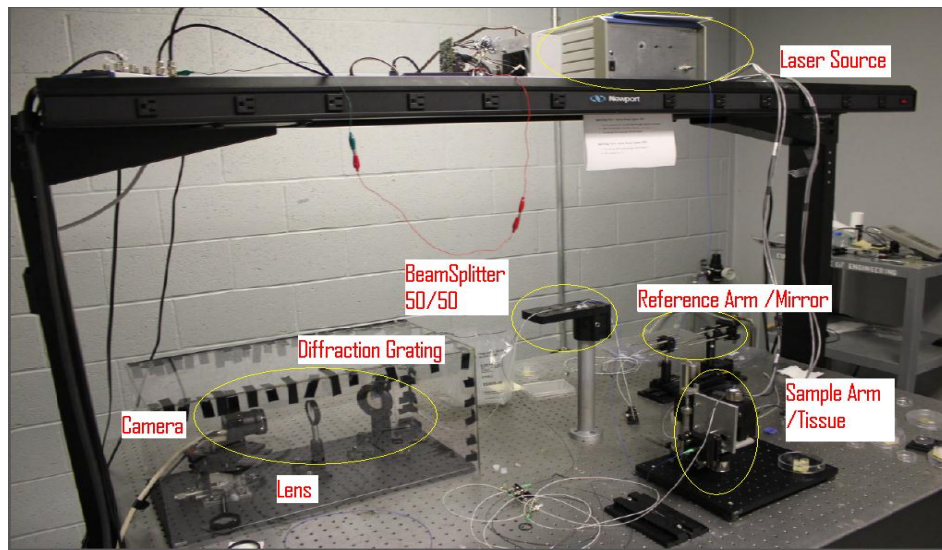


Figure II.4.1. SD-OCT measurement setup in the laboratory on a table against vibration.

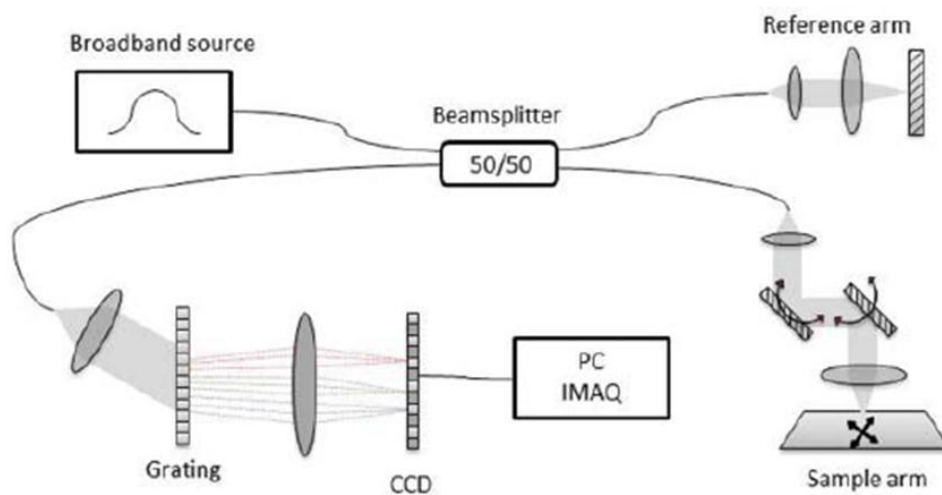


Figure II.4.2. SD-OCT scheme [24].

The Laser Source used is a SUPERLUM Broad Lighter S840-B-I-20 (data sheet shown and explained above) operating in high power mode, at a center wavelength of $\lambda_0 = 840 \text{ nm}$, and $\Delta\lambda = 50 \text{ nm}$ Spectrum Width determined at the FWHM of the power spectra yielding an axial

resolution of $\sim 10 \mu\text{m}$ coherence length (in air). The output full power mode of 20 mW is directed in a SM (single-mode) fiber output power.

The light intensity is halved in a 2:2 fiber coupler, and carried to the reference and sample arm by an optical fiber. The collimated light is focused onto the sample through a galvo mirror for transversal scanning (Thorlabs Scanning Lens LSM03) over an area usually $3 \times 3 \text{ mm}$, and the laser beam waist spot size is set for a lateral resolution of $\sim 8 \mu\text{m}$ (in air). The axial sampling density was $\sim 4.4 \mu\text{m}$ per pixel measured empirically, and the lateral sampling density was $6 \mu\text{m}$ per pixel set on 500 A-lines over a 3 mm line.

The light reflected back from the reference mirror can be attenuated through a pinhole to get a visible interference signal. The backscattered light from both arms are recombined and spectrally decomposed through a spectrometer, which consists of an achromatic doublet lens that collimates the beam to a diffraction grating (Wasatch Photonics, 1200 grooves per mm), and another lens focuses the spectrum to the CCD Line Scan Camera (Basler L104K-2k, 2048 pixel resolution, $10 \times 10 \mu\text{m}^2$ pixel size, 29.2 kHz line scan rate).

The detected signal in function of wavelength is digitized by an analog-to-digital converter (National Instruments NI-IMAQ PCI-1428 frame grabber card), then processed in LabView environment. The Discrete Fourier Transform is calculated after spectral shaping using Hanning window, and resampling the interferogram from wavelength space to wavenumber space through phase correction.

After recording one A-scan, the OCT beam is positioned to the adjacent point through the galvo mirror in the sample arm, so scanning laterally to obtain 2D B-scan and 3D C-scan. The imaging depth is $\sim 3.4 \text{ mm}$ in air and $\sim 2.2 \text{ mm}$ in tissue.

II/4/b. Interference in the SD OCT system

The laser source generates the broadband laser signal. The electric field of one wavelength (i) is [59, 60]:

$$E(\lambda_i) = E_i = (A_i e^{-i\omega_i t}) \quad (\text{II.4.1})$$

This signal is directed through a waveguide to the beam-splitter (fiber coupler), which halves the intensity of the signal. When the intensity is halved, the electric field is divided by square root of 2. One part goes to the Reference arm, another part goes to the Sample arm.

The signal reflects perfectly from the reference mirror (assumed reflectance: $r_R = 1$, in reality $r_R = 0.95-0.99$ dependent upon wavelength) and goes back the same way to the beam-splitter through a pinhole that attenuates the intensity amplitude by a factor v , and halves again. The electric field of one wavelength (i) from the Reference arm is:

$$E_{Ri} = \left(\frac{A_i}{2} v e^{-i\omega_i t} \right) \quad (\text{II.4.2})$$

The attenuation in the reference arm is important to avoid saturation upon detection, and to get a visible interferogram, since the back-reflection from the sample arm is about 2-3 order magnitude smaller. The signal from the Sample arm reflected back from each layer (j) of the tissue goes back to the beam-splitter where the intensity halves again:

$$\Sigma_j E_{Sij} = \Sigma_j \left(\frac{B_{ij}}{2} e^{(-i\omega_i t + \varphi_{ij})} \right) \quad (II.4.3)$$

where B is the amplitude of the back-reflected light per wavelength (i), reflected from a specific layer (j) of the tissue. Upon recombining the sample and reference arm at the beam-splitter, the two signals will arrive with a phase-shift (φ), which depends on the wavenumber ($k_i=2\pi/\lambda_i$) and the pathlength-difference (z_{ij}) between the mirror and the specific layer:

$$\varphi_{ij} = k_i z_{ij} \quad (II.4.4)$$

The back-reflected electric signals coming from the reference mirror and the sample are summed up at the beam-splitter.

$$E_i = E_{Ri} + \Sigma_j E_{Sij} \quad (II.4.5)$$

The intensity of this interference signal going through the spectrometer is detected at one pixel of the camera array $I(\lambda)$, which has a detector factor (ρ):

$$I(\lambda_i) = I_i = \rho \left\langle |E_{Ri} + \Sigma_j E_{Sij}|^2 \right\rangle \quad (II.4.6)$$

The intensity at specific wavelength (λ) neglecting the factor of the pinhole (v) and the detector (ρ), first considering a one-layer-tissue-sample is:

$$\begin{aligned} I(\lambda) = I &= \langle |E_R + E_S|^2 \rangle = (E_R + E_S)(E_R + E_S)^* = E_R^2 + E_S^2 + E_R^* E_S + E_R E_S^* \\ &= |E_R|^2 + |E_S|^2 + |E_R||E_S|e^{-i\omega t} e^{+i(\omega t + \varphi)} + |E_R||E_S|e^{+i\omega t} e^{-i(\omega t + \varphi)} \\ &= |E_R|^2 + |E_S|^2 + |E_R||E_S|(e^{+i\varphi} + e^{-i\varphi}) \\ &= |E_R|^2 + |E_S|^2 + |E_R||E_S|[(\cos \varphi + i \sin \varphi) + (\cos \varphi - i \sin \varphi)] \\ &= |E_R|^2 + |E_S|^2 + 2|E_R||E_S|(\cos \varphi) \end{aligned} \quad (II.4.7)$$

For a sample composed of multiple layers (j, l):

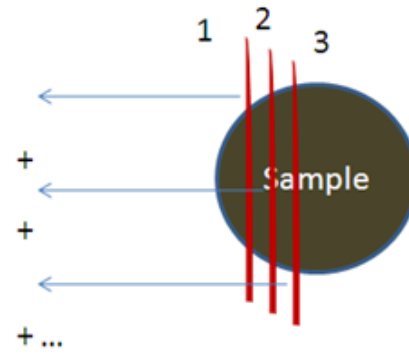
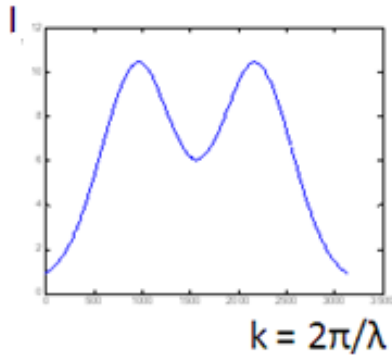
$$I(\lambda) = I = |E_R|^2 + \Sigma_j |E_{Sj}|^2 + 2|E_R| \Sigma_j |E_{Sj}| (\cos \varphi_j) + 2 \Sigma_j |E_{Sj}| |E_{Sl}| (\cos \varphi_{jl}) \quad (II.4.8)$$

where the first two terms are the DC term, the sum of the intensity amplitudes reflected back from the mirror and each layer, the third term is the interference term between the reference mirror and each layer, and the last term is the interference between the sample layers, which can be neglected.

The intensity variation of the interferogram on the pixel array of the line scan camera detected in function of wavelength (i) is a periodic signal for each layer (j):

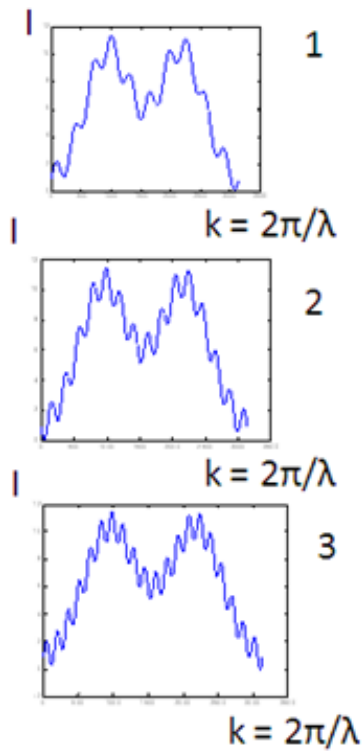
$$I(\lambda_i) = I_i = |E_{Ri}| \Sigma_j |E_{Sij}| (\cos(k_i z_{ij})) \quad (II.4.9)$$

Resampling the intensity from wavelength λ to wavenumber space ($k_i=2\pi/\lambda_i$) and Fourier Transforming will give the reflectivity (z_{ij}) of each layer (Figure II.4.3).

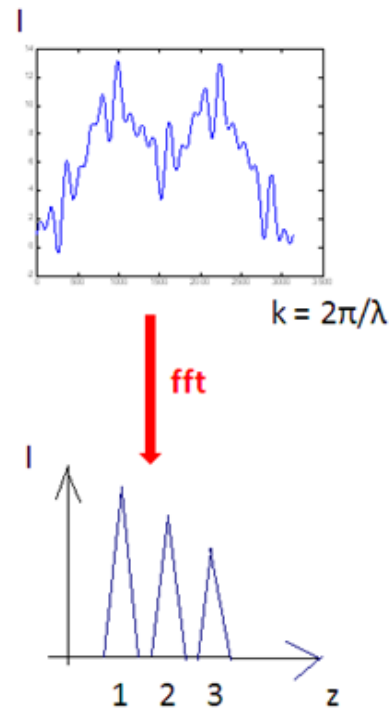


a) DC term, deduced from the input spectral shape.

b) Light scattered back from multiple layers of the sample.



c) The reflectivity per layer. Bigger path-length difference means higher frequency.



d) Intensity Output superposed from each layer on the DC term, and Fourier Transform shown without the DC term component.

Figure II.4.3. Fourier Transform of the Interferometer Exit.

II/4/c. Interpolation of the intensity range, light attenuation in tissue

Interference signal detected on the detector from a Human Normal Fat tissue is shown on Figure II.4.4. The wavelength range between 800-890 nm is spread over 2048 pixels.

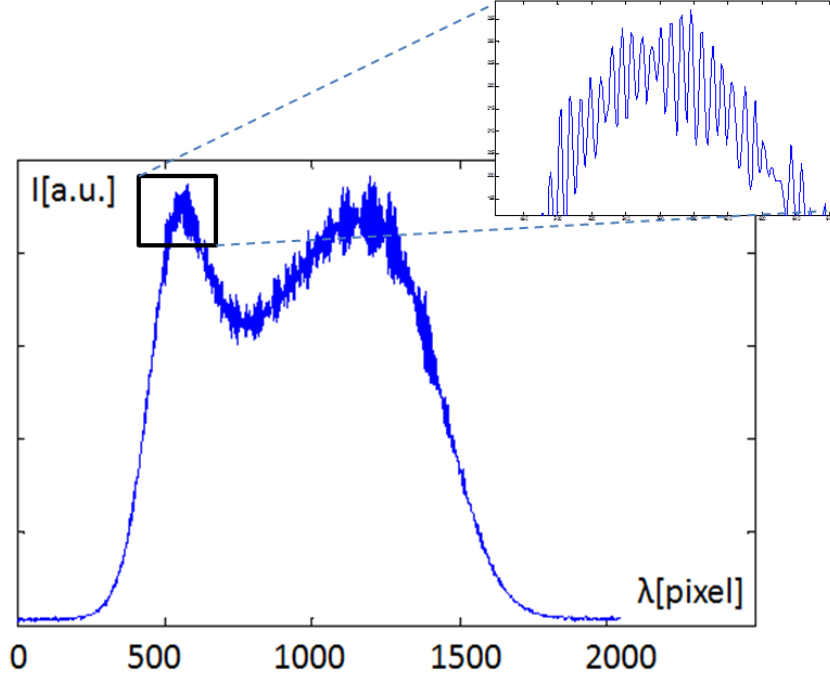


Figure II.4.4. Interferometer Exit recorded on Normal Fat Tissue.

These interference fringes contain the structural information of the tissue subsurface at one spatial position by yielding the back-scattering intensity in function of depth (A-line). Before Direct Fourier Transform, the data points should be evenly sampled in wavenumber k -space. An interpolation method is required to resample the interferogram from wavelength λ -space [126].

First N linearly spaced k values are defined between the minimum ($\lambda_{min} = 800$ nm) and maximum ($\lambda_{max} = 890$ nm) recorded wavelength.

$$k_i = \frac{2\pi}{\lambda_i} = 2\pi \left(\frac{1}{\lambda_{max}} + \frac{i}{N-1} \left(\frac{1}{\lambda_{min}} - \frac{1}{\lambda_{max}} \right) \right) \quad i = 1, 2, \dots, N \quad (II.4.10)$$

Each 2048 intensity points ($I(\lambda_i)$) will be resampled from λ -space to k -space $I(k_i)$ through a non-linearity parameter s_i . The new sampling positions are defined from:

$$\lambda_i = \lambda_{min} + s_i \frac{\lambda_{max} - \lambda_{min}}{N - 1} \quad (II.4.11)$$

The non-linearity array $\{s_i\}$ gives the new interpolation sampling points defined from the wavelength range to resample the intensity points linearly in k -space.

$$s_i = \frac{N-1}{\lambda_{max} - \lambda_{min}} \left[\left(\frac{1}{\lambda_{max}} + \frac{i}{N-1} \left(\frac{1}{\lambda_{min}} - \frac{1}{\lambda_{max}} \right) \right)^{-1} - \lambda_{min} \right] \quad 1 \leq i \leq N \quad (II.4.12)$$

The more complex and more accurate Cubic B-spline interpolation is preferred than linear interpolation. The accuracy of any interpolation can be improved by up-sampling the data by Fast Fourier Transform, zero-padding and then performing Inverse FFT [127].

The Discrete Fourier Transform of the interferogram sampled equally in k-space $I(k_i)$ will give the both-side spectra of the real valued signal spread on 2048 intensity points. Only the one-side spectrum provides the useful structural information spread on 1024 intensity points ($I(z_i)$). 1024 pixels are equal to ~ 4.5 mm measured empirically (Figure II.4.5a).

This digital conversion is applied to the adjacent A-lines recorded by scanning process. 500 A-lines with ~ 6 μm shift will give the B-scan to cover a ~ 3 mm wide cross-section (Figure II.4.5b), and multiple cross-section will record the volume (C-scan).

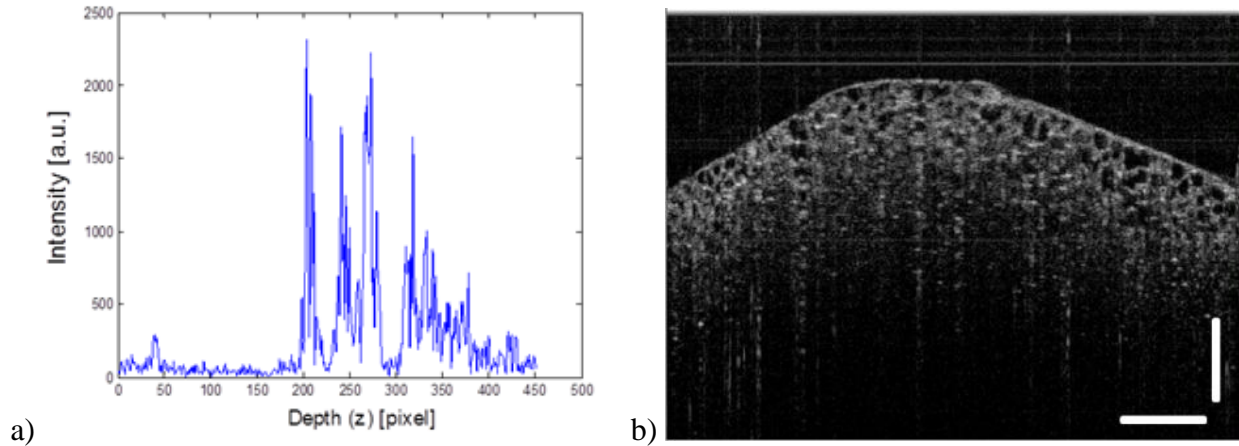


Figure II.4.5. Normal Fat Tissue.a) OCT A-line (1mm = 228 px) b) B-scan composed of 100 A-lines (white bar = 500 μm).

The dB representation of the OCT image is preferred to get a better visibility, and to recover the light attenuation (slope) in function of depth directly from the signal. The intensity decreases exponentially:

$$I(z) = I_0 e^{-u_t z} \quad (II.4.13)$$

where the attenuation coefficient is the sum of the scattering and absorption coefficient $u_t = u_s + u_a$, but the absorption coefficient can be neglected ($u_a = 0$) in the near infrared range, where OCT usually operates. Taking the logarithm of the intensity variation will provide the slope of the intensity attenuation in linear scale, which can be measured now from the figure after averaging or filtering the A-lines:

$$\log(I_z) = \log(I_0) - u_s z \quad (II.4.14)$$

Due to the Digital Signal Processing effect, there are other factors explained later, which affect the Intensity signal attenuation in function of depth. The resampling process should also be corrected using phase correction due to the dispersion explained below [59].

II/4/d. Dispersion compensation by phase correction

Dispersion occurs because the velocity of the different frequency components of the light travels at different velocity in the dispersive medium (interferometer arms and tissue sample), and their speed is dependent of the refractive index of the medium, which slows down or speed up certain frequency components dispersing the light. The wavevelocity in a given media is:

$$v(\lambda) = cn(\lambda) \quad (II.4.15)$$

The effect of dispersion on a light pulse going through the material will result a pulse output spread in time, called chirped signal. The consequence is a degraded signal, and blurred image quality.

The interference signal for one sample layer is described generally:

$$I(\lambda) = |E_{R(\lambda)}|^2 + |E_{S(\lambda)}|^2 + 2|E_{R(\lambda)}||E_{S(\lambda)}| \cos(f(\lambda)2\Delta z + g(\lambda)) \quad (II.4.16)$$

Ideally the phase constant $g(\lambda)$ can be neglected, but due to dispersion:

$$g(\lambda) = [2d/f(\lambda)][n(\lambda) - 1] \quad (II.4.17)$$

where $n(\lambda)$ is the wavelength dependent refractive index of the dispersive material (tissue sample) with a thickness of d , where light travels back and forth. The dispersion $dn(\lambda)/d\lambda$ broadens the envelope of the time domain signal [59].

The phase term $(f(\lambda)2\Delta z)$ is the product of twice the path-length difference Δz between two arms, since light travels back and forth, and $f(\lambda) = k = 2\pi/\lambda$, as described earlier. This wavenumber - wavelength nonlinearity is affected by the dispersion of the waveguides, diffraction grating, and optical imaging errors, and should be corrected to get the correct resampling function.

The OCT signal is based on the phase shift due to the path-length differences between two arms. For any given material the phase is the function of frequency, and can be expanded in a Taylor series around the central frequency of the light source:

$$\begin{aligned} \phi(\omega) = & \phi(\omega_0) + (\omega - \omega_0) \left. \frac{d\phi}{d\omega} \right|_{\omega_0} + \frac{1}{2} (\omega - \omega_0)^2 \left. \frac{d^2\phi}{d\omega^2} \right|_{\omega_0} + \frac{1}{6} (\omega - \omega_0)^3 \left. \frac{d^3\phi}{d\omega^3} \right|_{\omega_0} \\ & + \dots \end{aligned} \quad (II.4.18)$$

The zeroth order term is the phase shift of central frequency $\phi(\omega_0) = \frac{\omega_0}{c} 2L$. The constant phase velocity of the central wavelength in the spectral bandwidth (Figure II.4.6b):

$$v_p = \left. \frac{\omega}{k} \right|_{\omega_0} \quad (II.4.19)$$

The first order term $\frac{d\phi}{d\omega} = 2L \frac{dk(\omega)}{d\omega}$ is the group delay, the inverse group velocity.

$$v_g = \left. \frac{d\omega}{dk} \right|_{\omega_0} \quad (II.4.20)$$

The group velocity is the envelope shift, the speed of the broadband light propagation (Figure 6c). In ideal case the refractive index of a material is independent of the wavelength $d\omega/dk = \omega/k$, the medium is no dispersive, and $v_g = v_p$. However this is not valid generally.

The second order term $\frac{1}{2} \frac{d^2\phi}{d\omega^2} = \frac{1}{2} 2L \frac{d^2k}{d\omega^2}$ is the group velocity dispersion (GVD), which describes the variation in group velocity with frequency.

$$GVD = \left. \frac{d^2k}{d\omega^2} \right|_{\omega_0} = \frac{\partial}{\partial \omega} \left(\frac{1}{v_g} \right) \quad (II.4.21)$$

This term is responsible for the broadening of the Point Spread Function, degrading the axial resolution of OCT images, changing the amplitude or phase (Figure 6d). $[GVD] = s^2/m = s/Hz \cdot m$. GVD measures the delay per unit frequency bandwidth, or per unit length of propagation.

The third order term $\frac{1}{6} \frac{d^3\phi}{d\omega^3} = \frac{1}{6} 2L \frac{d^3k}{d\omega^3}$ causes the asymmetric distortion of the PSF [104, 128].

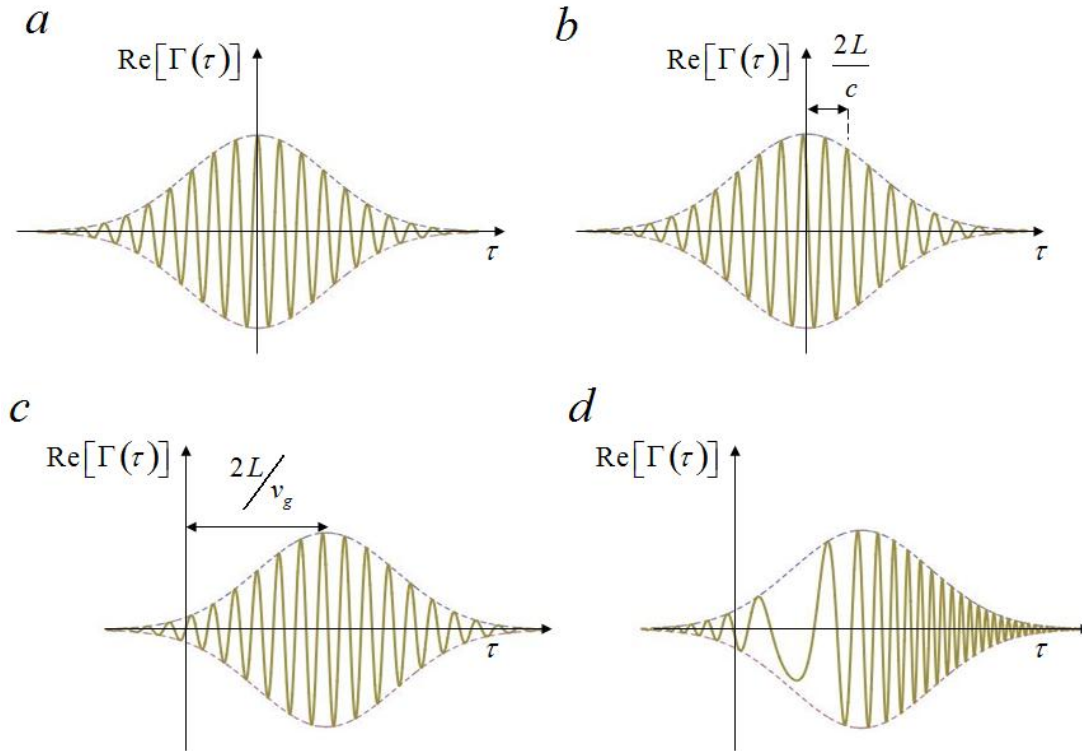


Figure II.4.6. a) Autocorrelation for a perfectly balanced detector b) Phase delay (zeroth order) c) Group delay (first order) d) GVD (second order) [128].

Figure II.4.7 shows the dispersion in Spectral Domain OCT system with the increase of the optical path-length distance between the sample and reference arm by moving a sample mirror in axial distance, and extract PSF at each position.

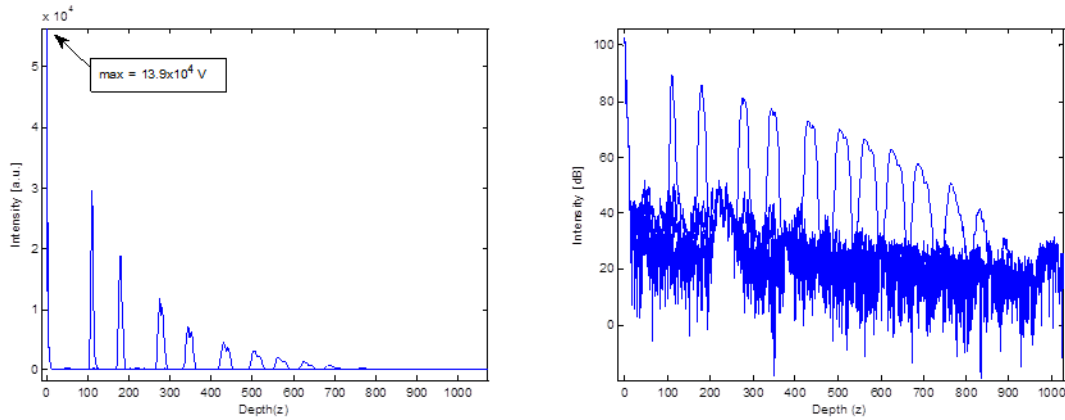


Figure II.4.7. Degradation of PSF (point spread function), peak broadening and intensity loss at increasing path-length differences without dispersion compensation (linear & logarithmic scale).

Dispersion in the sample is problematic since it is not known, and varies during axial scanning. For most OCT imaging applications, the axial depth of imaging is shallow, so this effect can be negligible. Around $10 \mu\text{m}$ resolution, as in our system, this becomes significant only at deeper positions, for a system of $1 \mu\text{m}$ resolution using broader bandwidth, this error should be corrected for each sample depth (e.g. placing the media in the reference arm also, using a frequency-domain delay line, by convolution or by post-processing, digitally with an iterative procedure by optimizing the sharpness of the image [129]).

The unbalanced dispersion of the instrument does not vary per axial scanning, and it can be compensated. Dispersion correction from the system components can take place both in the hardware (frequency-domain delay line) and the software (post-detection from amplitude and phase information) [104].

In our OCT setup the dispersion compensation of the system is solved digitally by retrieving the spectral phase from the Fourier Transform of the interference spectrum from a calibration signal, method called Fourier-Transform Spectral Interferometry (FTSI). The calibration signal will be the interference signal recorded from two perfectly reflecting mirrors at a path-length-difference which gives a resolvable spectral period (Figure II.4.8).

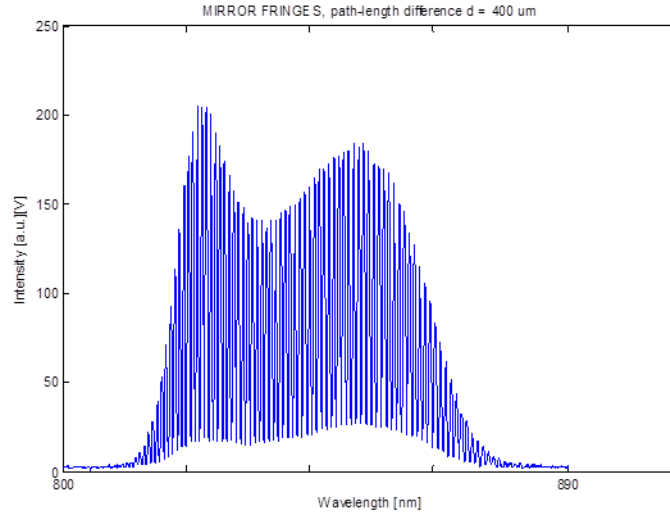


Figure II.4.8. Interferometer Exit; Spectrum from two interfered signals, one is delayed by a path-length-difference $l = 400 \mu\text{m}$; and chirped due to dispersion.

The path-length difference determines the interference spectrum oscillation. In addition the phase of the oscillation is nonlinear due to dispersion, which causes the chirped signal. The retrieved phase nonlinearity will be the functional relation to resample the interferogram from wavelength space to wavenumber space. The resampling method in the system is developed according to [130].

The unwrapped phase of the interference fringes is retrieved from the complex analytic representation of the signal $S(\omega)$. The complex signal is recovered from the Real part detected on the Interferometer Exit. First Discrete Fourier Transforming the detected Real signal will provide both-side spectra, the position of the mirror at positive and negative path-length difference. The obtained Point Spread Function is broad due to the nonlinear sampling, and side-lobes can be present due to the Gaussian spectral shape of the light source (Figure II.4.7). Zero-filling interpolation could improve the calibration algorithm.

Inverse Fourier Transforming the positive frequencies (one-side spectra) obtained by Heaviside window (unit step function) and keeping the same pixel range (2048), results in the complex signal (Figure II.4.9a):

$$S(\omega) = |S(\omega)|e^{i\phi(\omega)} \quad (II.4.22)$$

Eliminating the mirror-image caused by the Fourier Transformation of the Real valued signal will increase the ranging depth by a factor of two [130, 131, 132].

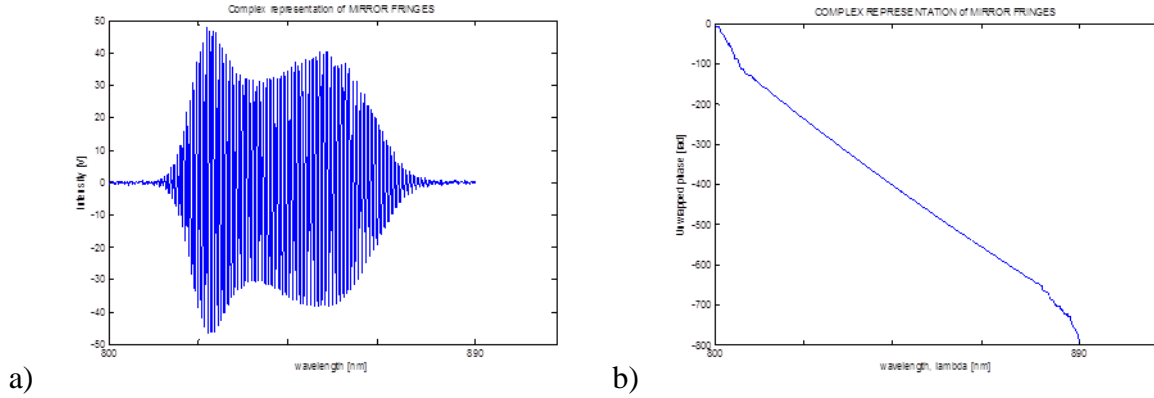


Figure II.4.9. a) Complex representation of the fringe signal b) Unwrapped phase.

The unwrapped phase from the complex fringe signal is nonlinear, and will be the resampling function (Figure II.4.9b). The function parameters are computed by a polynomial fit to the retrieved unwrapped phase after cutting the edges where the laser power can be neglected. Correcting the signal by this phase nonlinearity of $S(\omega)$ will compensate the dispersion:

$$\varphi(\omega) = -a_2(\omega - \omega_0)^2 - a_3(\omega - \omega_0)^3 \quad (II.4.23)$$

The second-order coefficient a_2 balances the GVD, and the third-order coefficient a_3 balances the asymmetric PSF distortion. Higher order terms can be neglected. The non-linearity array can then be expressed as [127]:

$$s_i = i + a_2 i^2 + a_3 i^3 \quad 1 \leq i \leq N \quad (II.4.24)$$

This third-order polynomial will provide the fractional indexes of resampling intensity from λ - to linearly spaced k -space. The Fourier Transform of the corrected spectrum will provide the appropriate PSF and axial depth scan (Figure II.4.10). The remaining sensitivity roll-off is due to DSP errors because of the limitation of the electronic devices explained below.

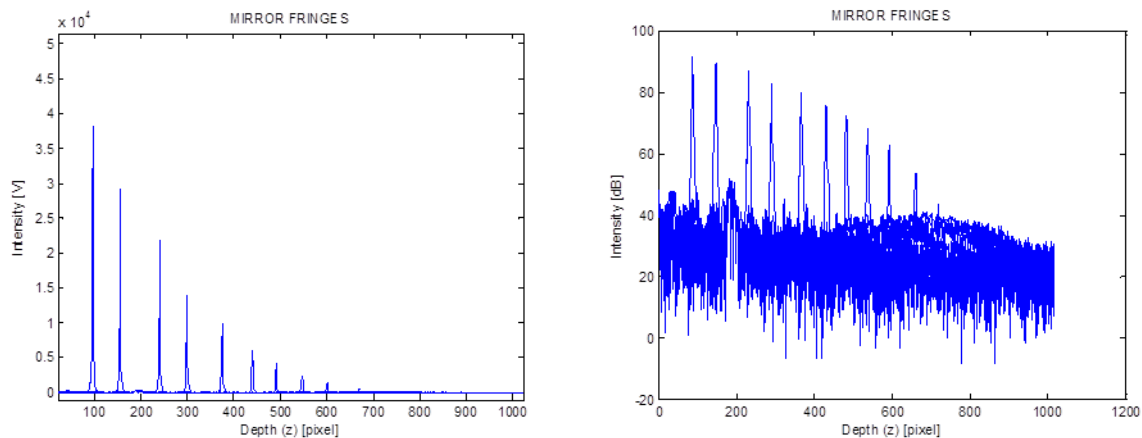


Figure II.4.10. Point Spread Functions in function of path-length difference with dispersion compensation (linear & logarithmic scale).

The calibration procedure is performed only once and then calibration coefficients are used for rescaling each A-scan. The long-term stability of this calibration method is dependent on the long-term stability of the light source, and can be applied also to SS-OCT systems.

SS-OCT resampling method can be solved using additional device, e.g. oscilloscope for zero-crossing point detection or second interferometer for 2-channel detection (non-linear clocking scheme) [133-135]. Instead of phase information, the calibration parameter can be the positions of consecutive minima and maxima of the fringes to generate optical frequency comb [136].

The signal post-processing can be improved by background subtraction present in all the A-lines by averaging the interferograms and subtracting the reference spectrum or measured only from the reference arm reflection [103]. Instead of the usual FFT procedure, filter-bank approach can be applied on the raw data [137].

II/4/e. Sensitivity roll-off

Sensitivity fall off and reduced contrast is shown on Figure II.4.10. The reason is explained on Figure II.4.11 following [136].

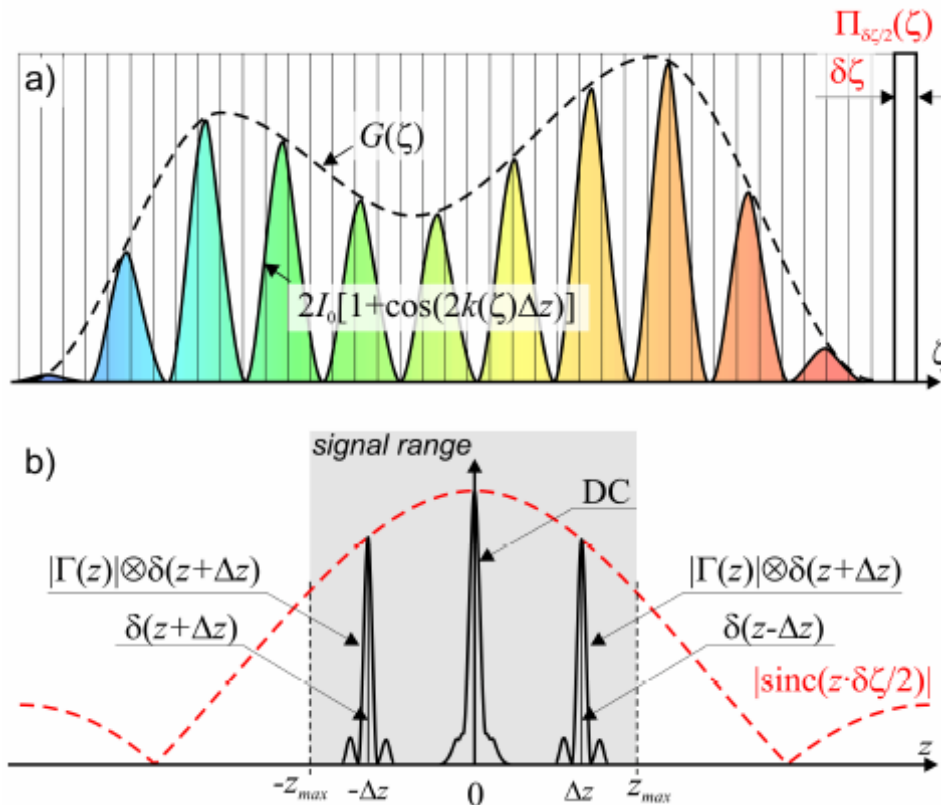


Figure II.4.11. a) Simulated interferogram; Dotted line: light source spectrum $G(\zeta)$; Solid line: interferometric modulation; $\delta\zeta$: pixel width b) Fourier transform of the interferogram [136].

Sensitivity roll-off and degraded resolution is due to the physical limitations of the elements of the OCT system, beside the light dispersion and scattering effects. The physical limitations in the measurement systems come from the non-linear characteristic of the OCT elements (beamsplitter, wave-guides...), from the light source spectral shape and the finite resolution of the spectrometer and array detector. Figure II.4.11a shows the simulated interferogram PSD with the signal envelope $G(\zeta)$ and interference fringes detected on the detector pixels:

$$I(\zeta) = 2G(\zeta)[1 + \cos(2k(\zeta)\Delta z)] \quad (II.4.25)$$

where $G(\zeta)$ is the intensity of the light source, $k(\zeta)$ is the wavenumber at pixel position ζ on the camera array, multiplied by the doubled path-length difference Δz between the two mirrors. Figure II.4.11b shows the Fourier Transform of the interferometric signal yielding the PSF $\delta(z \pm \Delta z)$ at positions of $\pm \Delta z$ and the DC term:

$$|FT\{I(\zeta)\}| = DC + |\Gamma(z)| \otimes \delta(z \pm \Delta z) \quad (II.4.26)$$

The camera array has a limited number of pixels (ζ) and the pixels have a finite width ($\delta\zeta$). The sampling cannot be described by Dirac delta function but with a box function with width equal to the pixel width:

$$\Pi_{\delta\zeta/2}(\zeta) \quad (II.4.27)$$

This finite width causes loss of sensitivity with the depth measurement. The Fourier Transform of the box function is a sinus cardinal function:

$$|\text{sinc}(z \delta\zeta/2)| \quad (II.4.28)$$

The array detector has finite width, which means it integrates the spectrum over a finite wavelength range. The finite spectral resolution of the interferometer gives errors on the DFT calculation (*Aliasing*(ζ)). The signal processing aliasing error in our system is corrected using Hanning window on the generated signal. The sampling rate at low frequencies is better than in high frequencies resulting to partial aliasing of the signal, furthermore reaching the Shannon-sampling rate the higher frequencies cannot be detected.

Inter-pixel crosstalk happens when the charge of a pixel is transmitted to the other pixels of the camera array deteriorating the signal (*Crosstalk*(ζ)). Finally the finite spot size of the laser at each pixel on the detector gives errors in the signal acquisition procedure (*Spotsize*(ζ)).

The interferometric signal is convolved with all the degrading DSP effects, which deteriorates the signals from longer path-length differences, and the registered decay is usually approximated by a Gaussian function:

$$I_{reg}(\zeta) = [\Pi(\zeta) \otimes \text{Crosstalk}(\zeta) \otimes \text{Spotsize}(\zeta) \otimes \text{Aliasing}(\zeta)] I(\zeta) \quad (II.4.29)$$

where $I_{reg}(\zeta)$ is the registered interference signal. The Fourier Transform of the interferogram is multiplied with the FT of all the errors.

The spectrometer resolution limits the theoretically calculated axial resolution vs. imaging depth range in SD OCT systems. However broader spectral light sources provide better

axial resolution, they induce higher sensitivity roll-off, and so less imaging depth range as explained here [138]:

SD-OCT pixel interval is defined from the detected full spectral source bandwidth (λ_{full}) and central wavelength λ_0 .

$$\delta z = \frac{\lambda_0^2}{2\lambda_{full}} \quad (II.4.30)$$

This equation comes from the depth range limitation (z_{max}) in the Fourier domain:

$$z_{max} = \frac{\pi}{2\delta k} \quad (II.4.31)$$

where δk is the wavenumber spacing between pixels defined from the spectral source and the number of pixels (N):

$$\delta k = \frac{2\pi\lambda_{full}}{N\lambda_0^2} \quad (II.4.32)$$

The pixel interval δz is the depth range (z_{max}) divided by half of the length of the spectrometer array ($N/2$).

The spectral bandwidth detected by the camera should fulfill the Nyquist sampling theorem:

$$\delta z \leq 1/2 \Delta z \quad (II.4.33)$$

where $\Delta z = \frac{2 \ln 2}{\pi} \frac{\lambda_0^2}{\Delta \lambda}$ is the theoretical axial resolution. This results in:

$$\lambda_{full} \geq \frac{\pi}{2 \ln 2} \Delta \lambda = 2.26618 \Delta \lambda \quad (II.4.34)$$

Overall the sensitivity roll-off and the error analysis of the system should consider multiple factors. The physical limitation of the system affects the theoretical resolution of the system, due to e.g. the electronic device non-linear characteristics, camera heating, optical imperfections, and the spectrometer limitation with the DSP computations. Errors coming from the light source behavior include the spectral shape limitation, dispersion and scattering effects in turbid media [136].

OCT signal is based on the detection of ballistic photons after single back-scattering, however photons which underwent multiple scattering can contribute to the OCT signal degrading the resolution. Speckle scattering, a secondary interference phenomena makes the images noisy. The polarization state of the electric field is not mentioned here (Figure II.4.12).

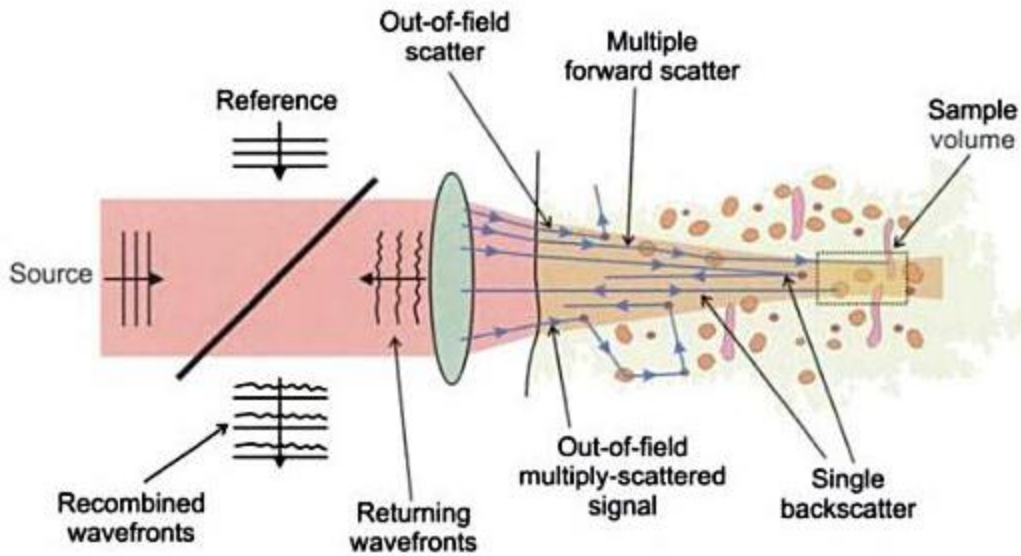


Figure II.4.12. Scattering process and wavefront dispersion affecting OCT images [104].

To set up an experiment independently from the settings (focus position, exposure time, spectral shape and intensity input to the sample arm, pinhole attenuation from the reference mirror, path-length difference between sample surface and mirror) is an additional difficulty to be solved. Furthermore the setting up of the measurement is robust, controlled manually depending on the viewer.

III. Quantifying tissue structural properties from OCT to diagnose cancer

III/1. Literature of quantifying imaging-based data

Imaging in OCT based on intensity detection is qualitative, since it depends on the system setups. The main challenge today is to provide a quantitative description of the images, to overcome the limitations of the different measurement settings, so as to adopt OCT in clinical environment. In the literature, some approaches based on experiments or theoretical assumptions have been elaborated that could differentiate quantitatively between various tissue types and specifically between healthy and cancerous tissue recorded with Optical Coherence Tomography.

To date it has already widely studied to characterize different tissue types or different layers in complex tissue based on the backscattering coefficient of the OCT signal. First method is based on the assumption of single-scattering assuming that only ballistic photons which backscatter once from deeper layers in the tissue remain coherent and contribute to the OCT signal. In this case the intensity of backscattered laser light in the biological material theoretically follows an exponential function in depth (z) given by the Lambert-Beer law [26, 97, 139, 140]:

$$I(z) = I_0 e^{-2u_t z} \tag{III.1.1}$$

defined by the attenuation coefficient u_t characterizing different tissue types, calculating from the slope of the intensity attenuation in dB scale (Figure III.1.1).

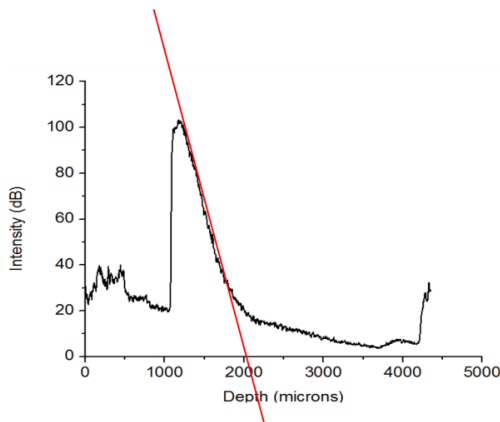


Figure III.1.1. Attenuation of backscattered light (red line) in tissue after averaging 500 A-lines. Tissue surface begins at around 1000 μm (Intensity on logarithmic scale).

This implies the abstraction of the tissue structure. For inhomogeneous material the slope is calculated by averaging or filtering/smoothing. Even for homogenous tissue digital processing on the raw OCT signal is required, since the A-scan profile is noisy due to electrical and speckle noise [141].

Laser speckle makes the images grainy due to random interference effect of coherent laser light illumination. This pattern is called texture. However OCT images are affected by the

speckle noise reducing structural resolution and contrast, some useful information can be detected from this phenomena [59, 142].

The attenuation coefficient of the tissue in Eq. (1) is the sum of scattering and absorption coefficient [26]:

$$u_t = u_s + u_a \quad (III.1.2)$$

where u_s is the scattering coefficient, u_a is the absorption coefficient. In the near infrared (NIR) spectral range: $u_s \gg u_a$, the absorption coefficients can be neglected, and the backscattering coefficient is closely equal at each wavelength.

In a simple model of scattering spheres with approximation the scattering coefficient depends on the focusing beam and the heterogeneity of the tissue, and it is calculated as:

$$u_s = \frac{3.28\pi r^2 \rho_s}{1-g} \left(\frac{2\pi r}{\lambda}\right)^{0.37} \left(\frac{n_s}{n_{ISF}} - 1\right)^{2.09} \quad (III.1.3)$$

where g is the tissue anisotropy factor, r is the radius of the scattering centers, ρ_s is the volume density of scatterers, λ is the wavelength of the incident light and n_s , n_{ISF} are the refractive indices of the scatterers and surrounding medium [26].

Based on this equation the backscattering coefficient u_s can quantify cancerous tissue assuming that cancer has higher cellular density ρ_s which linearly increases the scattering effect. This is validated on normal adipose tissue and Liposarcoma with dissimilar optical characteristics (Figure III.1.2) [26].



Figure III.1.2. OCT image of the boundary between healthy tissue and DDLs. The left part of the image is the denser tumor area; the right part is the normal fat tissue containing adipose cells [26].

Besides the structural properties of tissue, the backscattering coefficient has already been studied for measuring dynamic changes, e.g. quantifying molecular diffusion, in particular detecting blood glucose diffusion separately at each layer [26, 143-145] (Figure III.1.3).

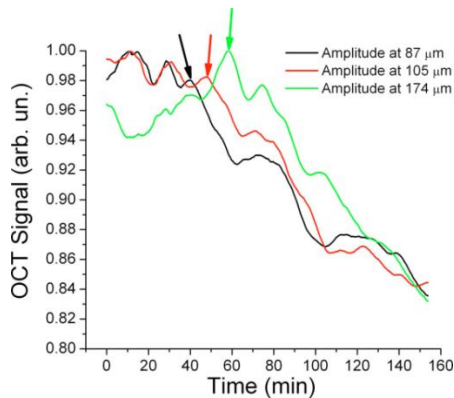


Figure III.1.3. Three curves show the backscattered intensity in time at three different positions in the sclera reduced from OCT measurements. The arrows show the diffusion starting point [143].

The single scattering assumption is valid at the superficial layers, and has been proved in weakly scattering media ($u_t < 6mm^{-1}$, e.g. human artery). For highly scattering media (e.g. human skin), and at larger depth, implementing of multiple-scattering model could provide better

accuracy. Multiple-scattering reduces the imaging contrast, resolution, and the steepness of the intensity slope [97, 139, 140].

Models including multiple-scattering effects are reduced from experiments [146], hybrid Monte Carlo theory [147], linear systems theory [148], and the extended Huygens–Fresnel principle without [149] or including the shower-curtain effect [140].

In most cases, single-scattering is valid in the focal volume, because the focusing optics in the sample arm suppresses the multiple-scattering effect scattered from outside the focal volume [139].

In clinical practice dynamic focusing is not possible, and for fix focusing the signal loses sensitivity, the Point Spread Function (PSF) broadens with depth, and the intensity slope gets higher steepness due to divergence of the light beam. The confocal properties of the sample arm optics, thus the position of the focal plane in the tissue and the depth of focus affect the detected light and the OCT signal [97, 139, 150, 151].

Several theories have been developed to correct the modulation of the confocal aperture in the OCT system, e.g. beam-divergence function, a confocal function, or an axial point spread function (PSF) [152-154]. In these cases a Gaussian beam intensity profile is assumed valid in the paraxial approximation at low numerical aperture (NA), as usually applied in OCT. For high NA (Optical Coherence Microscopy), further study is needed [139, 154]. The probe beam is assumed not to be distorted by the tissue, measurements are compared to Mie theory, and the attenuation or backscattering coefficient depends on the beam focusing/collection optics, the heterogeneity of the tissue, and affected by speckle noise. The axial confocal PSF provides the simplest practical solution [139, 154, 155]:

$$h(z) = \left(\left(\frac{z - z_f}{z_R} \right)^2 + 1 \right)^{-1} \quad (III.1.4)$$

where z_f is the position of the focal plane, and z_R is the “apparent” Rayleigh length of the PSF [97, 139, 151]. The Rayleigh length z_0 of a Gaussian beam is given by:

$$z_0 = \pi n \omega^2 / \lambda_0 \quad (III.1.5)$$

where λ_0 is the center wavelength of the light source, ω is the beam waist at the focus ($\omega = f(\lambda_0, NA)$), n is the refractive index of the media [139]. The apparent Rayleigh length is calculated from the Rayleigh length z_0 :

$$z_R = \alpha z_0 \quad (III.1.6)$$

where $\alpha = 1$ for specular reflection, and $\alpha = 2$ in diffuse biological media. This distinction is based on measurements comparing reflections from mirrors as perfect reflectors for specular -, and epoxy for diffuse scattering. In some literature the factor of specular or diffuse reflection is neglected. The Rayleigh length is almost constant in function of depth, however further investigation is needed [139, 154].

In conclusion, the coherence gating of the single-scattering model in conjunction with the confocal gating from the sample arm optics geometry using $\alpha = 2$ can describe the OCT signal accurately [139, 154]:

$$I(z) = h(z)I_0e^{-2u_tz} = \frac{I_0e^{-2u_tz}}{\left(\frac{z - z_f}{z_R}\right)^2 + 1} \quad (III.1.7)$$

Deviation from this theoretical function is due to optical properties of the tissue, including the large index of refraction mismatch at the tissue surface and inner boundaries in inhomogeneous media, speckle noise, multiple scattering and maybe the effect of temperature and bandwidth of the light source [151, 154].

The attenuation coefficient in the single scattering model with the proposed confocal optics correction calculated from averaged A-line profiles has been compared in normal and malignant ovarian tissue with good accuracy from a statistically significant number of samples. The surface of the tissue was in the focus of the sample arm optics. The structural change is the collagen content loss in cancerous ovarian tissue, which is revealed on histological changes, and on the lower attenuation coefficient measured with OCT (Figure III.1.4) [150].

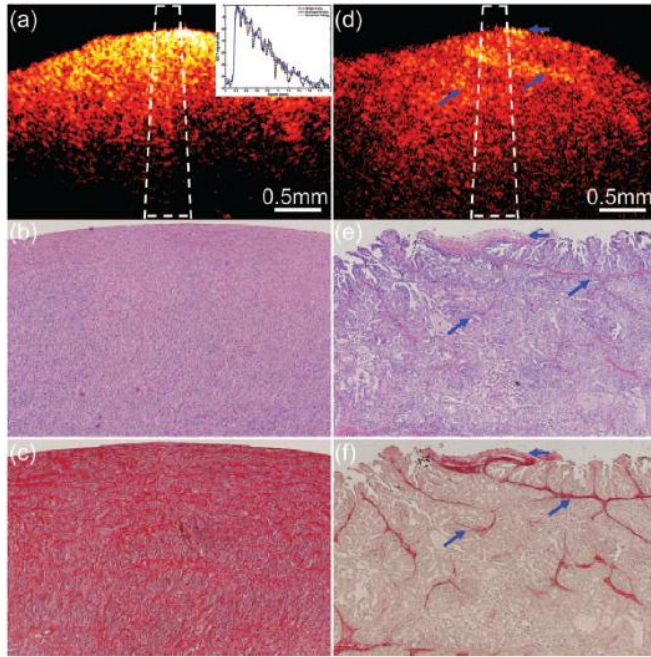
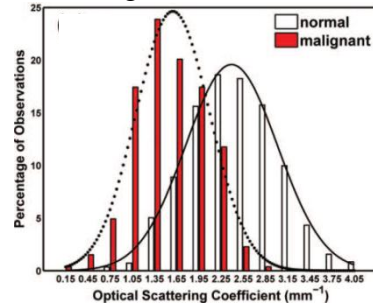


Figure III.1.4. Ovarian Tissue.

(left) Normal [(a)(b)(c)] and malignant [(d)(e)(f)] ovarian tissue. (a)(d) OCT images, (b)(e) H&E histology, (c)(f) SR stains. Inset on (a): slope on an OCT scan line; Blue arrows on (b): collagen.

(down) Histograms of μ_s obtained from normal ($n = 833$) and malignant ($n = 264$) ovarian tissue. Gaussian distribution fits the histogram.



[150]

The diagnostic ability of the method is evaluated by the Sensitivity/Specificity analysis calculating the percentage of correctly diagnosed cancerous or normal tissue:

$$Sensitivity = \frac{TP}{TP+FN} \text{ and } Specificity = \frac{TN}{FP+TN} \quad (III.1.8)$$

where TP = true positive – correctly diagnosed as cancer, TN = true negative – correctly diagnosed as normal tissue, FP = false positive – misdiagnosed as cancer, FN = false negative – misdiagnosed as normal tissue [49, 156].

ROC curve is also calculated from different Optical Scattering Coefficient thresholds. Receiver Operating Characteristics (ROC) curve plots the true positive ratio versus false positive ratio. By selecting different thresholds of u_s located in the overlapping part of the two distributions, the sensitivity and specificity show good results [150, 156].

The area under the ROC curve is a measure of the power of the test. It is the probability that a randomly selected positive has a higher test value than a randomly selected negative [156]:

$$AUC = \int_0^1 ROC(t) dt \quad (III.1.9)$$

The above described method is based on the assumption that the tissue is not complex, one A-line crosses only one layer properties. This issue was addressed first in the case of arterial layers and plaque components [141, 151]. One multiple section can be seen on Figure III.1.5:

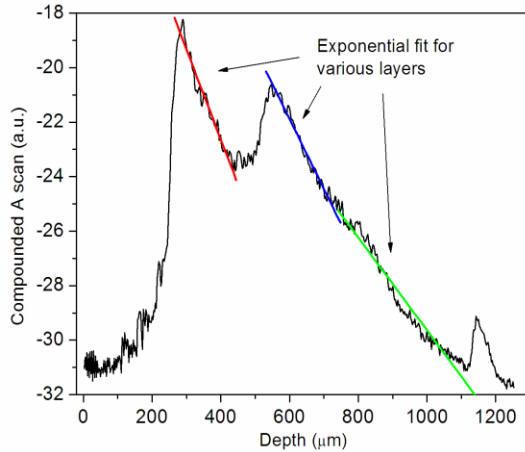


Figure III.1.5. Averaged OCT profile with numerical fit to three layers: Red-Intima, Blue-Media, Green-Adventitia, logarithmic scale [141].

In [151] the confocal properties of the sample arm optics are also included and the results are statistically verified with t-test and ANOVA generalized t-test applied on multiple groups (Figure III.1.6). Student's t-test approves if the different data sets differ significantly from each other.

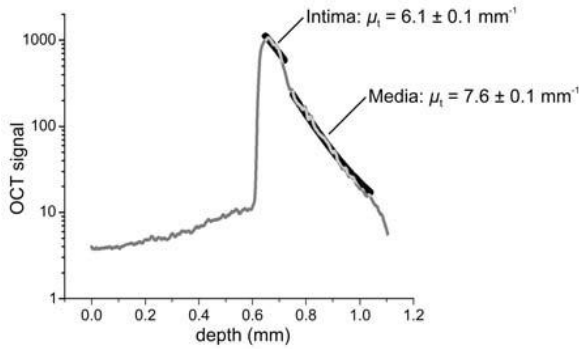


Figure III.1.6. Averaged OCT A-scan (thin grey line), and the fitted signal using equation (III.1.7) (thick dark line) with the calculated attenuation coefficient μ_t (\pm 95% confidence interval) reduced from two layers; logarithmic scale [151].

Related to tissue quantification from the attenuation coefficient, the slope analysis on healthy human lymph nodes vs. nodes containing malignant cells should be mentioned [155, 157]. In these measurements the focal plane was set within the tissue contrary to the above described analysis where it usually positioned at the tissue surface.

The lymphatic system marks metastatic spread in the body. The slope (attenuation characteristics) is calculated separately from each logarithmic A-line using linear least-squares fitting. After obtaining the coefficients on the entire surface, it gives a 2D parametric image on

the xy -plane. The structure is comparable with histology and the contrast is enhanced comparing with the so called en face image, which is the cross-section (x - y) at optimal depth position (optical biopsy). The noncancerous cortical part of the tissue (circled areas on Figure III.1.7) is distinguished well from the diffuse malignant involvement [157].

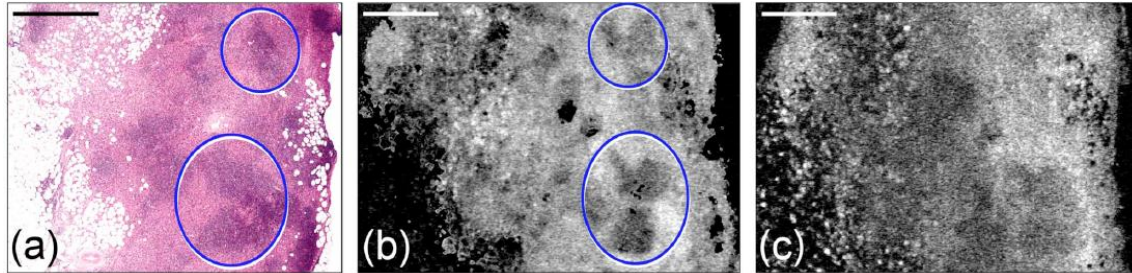


Figure III.1.7. Involved (malignant) human axillary lymph node with diffuse involvement of the node tissue a) H&E histology b) parametric OCT image c) en face OCT image at a specific depth position; Scale bar = 1 mm [157].

To get a correct quantification measurement in some cases a glass plate is put over the tissue as reference surface for the measurement of attenuation [152]. Furthermore it can be immersed in glycerol or phosphate-buffered saline (PBS) to reduce the specular reflection due to the refractive index mismatch between the glass slide and tissue sample [155, 157]. Anyway a digital processing method is implemented to find the tissue surface and the different sections in one A-line defined from the fitting algorithm [141].

In [155] the absolute attenuation coefficient is corrected implementing not only the modulation of the confocal optics, but also the modulation of the OCT scan depth-dependence, called sensitivity drop-off in FD-OCT, or the intensity loss due to the tilted mirror at higher angle in the galvanometer at the scanning reference arm in TD-OCT system [158]. The correction was based on experiments on homogenous tissue phantom which optical properties were also calculated with Mie theory and Monte Carlo simulation, then a reference coefficient was reduced from the division of the theoretical and measured value, and it was applied to correct the lymph node A-scans.

Beside the analysis and correction of the attenuation coefficients to quantify tissue types, new quantification methods are proposed in the literature to extract the structural properties of the tissue types. They provide new insights for tissue characterization, but they are not comparable yet between different measurement settings. To get an absolute quantification method, further investigations are needed in all the below explained methods!

In [159] the logarithmic OCT A-scan signal is analyzed further after subtracting the slope (Figure III.1.8). The standard deviation of the intensity points around the slope is calculated on Healthy Fat Tissue vs. Well-Differentiated Liposarcoma and Healthy Smooth Muscle Tissue vs. Leiomyosarcoma. There is a tendency to differentiate healthy vs. cancerous tissue, however there is still an overlap (Figure III.1.9). The results were validated by the two-sample unequal-variance Student's t-test.

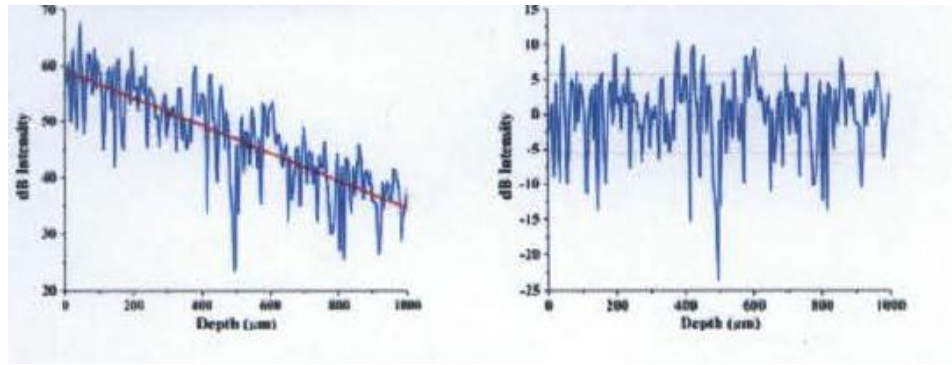


Figure III.1.8. OCT signal with slope, and after subtracting the slope from the raw A-scan, logarithmic scale [159].

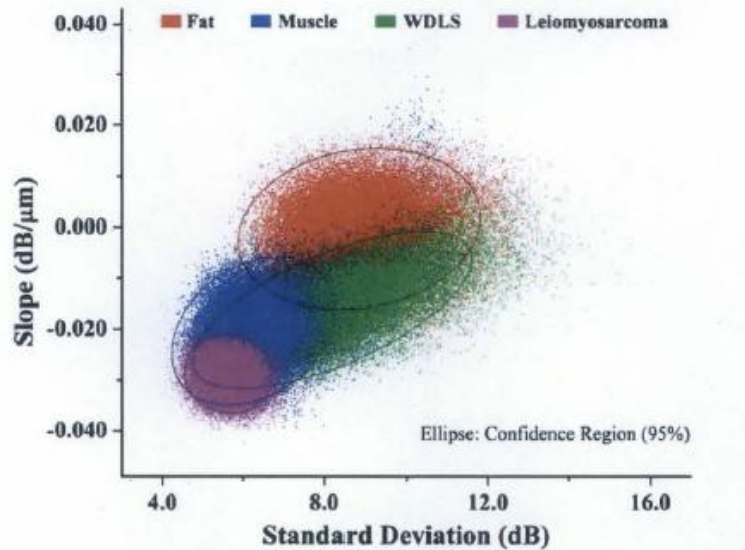


Figure III.1.9. Slope and standard deviation of Fat Tissue, WDLs, Smooth Muscle Connective Tissue and its cancerous version: Leiomyosarcoma. 40000 sample points per sample, and 1 sample per tissue type are represented with 95% confidence intervals [159].

The A-lines were truncated below the surface to avoid specular surface reflection. At a given measurement settings, the slope can be affected by the focus position, but the second parameter, the standard deviation obtained after slope subtraction is sensitive also to the input power, and so as it should be normalized, or the A-scans should be recorded at the same exposure time, with the same path-length difference between the reference mirror and the tissue surface to get an absolute value, since the measurements were done on a Fourier-Domain OCT version, the Swept-Source (SS-) OCT System.

The analogy of the finite pixel width in SD-OCT is the finite linewidth of the swept-source. The SS-OCT detector diode records the spectral information in time. If this spectral channel width $\delta k(\lambda)$ is narrower than the source spectral linewidth, intensity fall-off will occur [160].

The analysis of slope and standard deviation around slope was applied first to distinguish adipose tissue, fibroglandular tissue, and invasive ductal carcinoma in breast cancer [161]. The main motivation behind the study is to diagnose based on one A-line detected with a manually portable Low-Coherence Interferometry, and get sample with Fine Needle Aspiration for genetic analysis (Figure III.1.10). Looking at the A-lines on Figure III.1.11 the A-line basis diagnosis can be accomplished, however for higher accuracy the analysis of more adjacent A-scans should be analyzed or more parameters are needed [161].

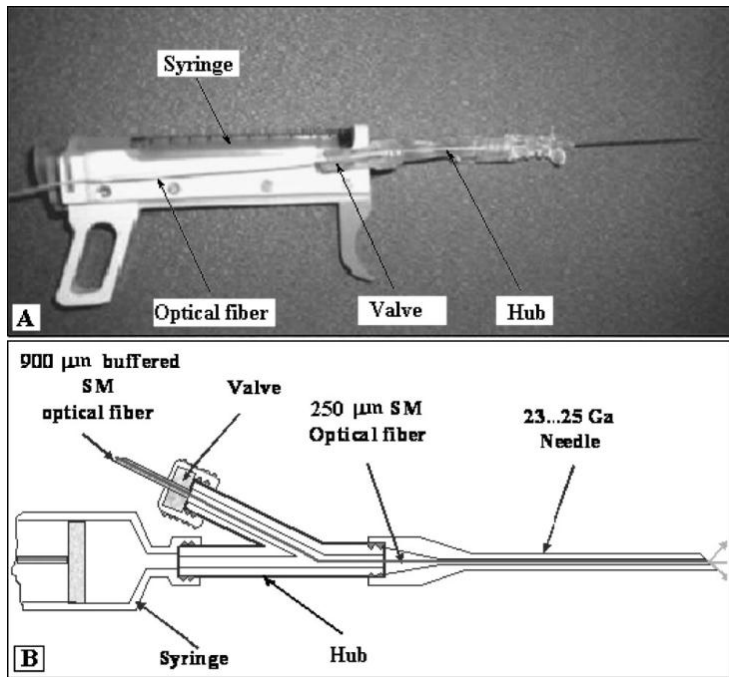


Figure III.1.10. (A) Photograph (B) Schematic of the Biopsy guidance probe [161].

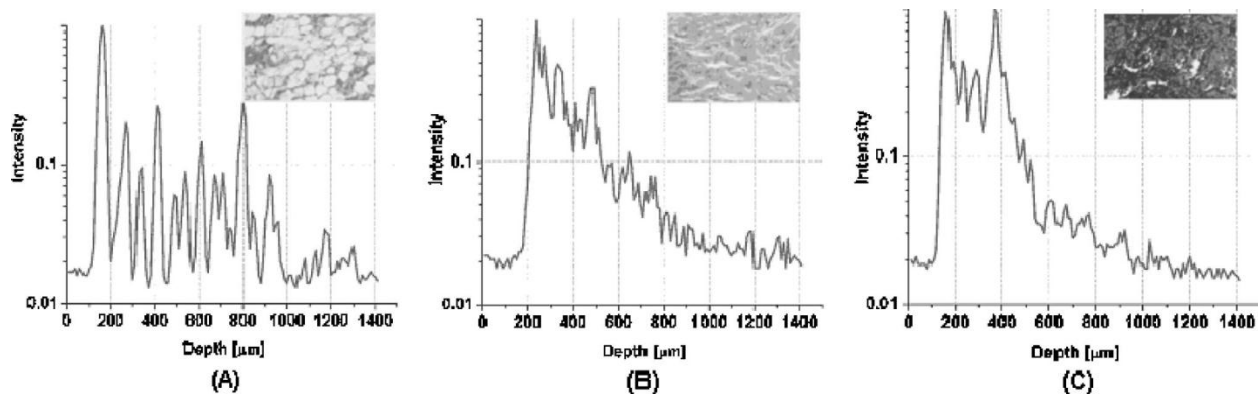


Figure III.1.11. OCT A-scan profiles of breast tissue specimens: (A) adipose; (B) fibroglandular tissue; and (C) adenocarcinoma recorded with Low-Coherence Interferometry. Insets are the histological sections [161].

The focusing problem is solved without using a focusing lens, so the location of the beam focus is fixed contrary to a lensed fiber probe. The limitation is to detect half the range of the data points, which is compensated with a high fixed exposure time/input power [161].

In [162] a third parameter, the signal frequency content is also extracted with the portable low-coherence interferometer (LCI) in time-domain mode. Slope, standard deviation of depth profile around linear fit, and spatial frequency content is compared in breast cancer for adipose-, fibroglandular -, and cancerous tissue (Figure III.1.12). The classification method was developed on 2 tissue types excised from 58 patients, the adipose tissue and the fibroglandular tissue which contained benign fibrous parenchyma, and malignant adenocarcinoma, and ductal carcinoma in situ (DCIS).

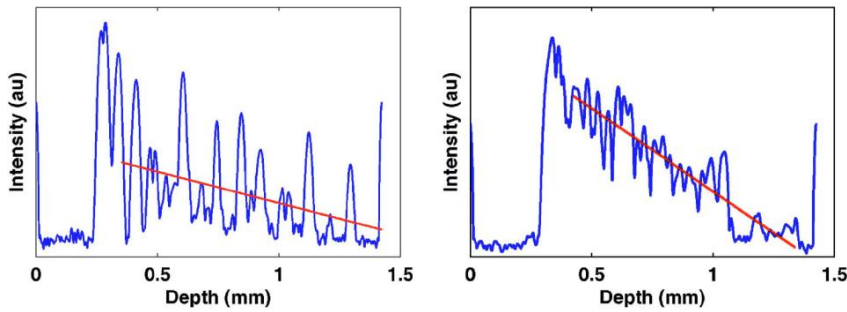


Figure III.1.12. OCT A-line from adipose (left) and fibroglandular (right) human breast tissue with first-order fit (red line); Logarithmic scale [162].

The slope was linearly fitted beginning below the digitally defined surface position to avoid specular reflection (red line on Figure 12), then subtracted to analyze standard deviation around slope and the frequency content of the signal. The parameter analysis was applied per A-line, and the mean from 10 A-line's parameter was calculated per sample.

Focusing lens was not used, and the input power (T_{exp}) was fixed to the sample arm. The tissue surface position and the ROI of the segment were digitally defined. The Discrete Fourier Transform was calculated after subtracting the mean (dc component) of the signal. The Fourier response was averaged from all the samples, and normalized by integrating over area at the given Region of Interest (ROI) where the two tissue types differ significantly (Figure III.1.13).

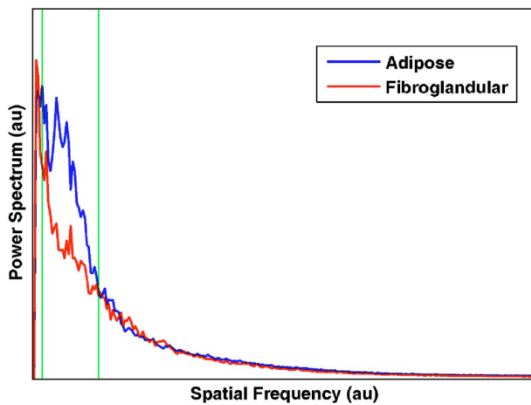


Figure III.1.13. Averaged, area normalized power spectra on human adipose and fibroglandular tissue in breast, calculated from training set. Green window shows ROI [162].

The data analysis is developed on a training set (37 adipose + 35 fibroglandular = 78 tissue samples, 7 tumorous amongst fibroglandular type: 5 adenocarcinoma, 2 DCIS). The next scatter plot from the training set is representing relationship between parameters Slope/Standard deviation around Slope/Spatial frequency (Figure III.1.14).

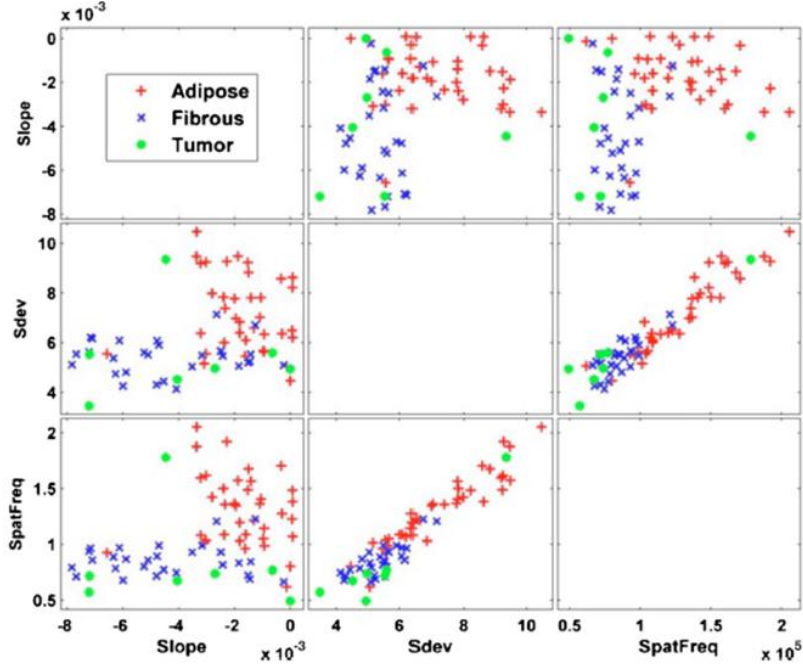


Figure III.1.14. Adipose, fibroglandular and tumor tissue characteristics in breast. Parameters of Slope, Standard Deviation around slope and Spatial Frequency are calculated from a training set. The last two parameters show similar characteristics [162].

The validity of the method is verified with a classification method applied to a validation set. The analysis assumes the parameters were fit to a multivariate normal density (multivariate Gaussian model, meaning that each parameter's probability density function (PSD) follows a normal distribution, so the class can be characterized by the mean vector and the covariance matrix. Linear Discriminant Analysis (LDA) assumes the same covariance matrix for each class, using the pooled estimate of the covariance matrixes. Mean \bar{x}_i for each parameter per tissue type and a pooled Covariance matrix S_p are calculated from the training set of 72 samples [162, 163].

$$\bar{x}_i = [\bar{x}_1, \bar{x}_2, \bar{x}_3]_i - \text{mean of 3 parameters}$$

$$S_p = \frac{1}{N} \sum_{j=1}^N (x_{i,j} - \bar{x}_i)(x_{i,j} - \bar{x}_i)^T - \text{pooled covariance matrix} \quad (III.1.10)$$

$$i = 1, 2; \quad j^{\text{th}} \text{ training sample};$$

$$n_1 = 37 - \text{adipose}; \quad n_2 = 35 - \text{fibroglandular} \quad N = \sum_1^2 n_i = 72.$$

To classify tissue type the model was applied on a validation set containing 34 adipose + 52 fibroglandular = 86 tissue samples, 9 tumorous amongst fibroglandular type: 8 adenocarcinoma, 1 DCIS. The classification was determined using likelihood ratio, which assigns the tissue under analysis to a given tissue class based on highest probability. Two-sided unpaired t-test showed that parameters' mean has a significant p-value for each sample, and sensitivity (98.1%) / specificity (82.4%) analysis is calculated on the validation set. The overall accuracy was 91.9 % defined as the percentage of all the correctly diagnosed tissue samples.

An additional experiment was led to check intra-sample validity from a separate data set sampling at the same position several times in each case. Results on 14 samples from 6 patients show that adipose tissue can be easily misdiagnosed as fibroglandular type due to low signal content. Error analysis of slope fit and subtraction affecting the parameters was also verified.

In [164] the frequency content and the periodicity of the A-lines are investigated after removing the slope obtained with first-order linear fitting. Figure III.1.15 shows the axial scans on adipose, carcinoma tumor and stroma connective tissue in breast on logarithmic scale. One tissue sample was excised per patient.

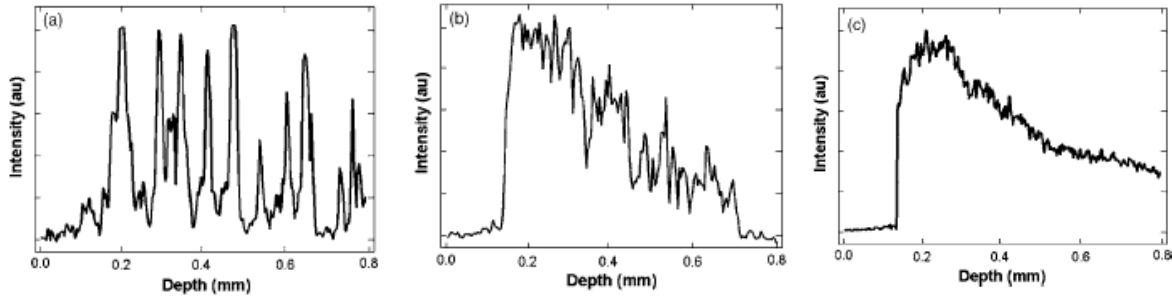


Figure III.1.15. OCT A-line a) Adipose tissue b) Inductive ductal carcinoma tumor tissue c) Stroma tissue; Logarithmic Scale [164].

The data was truncated at the tissue surface then the attenuation effect was subtracted. The data were recorded in TD-OCT settings, with fixed input power to sample arm. The focus was positioned within the tissue, exactly not known. The attenuation effect has been removed subtracting the linear fit of each A-line. Two analyses were applied on the modified curves. First Fourier Transform was calculated from the A-lines which distinguish tissue types based on distinct cell size and density, periodic response and frequency oscillation.

If the intensity function is described as $r_{tissue}(z)$, the Fourier-domain response from each tissue type is calculated, as

$$R_{tissue}(k) = FFT[r_{tissue}(z)] \quad (III.1.11)$$

then normalized over area, and averaged (Figure III.1.16).

The second suggested method is based on peak-detection above a certain threshold - defined as higher than half of the maximum of the A-line - to reduce noise effect. The mean distances between peaks are calculated, and the histogram is shown on Figure III.1.17.

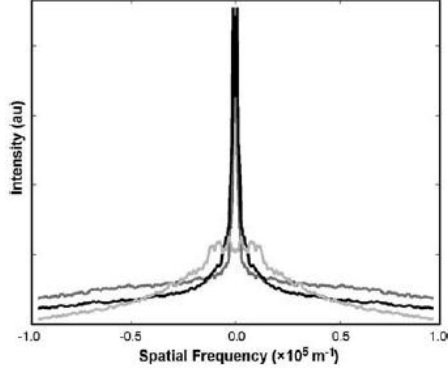


Figure III.1.16. Fourier-Domain data normalized by area, and averaged from tumor (black), stroma (dark gray), and adipose (light gray) tissue A-lines [164].

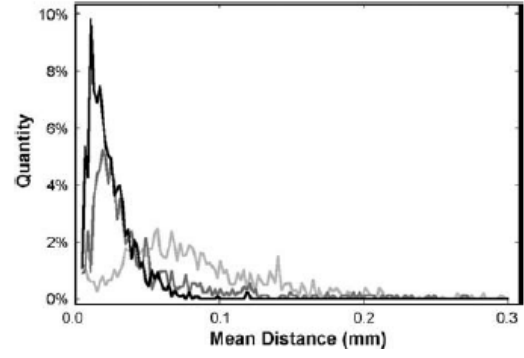


Figure III.1.17. Histogram of the mean distance between high-intensity backreflections from 1 OCT A-line of human tumor (black), stroma (dark gray) and adipose (light gray) tissues [164].

In both and a combined cases the method is developed on a so called training set then to prove the diagnostic ability the tissue is digitally classified on new measurements, called validation set, excised from a 4th patient at the tumor boundaries [164].

The classification method compares first the unique FD signature and periodic content of each unknown A-line, $F(k)$ with the formerly calculated averaged values, including a weighting function $w(k)$ emphasizing the most relevant regions of spatial frequencies. The classification is based on the lowest cumulative error.

$$E_{tissue} = \sum_k w(k) |F(k) - R_{tissue}(k)| \quad (III.1.12)$$

$$w(k) = \max \left\{ \begin{array}{l} |R_{adipose}(k) - R_{tumor}(k)|, |R_{stroma}(k) - R_{adipose}(k)|, \\ |R_{tumor}(k) - R_{stroma}(k)| \end{array} \right\} \quad (III.1.13)$$

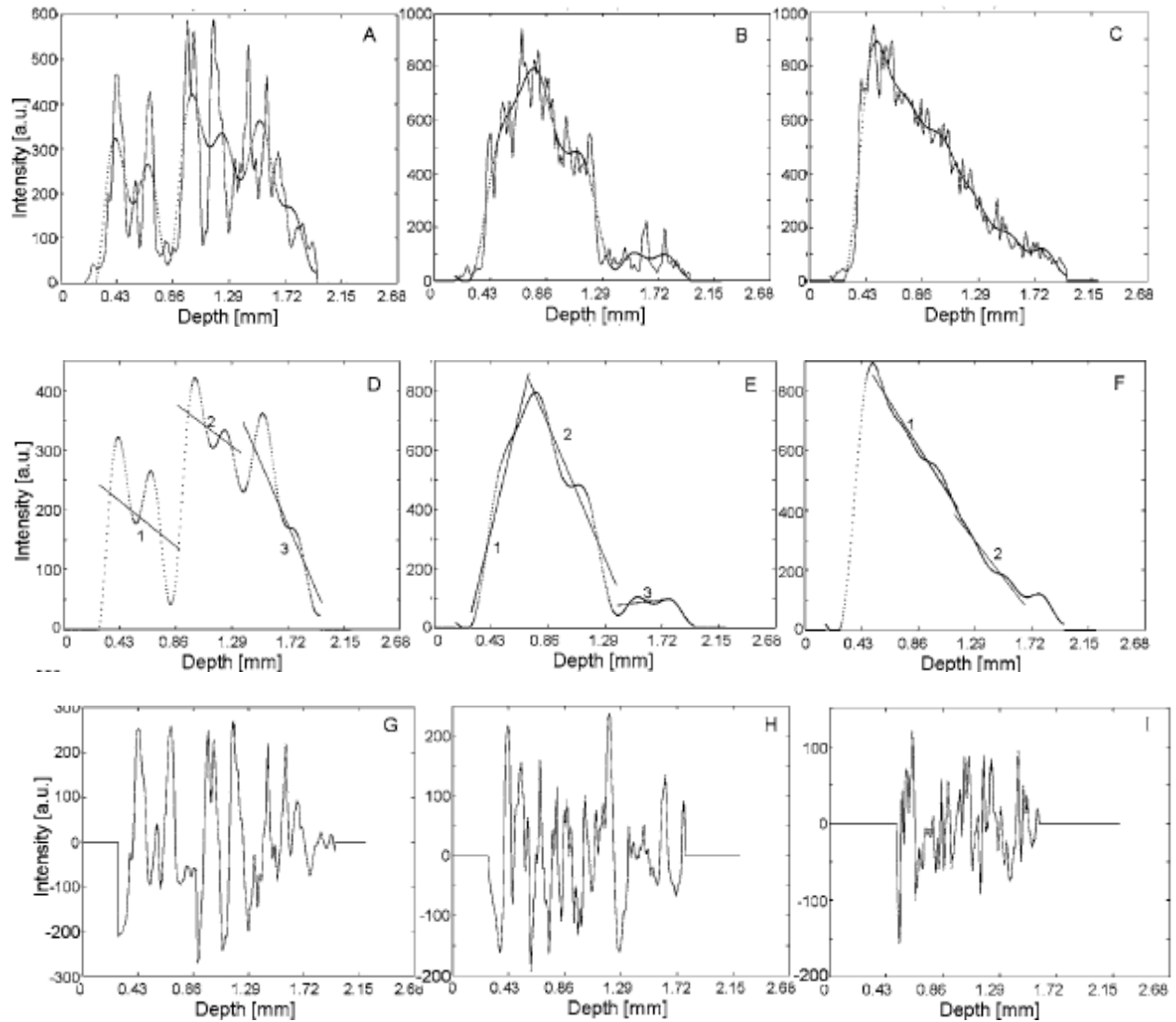
Second the tissue was classified according to the mean-distances between peaks of each A-line comparing with the known histogram at each distance d : $H_{tissue}(d)$. Finally these techniques were combined from the confidence ratings calculated from both method calculating the difference first between the cumulative errors, second between the histogram amplitude of the classified type and the next-best tissue type:

$$c_F = \min \{ |E_{classified\ tissue} - E_{other\ tissue\ 1}|, |E_{classified\ tissue} - E_{other\ tissue\ 2}| \} \quad (III.1.14)$$

$$c_P(d) = \min \left\{ \begin{array}{l} |H_{classified\ tissue}(d) - H_{other\ tissue\ 1}(d)|, \\ |H_{classified\ tissue}(d) - H_{other\ tissue\ 2}(d)| \end{array} \right\} \quad (III.1.15)$$

Sensitivity (97%) / specificity (68%) analysis was calculated from adjacent A-lines yielding better accuracy then to diagnose cancer from only one A-line. The method can be applied to complex layered tissue structure with a windowing scheme [164].

In [163] adipose, fibrose/adipose and tumorous tissue is sampled from the breast. After a constant background subtraction the A-lines are smoothed (Fig. III.1.18a, b, c) and cut into separate sections since one A-line can cross multiple tissue types (Fig. III.1.18d, e, f). The next parameters are calculated: slope from different sections (Fig. III.1.18d, e, f), standard deviation of the depth profile variations around the slope linear fit, mean distance between peaks, standard deviation of the peaks spreading over depth (Fig. III.1.18g, h, i), power spectrum parameters: normalized power spectra to its maximum for each tissue section in one A-line calculated from Fourier analysis (Figure III.1.18k, l, m), weighted mean frequency, standard deviation around this mean, number of frequency peaks above a certain threshold and total area under peaks above the threshold (Figure III.1.18). The digital signal processing steps are clearly described in the paper.



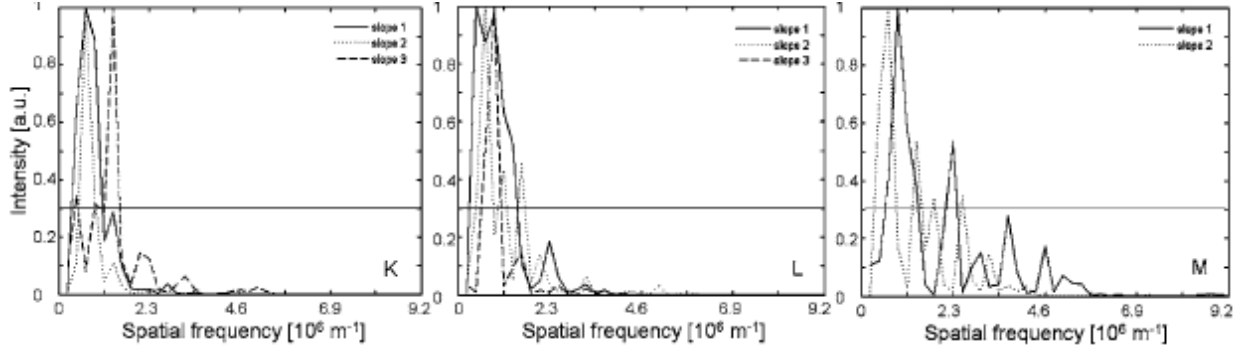


Figure III.1.18. Steps of A-line processing: first column – adipose tissue; second column – fibrous and adipose tissue; third column – tumor tissue; 8 parameters are extracted [163].

Assuming multivariate normal distribution, the mean values \bar{x}_i and covariance matrix S_i is calculated from all the 8 parameters for all the 3 tissue types, as a training set from 48 samples.

$\bar{x}_i = [\bar{x}_1, \dots, \bar{x}_8]_i$ – mean of 8 parameters

$$S_i = \frac{1}{n_i} \sum_{j=1}^{n_i} (x_{i,j} - \bar{x}_i)(x_{i,j} - \bar{x}_i)^T \quad (III.1.16)$$

$$i = 1,2,3 \quad \sum_1^3 n_i = 48$$

For classification of the tissue type the quadratic discrimination score d_i^Q is calculated from a validation set (89 samples), which is the logarithm of the probability to assign the tissue under analysis to a tissue type, correctly identifying 93% adipose, 75.5% fibrous, 88% tumor tissues, and yielding to a sensitivity and specificity of 88% of Normal (adipose, fibroadipose, fibroglandular) and Abnormal tissue (tumor, tumor admixed with normal). The diagnosis is based on multiple A-lines per tissue sample.

$$d_i^Q = -\frac{1}{2} \ln|\det(S_i)| - \frac{1}{2} (x - \bar{x}_i)^T S_i^{-1} (x - \bar{x}_i) \quad (III.1.17)$$

$$x = [x_1, \dots, x_8]_{unknown\ tissue}$$

The parameters which are considered the best discriminating factor are the slope, standard deviation of the depth profile variation and the total area above the threshold under the peaks are represented in a 3D coordinate system (Figure III.1.19) [163].

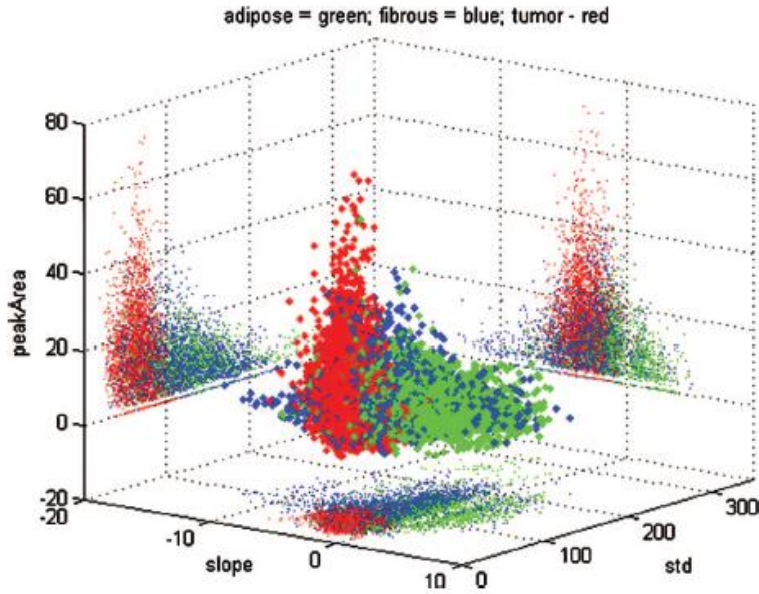


Figure III.1.19. Scatter plot illustrating the clustering of the three main tissue types (adipose – green, fibrous – blue, tumor - red) and their projections on the x, y, and z planes for three parameters: Slope, Std, and PeakArea [163].

One can see a difference for each tissue types, but there is still a significant overlap on the projection planes, so the diagnosis is better including the other parameters. More efficient classification could be achieved by weighting the parameters or instead of assuming multivariate normal distribution of factors, deducing the correct PDF from an expansive training set. The measurements are recorded on Spectral Domain OCT, so the path-length difference between the reference mirror and the sample surface, the input power to the sample, and the focus position could be fixed.

A different approach to quantify morphological pattern of cancer in OCT images has been studied by fractal analysis. Fractal dimension measures the complexity and self-similarity of a pattern. Normal adipose, normal fibroglandular stroma and cancerous breast tissue was analyzed [165].

Cancer can be diagnosed based on fractals due to its disordered feature and irregularity. Fractal dimension was calculated per each A-line using the 1D box-counting analysis. The computation were based after background subtraction, measured from mean value within an empty top portion of the image and normalized by max Intensity value, then rescaled to 8-bit. One A-line section is divided to different intervals/boxes, and the number of boxes containing values above a certain threshold was counted. The A-line section was divided successively, and the number of boxes containing at least one pixel above threshold vs. the given interval/box-size at log-log scale gives a linear function which slope gives the fractal dimension between 0 (dot) and 1 (line) [165].

The distribution of the fractal dimensions of the A-lines per B-scan is shown for adipose, stroma, and cancer in Figure III.1.20. Their mean and standard deviation clearly characterize the tissue type. The adipose tissue is more ordered and has smaller mean fractal dimension, but larger distribution then the more homogenous stroma and cancer. This method gives better separation between cancer and stroma then other methods.

The diagnosis was verified by t-test with Bonferroni correction, sensitivity/specificity analysis, ROC-curve. The accuracy of the method should be verified with digitally defining the ROI, tissue surface position, and measurement settings. The images were recorded at SD-OCT at fixed input power to sample arm.

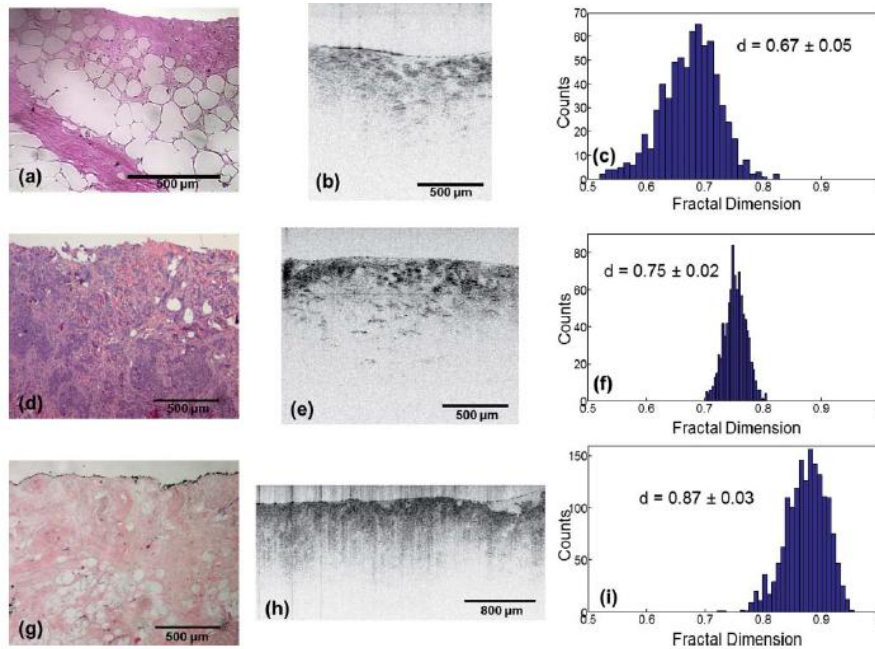


Figure III.1.20. H&E images of adipose with stromal regions (a), cancer with adipose cells (d), and stroma (e), their corresponding OCT B-scans [(b)(e)(h)], and fractal dimension distribution calculated from the A-lines of the B-scan [(c)(f)(i)] [165].

Fractal analysis in OCT was applied first time on artery segments (intima, media, adventitia) using 2D box-counting fractal dimension covering the A-line with square boxes - one side is the depth, the other side is the Intensity - yielding a fractal dimension between 1 (line) and 2 (plane) [141].

Fractal dimension was calculated for each layer. Since there is not visible structure by layer, the results reveal the texture characteristics in the medium due to the speckle phenomena. Figure III.1.21 shows the recorded B-scan and one A-scan profile [141]. The results show that the analysis of speckle can characterize tissue type in case the measurement settings does not have a sufficient resolution.

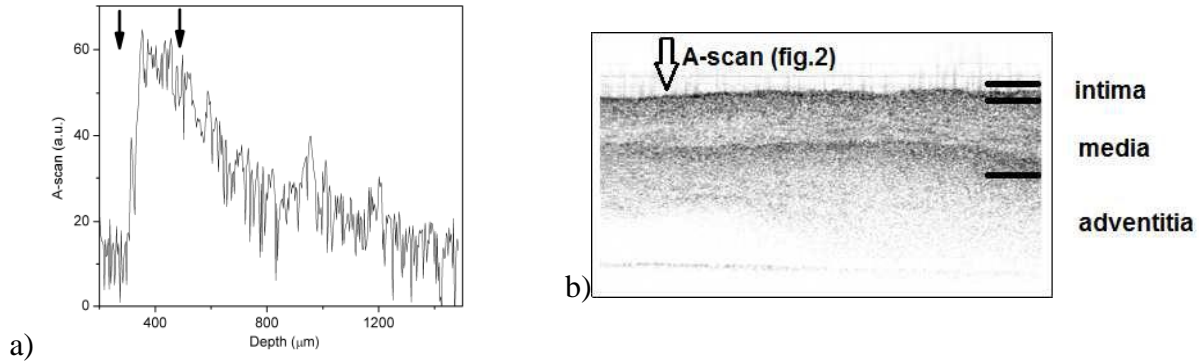


Figure III.1.21. a) A-scan profile selected from b) B-scan at porcine artery. Arrows show the approximative region of intima (image size: $1.5 \times 3 \text{ mm}^2$); Logarithmic scale [141].

The A-scan profile reveals the 3 sections of the artery segments. The attenuation coefficient is reduced from the compounded profile shown in Figure III.1.5. Beside this the unique A-line section can provide further information. The noisy feature is due to electronic and speckle noise.

In distinguishing artery layers SS-OCT was used with a fixed power to the sample arm. The region under analysis was small neglecting the effect of the sensitivity roll-off. The mean and standard deviation of the fractal dimensions calculated per each B-scan characterizes artery segments, however the attenuation coefficients provide better classification in this case.

Texture analysis of OCT images first was applied on portions of normal lung, abnormal lung, testicular fat, and normal skin (Figure III.1.22) [166]. Similar method was applied comparing various endothelial cell concentrations in collagen, and tissue phantoms using various sizes and concentrations of microspheres [167].

Texture analysis is a secondary method, and it can provide additional information to characterize tissue type in case of invisible structural information. The disadvantage of the texture examination is the high dependence on the measuring settings and resolution. Speckle size is function of lens aperture diameter and Numerical Aperture, operating wavelength, position of imaging system: object-lens distance. During the measurements all system settings (gain, imaging depth in tissue close to surface, focal depth position) remained fixed during the entire imaging experiment [167].

The analysis of texture is a relative quantification method, and needs further improvements to use in clinical practice [165].

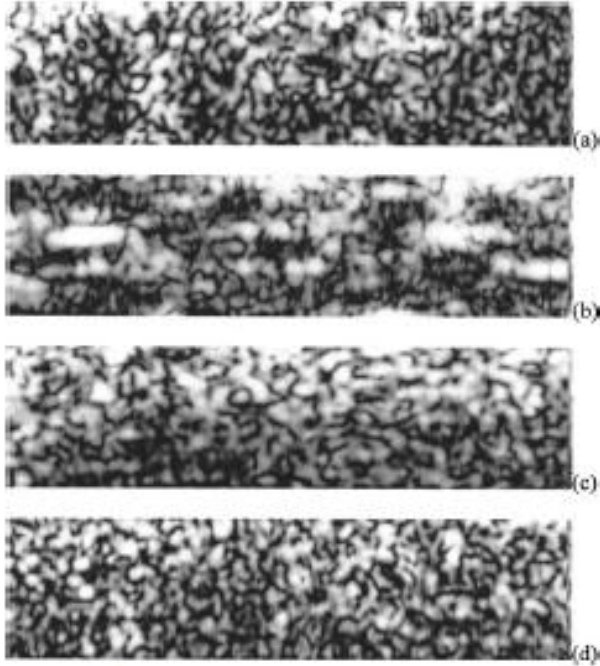


Figure III.1.22. Example OCT images (after 4x4 local average filtering – better result) of mouse (a) skin, (b) fat, (c) normal lung and (d) abnormal lung. Image size: 1x0.25 mm [166].

In [166, 167] two types of statistical properties of the texture or brightness variation are extracted after enhancing the image. The images were corrected with averaging and histogram equalization, rescaled to 0-255 intensity scale, and represented in logarithmic scale [166, 167].

First spatial gray-level dependence matrices (SGLDM), or co-occurrence matrix was calculated. SGLDM quantifies texture based on 5 parameters: energy, entropy, correlation, local homogeneity and inertia calculated from the grey pixel points in 4 directions on the plane. Second, spatial frequency was calculated using 2D Discrete Fourier Transform, the frequency content was divided to 4 regions and the parameters extracted show the percentage contribution of each region [166, 167].

The data analysis was developed on a training set, the 24 parameters were normalized subtracting the mean, and divided by the standard deviation. The features were ranked using unequal-variance student t-test. The classification method is based on the best 3 features calculating the Mahalanobis distance between the training and validation set, and the shortest distance classifies the given tissue type. The method was also applied on Brodatz texture [166, 167].

$$\bar{x}_i = [\bar{x}_1, \dots, \bar{x}_3]_i - \text{mean of 3 parameters}$$

$$D_{M,i}(x_{i,j}) = \sqrt{(x_{i,j} - \bar{x}_i)^T S_i^{-1} (x_{i,j} - \bar{x}_i)} \quad (III.1.18)$$

S_i – covariance matrix and D_M – Mahalanobis distance

Speckle noise in coherent imaging methods, in particular in laser techniques and OCT has been widely studied. The statistical property of fully developed static speckle pattern is described with an exponential function. However in OCT this characteristic theoretically follows Rayleigh distribution [59, 142].

The statistical theory of texture distribution is based on central limiting theorem of statistics. The Exponential and Rayleigh distributions have one parameter. There are studies to validate the theory experimentally, comparing different distribution to model speckled image formation: distribution with one parameter: Exponential, Rayleigh and with two parameters: Lognormal, Gamma, K, Nakagami, Weibull.

The special case of gamma is the exponential distribution; the special case of Nakagami is the Rayleigh distribution. The special case of Weibull is the Exponential, Rayleigh, Chi and closely the Normal distribution. K is the approximation of Rayleigh-lognormal distribution. Distributions with three parameters provide higher flexibility. An example is the Generalized Gamma (GG3), already proved as the best candidate to model speckle noise. It includes the gamma (+Exponential), Weibull (+Exponential, Rayleigh, Chi, Normal), Nakagami (+Rayleigh) and approaches the lognormal distribution.

Figure III.1.23 illustrates dermatological texture characteristics of finger epidermis and stratum corneum with the corresponding speckle intensity distribution. This segmentation method by speckle analysis is validated using support vector machine classification method [168].

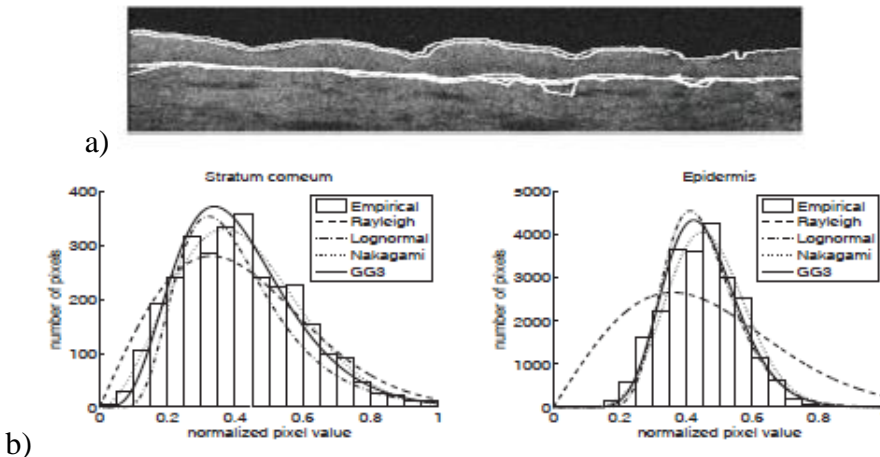


Figure III.1.23. a. OCT B-scan of Stratum Corneum (up) and Epidermis (down) segmented manually. **b.** Different fitting distributions to the B-scan data of Stratum corneum and Epidermis [168].

Beside the distribution of the grey-level parameters, the contrast (standard deviation over mean at given region) distribution can be also analyzed for image segmentation (Figure III.1.24). The theoretical computation yields log-normal distribution. This method is more valuable to differentiate background region from flow which reduces contrast at given integration or exposure time [169, 170].

Since the quantitative parameters calculated from speckle distribution or contrast is extremely sensitive to the measurement settings affecting speckle size, and dependent on the neighboring region from which the distribution is calculated, a differential contrast within one image can give comparable information for image segmentation [169].

Image segmentation techniques or edge detectors in OCT are not broadly studied, and mainly applied to retinal layer identification. Some examples are: Marr-Hildreth (Laplacian of a Gaussian) algorithm, manual boundary tracing and thresholding, Markov boundary model, edge detection followed by edge linking using graph searching [60].

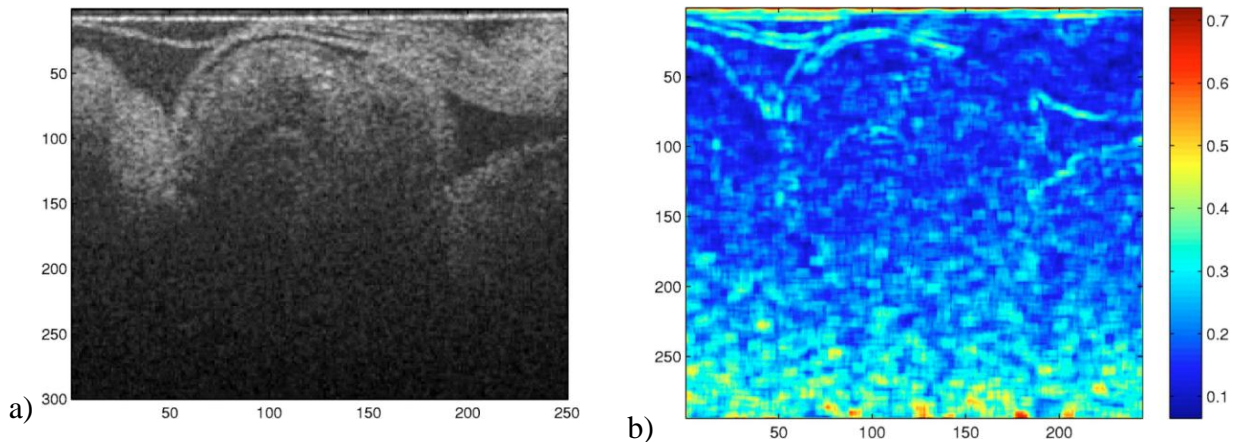


Figure III.1.24. a) OCT image of chick embryo b) Spatial contrast computed from a 7x7 moving window [169].

The contrast calculated on Figure III.1.24 represents not only the texture due to speckle, but also the structure due to scattering from layer boundaries having different index of refraction. The real contrast value should be calculated at the image section without structural information [169].

The question is whether the structural information should be enhanced removing speckle with denoising methods (spatial averaging, linear filters, median filters, wavelet analysis, adaptive smoothing, frequency compounding, polarization, averaging), or the texture analysis in case the tissue structural characteristics are not revealed with the OCT signal at given resolution. We are interested to classify tissue types based on unique structural properties, however in case of ambiguity, texture analysis can refine the diagnosis.

In this manuscript the main interest is to study tissue structural properties of OCT using Digital Signal Processing Techniques. Image processing methods (e.g. cell counting analysis applied on Liposarcoma in OCT [24]) and complex modeling techniques are out of scope of this study. These analyses can have a good diagnostic ability, but our approach is different by providing a parametric description of the images where the function parameters diagnose tissue types, instead of quantifying images in a non-parametric way.

Further study will be to get a quantification method comparable between different OCT measurement devices so as to use a standardized measuring technique in clinical environment. In [171] the signal quality on different devices is analyzed with intensity histogram decomposition model. A ratio between the histogram of the background and the foreground on SD-OCT images is calculated. The factor is independent from the device characteristics, and can be designated as the analogy of the signal-to-noise ratio.

Recent attempts are based on the standardization of the unique A-line from the same sample recorded with different devices, light sources, acquisition speeds, settings, scan protocols, image processing, data formats. The method is developed on retinal OCT images and still requires a lot of signal processing steps, and remains a main challenge (Figure III.1.25) [172].

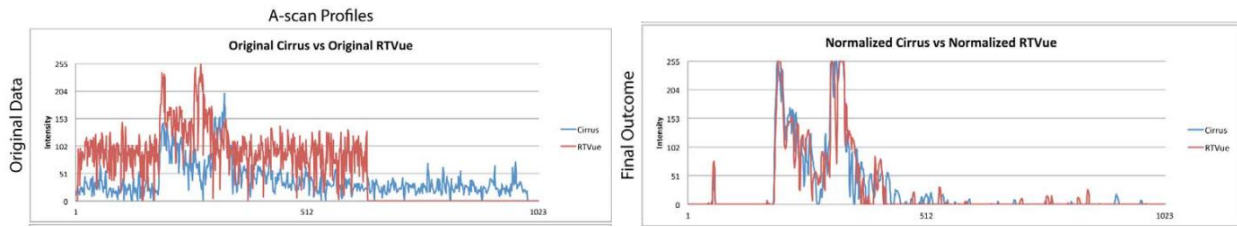


Figure III.1.25. Original A-scan profile and similar A-scan at the end of the process recorded at two SD-OCT devices [172].

Retinal OCT images can be normalized based on the brightest layer yielding a relative intensity map. However the attenuation coefficients calculated from relative reflectivity is more trustworthy to diagnose pathological changes, the assumptions cannot be neglected related to constant attenuation of the reference layer, and constant sub-layer backscattering properties. Furthermore different eyes have different retinal layers, and different OCT devices can measure different retina layer segment distances of the same eye [173, 174].

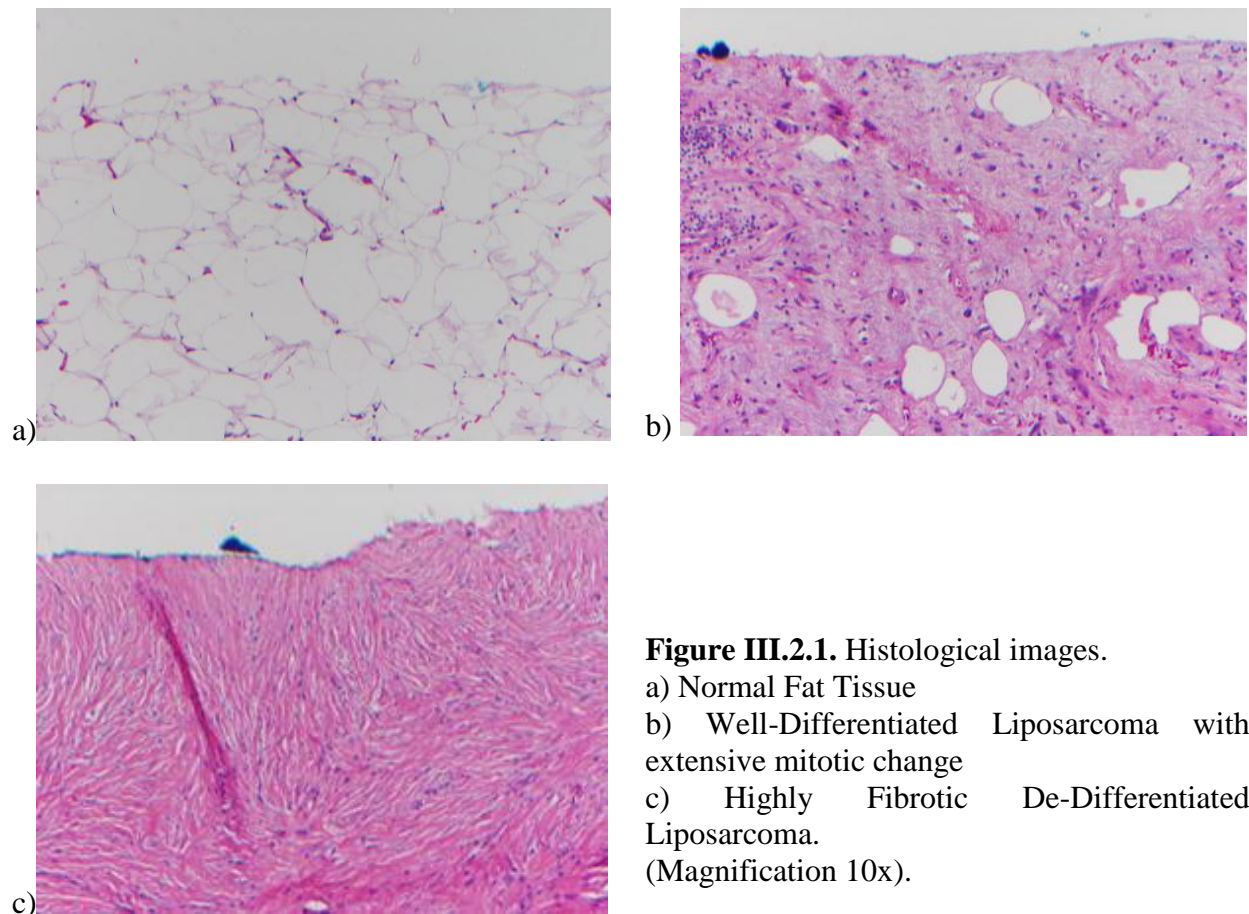
Image registration methods can also provide solution for the comparative analysis of OCT images. This technique can align images of the same object recorded with different measuring device. It includes similarity measures like feature-based registration, e.g. points, surfaces, and intensity-based registration methods, e.g. correlation coefficient (CC), sum of squared intensity differences (SSD), sum of absolute differences (SAD), techniques based on probability theory (joint entropy, mutual information), correlation in frequency domain e.g. phase correlation measure (PC). Transformation models pertain to image registration method, e.g. similarity transform, affine transform, perspective or homographic model [175].

III/2. Data analysis, Results

III/2/a. Introduction

The methodology to quantify tissue properties was developed on healthy and cancerous tissue samples. The tissue example was the Healthy Fat Tissue vs. two types of Liposarcoma. The analysis was developed on all the three tissue types, one sample from each class, and then statistically verified on new measurements.

The tissue samples were excised from human patients' abdomen/retroperitoneum at the University of Texas M. D. Anderson Cancer Center (UTMDACC). Protocols for tissue processing were approved by the UTMDACC and University of Houston Biosafety Committees. Normal Fat tissue, Well-Differentiated Liposarcoma and De-Differentiated Liposarcoma were acquired. Histological diagnosis and classification of samples was performed by a UTMDACC sarcoma pathologist (Figure III.2.1). The tissue was preserved in sterile phosphate buffered saline then stored in refrigerator until imaged using OCT system.



Each tissue sample was recorded on the above explained Spectral-Domain (SD) OCT measuring rig in the BioOptics Laboratory at the University of Houston, and processed in LabView environment (Figure III.2.2).

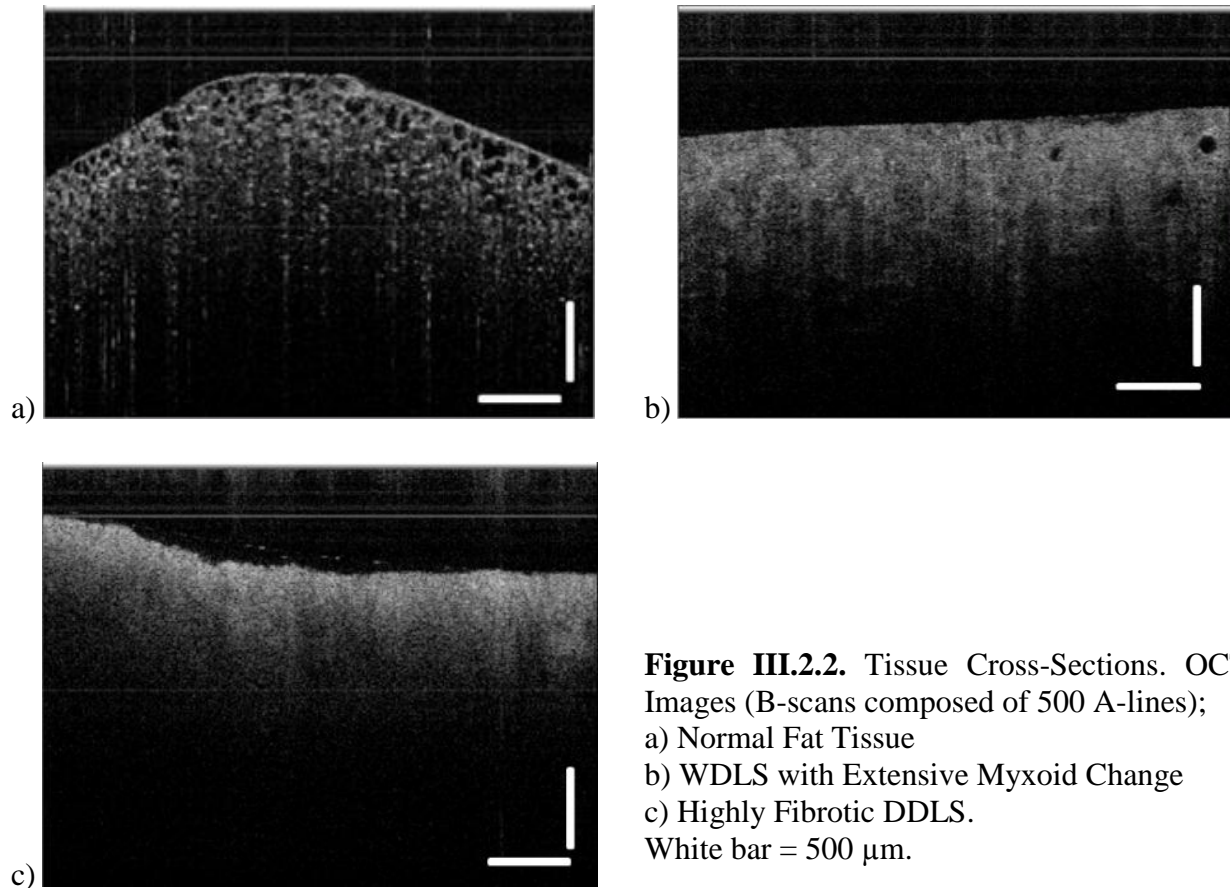


Figure III.2.2. Tissue Cross-Sections. OCT Images (B-scans composed of 500 A-lines);
a) Normal Fat Tissue
b) WDLS with Extensive Myxoid Change
c) Highly Fibrotic DDLS.
White bar = 500 μm .

The above images show the cross-section of Normal Fat tissue, WDLS and DDLS. This 2D cross-section called B-scan is composed of 500 adjacent A-lines. One A-line (1D) shows the backscattered intensity variation in function of depth from a laser footprint of 8 μm in focal plane (in air). The region is $\sim 3\text{mm}$ wide scanned with a galvanometer mirror, with backscattered light collected from a region of up to $\sim 1\text{ mm}$ in depth.

The internal structure is revealed, and the OCT images are comparable to the stained histology. The structure is detected from the scattering properties of the tissue types. The laser clearly reveals the adipose cells seen in Normal Fat Tissue. WDLS has extensive myxoid change including vasculature, but still has some adipose cells with varying size, which is a diagnostic of WDLS. The part of DDLS imaged here resembles fibrotic tissue.

We can see the differences of the different tissue types on the gray-scale images. We intend to transform the qualitative information from the images to a quantitative statistical parametric description of the tissue. The statistical model is based on the variability of the A-lines in the cross-section at a given region. One A-line example of the different tissue types is seen on Figures III.2.3&4&5 in arbitrary unit and dB scale:

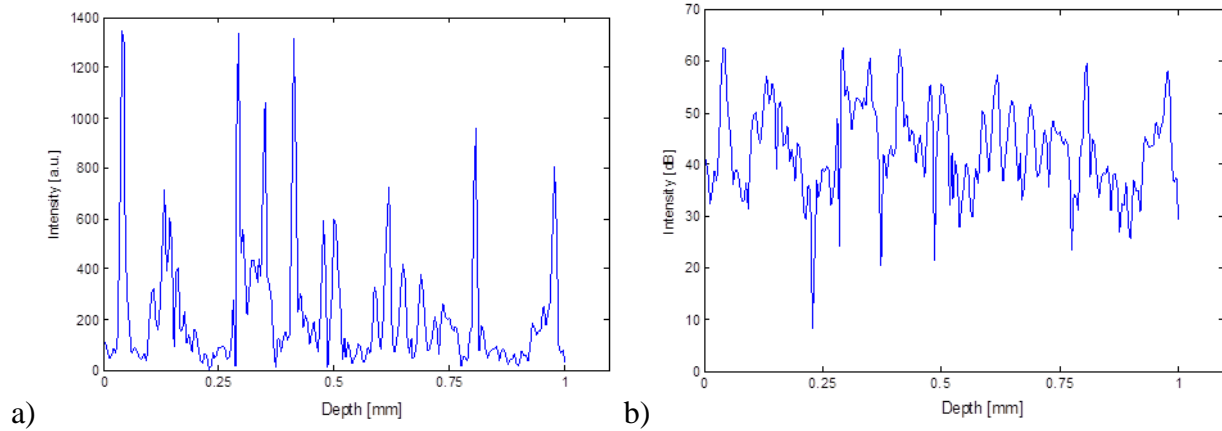


Figure III.2.3. OCT A-line of Normal Fat Tissue a) arbitrary unit b) dB scale.

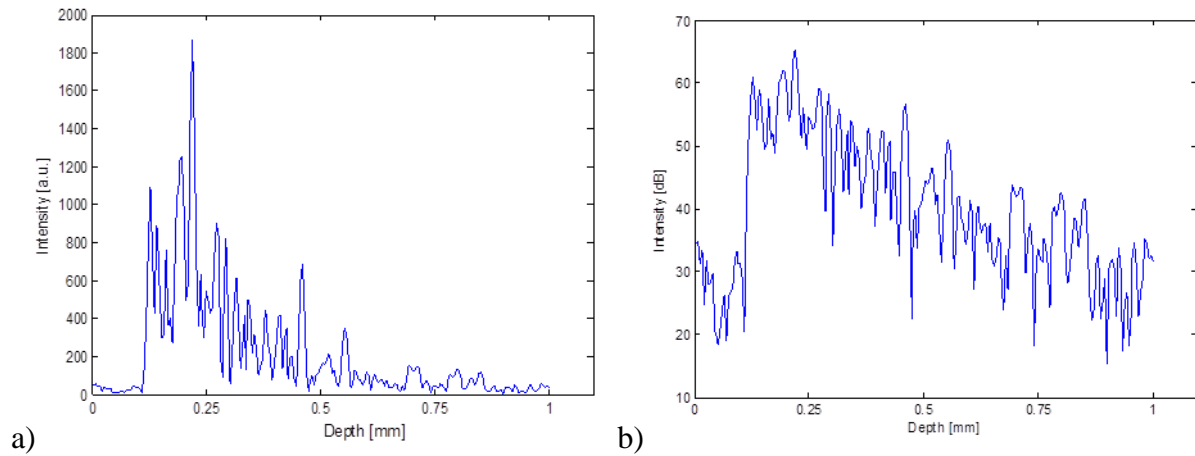


Figure III.2.4. OCT A-line of WDLS a) arbitrary unit b) dB scale.

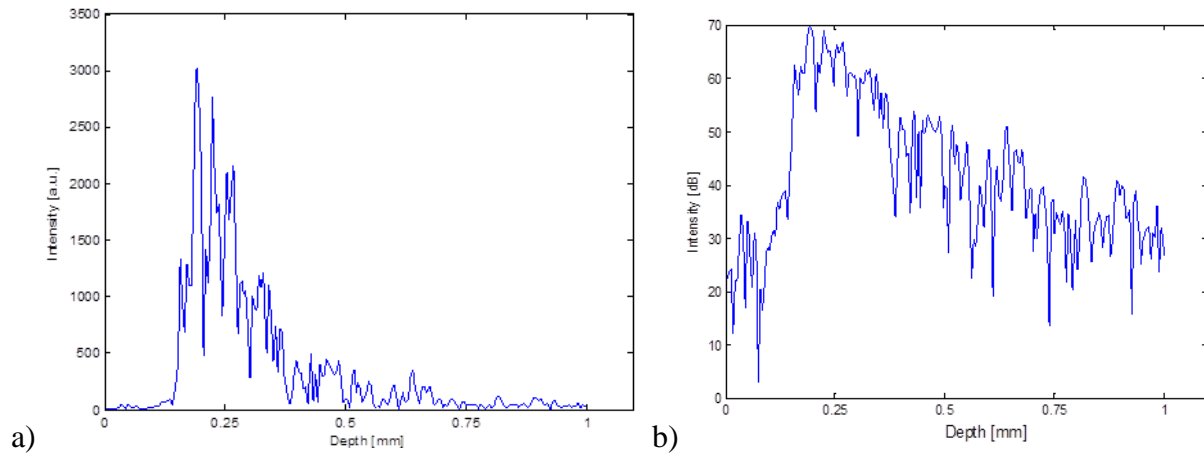


Figure III.2.5. OCT A-line of DDLs a) arbitrary unit b) dB scale.

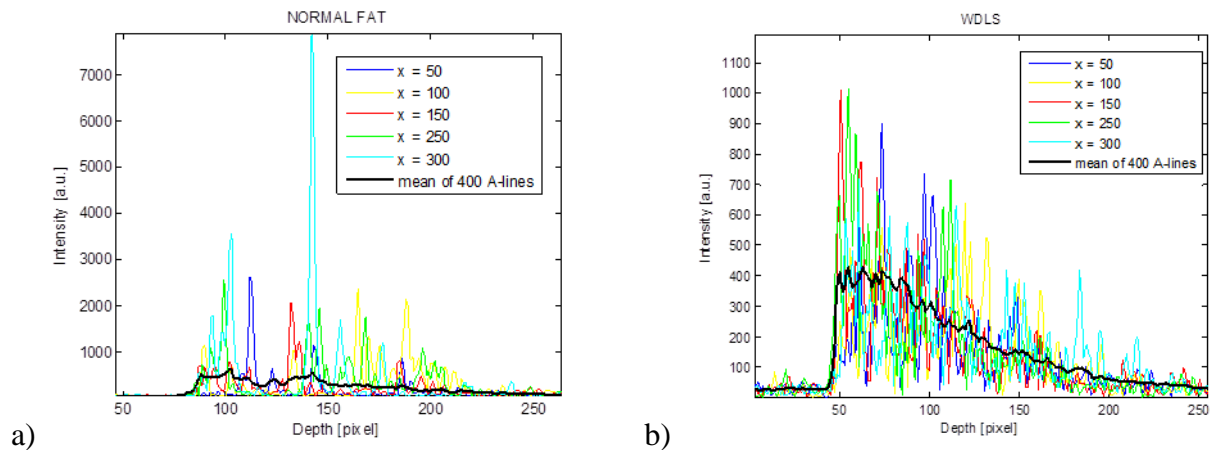
Cancerous tissue is much denser than healthy tissue. Since light scattering occurs chiefly at interfaces, scattering is much stronger in cancerous tissue. The inhomogeneous Normal Fat Tissue is distinguished with periodic scattering at the cell boundaries. The attenuation of light is higher in the dense tissue, and the back reflection loses the periodicity as the adipose cells dedifferentiate in the cancerous tissue. The optical properties show the morphology of the tissues, the scattering effects reveal the cellular structure at a good resolution for our analysis.

However only one A-line is presented, they can distinguish tissue types by sight by the steepness of the slope and the periodicity or standard deviation around this slope. As stated also in the literature, the analysis of more adjacent A-lines provides statistical significant results. We will keep analyzing a bunch of A-lines instead of focusing on one A-line-based feature. The variability of the intensity pixel points in these A-lines per B-scan will be the basis of our modeling approach. The inhomogeneity of the various tissue types is described expressing this variability with parameters and so classifying tissue types. The data analysis is developed in arbitrary unit. After retrieving the raw data from LabView, the post-processing step of the quantification process is developed in MatLab environment.

III/2/b. Steps of Data analysis

Step 1: First Steps towards quantitative tissue analysis

5 A-lines from a B-scan will be plotted as an example to represent the variability (Figure III.2.6):



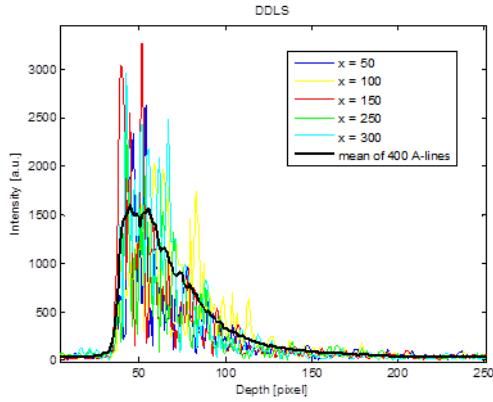
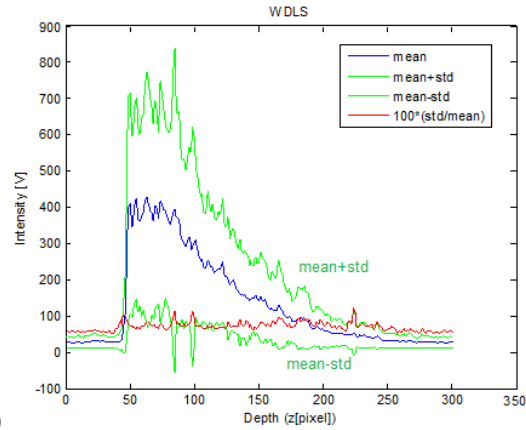
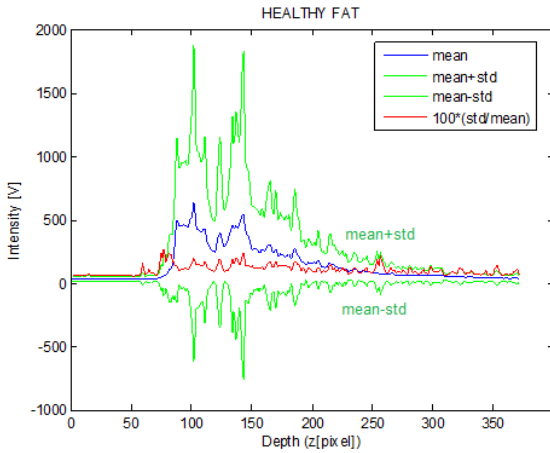


Figure III.2.6. 5 A-line-plots $x =$ pixel position of the A-line from the B-scans of Figure III.2.2, and the mean value of 400 A-lines. A) Normal Fat Tissue b) WDLS (Well-Differentiated Liposarcoma) c) DDLS (De-Differentiated Liposarcoma) .

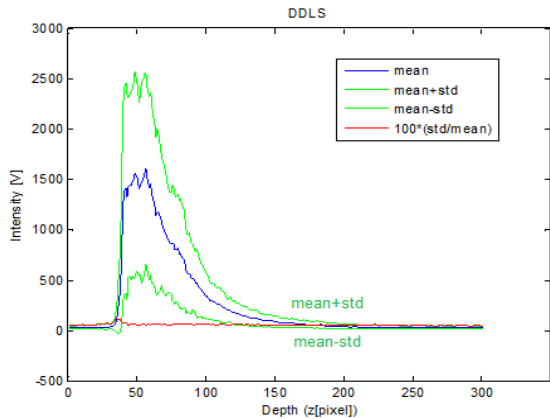
c)

In appearance the variation of the A-lines is characteristic to differentiate the material types. The first step to describe this variability is to compute the mean, standard deviation, and standard deviation over mean at each depth position (Figure III.2.7):



a)

b)



c)

Figure III.2.7. Mean, standard deviation, and standard deviation over mean of 400 A-lines of the OCT images on Figure III.2.2.

a) Normal Fat Tissue
b) WDLS (Well-Differentiated Liposarcoma)
c) DDLS (De-Differentiated Liposarcoma).

For each tissue type the standard deviation from the mean is extremely big, and this “noise” might contain useful information. The aim of the study is to extract information from the standard deviation which can characterize material properties.

First, different depth positions (z_i) were chosen and the Intensity values of the 400 A-lines were plotted at the given depth position $I(z_i)$ (Figure III.2.8).

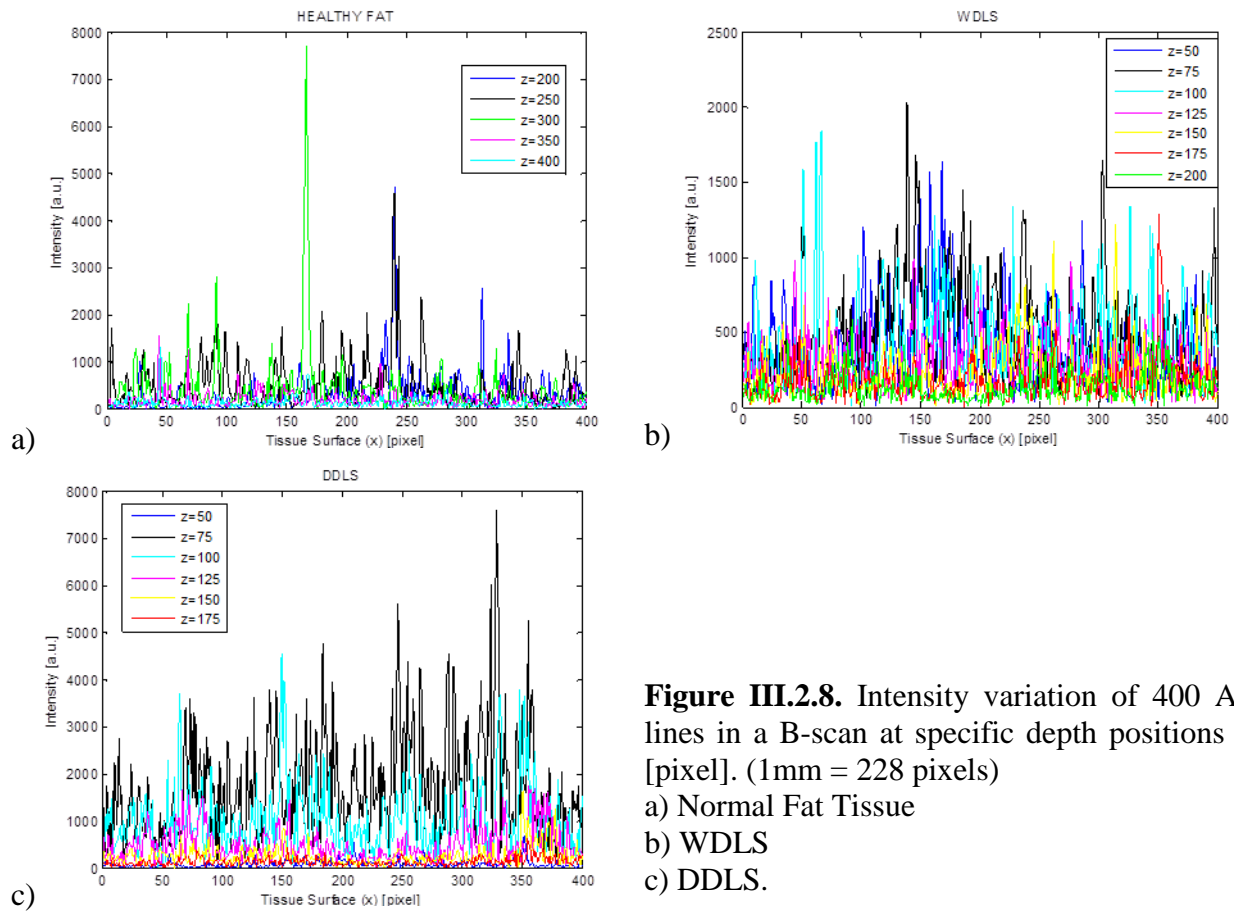
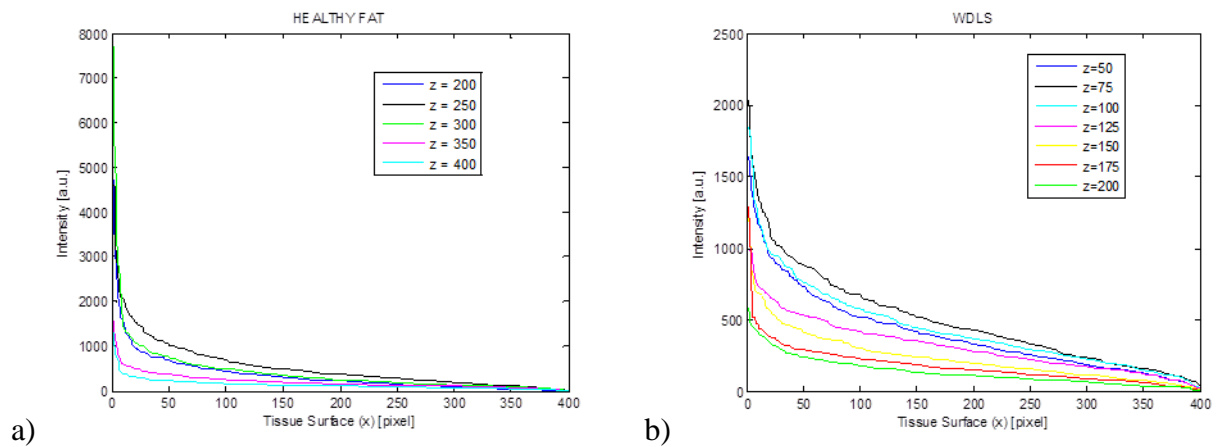


Figure III.2.8. Intensity variation of 400 A-lines in a B-scan at specific depth positions z [pixel]. (1mm = 228 pixels)
a) Normal Fat Tissue
b) WDLS
c) DDLS.

The Intensity values are reordered in descending order, and plotted on Figure III.2.9. The results show clearly different functions for healthy and cancerous tissue. The parametric function will be defined from these curves.



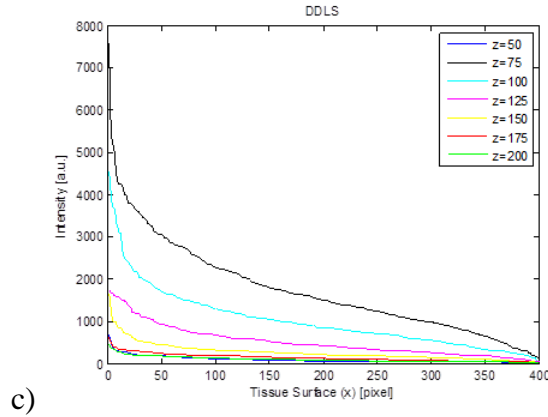


Figure III.2.9. Reordered Intensity Values from Figure III.2.8 at specific depth positions z [pixel] (1mm = 228 pixels)
a) Normal Fat Tissue
b) WDLS
c) DDLS.

The curves change as we go deeper in the tissue. The intensity decreases due to the light attenuation effects, and the sensitivity roll off explained in former chapter. At the first try to compare the tissue types, these reordered intensity values at a given depth position were chosen close to the surface, and normalized according to maximum value (Figure III.2.10.a).

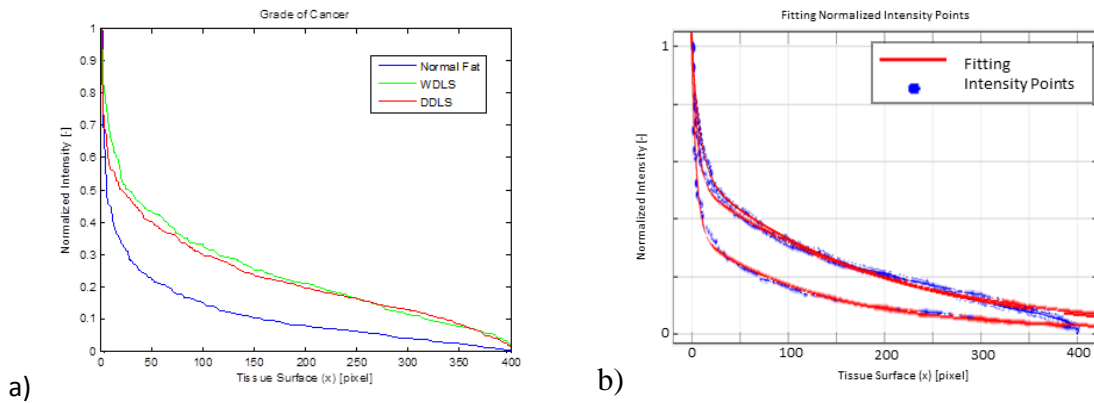


Figure III.2.10. Reordered Intensity Values of Normal Fat Tissue, WDLS, DDLS, normalized to the maximum value at a depth position z [pixel] close to surface.

The best fit of these curves ($R > 0.985$) is the exponential equation, whose parameters describe the material types:

$$f(x) = ae^{-bx} + ce^{-dx} \tag{III.2.1}$$

	a	$b \cdot 10^{-2}$	c	d
Normal Fat	0.3429	0.7682	0.8073	0.2022
WDLS	0.5616	0.5258	0.4512	0.1185
DDLS	0.5226	0.5061	0.4643	0.1817

Table III.2.1. Coefficients of the exponential equations discriminating Normal Fat Tissue vs. WDLS and DDLS.

MatLab Curve Fitting Toolbox software uses the method of least squares when fitting data (Figure III.2.10.b). The intensity values reordered in ascending order are the same as the inverse of the Cumulative Distribution Function (CDF) called Quantile Function.

Step 2. Histograms characterize different tissue types

Instead of CDF analysis, we will analyze the Probability Density Function (PDF) or Histogram of the pixel intensity values at a specific depth position (z_i) or at a given region ($\sum_1^n z_i$). Histogram analysis of intensity values in OCT images have already been studied for speckle analysis, or for signal image quality distinguishing foreground from the background, but never applied to study the structural properties of tissue.

The Histogram analysis provides multiple fitting distributions. We chose a universal model, the Generalized Extreme Value distribution, which includes the family of more distribution models:

$$y = f(x|k, \mu, \sigma) = \left(\frac{1}{\sigma}\right) \exp\left(-\left(1 + k \frac{(x - \mu)}{\sigma}\right)^{-\frac{1}{k}}\right) \left(1 + k \frac{(x - \mu)}{\sigma}\right)^{-1 - \frac{1}{k}} \quad (III.2.2)$$

where k is the shape-, μ is the location- and σ is the scale parameter. The Generalized Extreme Value Distribution with three parameters is the emergence of three distributions. One is the Weibull distribution as an example of central theorem statistics. Fréchet - and Gumbell distributions describe extreme value statistics. The special case of Fréchet is the Pareto-, Cauchy- or Student-t distribution, and the special case of Gumbell is the Normal, Exponential, Gamma or Lognormal distributions.

The comparison of the intensity distribution fits at a given depth position close to surface can be seen on **Figure III.2.11**. The histograms are normalized by the area, and their mean is subtracted. MatLab Statistics Toolbox fits the distribution by Maximum-Likelihood Estimation (Table III.2.2).

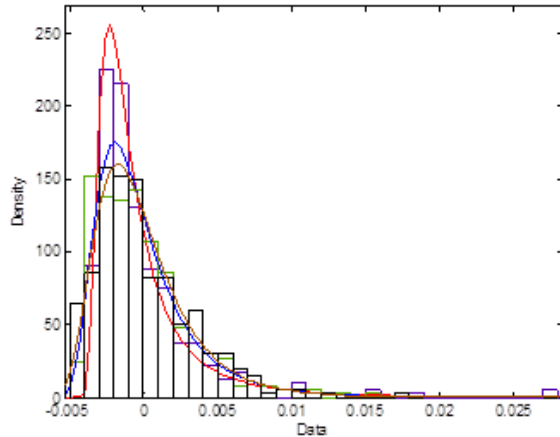


Figure III.2.11. Histogram fitted to the Intensity Values at a depth position z [pixel] close to surface, normalized by area, with subtracted mean; red-Normal Fat Tissue, blue-WDLs and brown-DDLS.

	k	$\sigma * 10^2$	$\mu * 10^2$
<i>Normal Fat Tissue</i>	0.427325	0.15548	-0.180471
<i>WDLs</i>	0.172213	0.213281	-0.162799
<i>DDLs</i>	0.0895055	0.230444	-0.154994

Table III.2.2. Coefficients of the Normalized Histograms at specific depth position discriminating Normal Fat Tissue vs. WDLs and DDLs.

This basic idea will be developed further below. The same problems arise as in the literature analysis: to find the tissue surface and Region of Interest where backscattering still occurs; to remove measurement settings, the effect of exposure time, focus position, path-length difference between mirror and tissue surface, camera sensitivity.

Step 3: Removing Tissue Surface Irregularity

For the computation in each quantification processes, the tissue surface topology first is numerically straightened to align each depth position. For each B-scan, we translate the A-line sections for different scanning positions so that the depth variable has a common reference in all cases.

The tissue characterization is strongly affected by fixing the correct edge of the tissue. The identification of the surface position was analyzed in different way. The A-lines are aligned according to the highest intensity points (Figure III.2.12), shifting using cross-correlation functions between a fix and the adjacent lines (Figure III.2.13), and shifting according to an absolute intensity threshold (Figure III.2.14). The next figures show the different methods on two different biological materials cut from the meat (a) and fat (b) part of a piece of ham.

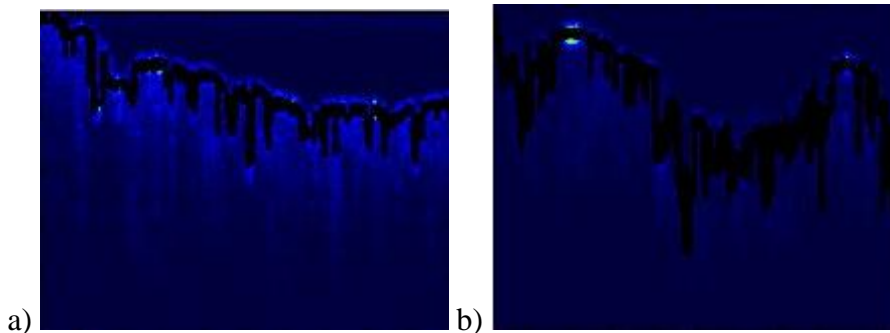


Figure III.2.12. Edge detection. Black lines mark the Highest scattering maximum a) meat b) fat.

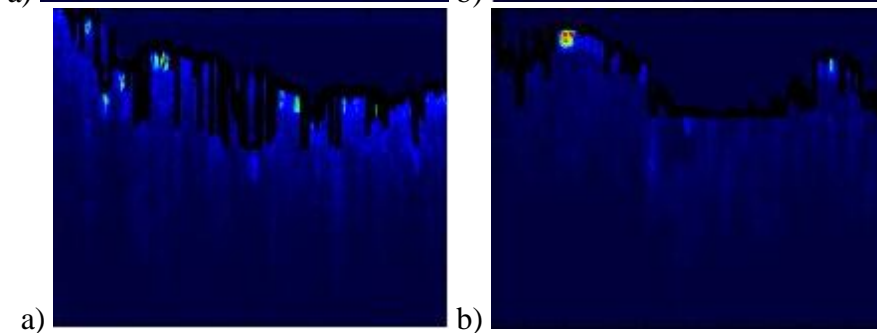


Figure III.2.13. Edge detection. Black lines mark the best correlation between adjacent A-lines a) meat b) fat.

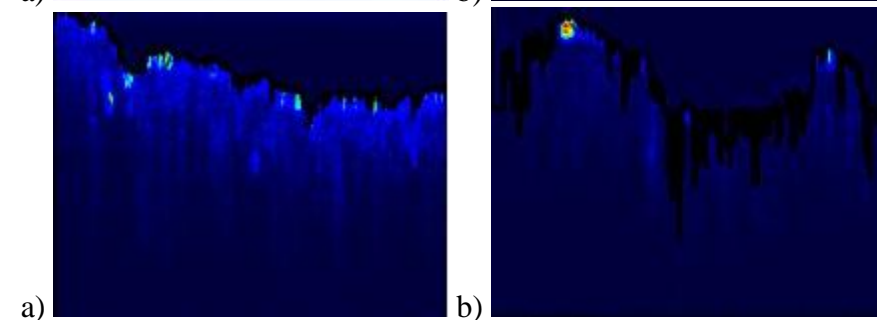


Figure III.2.14. Edge detection. Absolute threshold at a given intensity value a) meat b) fat.

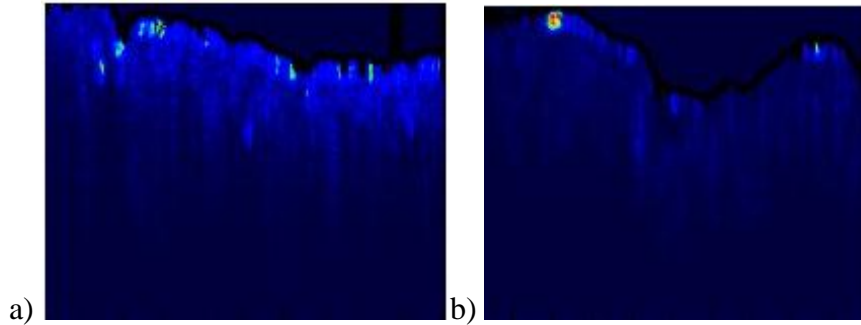


Figure III.2.15.
Edge detection.
Canny edge detector
applied 3x a) meat b)
fat.

These methods are uncertain and do not follow the real border of the surface. Due to the inhomogeneity of the tissue, the A-lines cannot be correlated, and higher intensity points can be found deeper in the tissue. The edge defined at a given threshold can vary according to tissue types and can yield erroneous result. Matlab provides implemented edge detectors (Canny, Sobel, Log, Prewitt, Roberts, Zerocross). After investigating the utility of these methods, the canny edge detector algorithm is applied three times successively to find the border of the tissue and to straighten the image surface (Figure III.2.15).

The canny edge algorithm implements more consecutive steps to find edges. First the raw image is filtered with a Gaussian filter to remove noises, and then the intensity gradient is calculated from the first derivatives in x/y direction. The non-maximum points are suppressed from this image so to obtain a binary image, finally the edges are drawn with hysteresis: based on the gradient there are weak and strong edges, and the final edge includes strong edges, and weak edges only if they are connected to strong edges (Figure III.2.16).

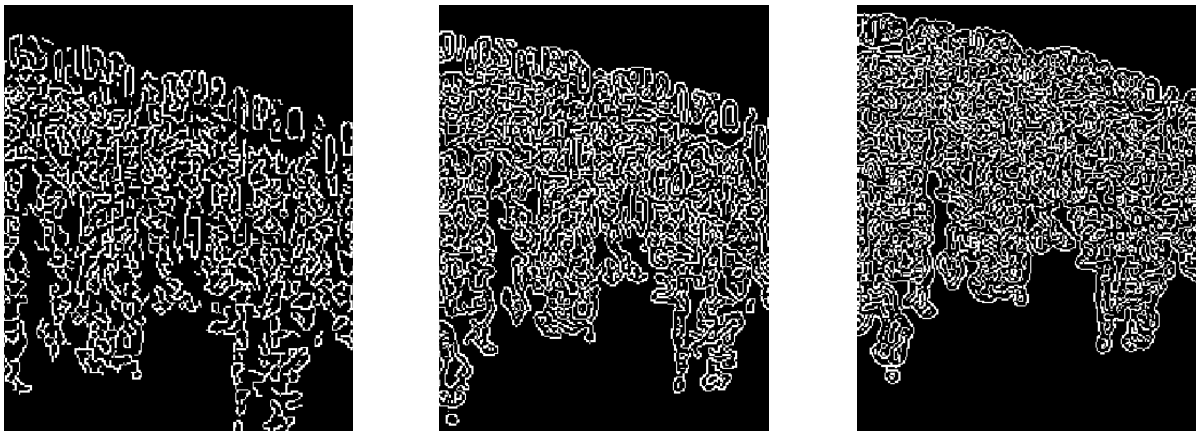


Figure III.2.16. Canny edge binary images applied successively to obtain the surface of the tissue. White pixel value '1' showing edges, black pixel value '0' showing no edge. The border of the tissue becomes continuous only on the third image.

The tissue surface is defined from the last binary image pointing to the first '1' digit in each A-line. This method is sensitive to background noise as well so the images should be filtered first. For further improvement Matlab Image Processing Toolbox can provide other tools to find the surface digitally (edge detectors, histogram equalization, high or band pass filters, adaptive threshold).

Finally we apply the canny edge detector implemented in Matlab Image Processing Toolbox three times on the B-scans after median filtering the images (Figure III.2.17-20). Before further analysis, we screen all the B-scans to verify that each one is straightened properly. The saturation points on the images and the background noise can give erroneous results without correction (Figure III.2.21-22).

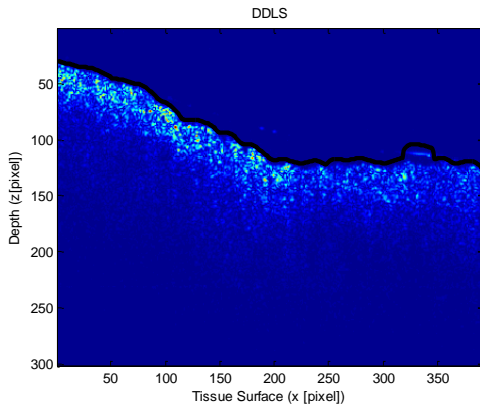


Figure III.2.17. Original image with the straightening line found after the algorithm.

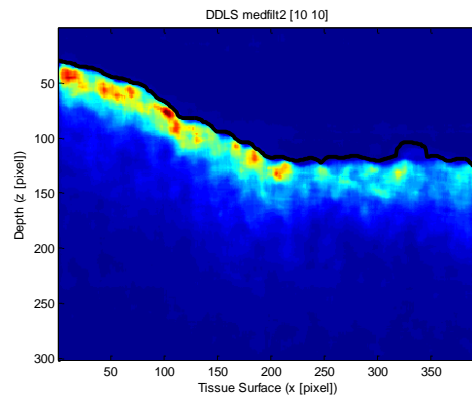


Figure III.2.18. Step 1. 2D median filter applied on the raw image. The median filter is calculated from a moving 10x10 pixel box.

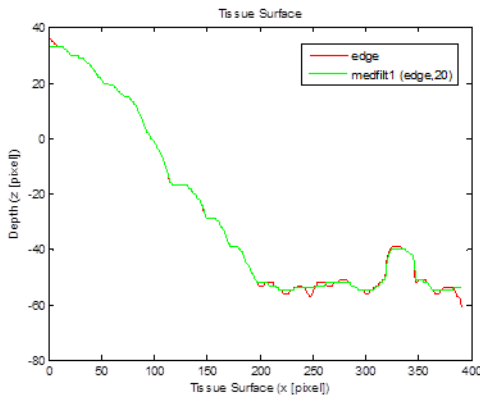


Figure III.2.19. Canny edge detector is applied 3x on the 2D filtered image, then the surface is straightened according to the first '1' value at each line of the binary image (red line). The obtained edge is median filtered. The median intensity value is calculated from 20 adjacent pixel points successively (green line).

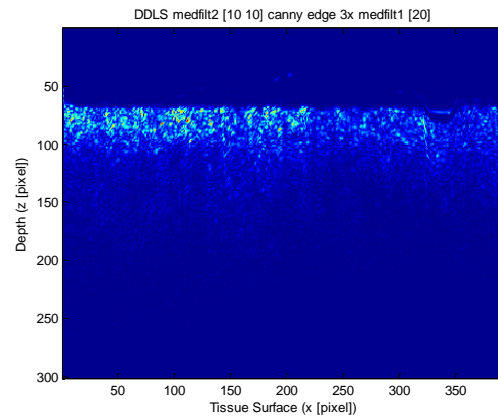


Figure III.2.20. The original image is properly straightened applying the filtered edge.

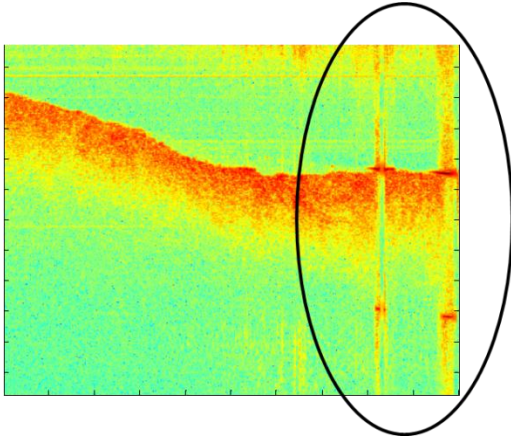


Figure III.2.21. Saturation points affecting the images.

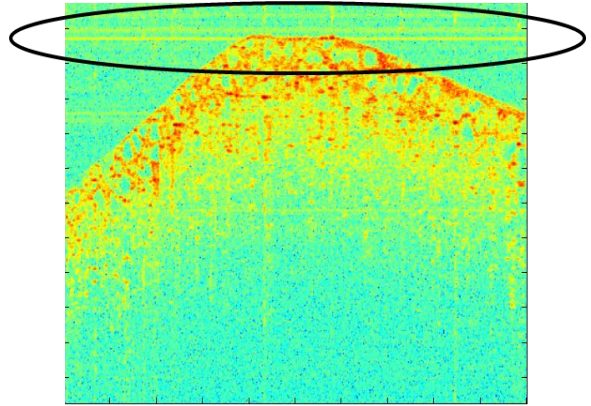


Figure III.2.22. Noise crossing the tissue.

The problem of tissue surface straightening and edge detection is a common issue for each quantitative method described above, where the mean or variation of the adjacent A-lines is used to determine tissue scattering properties.

Step 4: Compensate measurement settings and light attenuation effect

After straightening the OCT images the statistical analysis has to be able to compare the data measured at different experimental setup. The normalization process will be defined by reducing the effects of the measurement setup, the sensitivity roll off from farther path-length differences, and the light attenuation effect.

At each depth position the mean and standard deviation of the A-lines are calculated (Figure III.2.23). As stated in the literature, the attenuation of the light can be obtained by filtering per A-line, or by averaging adjacent A-lines in the B-scan. The attenuation effect can be removed by dividing the intensity points by their mean at each depth position, and this way to normalize every scan line. This process will also compensate the different exposure times for different measurements without affecting the material scattering properties and structural characteristics.

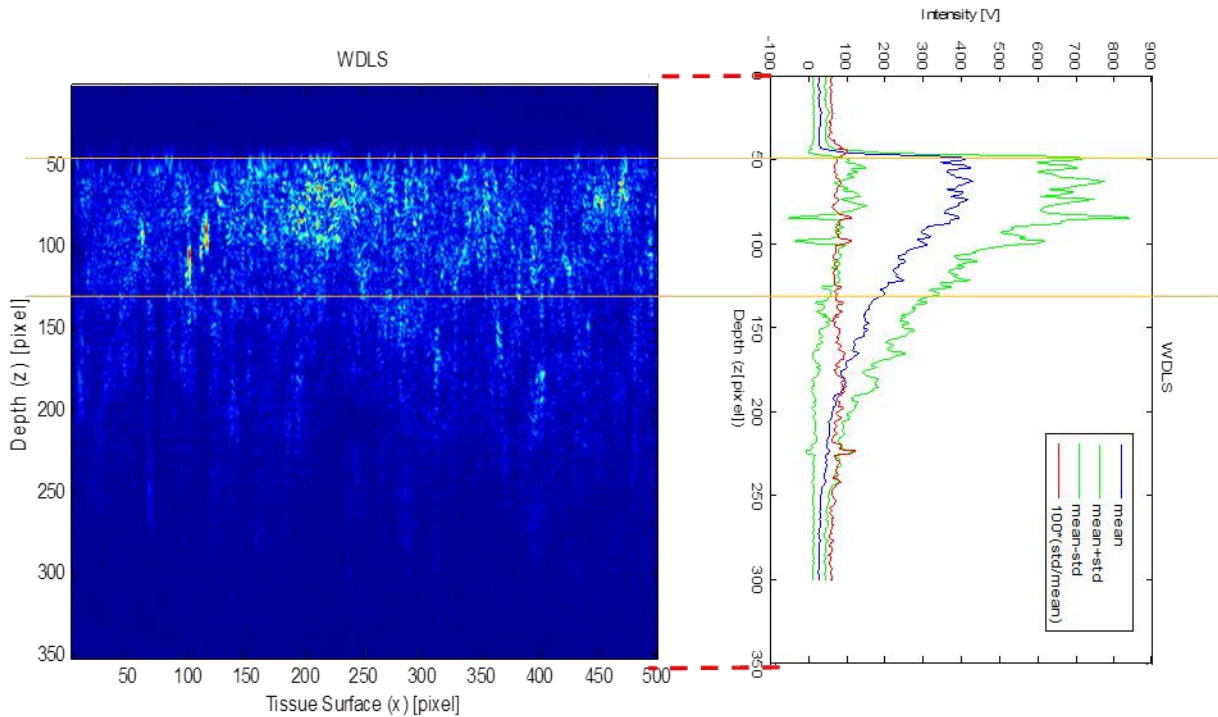


Figure III.2.23. Straightened Tissue Surface, and $\text{mean} \pm \text{std}$ at each depth position.

The control of the setup for the measuring rig is robust, the optimal recording position is set manually, which enhance the uncertainty to get a universal model. However the normalization process neglects the exposure time setting, and light attenuation effect, there is still the problem of the focus position, and the path-length difference between the tissue surface position and the reference mirror which are varying at each measurement.

To overcome this problem, first we measured the curve of the sensitivity roll-off recording the same sample point at lower intensity from farther path-length differences as explained in former chapter. This reduces the errors of straightening coming from the intensity variations because of the oblique or irregular tissue surface.

This sensitivity curve can be calculated from experiments with a second mirror in the sample arm by dynamic focusing. We shift the mirror toward depth and we place the mirror to the perfect focus position for recording, so as the camera sensitivity curve is obtained, and normalized by the maximum intensity value (black and blue dots on Figure III.2.24).

This normalized curve is independent from the measurement settings, but it is affected by the focus position which varies at each measurement. To get a comparable measurement, the sensitivity roll-off curve distorted due to the intensity variation in the focal region should be corrected, independently from the measurement settings.

During tissue measurements the focus position should be always set at the beginning of each sample measurement, usually in the tissue volume. In conventional SD OCT system, the focus position does not change during recording, a fixed focusing system is set up. The coherence plane at zero path-length differences (position of the DC term) does not correspond with the focal plane. The coherence plane is outside of the tissue volume, and does not change during recording. However SD OCT system uses low NA with large depth of focus, the imaging

range is deeper than the focal region, and so the OCT image at a specific depth region will show backscattering from the out-of-focus region.

The effect of the focus is measured and described below. New measurements were made with the same mirror shifting in depth in the sample arm, but the backscattering signal was recorded keeping the same focus position, which was set up from a former measurement with tissue in the sample arm (fixed focus). The normalized values of these measurements are shown with red dots on Figure III.2.24.

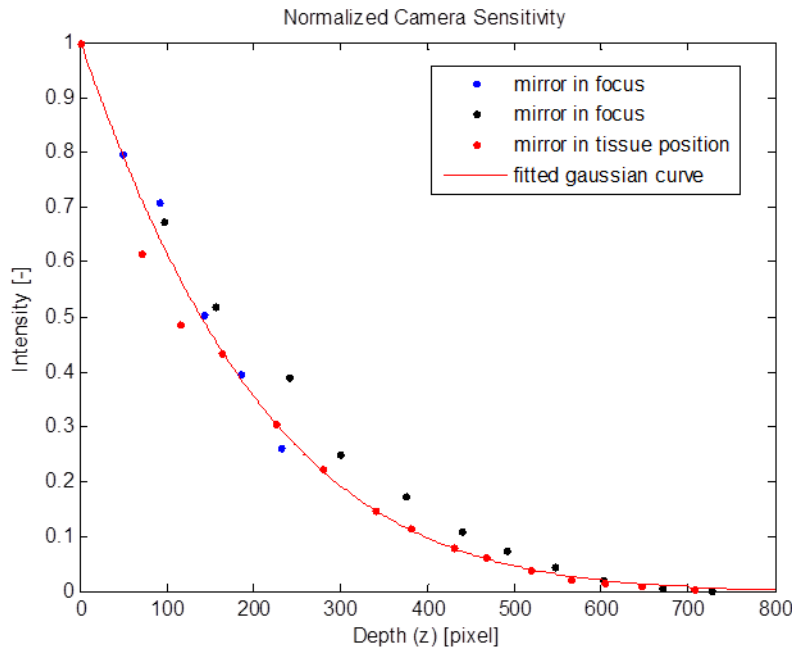


Figure III.2.24. Normalized Sensitivity roll-off. Black and Blue dots mark measurements from a mirror in the sample arm shifted in depth at focus position, red dots mark measurement from the mirror shifted in depth in the sample arm at fixed focus.

These curves show that the camera sensitivity curve is hardly affected by the intensity variation of the focal region. During measurements the exact focus position is not verified, and it is farther from our Region of Interest where the tissue backscattering is detected, and so this effect can be neglected.

The measurement was made on mirror featuring specular reflection. In this case the apparent Rayleigh length (z_R) is equal to the Rayleigh length (z_0), because the factor α is equal to 1 ($z_R = \alpha z_0$). The Rayleigh length in diffuse media is doubled ($\alpha = 2$), so the focal region is broadened, or it can be neglected.

We will not investigate further the focus depth limitation already analyzed in the literature, and will accept the correction computed from the curve coefficients fitted on the normalized intensity points at the shifted mirror in depth at fixed focus position.

Matlab Curve Fitting Toolbox computes the parameters by Least Squared fitting procedure. The equation of the fitted curve is a Gaussian:

$$f(z) = 5.222e^{-\left(\frac{(z+724)}{563.8}\right)^2} \quad (III.2.3)$$

During analysis each A-line will be corrected according to this curve before calculating the histograms. The A-line plot of Figure III.2.7 after Gaussian correction can be seen on Figure III.2.25:

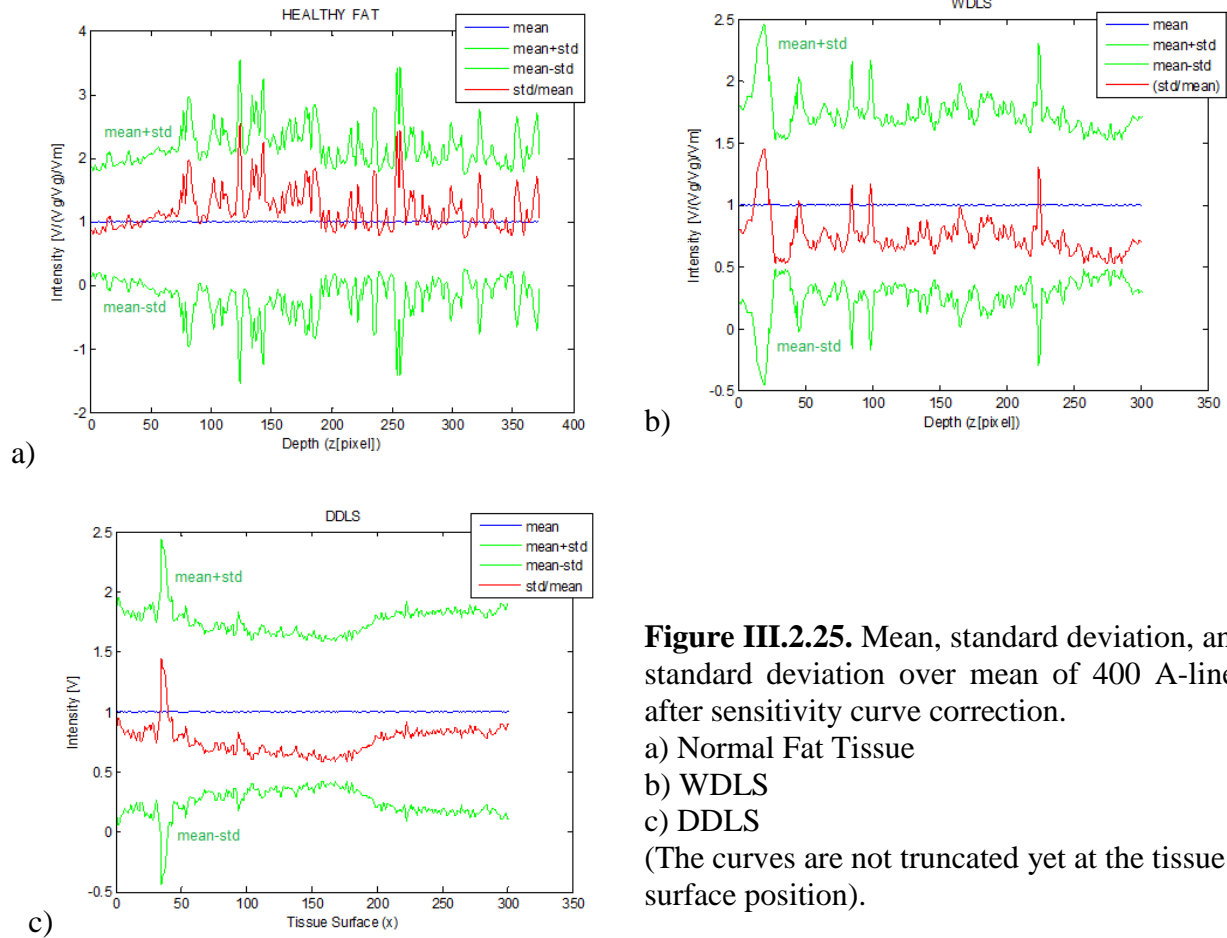


Figure III.2.25. Mean, standard deviation, and standard deviation over mean of 400 A-lines after sensitivity curve correction.
a) Normal Fat Tissue
b) WDLs
c) DDLS
(The curves are not truncated yet at the tissue surface position).

One can state from these figures that the standard deviation over mean (red on Figure III.2.25) can differentiate tissue types, and the first analysis will extract information from these curves.

Step 5. Define Region of Interest (ROI) on the STD/MEAN curves

After the surface is straightened numerically, the correct mean and STD can be obtained at each depth position. For each B-scan, we translate the A-line sections so the tissue surface will be positioned at common pixel position.

The STD/MEAN ratio at each depth position of a B-scan from the three tissue types calculated on the raw image, and the sensitivity-corrected image is shown on Figure III.2.26.

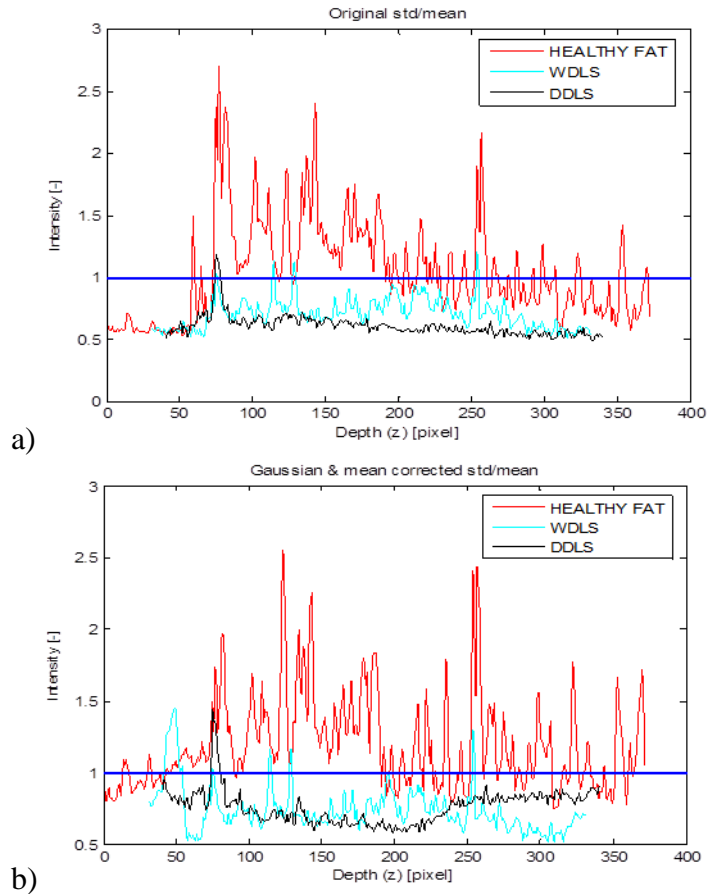


Figure III.2.26. STD/MEAN ratio at each depth position in a B-scan on Normal Fat (red), WDLS (cyan), DDLS (black).
a) Original data
b) Gaussian corrected data.
(The curves are not truncated yet at the tissue surface position).

The curves by sight represent different features regarding mean or standard deviation for healthy vs. cancerous tissue. The Probability Density Functions (PDF) of the STD/MEAN curves will be plotted, and the Generalized Extreme Value (GEV) Distribution will be fitted on the intensity values.

To draw the correct distribution functions, the tissue surface and the Region of Interest (ROI) from the scattering region should be determined properly. The straightening process aligns the tissue border, but it does not yield the exact position separating from the background. To localize the tissue surface on the straightened images the mean of the A-lines in one B-scan, and the first derivatives of the mean are calculated from the uncorrected images (Figure III.2.27). The tissue surface is defined at the highest derivative point.

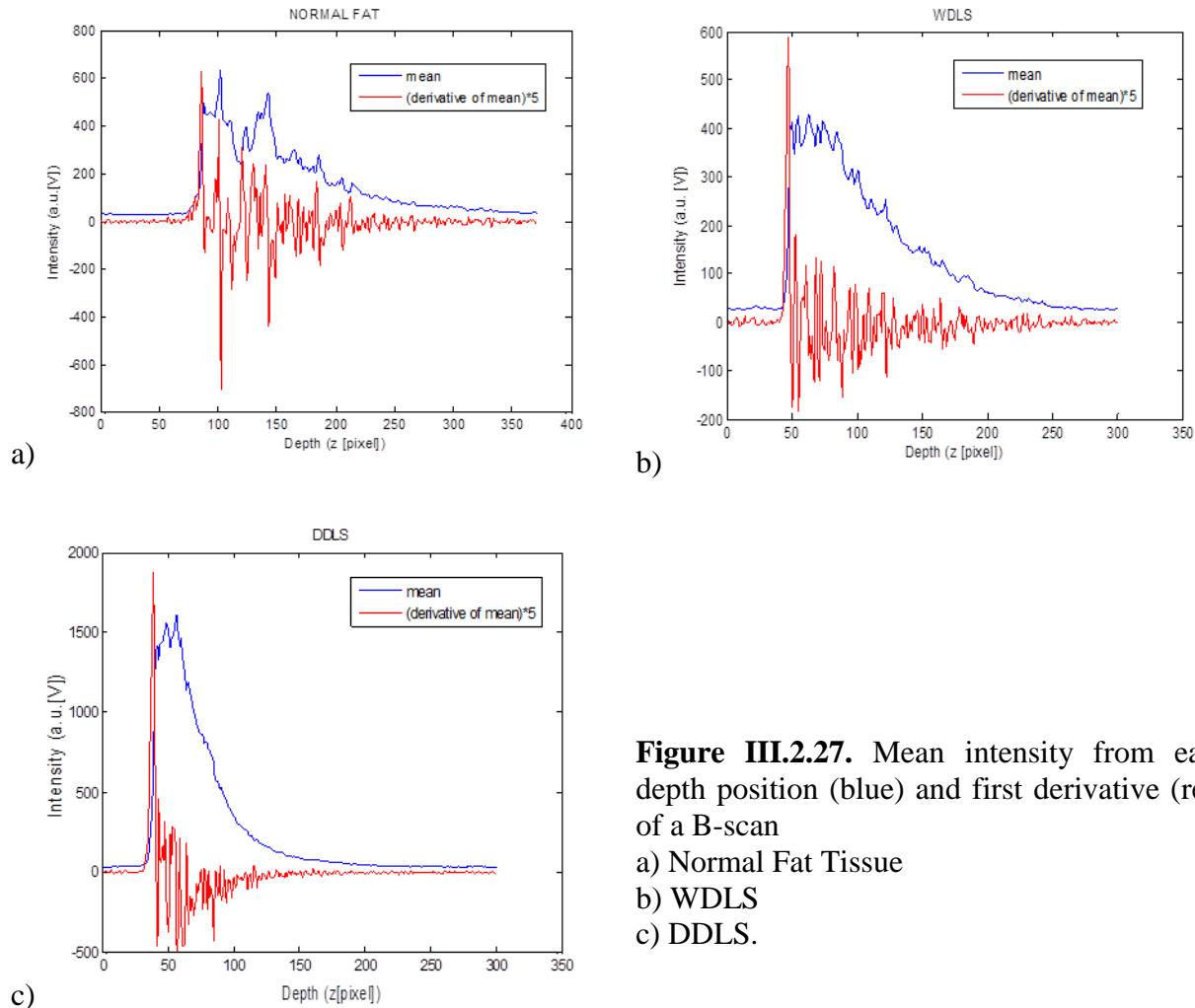


Figure III.2.27. Mean intensity from each depth position (blue) and first derivative (red) of a B-scan
a) Normal Fat Tissue
b) WDLs
c) DDLS.

The tissue surface is identified. The next question is till which depth position the backscattering provides useful information revealing structural properties of the tissue and characterizing tissue types. 150 pixel = 0.659 mm depth is considered for analysis because the most dense tissue (DDLS) does not reflect light from deeper region at this wavelength range and camera settings.

The Region of Interest (ROI) should be defined between the tissue surface and end before the 150th pixel depth. This analysis relies on the use of a windowing scheme, in which sections of the intensities as function of depth are evaluated separately (Figure III.2.28).

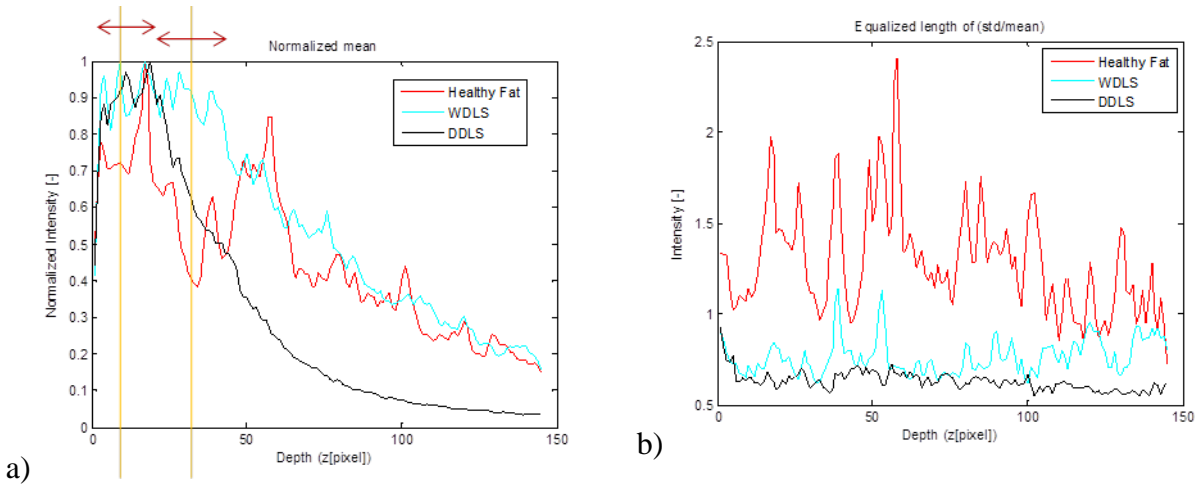


Figure III.2.28. a) Windowing scheme on the normalized mean intensity signals from Figure III.2.27 and b) Standard Deviation over Mean at each depth position in the same region. Normal Fat (red-), WDLS (cyan-), DDLS (black line). The region shows 150 pixel - depth from the tissue surface.

The ROI was defined after moving a window at different size and position on the 150 pixel points. Standard deviation over mean was calculated and the Generalized Extreme Value (GEV) Distribution parameters (k, σ, μ) were computed for each region in multiple B-scans.

Window sizes from 50 to 150 pixels in 1 pixel increment were investigated first beginning at the tissue surface, and then shifted pixel by pixel deeper in the tissue. The optimal window size and position produces the largest separation of the Normal Adipose and Cancerous Tissue (WDLS, DDLS) parameters on the σ, μ plane (Figure III.2.29).

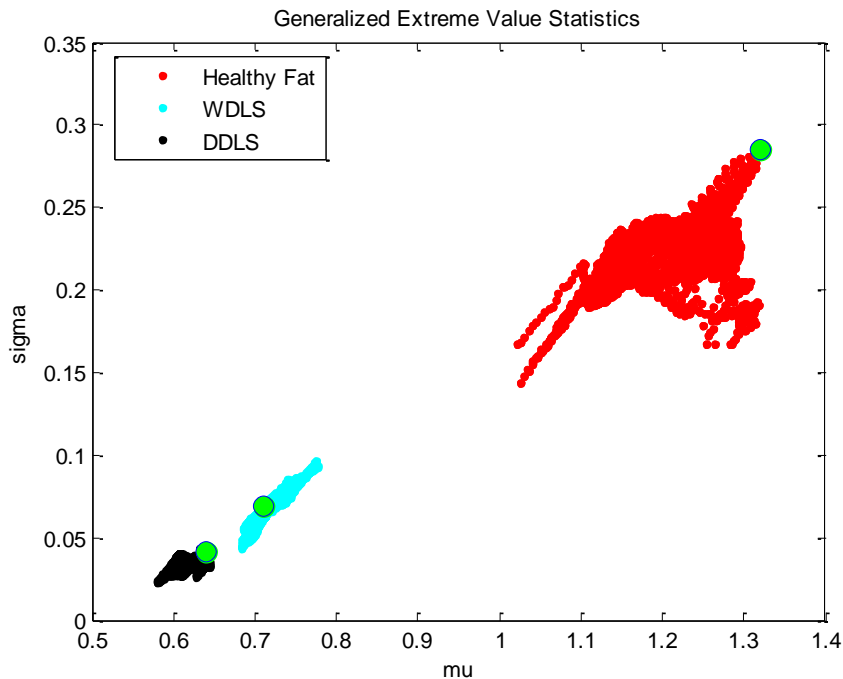


Figure III.2.29. GEV Distribution parameters after windowing process, green dots show the optimal window size, the largest separation on the μ - σ plane. One B-scan is analyzed here.

At this specific B-scan each region differentiates well the tissue types. The optimal window position begins at 11th pixel, and the width is 50-pixel deep. Further window shifting procedure is applied on adjacent B-scans with a window size increasing from 20 pixels up to 150 pixels beginning at the tissue surface (Figure III.2.30).

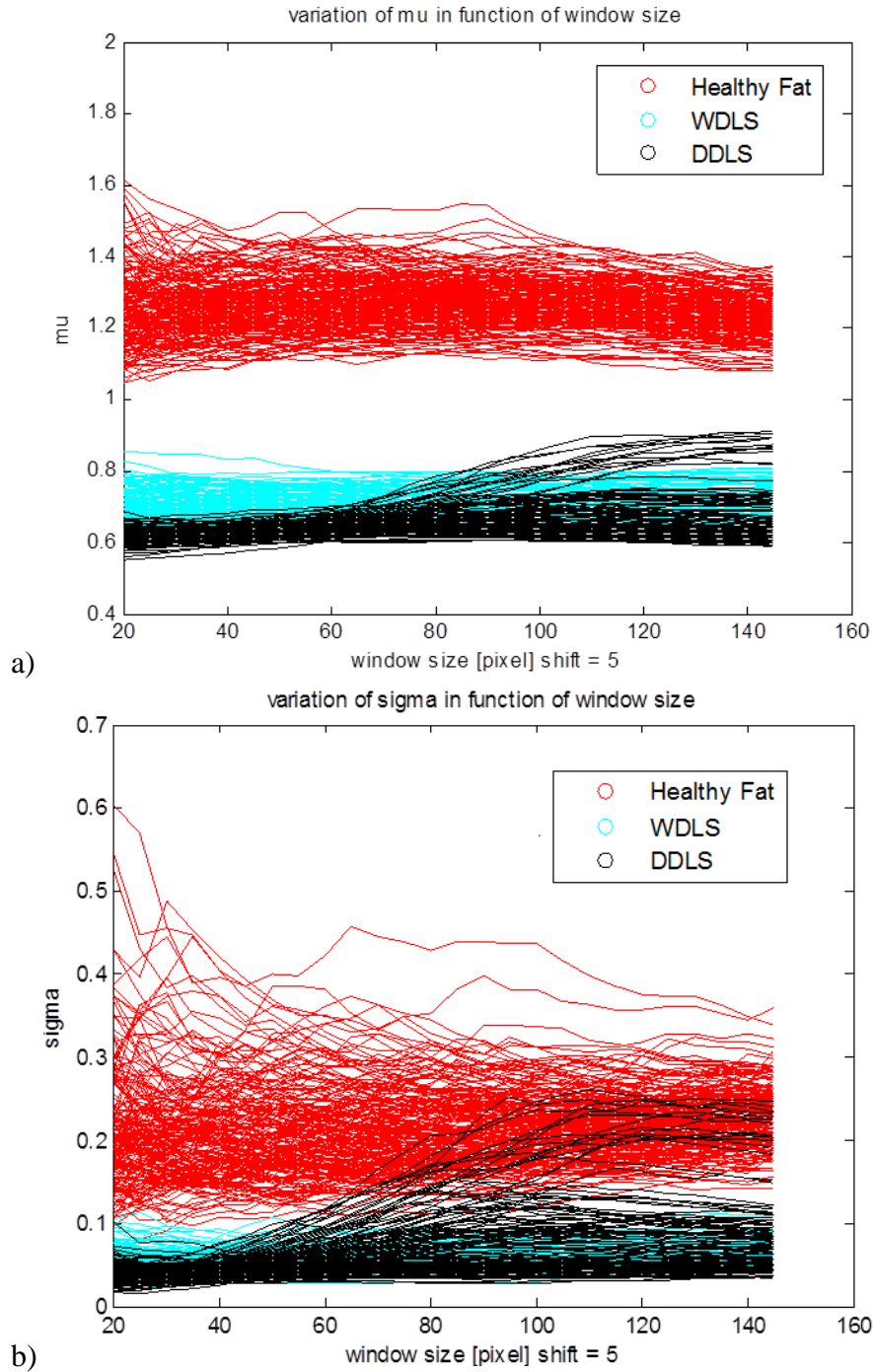


Figure III.2.30. Variation of a) μ and b) σ by incrementing window size beginning from the tissue surface, 200 B-scans on Normal Fat Tissue, 160 B-scans on WDLS and DDLS.

However smaller region also gives characteristic parameters, the 40 pixel region gives the optimal separation between the different tissue types regarding the σ - μ parameters. This 40-pixel-window was then shifted by 5 pixels successively deeper in the tissue (Figure III.2.31).

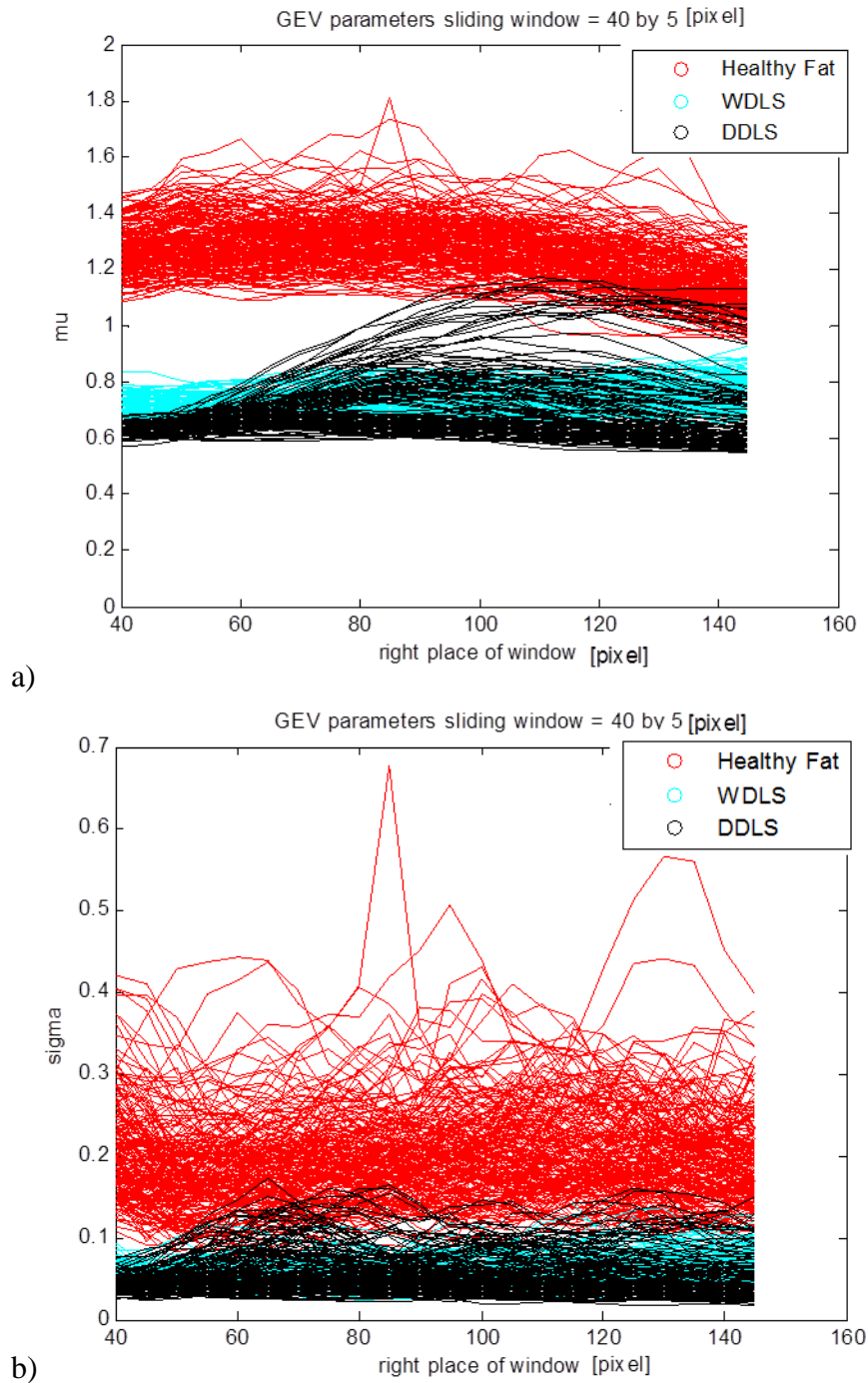


Figure III.2.31. Variation of a) μ and b) σ by shifting a 40-pixel size window beginning from the tissue surface, 200 B-scans on Normal Fat Tissue, 160 B-scans on WDLS and DDLS.

After investigating the variation of σ and μ at different position from the 40-pixel (= 0.1758 mm) window size, the tissue surface was chosen as optimal solution as the beginning of ROI. In this case, the surface scattering has no significant effect either whether the ROI begins at

the surface or some pixel deeper in the tissue. In deeper region, where the backscattering is weak, the statistical analysis becomes irrelevant.

The 40 pixel deep window size beginning at the surface is applied on 200 B-scans of Normal Fat tissue and 160 B-scans of WDLS and DDLS, and the GEV parameters σ and μ were calculated (Figures III.2.32&33).

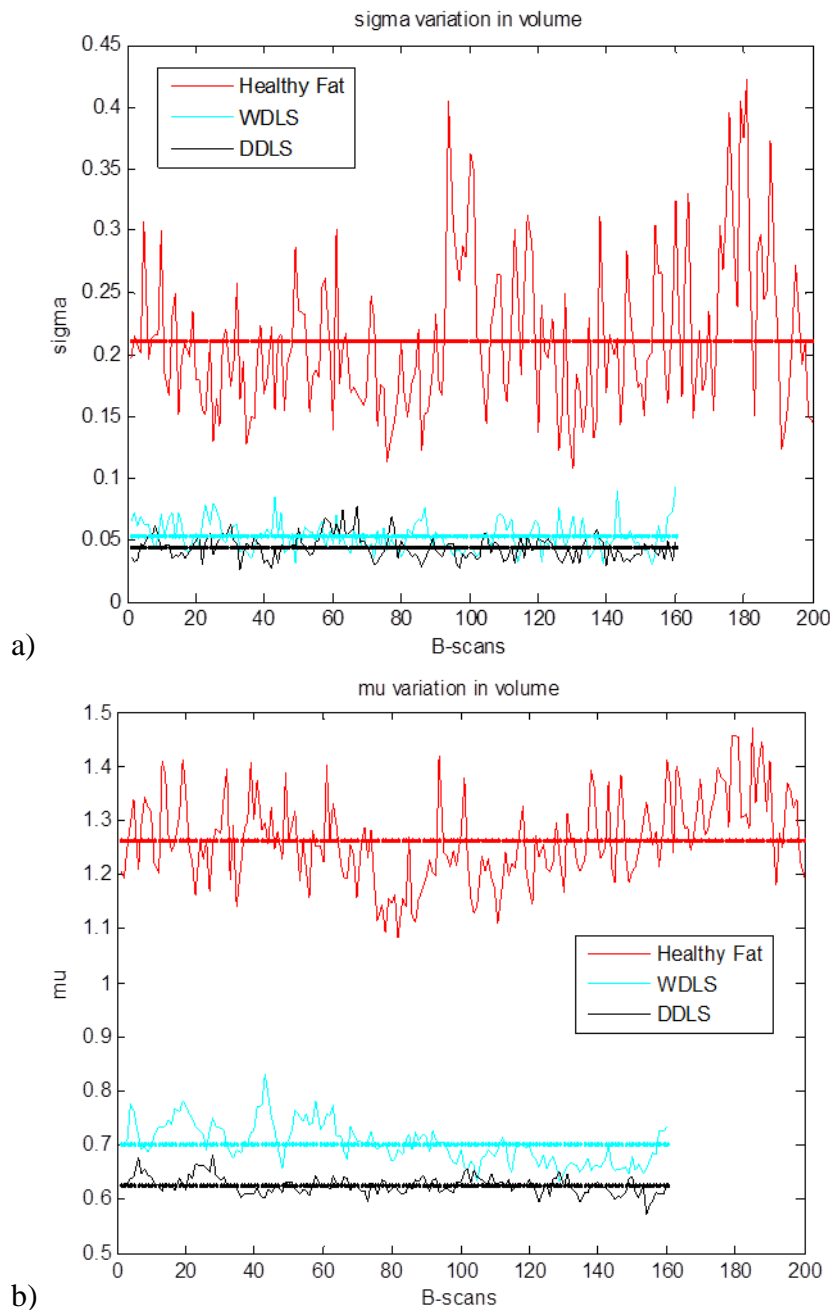


Figure III.2.32. GEV parameters, 200 B-scans for Normal Fat Tissue, 160 B-scans for WDLS and DDLS a) σ -, b) μ - variation of B-scans in a tissue volume.

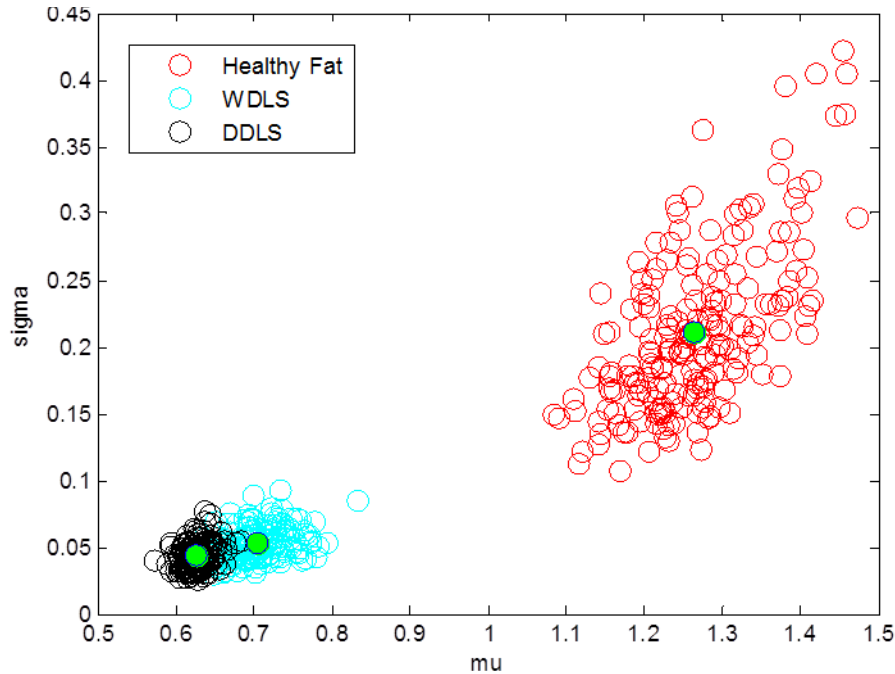


Figure III.2.33. GEV parameters on the σ - μ plane. 200 B-scans for Healthy Fat 160 B-scans for WDLs and DDLS. Green point marks the Center of Gravity.

The analysis applied for the three tissue types distinguishes well healthy vs. cancerous tissue, however the DDLS and WDLs parameters are overlapped. Further we will analyze tissue scattering properties at this Region of Interest.

Step 6. Results of the STD/MEAN curves

The final results were applied on the sensitivity roll off – corrected curves. The GEV Distribution parameters (k, σ, μ) were calculated on the above defined ROI of the std/mean intensity curves. The GEV Distribution parameters (k, σ, μ) were calculated from 200 Normal Fat Tissue, 160 WDLs and DDLS B-scans (GEV parameters per B-scan in **Appendix 2**).

The mean and standard deviation of each parameter were calculated yielding this way to a theoretical universal GEV Distribution specific for each tissue type, deduced from the experiments. The PDFs are plotted on Figure III.2.34, and the coefficients are represented in Table III.2.3.

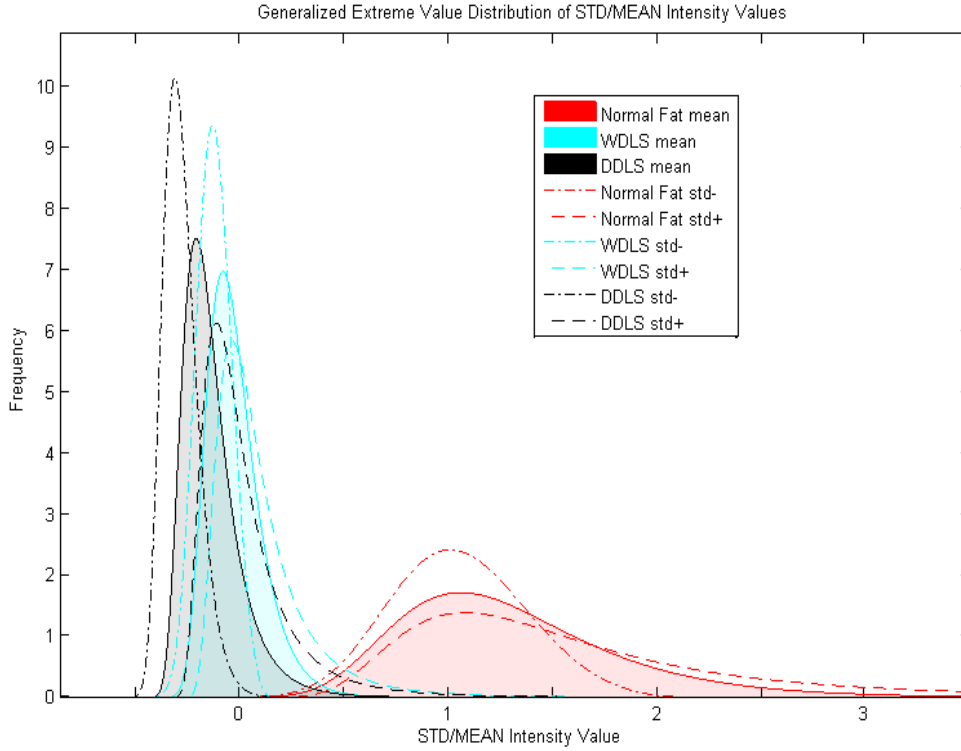


Figure III.2.34. Histogram, GEV Distribution parameters (k, σ, μ) fitted to the STD/mean ratio of the intensity values in ROI; Mean \pm standard deviation on 200 B-scans of Normal Fat, and 160 B-scans of WDLs and DDLS.

<i>STD/MEAN</i>	<i>k</i>	<i>σ</i>	<i>μ</i>
<i>Baseline</i> <i>(Normal Fat)</i>	0.0007 ± 0.2347	0.2151 ± 0.0579	1.2796 ± 0.0659
<i>Deviation 1</i> <i>(WDLs)</i>	-0.0128 ± 0.2443	0.0529 ± 0.0120	0.7093 ± 0.0359
<i>Deviation 2</i> <i>(DDLS)</i>	0.0857 ± 0.1673	0.0493 ± 0.0128	0.6502 ± 0.0584

Table III.2.3. GEV parameters calculated from the STD/MEAN ratio of the intensity in ROI, mean and standard deviation is calculated on 200 B-scans of Normal Fat Tissue, and 160 B-scans of WDLs and DDLS.

The curve coefficients well differentiate between the healthy and cancerous tissues, but there is less distinction between the grades of the cancer. To draw the deviation from the healthy tissue as baseline, the next parameters are calculated, where b index is the Baseline tissue, d index is the Deviated tissue parameter (Table III.2.4).

<i>STD/MEAN</i>	$\Delta k = \frac{k_d - k_b}{k_b}$	$\Delta \sigma = \frac{\sigma_d - \sigma_b}{\sigma_b}$	$\Delta \mu = \frac{\mu_d - \mu_b}{\mu_b}$
<i>Baseline</i> <i>(Normal Fat)</i>	0 ± 335.2857	0 ± 0.2692	0 ± 0.0515
<i>Deviation 1</i> <i>(WDLs)</i>	-19.2857 [-368.2857;329.7143]	-0.7541 [-0.8099;-0.6983]	-0.4457 [-0.4737;-0.4176]

Deviation 2 (DDL5)	121.4286 [-117.5714;360.4286]	-0.7708 [-0.8303;-0.7113]	-0.4919 [-0.5375;-0.4462]
------------------------------	----------------------------------	------------------------------	------------------------------

Table III.2.4. Comparison of the GEV Distribution parameters calculated from the STD/mean ratio at each depth position in ROI; mean and standard deviation on 200 B-scans of Baseline Tissue and 160 B-scans of Deviation 1&2 is calculated.

The coefficients shown in Table III.2.4 are illustrated on Figure III.2.35. The edges of the boxes represent the standard deviation with the mean values in the middle of the boxes.

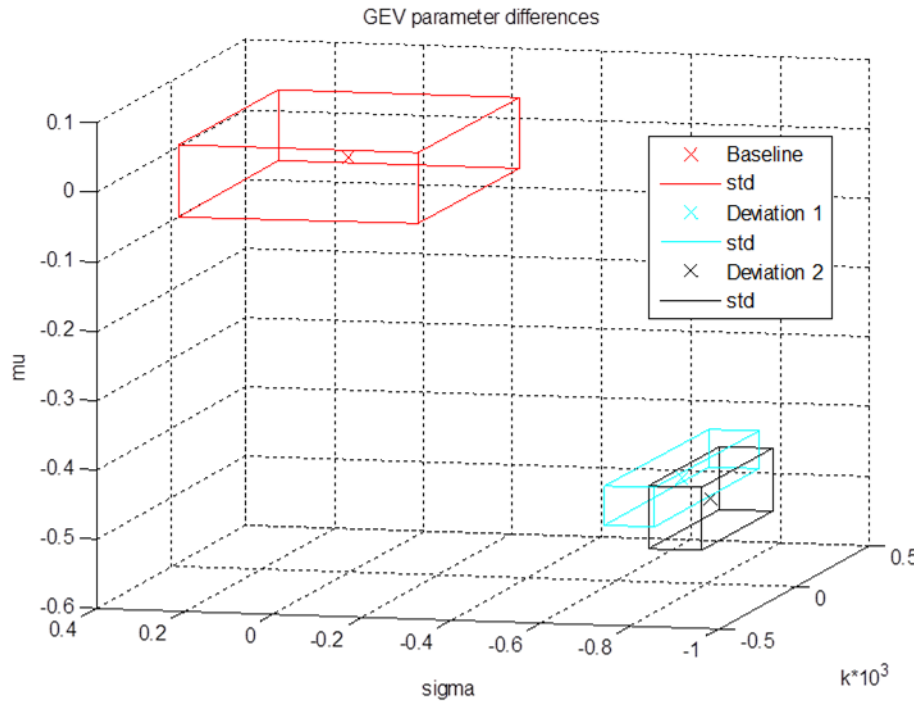
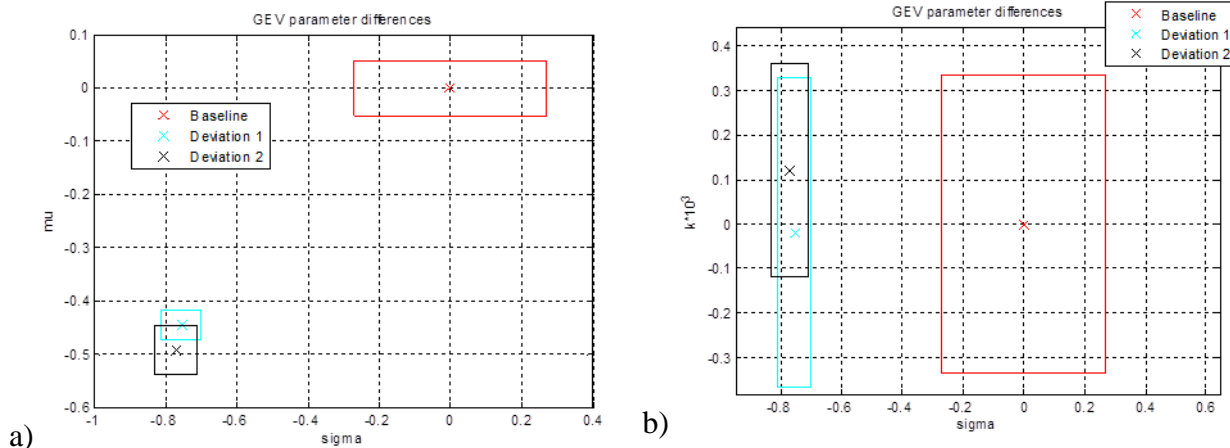


Figure III.2.35. Comparison of the GEV Distribution parameters (k , σ , μ) represented at each axe of the 3D coordinate system calculated from the STD/mean ratio of the intensity values; Mean and standard deviation on 200 B-scans of Baseline Tissue and 160 B-scans of Deviation 1&2.

It is clear, that there is a statistically significant separation between the healthy and cancerous tissue in each projection plane (Figure III.2.36).



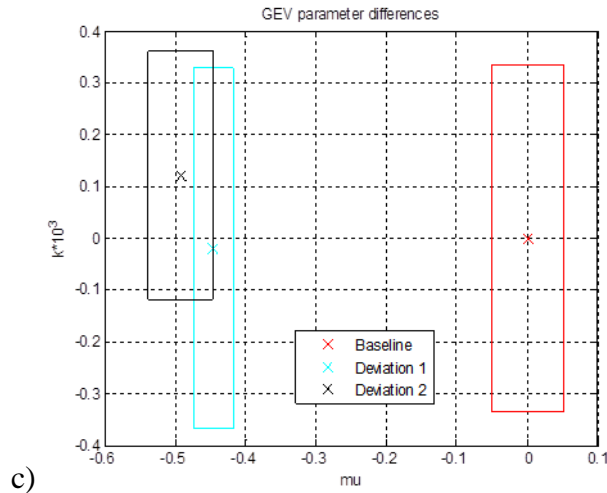


Figure III.2.36. Projection planes of the 3D coordinate system on Figure III.2.35. Comparison of the GEV Distribution parameters represented at each axe of the 3D coordinate system calculated from the STD/mean ratio of the intensity values; Mean and standard deviation on 200 B-scans of Baseline Tissue and 160 B-scans of Deviation 1&2.

Step 7. Define Region of Interest (ROI) on the mean normalized Intensity variations

A second method is developed to analyze the same data set. Instead of calculating the standard deviation over mean curves, all the measured intensity values are now considered, and also normalized by the mean intensity at each depth position. The same windowing process was applied on the B-scans, and the optimal window size of 40 pixels beginning from the surface has been demonstrated as shown here below (Figure III.2.37).

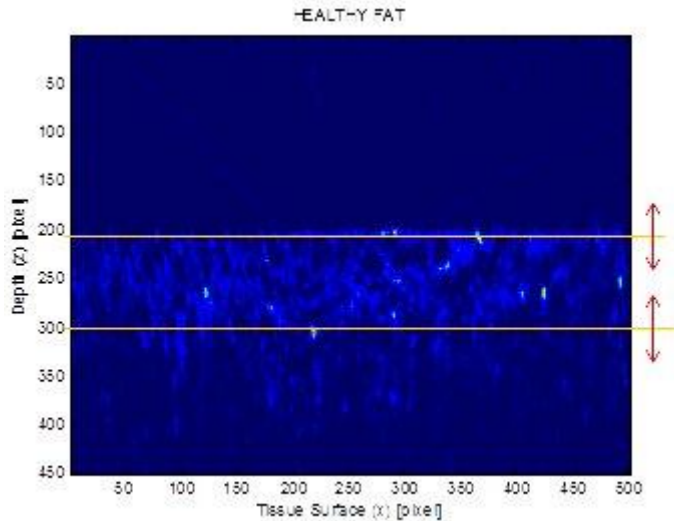


Figure III.2.37. Scheme of the windowing process on the mean normalized B-scans, from a minimum window size of 20 pixels, incremented successively with 1 pixel, and shifted pixel by pixel up to 150 pixel depth.

The parameters (k , σ , μ) of the GEV Distribution were calculated first on 1 B-scan from each windowing region and plotted on the σ - μ plane (Figure III.2.38).

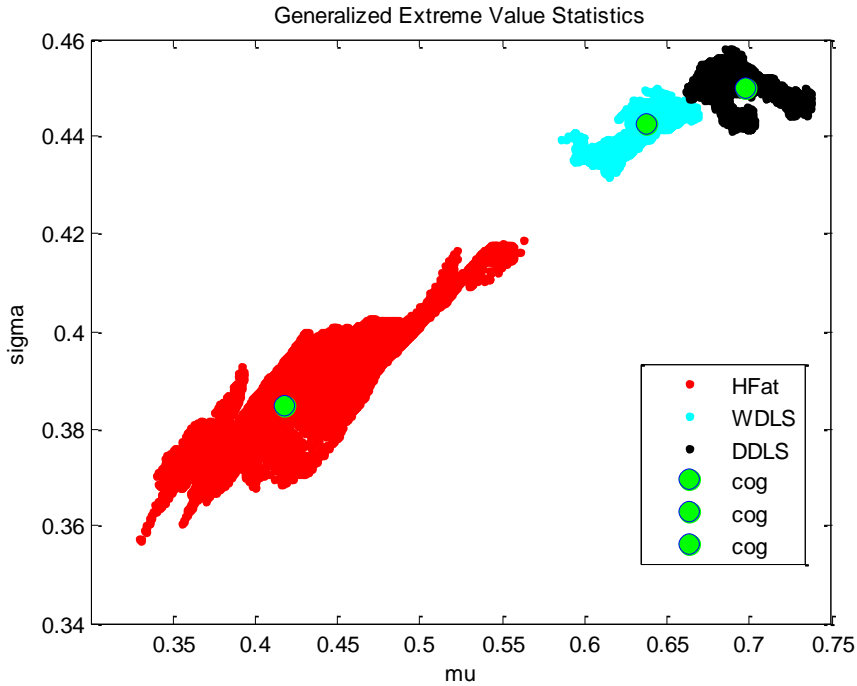
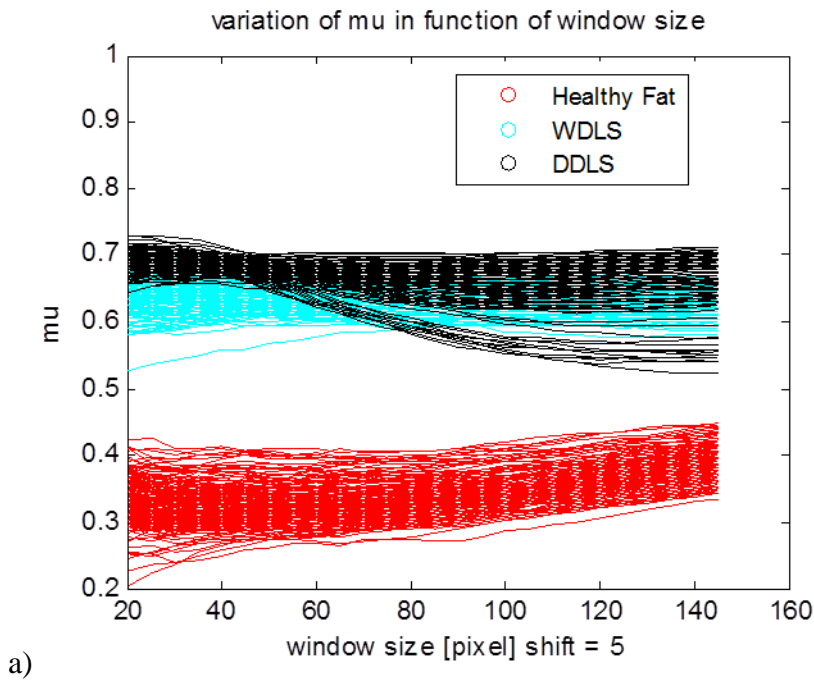


Figure III.2.38. GEV Distribution parameters (σ , μ) computed from windowing process; green dots show the Center of Gravity. Minimum window size of 20 pixels in a 1 pixel increment and shifted in depth.

After 1 B-scan analysis, any size of window at any position differentiates healthy vs. cancerous tissue, and the grade of cancer. The same window shifting procedure is applied on 200 B-scans of Normal Fat Tissue, and 160 B-scans of WDLS and DDLS (Figure III.2.39).



a)

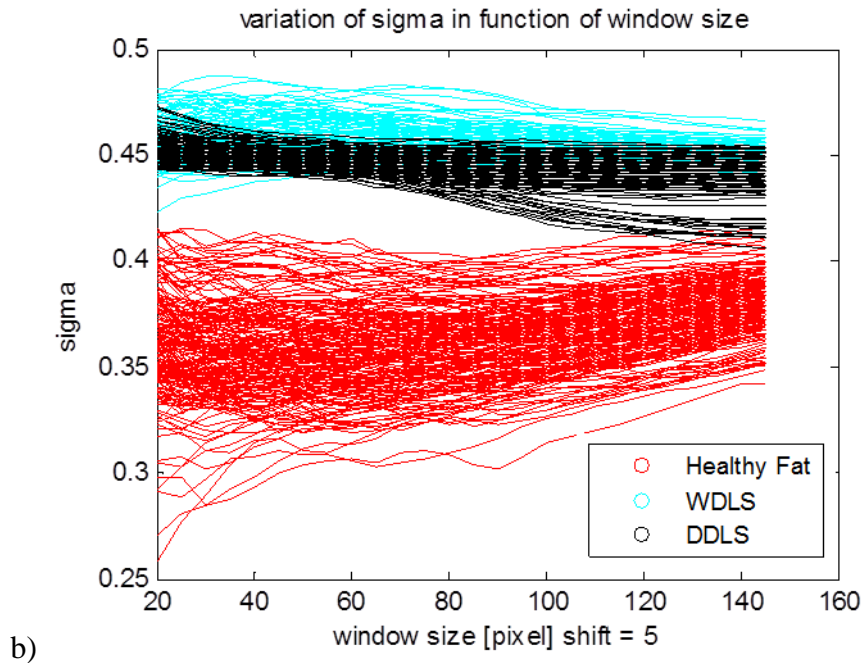
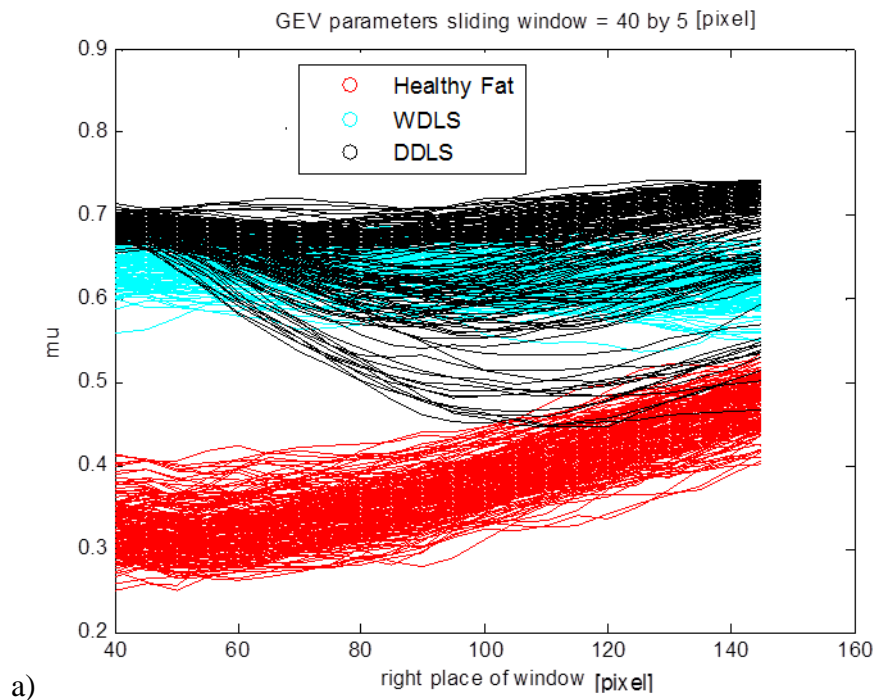
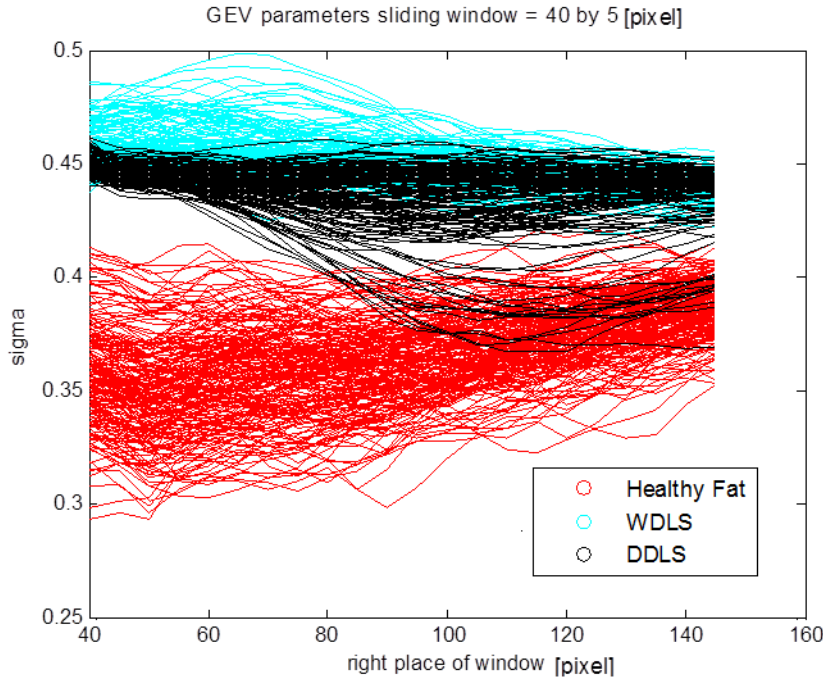


Figure III.2.39. Variation of a) μ and b) σ computed from a window size of 20 beginning from the tissue surface, and incremented by 5-pixel-shift till 150 pixel depth. 200 B-scans on Normal Fat Tissue, 160 B-scans on WDLS and DDLS.

We will accept the 40-pixel deep window size as an optimal solution. This 40-pixel-window was then shifted by 5-pixel-shift successively deeper in the tissue up to 150 pixel depth (Figure III.2.40).



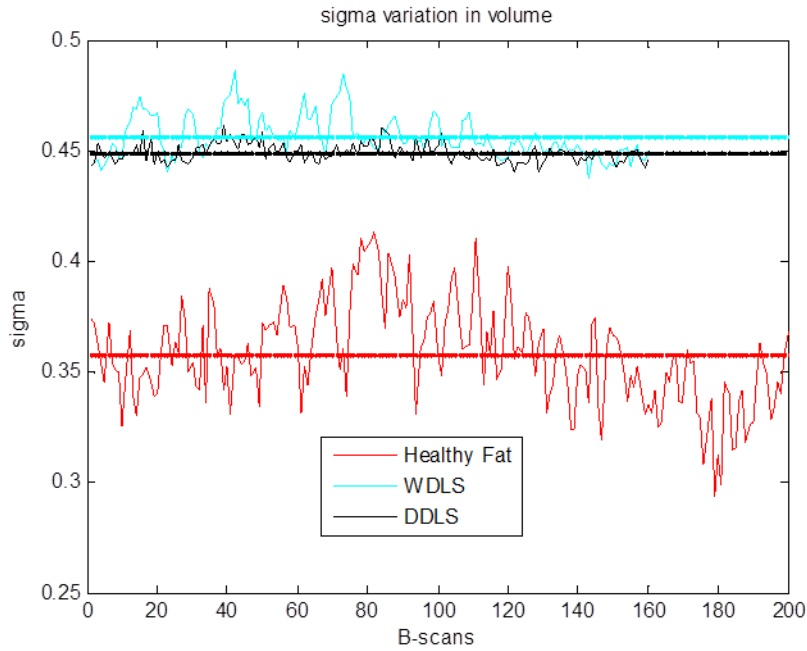


b)

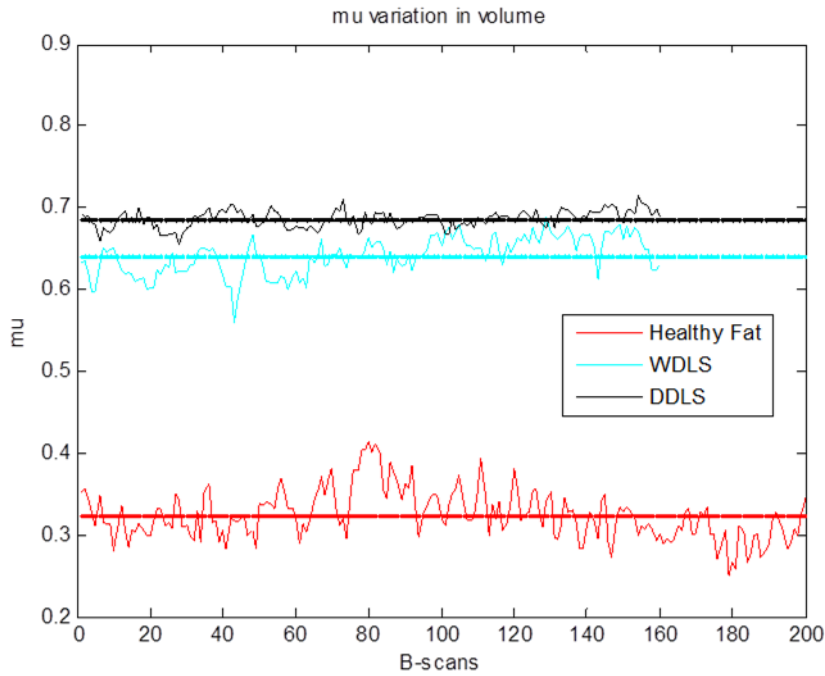
Figure III.2.40. Variation of a) μ and b) σ computed from a window size of 40 beginning from the tissue surface, shifted in depth by 5-pixel-shift till 150 pixel depth. 200 B-scans on Normal Fat Tissue, 160 B-scans on WDLS and DDLS.

After evaluation of the data in each window region at each B-scan via the parameters of the GEV distribution, a window size of 40 pixel = 0.1758 mm is chosen, beginning from the tissue surface. Our method turned out to be independent on the surface scattering effect. Smaller region can give large standard deviation on the parameters, while windowing deeper in the tissue, where backscattering hardly occurs can give erroneous results.

The 40 pixel-deep window size beginning at the surface is applied on 200 B-scans of Normal Fat Tissue and 160 B-scans of WDLS and DDLS, and the GEV parameters σ and μ were calculated and plotted on Figures III.2.41&42.



a)



b)

Figure III.2.41. GEV Distribution parameters computed from ROI on 200 B-scans for Normal Fat Tissue, 160 B-scans for WDLS and DDLS a) σ -, b) μ - variation of B-scans.

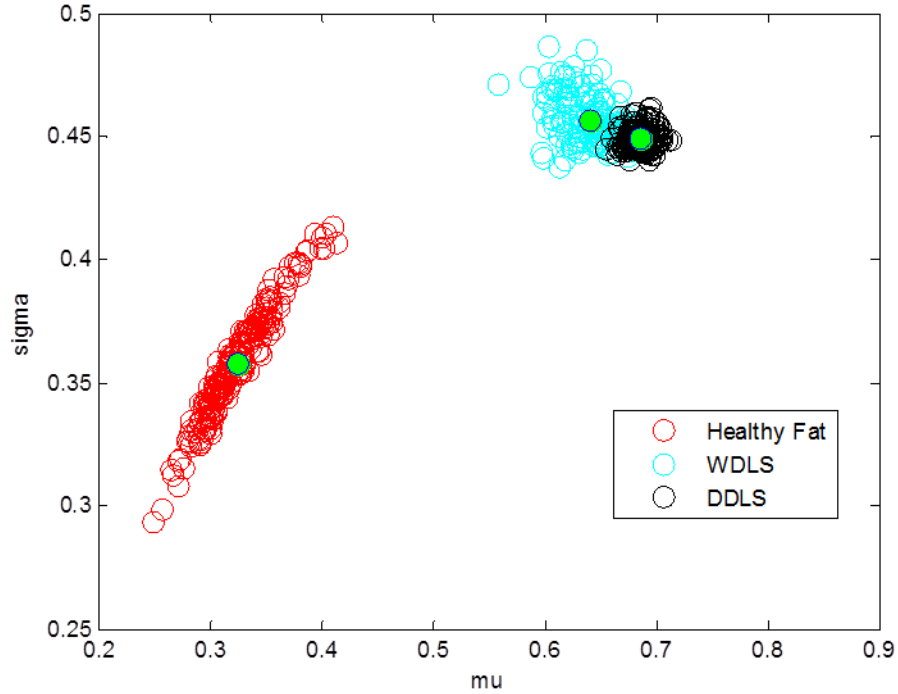


Figure III.2.42. GEV Distribution parameters on the σ - μ plane computed from ROI on 200 B-scans for Healthy Fat Tissue, 160 B-scans for WDLS and DDLS. Green point marks the Center of Gravity.

The results obtained at this Region of Interest are similar to the GEV Distribution parameters computed from the standard deviation per mean values regarding the capacity to distinguish healthy vs. cancerous tissue, and the overlapping of the Liposarcoma subtypes.

Step 8. Results of the mean normalized Intensity variation

The same procedure was applied on the mean normalized intensity values at this ROI, as to the std/mean analysis. Figure III.2.43 shows the PDFs drawn from the theoretical GEV parameters deduced from the sensitivity roll-off – corrected curves of 200 Normal Fat Tissue, 160 WDLS, and 160 DDLS B-scans (GEV parameters per B-scan in **Appendix 2**). The coefficients (k, σ, μ) are represented in Table III.2.5.

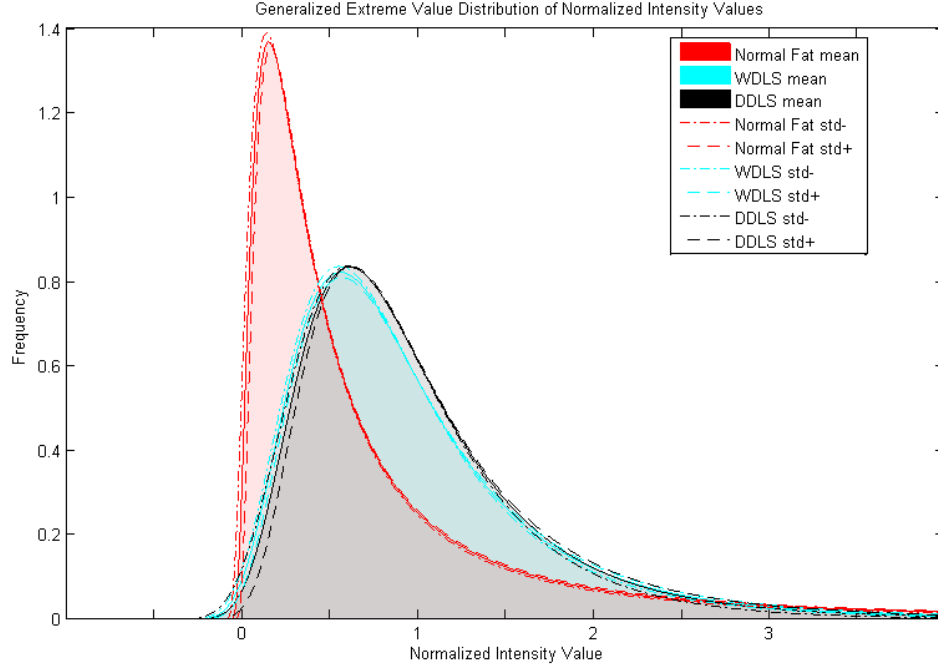


Figure III.2.43. Histogram, GEV Distribution parameters (k , σ , μ) calculated from the mean normalized intensity values in ROI. Mean and standard deviation on 200 B-scans of Normal Fat Tissue and 160 B-scans of WDLs and DDLS are analyzed.

<i>I/MEAN</i>	<i>k</i>	σ	μ
Baseline (Normal Fat)	0.8209 ± 0.0647	0.3532 ± 0.0181	0.3191 ± 0.0254
Deviation 1 (WDLs)	0.1905 ± 0.0358	0.4561 ± 0.0100	0.6381 ± 0.0229
Deviation 2 (DDLS)	0.1447 ± 0.0684	0.4462 ± 0.0044	0.6700 ± 0.0364

Table III.2.5. GEV parameters (k , σ , μ) from the mean-normalized intensity values in ROI. Mean and standard deviation calculated from 200 B-scans of Normal Fat, and 160 B-scans of WDLs and DDLS.

Similarly to the first method the PDF parameters characterize well healthy vs. cancerous tissue, furthermore the mean normalized intensity variation seems more accurate than the std/mean ratio. WDLs and DDLS coefficients are not sufficiently distinguished, and further analysis is needed. An additional parameter might provide a distinguishable feature.

We will follow the same analysis as above to represent cancer as a deviation from the healthy tissue. In Table III.2.6 b is the Baseline (Healthy) tissue parameter, d is the Deviated (cancerous) tissue parameter.

$\Sigma I/MEAN$ gc.	$\Delta k = \frac{k_d - k_b}{k_b}$	$\Delta \sigma = \frac{\sigma_d - \sigma_b}{\sigma_b}$	$\Delta \mu = \frac{\mu_d - \mu_b}{\mu_b}$
Baseline (Normal Fat)	0 ± 0.0788	0 ± 0.0512	0 ± 0.0796
Deviation 1 (WDLs)	-0.7679 [-0.8115;-0.7243]	0.2913 [0.2630;0.3196]	0.9997 [0.9279;1.0715]
Deviation 2	-0.8237	0.2633	1.0997

(DDLS)	[-0.9071;-0.7404]	[0.2508;0.2758]	[0.9856;1.2137]
--------	-------------------	-----------------	-----------------

Table III.2.6. Comparison of the GEV parameters calculated from the mean-normalized intensity values in ROI. Mean and standard deviation on 200 B-scans of Baseline Tissue and 160 B-scans of Deviation 1&2.

Figure III.2.44 shows similar results then the first method representing the coefficient differences in the 3D coordinate system separating well the healthy and cancerous tissue in each projection plane, with the overlapped WDLS and DDLS subtypes.

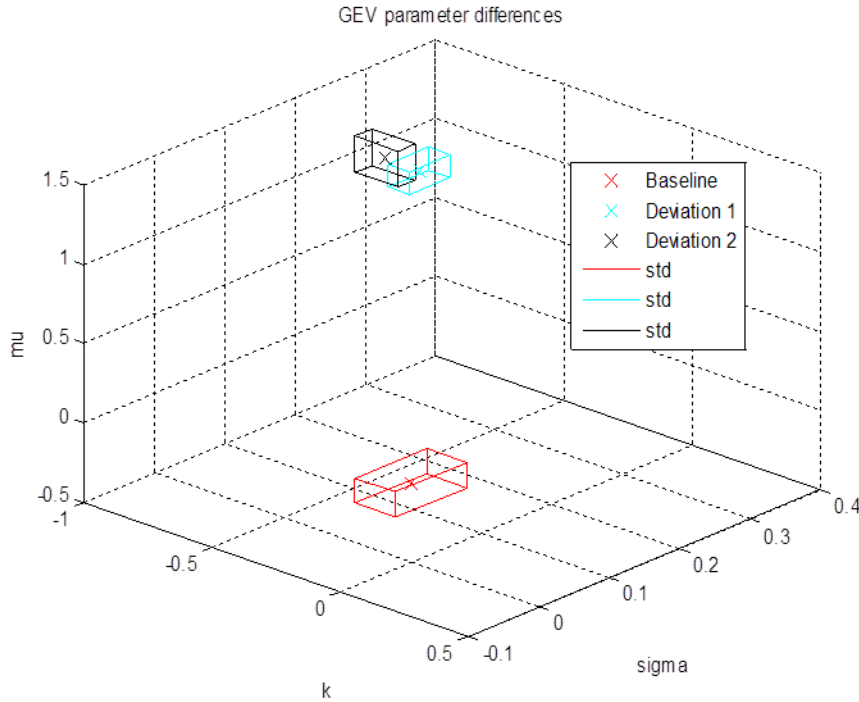
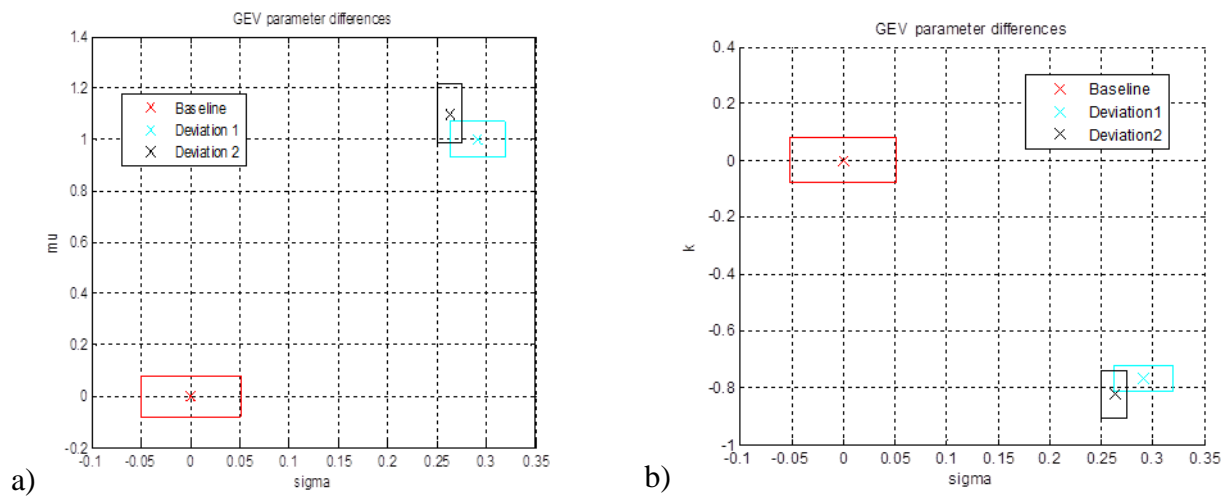


Figure III.2.44. Comparison of the GEV Distribution parameters (k , σ , μ) represented at each axe of the 3D coordinate system calculated from the mean normalized intensity values in ROI. Mean and standard deviation of 200 B-scans of Baseline Tissue and 160 B-scans of Deviation 1&2 are analyzed.

The projection planes of the 3d coordinate system are shown on Figure III.2.45.



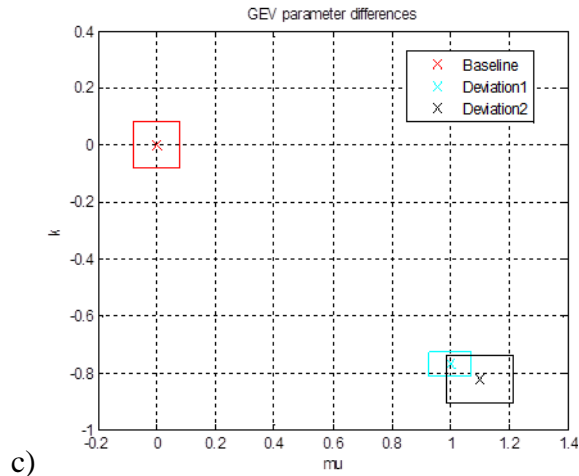


Figure III.2.45. Projection planes of the 3D coordinate system on Figure III.2.44. Comparison of the GEV Distribution parameters represented at each axe of the 3D coordinate system calculated from the mean normalized intensity values at each depth position in ROI. Mean and standard deviation of 200 B-scans of Baseline Tissue and 160 B-scans of Deviation 1&2.

Step 9. Discussion of the data analysis

We can deduce that both statistical analyses are a viable method to differentiate tissue types. The methods are independent of the measurement settings when the std/mean ratio is considered or when the intensity values are normalized by the mean at each depth position. The computation from the std/mean ratios yields larger uncertainty. This method can be more sensitive also to the way how we find the surface of the tissue since the data points from which the histogram is drawn is deduced calculating the std/mean from each depth position (40 pixels of ROI), compared to the second method where the histogram is drawn from the data points contained in all the Region of Interest (40x200 or 40x160 pixel points).

In addition the data were also corrected by the sensitivity roll-off characteristics. The usefulness of this correction is studied below. For comparison the data analysis was also applied on the images without this correction in the ROI. The same B-scan examples were chosen shown on Figure III.2.2 for Normal Fat Tissue, WDLS and DDLS. We expect bigger effect of the sensitivity roll-off by straightening an oblique or irregular tissue surface (Normal Fat Tissue, DDLS on Figure III.2.2).

The std/mean ratios are calculated on the original vs. corrected images, and compared for each tissue type on Figure III.2.46.

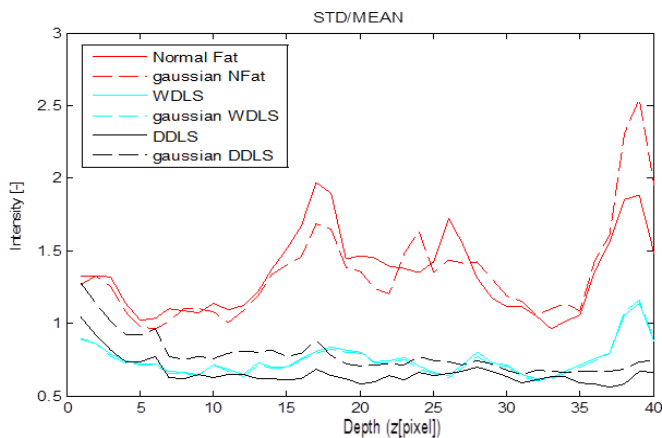


Figure III.2.46. Std/mean curves with and without sensitivity roll-off correction of Normal Fat Tissue, WDLS, DDLS on 1 B-scan shown on Figure III.2.2. Solid lines show the computation from the original image, dashed lines show the corrected version.

WDLs tissue surface is almost perpendicular to the light beam, so the sensitivity correction has no effect (cyan lines). DDLS tissue surface is steeper, and due to the dense tissue structure, the correction affects the curve characteristics (black lines). Although the Normal Fat Tissue surface also shows obliqueness, the correction effect is not significant (red lines). This can be explained with the fact that the structure is less dense and composed of big cells, where the scattering occurs only at the boundaries of the adipose cells. The effect of tissue surface obliqueness will be considered in the error analysis of the quantification method in the next chapter.

The GEV coefficients are calculated on the std/mean curves of 1 B-scan per tissue type in both cases (Table III.2.7), and the PDFs are drawn on Figure III.2.47.

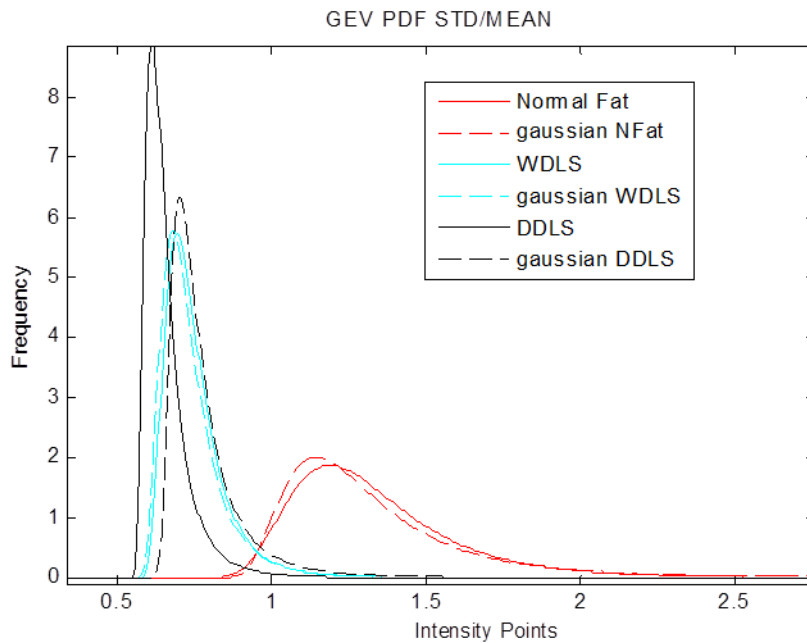


Figure III.2.47. PDF drawn from the GEV parameters of the std/mean curves shown on Figure III.2.46 with and without sensitivity roll-off correction of Normal Fat Tissue, WDLs, DDLS on 1 B-scan shown on Figure III.2.2. Solid lines show the computation from the original image, dashed lines show the corrected version.

<i>STD/MEAN</i>	<i>k</i>	σ	μ	<i>STD/MEAN_C</i>	<i>k</i>	σ	μ
<i>Baseline (Normal Fat)</i>	0.1008	0.1971	1.2067	<i>Baseline (Normal Fat)</i>	0.2422	0.1879	1.1845
<i>Deviation 1 (WDLs)</i>	0.1605	0.0649	0.7027	<i>Deviation 1 (WDLs)</i>	0.1947	0.0647	0.6906
<i>Deviation 2 (DDLS)</i>	0.2621	0.0425	0.6225	<i>Deviation 2 (DDLS)</i>	0.3463	0.0611	0.7198

Table III.2.7. GEV Distribution parameters, computed on the std/mean ratio at 1 B-scan of Normal Fat Tissue, WDLs and DDLS; left: no correction is applied (Solid line on Figure III.2.47), right: sensitivity-correction is applied (Dashed line on Figure III.2.47)

The comparison was also applied on each B-scan in the volume, and the mean, standard deviation of the parameters are shown on Figure III.2.48. and Table III.2.8. The percentage due to the differences between the original data set (*o*) (Table III.2.3) and the data corrected by the gaussian sensitivity roll-off (*gc*) (Table III.2.8) is calculated from the mean values and represented in Table III.2.9.

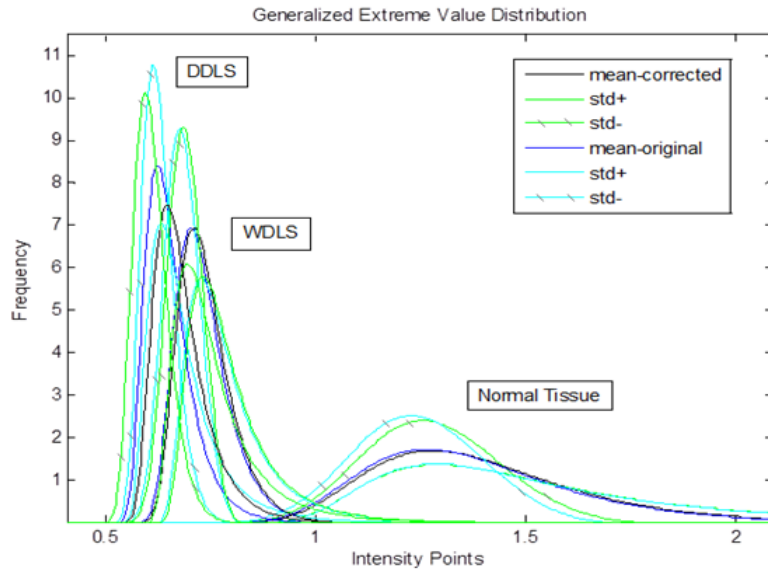


Figure III.2.48. PDF drawn from the GEV parameters of the std/mean ratio calculated from 200 Normal Fat Tissue, 160 WDLS and DDLS B-scans. Mean_±std are shown in black_±green for the sensitivity corrected images, and blue_±cyan for the original data.

<i>STD/MEAN</i>	<i>k</i>	<i>σ</i>	<i>μ</i>
Baseline (Normal Fat)	0.0001 +0.2532	0.2114 +0.0608	1.2649 +0.0799
Deviation 1 (WDLS)	-0.0070 +0.2255	0.0530 +0.0121	0.7030 +0.0370
Deviation 2 (DDLS)	0.0634 +0.1574	0.0438 +0.0095	0.6261 +0.0163

Table III.2.8. GEV parameters calculated from the std/mean ratio of the intensity values in ROI; mean and standard deviation on 200 B-scans of Normal Fat Tissue, and 160 B-scans of WDLS and DDLS are shown.

<i>STD/MEAN</i> (o/gc)	$\Delta k = \frac{k_o - k_{gc}}{k_{gc}}$	$\Delta \sigma = \frac{\sigma_o - \sigma_{gc}}{\sigma_{gc}}$	$\Delta \mu = \frac{\mu_o - \mu_{gc}}{\mu_{gc}}$
Baseline (Normal Fat)	-0.8571	-0.0172	-0.0115
Deviation 1 (WDLS)	1.5469	0.0019	-0.0089
Deviation 2 (DDLS)	-0.2602	-0.1116	-0.0371

Table III.2.9. Comparison of the mean GEV parameters calculated from the std/mean ratio of the intensity values in ROI with and without correction on 200 B-scans of Normal Fat Tissue, and 160 B-scans of WDLS and DDLS.

The table shows that the correction has significant effect on the *k* shape parameter, and also on the *σ* scale parameter in case of the dense DDLS with oblique surface.

The mean normalized intensity variation was also compared for each tissue type between the sensitivity-corrected data and the original data set. This method is less sensitive compared to the std/mean analysis explained below. First the same B-scan was studied (Figure III.2.49, Table III.2.10).

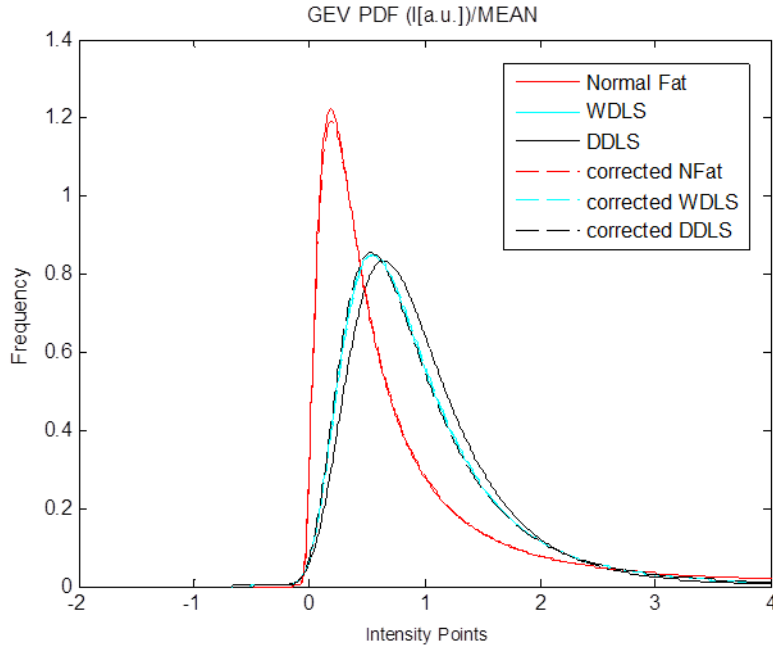


Figure III.2.49. PDF drawn from the GEV parameters of the mean normalized intensity curves with and without sensitivity roll-off correction of Normal Fat Tissue, WDLs, DDLS on 1 B-scan shown on Figure III.2.2. Solid lines show the computation from the original image, dashed lines show the corrected version.

<i>STD/MEAN</i>	<i>k</i>	<i>σ</i>	<i>μ</i>	<i>STD/MEAN</i>	<i>k</i>	<i>σ</i>	<i>μ</i>
<i>Baseline (Normal Fat)</i>	0.7253	0.3737	0.3529	<i>Baseline (Normal Fat)</i>	0.7060	0.3789	0.3597
<i>Deviation 1 (WDLs)</i>	0.2180	0.4434	0.6322	<i>Deviation 1 (WDLs)</i>	0.2068	0.4426	0.6390
<i>Deviation 2 (DDLS)</i>	0.1081	0.4433	0.6926	<i>Deviation 2 (DDLS)</i>	0.2329	0.4418	0.6251

Table III.2.10. GEV Distribution parameters computed on the mean normalized intensity values at 1 B-scan of Normal Fat Tissue, WDLs and DDLS; left: no correction is applied, right: sensitivity-correction is applied.

After 1 B-scan analysis, the results were compared on each B-scan in the same tissue samples. The mean and standard deviation of the PDFs in both cases are drawn on Figure III.2.50 and the coefficients are represented on Table III.2.11.

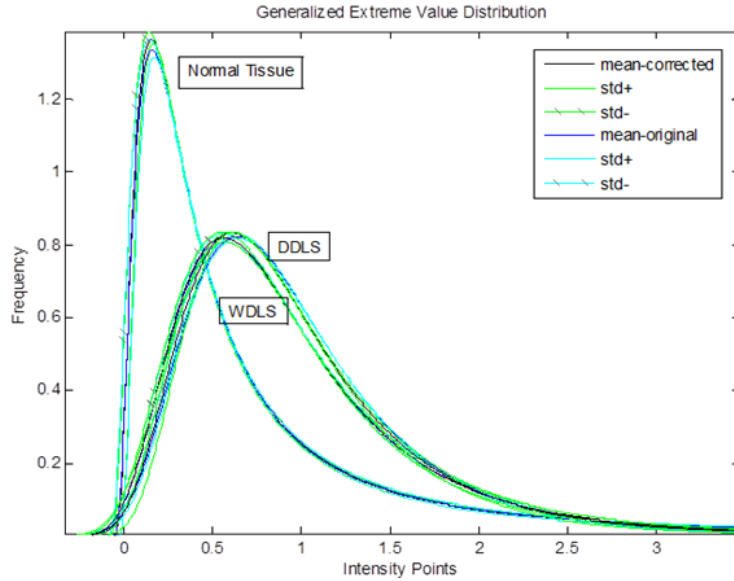


Figure III.2.50. PDF drawn from the GEV parameters of the normalized intensity values calculated from 200 Normal Fat Tissue, 160 WDLs and DDLS B-scans. Mean₊std are shown in black₊green for the sensitivity corrected images, and blue₊cyan for the original data.

<i>I/MEAN</i>	<i>k</i>	<i>σ</i>	<i>μ</i>
Baseline (Normal Fat)	0.8077 ±0.0742	0.3580 ±0.0225	0.3242 ±0.0303
Deviation 1 (WDLs)	0.1840 ±0.0360	0.4566 ±0.0094	0.6415 ±0.0228
Deviation 2 (DDLS)	0.1120 ±0.0215	0.4492 ±0.0042	0.6864 ±0.0104

Table III.2.11. GEV parameters calculated from the mean-normalized intensity values in ROI; mean and standard deviation from 200 B-scans of Normal Fat Tissue, and 160 B-scans of WDLs and DDLS.

Table III.2.12. shows the parameter differences calculated from the mean normalized intensity values, in case the correction is concerned (*gc*) (Table III.2.11) or the original data set was analyzed (*o*) (Table III.2.5). The ratios are calculated from the mean values revealing that only the shape parameter (*k*) is affected in a non-negligible way on the dense DDLS with oblique surface.

<i>I/MEAN</i> (<i>o/gc</i>)	$\Delta k = \frac{k_o - k_{gc}}{k_{gc}}$	$\Delta \sigma = \frac{\sigma_o - \sigma_{gc}}{\sigma_{gc}}$	$\Delta \mu = \frac{\mu_o - \mu_{gc}}{\mu_{gc}}$
Baseline (Normal Fat)	-0.0160	0.0136	0.0160
Deviation 1 (WDLs)	-0.0341	0.0011	0.0053
Deviation 2 (DDLS)	-0.2260	0.0067	0.0245

Table III.2.12. Comparison of the mean GEV parameters calculated from the mean-normalized intensity values in ROI with and without correction on 200 B-scans of Normal Fat Tissue, and 160 B-scans of WDLS and DDLS.

The computation from the std/mean ratios is more sensitive not only to the edge detection algorithms, but also to the sensitivity-correction. In case we want to get absolute parameters, which describe tissue types, the sensitivity correction is needed. For further analysis we accepted the computation from the mean normalized intensity values.

The method could be developed to distinguish better the different grade of cancer implementing with additional factors, e.g. the mean intensity values at each depth position. The weak point of the measurements is that setting the position of the tissue under the laser light to get a visible subsurface structure is set manually. Some saturated intensity points can also affect the statistics, which factor in the error analysis on the quantification process will be studied later. Here only the optimal ROI is considered, 40 pixel depths beginning from the surface, but applying different window size and window position also provides good differentiation. The only criterion to study is the minimum length of this window, from which region a reliable Probability Density Function can still characterize the tissue statistics.

The aim of our study is to develop a simple and rigorous analysis technique based on a parametric model that captures the structural features from the strength of scattering. We use the potential of OCT in that it is sensitive to the structural (morphological) details of the tissue. Here only one histological subtype of WDLS and DDLS is described; however they can represent several patterns. The comparison of the different histological subtypes is described in the next chapter. To study other histological types of Liposarcoma (Pleomorphic, Mytotic...), and the ability to differentiate from Normal Fat Tissue and Lipoma, benign tissue is future study.

III/3. Data Analysis applied on new measurements

III/3/a. Comparison of the Data

To verify the accuracy of the analysis, more tissue sample were analyzed to get statistically proven results. The data analysis explained above is applied on 4 samples per each tissue type recorded different time and enumerated in chronological order. The dataset of the 4 Normal Fat tissue samples cut from Abdomen/Retro-Peritoneum (A/RP) is shown on Figure III.3.1.

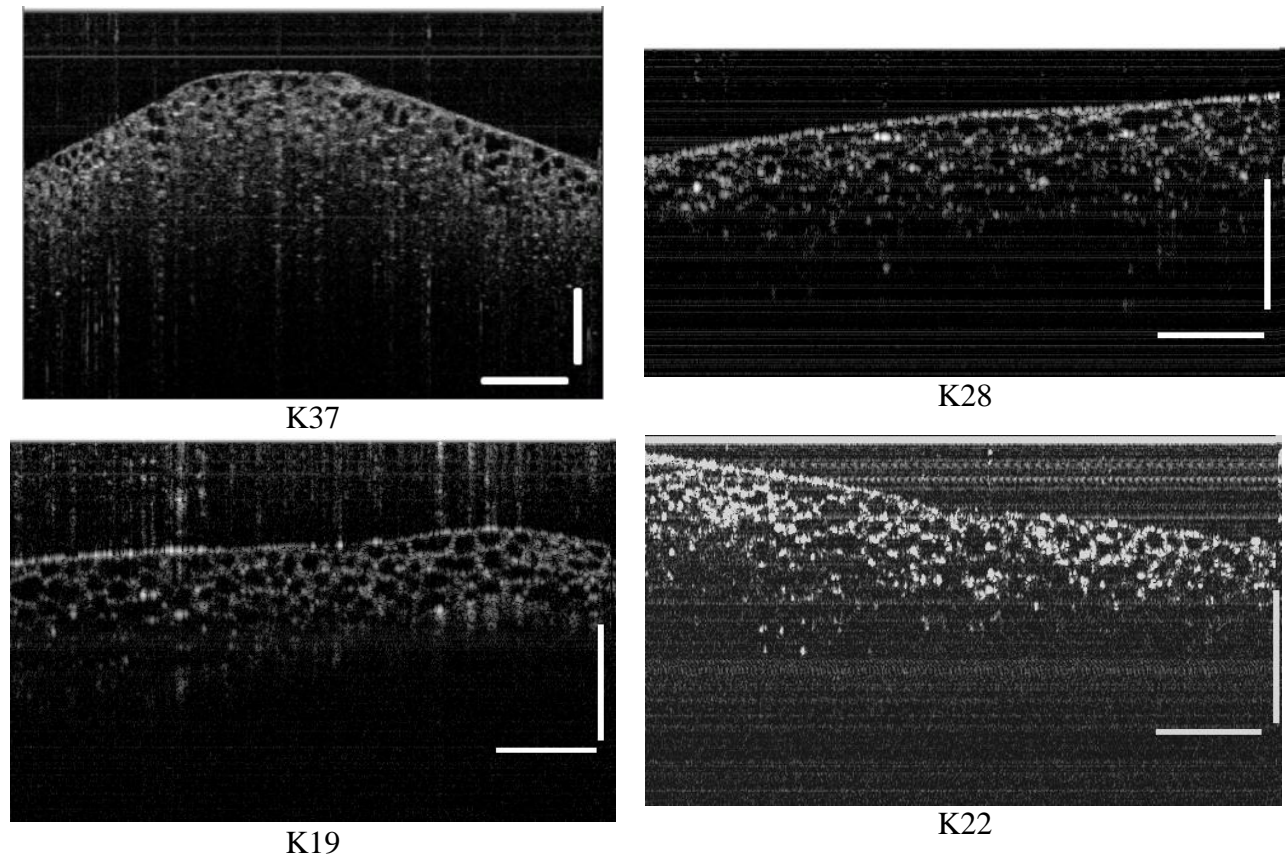


Figure III.3.1. OCT images of Normal Fat Tissue excised from Abdomen/RetroPeritoneum, white bar = 500 μ m

1 B-scan is composed of 500 A-lines and covers an area of 3 mm. 500 B-scans were also recorded to give a Surface of 3x3 mm, and the backscattered light is detected from around 1mm deep from the tissue. The typical A-line of a Normal Fat Tissue is represented on Figure III.3.2 in arbitrary unit and in dB scale.

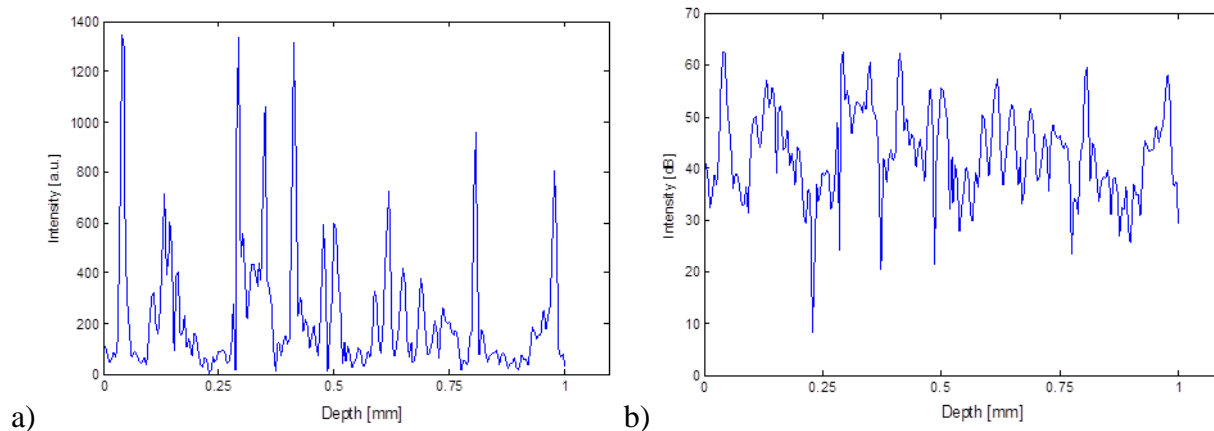


Figure II.3.2. OCT A-line of Normal Fat Tissue (K37) a) arbitrary unit b) dB scale

The H&E (Hematoxylin & Eosin) histology of Normal Fat tissue shows the correspondence with the OCT images revealing clearly the adipose cells (60-120 μm). (Figure III.3.3). The exposure time, the focus position and visibility, the pathlength difference between tissue surface and mirror is set manually independently from each measurement.

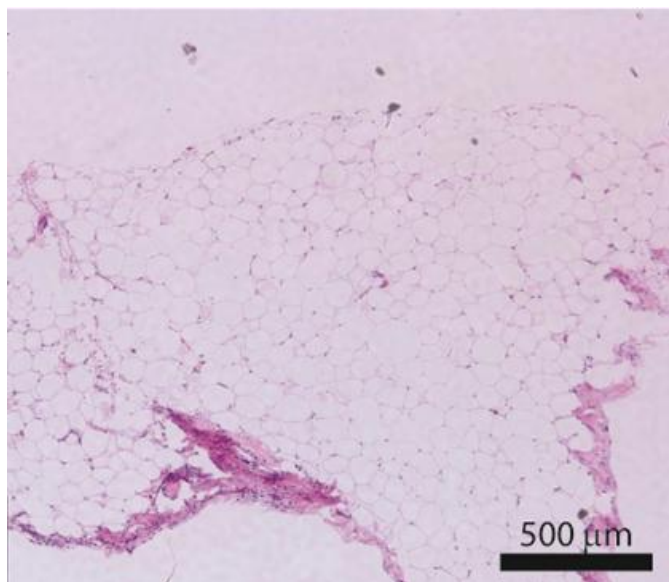


Figure III.3.3. Histology of Normal Fat Tissue from A/RP. The corresponding OCT image is K28.

The Normal Fat Tissue examples represent the same histological types. For the cancerous tissue types, the same sample number from Well-Differentiated Liposarcoma and De-Differentiated Liposarcoma were chosen. In these two cases the 4 samples were different histological subtypes of WDLS and of DDLS. The next figures show the structural OCT images with the corresponding histology at 4x Magnification. The OCT structure can be affected by artefacts.

The WDLS samples are named K36 (Figure III.3.4), K25 (Figure III.3.5), K47 (Figure III.3.6) and K58 (Figure III.3.7). K36 is WDLS with significant myxoid components analyzed above. Myxoid components are frequent in WDLS especially in A/RP, and so it resembles myxofibrosarcoma, though the scattered atypical adipocytes represent the diagnosis of Well-

Differentiated LS. Today the classification between these two Sarcoma types is clear, myxoid fibrosarcoma usually does not appear in the A/RP, and contains fine capillaries and small oval cells which distinguish from WDLS.

K25 is fibrous atypical lipomatous tumor (WDLS), with moderate cellularity. In Lipomatous Tumor the adipose cells lose their original shape and size (atypical lipoma) and the septa is thickened.

K47 is atypical lipomatous tumor (WDLS) with small mitotic changes. In contrast to the other histological subtypes, the B-scans of this measurement in the 3mm x 3mm x1mm Volume show various morphology. Depending on the B-scan some large adipose cells are still present or disappear, which will affect the computation.

K58 is Lipomatous tumor with mild cytological atypia. The tissue components are mature adipocytes with little size variation, and some slightly atypical cells scattered in the tissue. The diagnosis was not clear from the histological images. Fluorescence imaging was required to differentiate from Lipoma. The corresponding histology is made on another tissue sample (K49) with similar diagnosis to K58.

Figures III.3.4-11. show: a) OCT images with a white scale bar of 500 μm , b) Histology at 4x Magnification, except on Fig. III.3.6. at 5x Magnification (exact scale is not known) c) A-line example in arbitrary unit d) A-line example in dB scale.

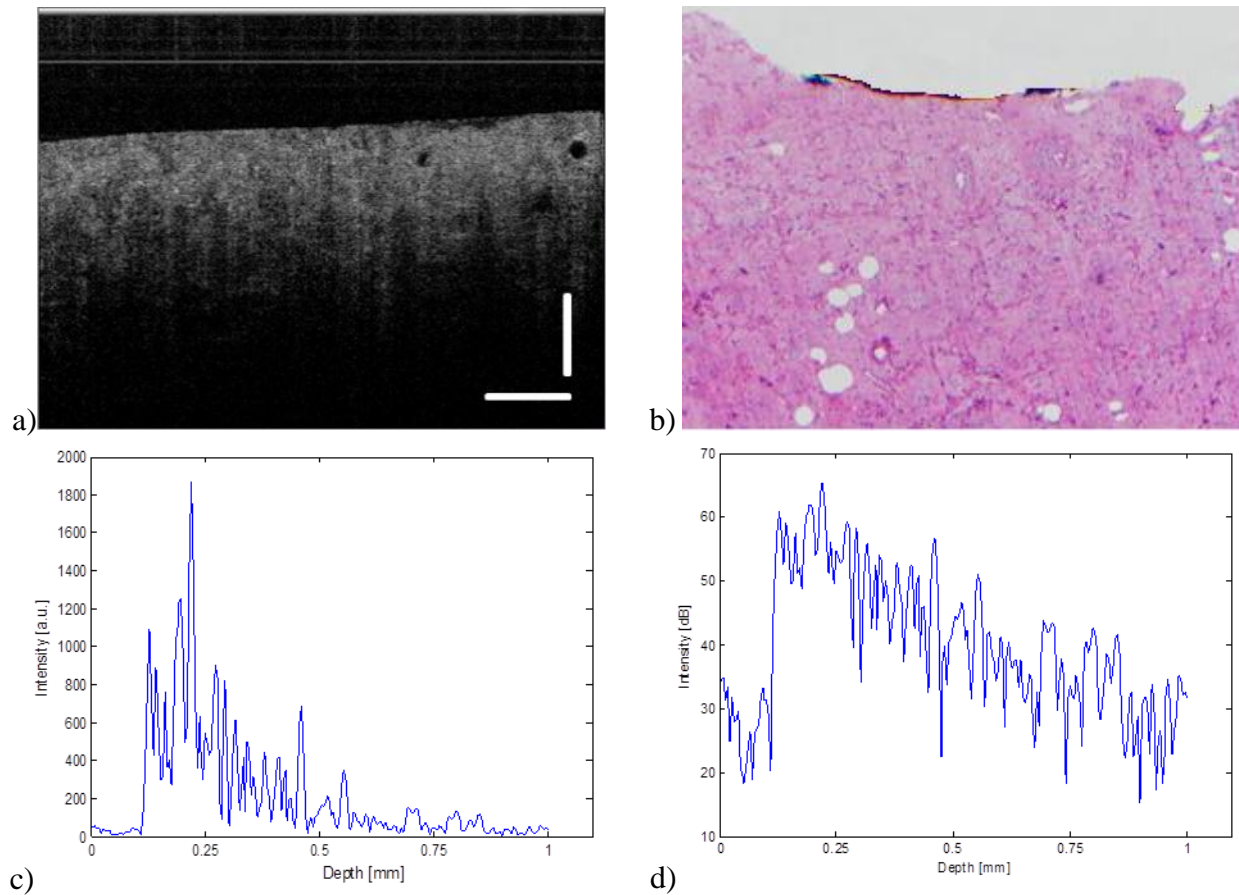


Figure III.3.4. K36 WDLS with mitotic change.

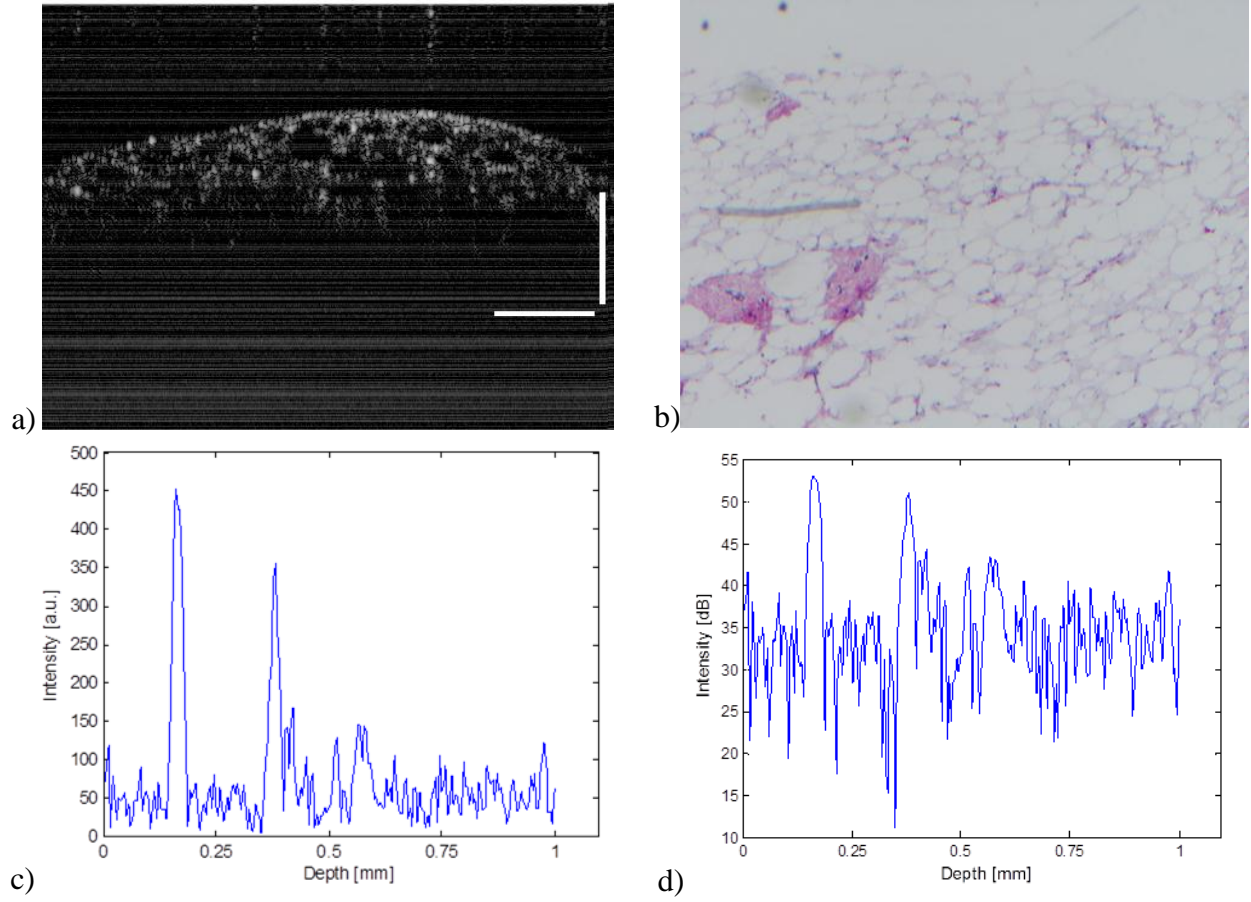
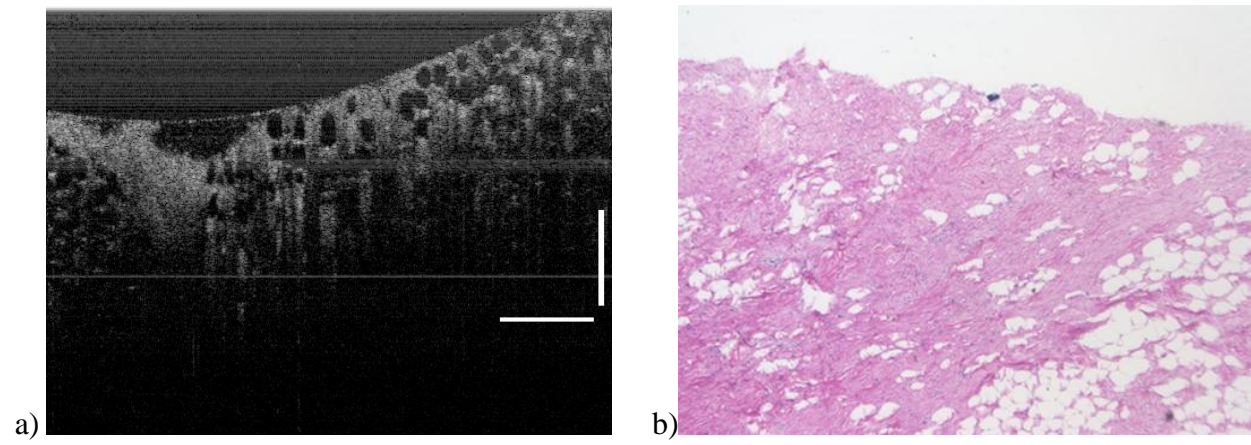


Figure III.3.5. K25 Fibrous Atypical Lipomatous Tumor.



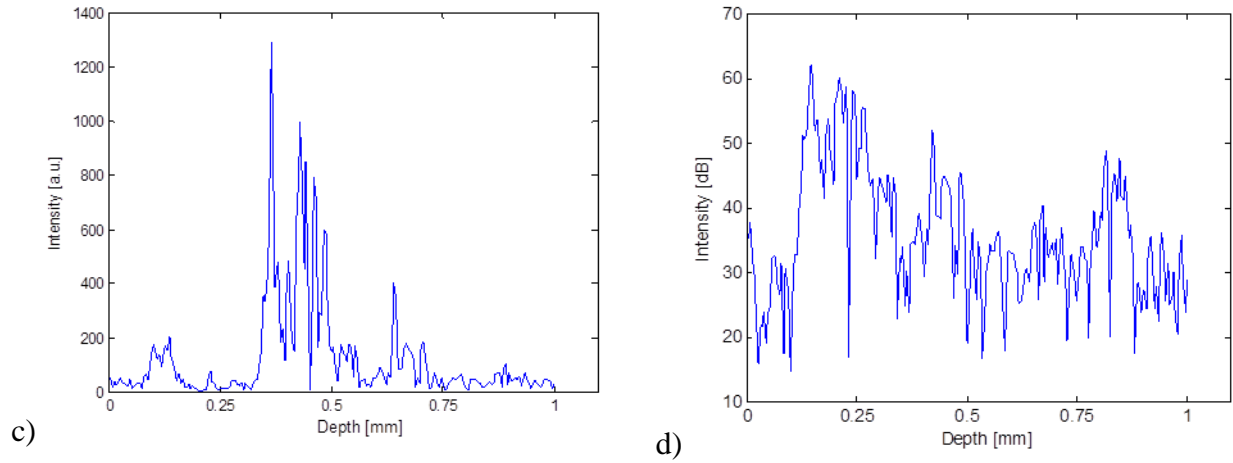


Figure III.3.6. K47 Atypical Lipomatous Tumor/ WDLs with small mitotic change.

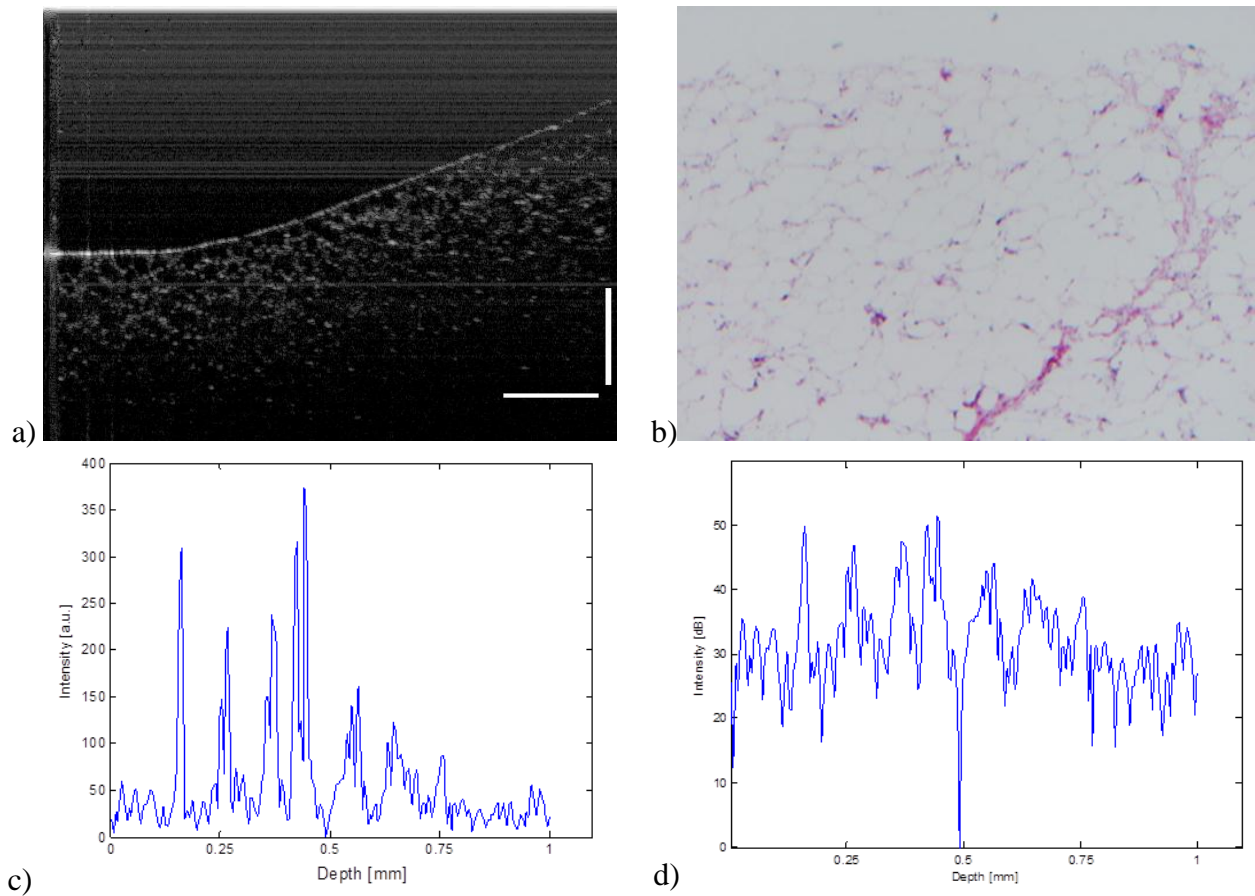


Figure III.3.7. K58 Lipomatous Tumor with mild cytological atypia.

The DDLS samples are named K35 (Figure III.3.8), K12 (Figure III.3.9), K33 (Figure III.3.10) and K26b (Figure III.3.11).

K35 is DDLS with highly fibrotic changes already represented in the data analysis. K12 is spindle cell sarcoma with osteoid and bone formation, consistent with DDLS [no bone formation is seen in this sample on the image]. K33 is DDLS with extensive myxoid change, arising in well-differentiated liposarcoma (atypical lipomatous tumor). Tumor involves mesentery adjacent to bowel wall (intestinal margins is negative). In K26b section reveals cellular pleomorphic fibromyxoid areas which contain mitotic figures focally. These findings are compatible with the diagnosis of DDLS.

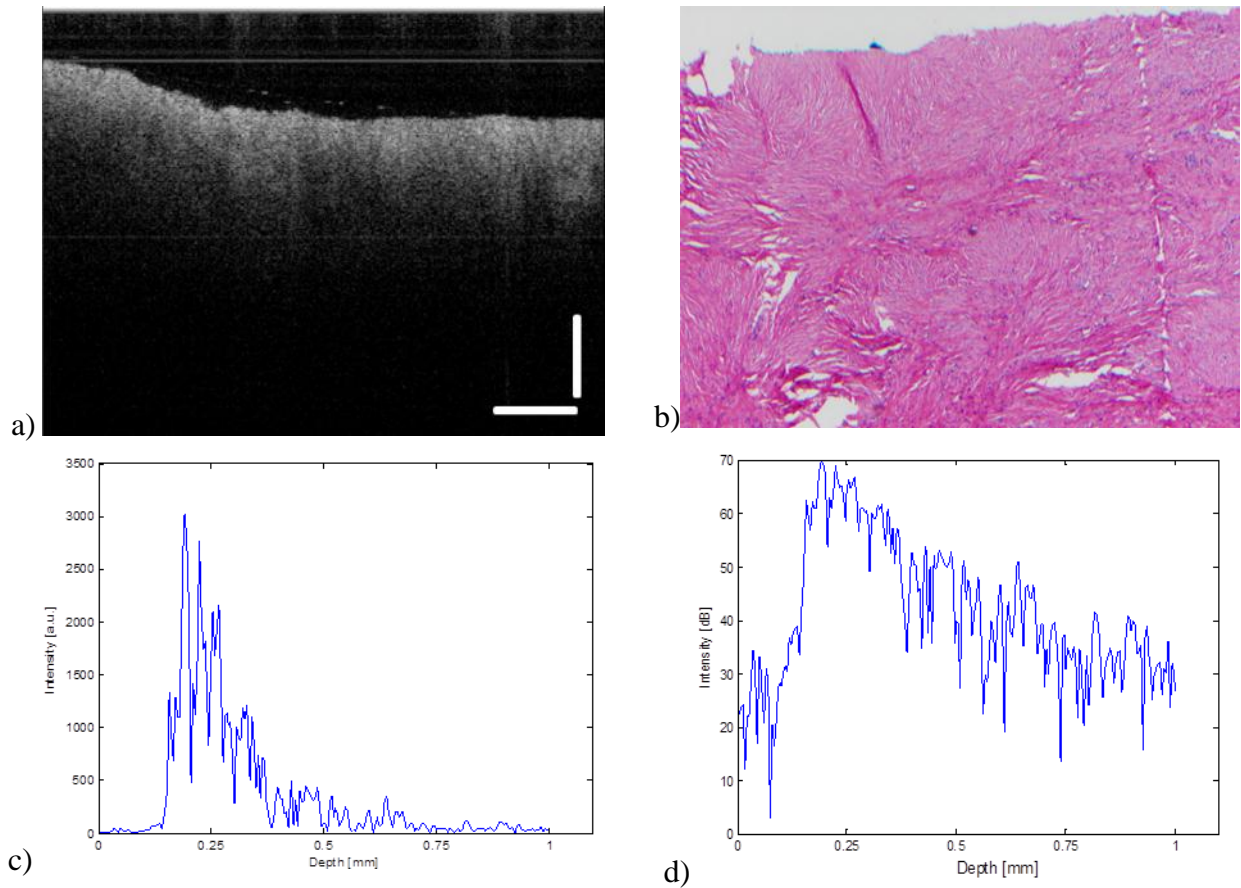
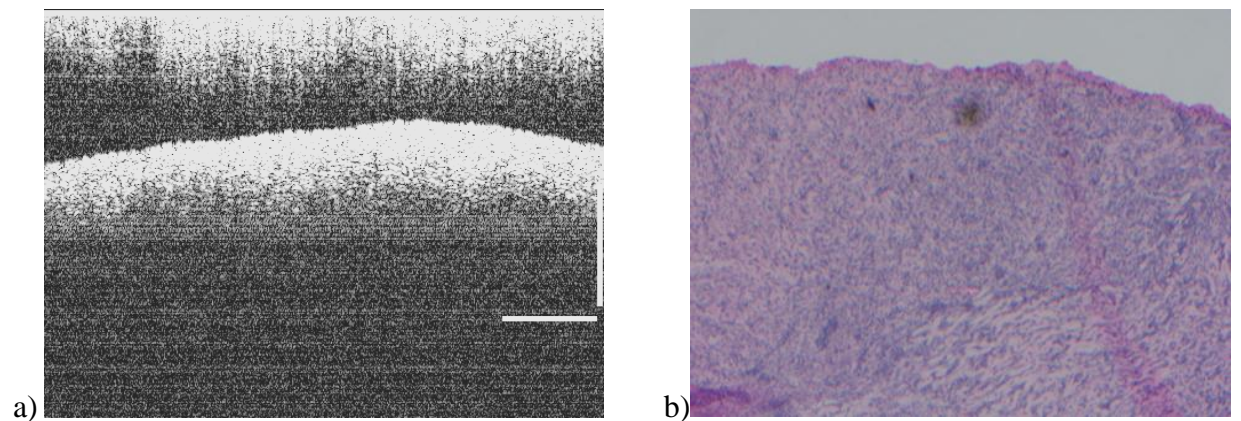


Figure III.3.8. K35 Highly fibrotic DDLS.



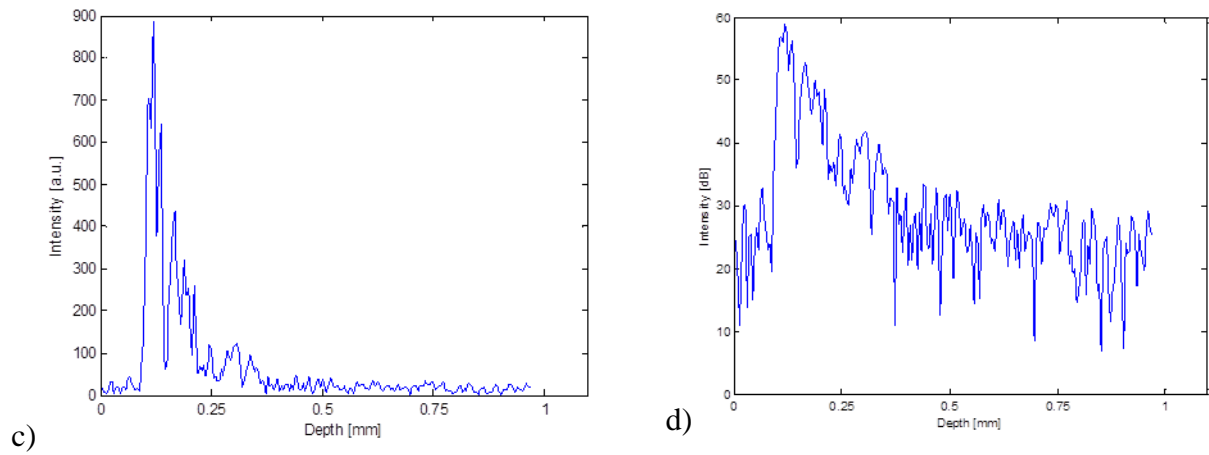


Figure III.3.9. K12 Spindle cell sarcoma (DDLs) with osteoid formation.

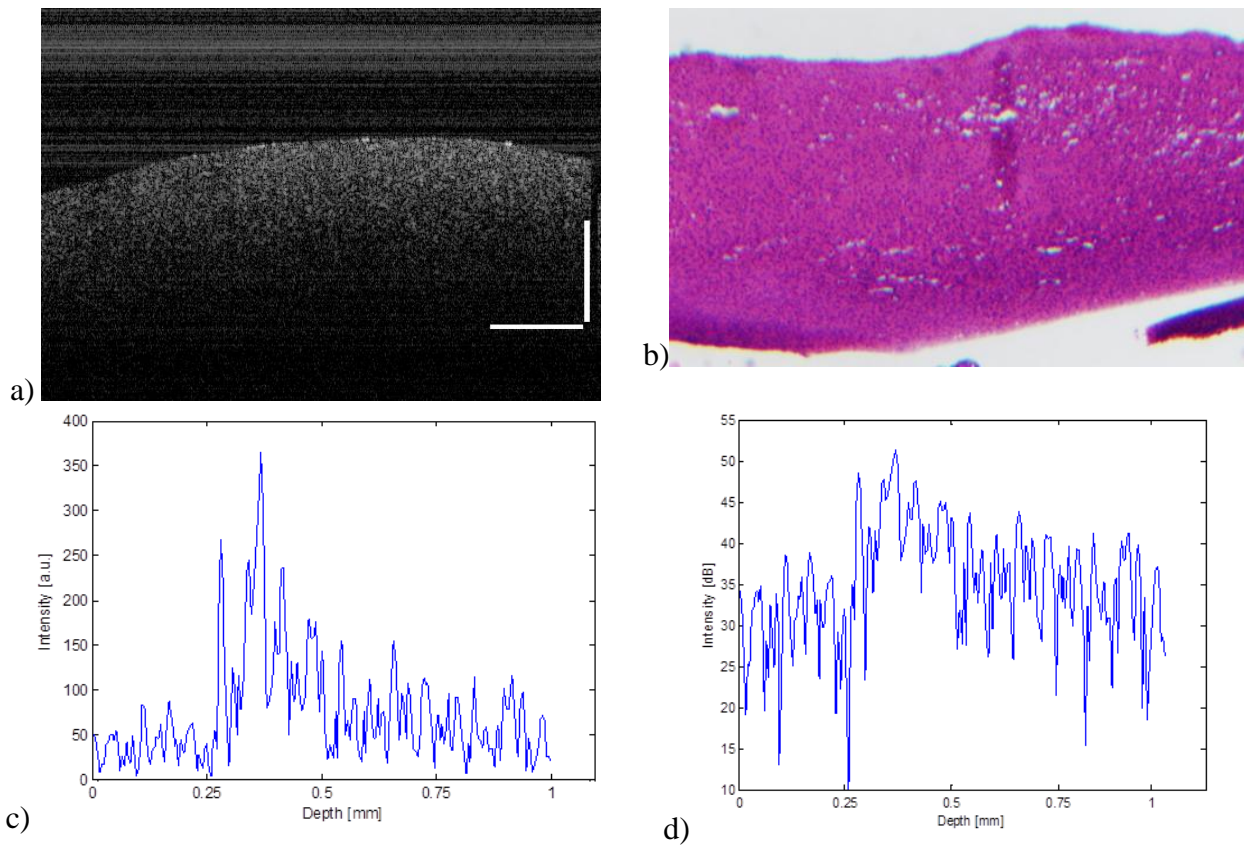


Figure III.3.10. K33 DDLs with extensive myxoid change.

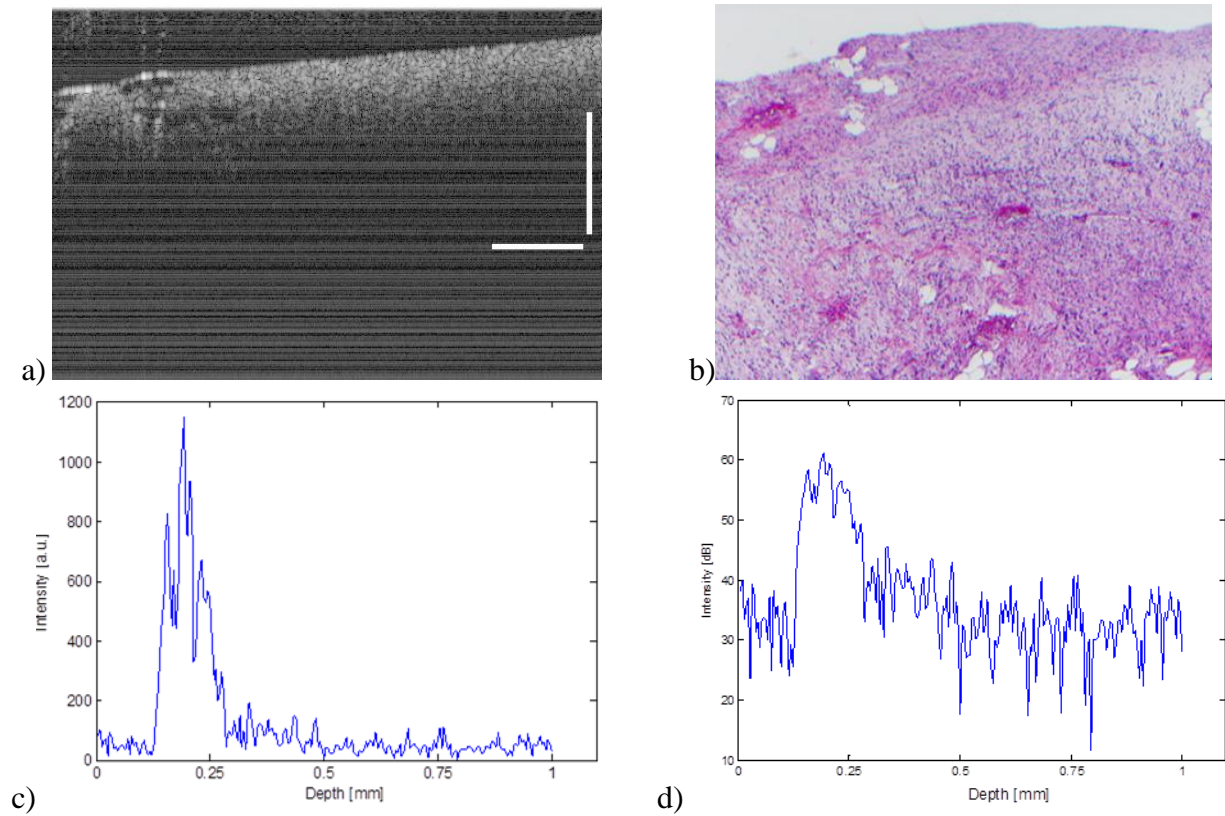


Figure III.3.11. K26b cellular pleomorphic fibromyxoid areas with mitotic figures.

60 B-scans per sample were chosen, and the mean normalized intensity values were calculated from 40 pixel deep ROI. The GEV Distribution parameters (k , σ , μ) were calculated for each B-scan, and plotted in a 3d scatterplot which axes represent the parameters (Figure III.3.12) (See Data Points in **Appendix 2**).

The data points projected on each plane are represented on Figure III.3.13 distinguishing Normal Fat Tissue, WDLS and DDLS.

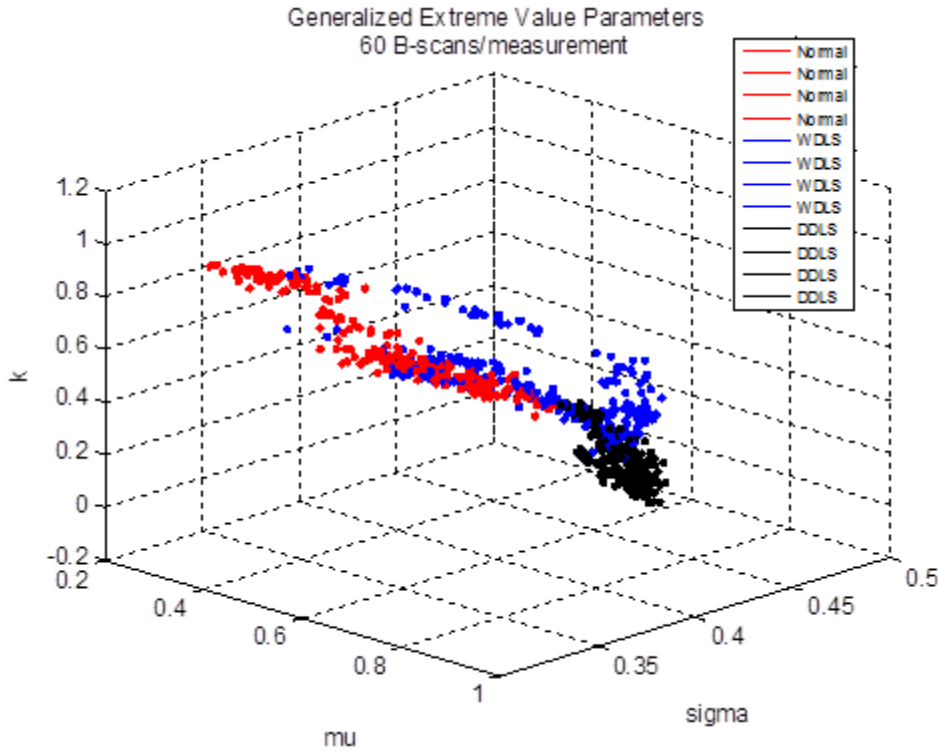
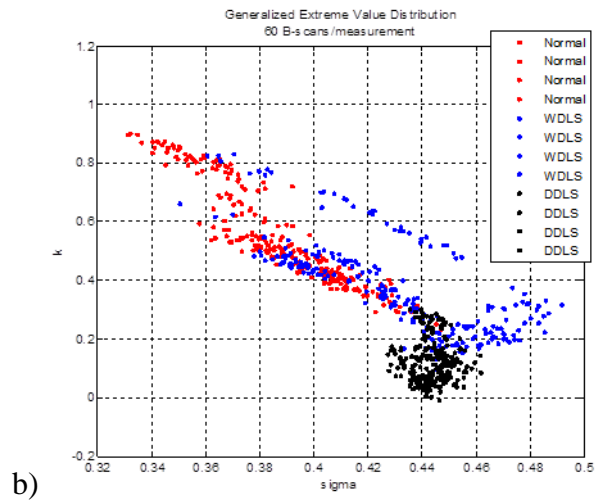
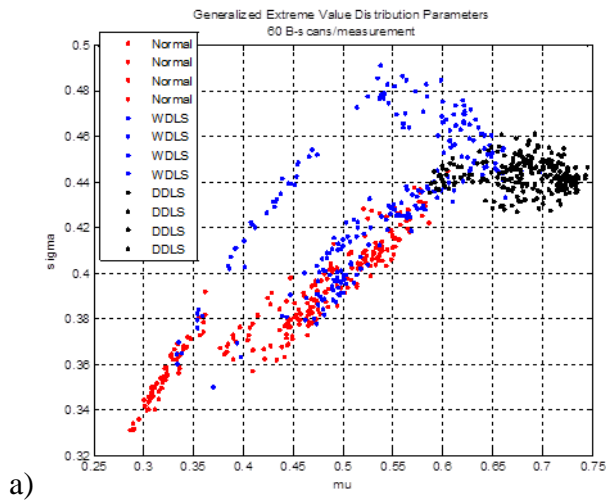


Figure III.3.12. Scatterplot classifying Normal Fat Tissue, WDLS and DDLS. 4 tissue samples per tissue type are analyzed, 60 data points per sample are considered.



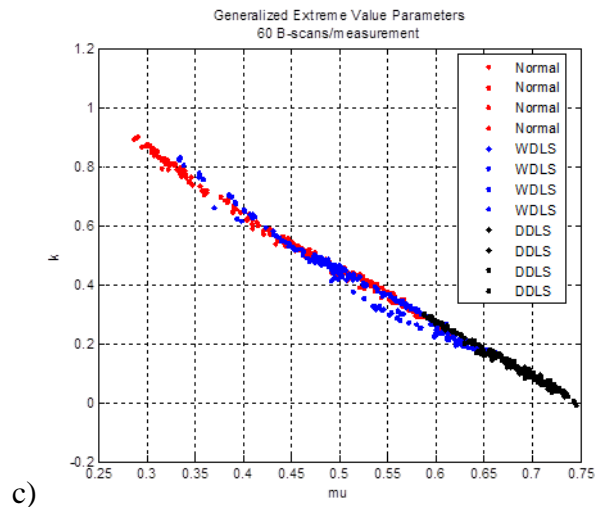


Figure III.3.13. Scatterplot classifying Normal Fat Tissue, WDLs, DDLS on the projections planes of the 3d coordinate system shown on Figure III.3.12. 4 tissue samples per tissue type are analyzed, 60 data points per sample are considered;

- a) μ - σ plane
- b) σ - k plane
- c) μ - k plane.

The classification of the three tissue types is furthermore separated to the 4 samples per tissue type, plotting the data points representing the 12 tissue samples on the k , σ , μ parameter axes in a 3d coordinate system (Figure III.3.14) and separately on the projection planes (Figure III.3.15).

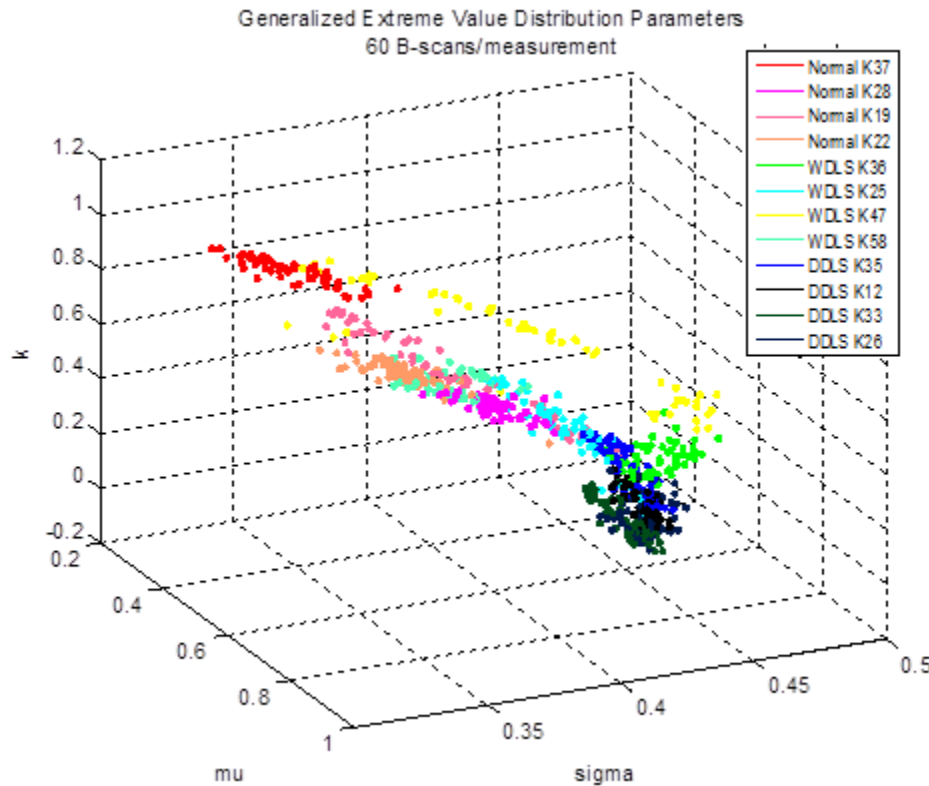


Figure III.3.14. Scatterplot representing 12 tissue samples; 4 tissue samples per Normal Fat Tissue, WDLs and DDLS are analyzed, 60 data points per sample are considered.

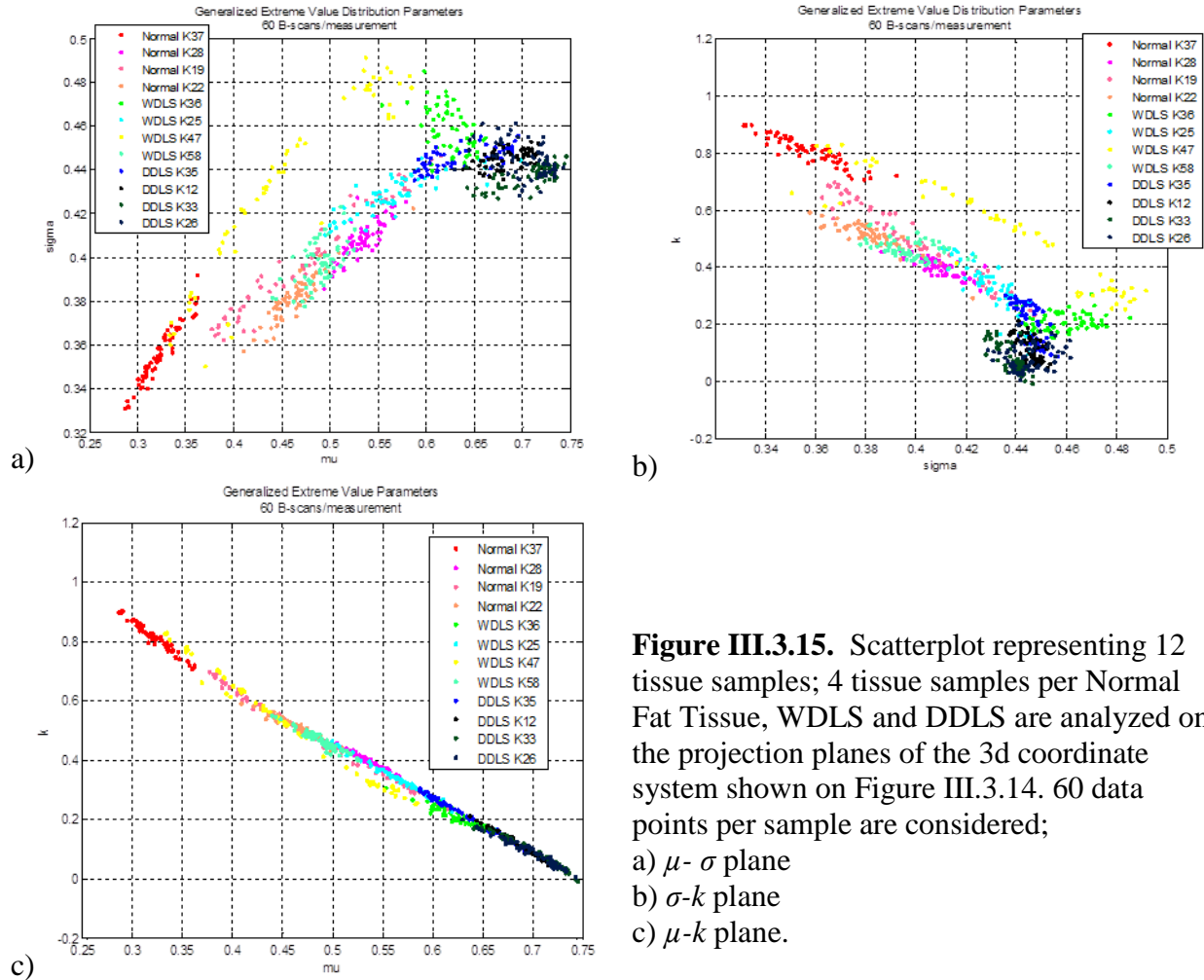


Figure III.3.15. Scatterplot representing 12 tissue samples; 4 tissue samples per Normal Fat Tissue, WDLS and DDLS are analyzed on the projection planes of the 3d coordinate system shown on Figure III.3.14. 60 data points per sample are considered;
a) μ - σ plane
b) σ - k plane
c) μ - k plane.

The quantification method will consider the mean and standard deviation of the parameters to distinguish tissue types (Table III.3.1). The Generalized Extreme Value Probability Density Function of the mean curves of each sample is drawn on Figures III.3.16&17.

The mean and standard deviation of the parameters in a 3d Coordinate System is plotted on Figures III.3.18&19 with each projection plane classifying Normal Fat Tissue, WDLS and DDLS. Figures III.3.20&21 separate all the 12 tissue samples in the 3d coordinate system projected on each plane.

<i>class</i>	<i>I/MEAN</i>	<i>k</i>	<i>std/mean</i>	σ	<i>std/mean</i>	μ	<i>std/mean</i>
<i>N O R M A L F A T</i>	<i>K37</i>	0.8209 ± 0.0647	7.88 %	0.3532 ± 0.0181	5.12 %	0.3191 ± 0.0254	7.96 %
	<i>K28</i>	0.3995 ± 0.0313	7.83 %	0.4092 ± 0.0086	2.10 %	0.5346 ± 0.0183	3.42 %
	<i>K19</i>	0.4915 ± 0.1334	27.14 %	0.3998 ± 0.0245	6.13 %	0.4768 ± 0.0694	14.56 %
	<i>K22</i>	0.5131 ± 0.0432	8.42 %	0.3817 ± 0.0108	2.83 %	0.4625 ± 0.0250	5.41 %
<i>W D L S</i>	<i>K36</i>	0.1905 ± 0.0358	18.79 %	0.4561 ± 0.0100	2.19 %	0.6381 ± 0.0229	3.59 %
	<i>K25</i>	0.3296 ± 0.0818	24.82 %	0.4295 ± 0.0090	2.10 %	0.5692 ± 0.0450	7.91 %
	<i>K47</i>	0.5256 ± 0.1792	34.09 %	0.4333 ± 0.0405	9.35 %	0.4550 ± 0.0776	17.05 %
	<i>K58</i>	0.4646 ± 0.0330	7.10 %	0.3971 ± 0.0098	2.47 %	0.4889 ± 0.0182	3.72 %
<i>D D L S</i>	<i>K35</i>	0.1447 ± 0.0684	47.27 %	0.4462 ± 0.0044	0.99 %	0.6700 ± 0.0364	5.43 %
	<i>K12</i>	0.1169 ± 0.0441	37.74 %	0.4452 ± 0.0041	0.92 %	0.6857 ± 0.0220	3.21 %
	<i>K33</i>	0.0792 ± 0.0496	62.66 %	0.4377 ± 0.0050	1.15 %	0.7064 ± 0.0282	4.00 %
	<i>K26b</i>	0.0857 ± 0.0444	51.58 %	0.4448 ± 0.0079	1.78 %	0.7006 ± 0.0262	3.74 %

Table III.3.1. Mean, standard deviation, and standard deviation per mean of Generalized Extreme Value Distribution parameters (k , σ , μ) computed from 4 samples per Normal Fat Tissue, WDLS and DDLS.

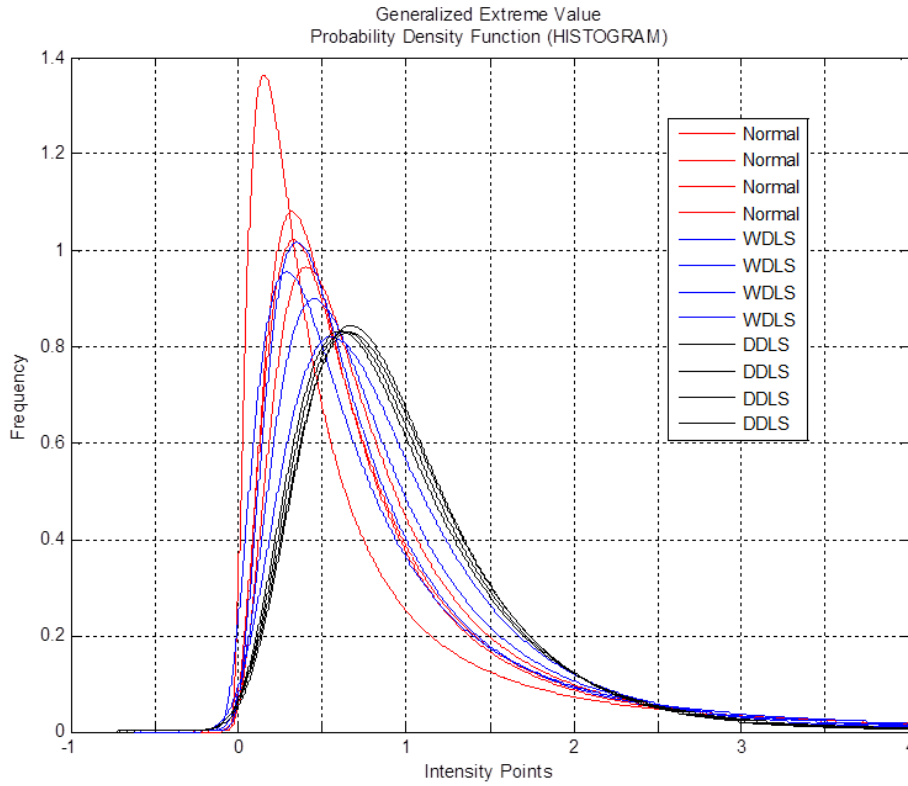


Figure III.3.16. GEV Distribution separating Normal Fat Tissue (red), WDLS (cyan) and DDLS (black); 4 samples per tissue type are presented.

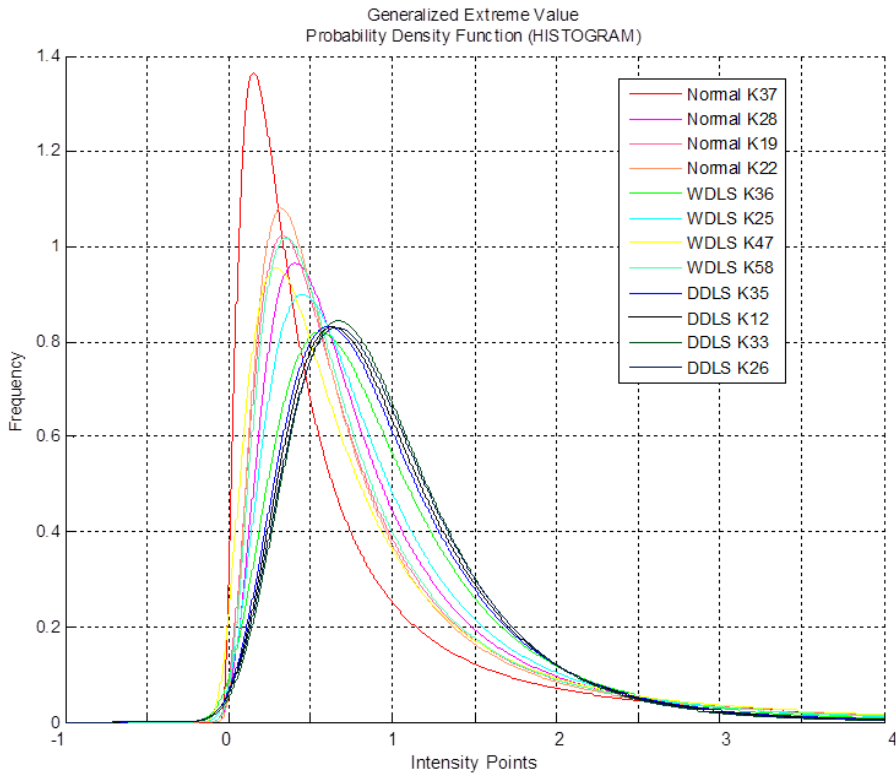


Figure III.3.17. GEV Distribution separating 12 tissue samples; 4 tissue samples per Normal Fat Tissue, WDLS and DDLS are presented.

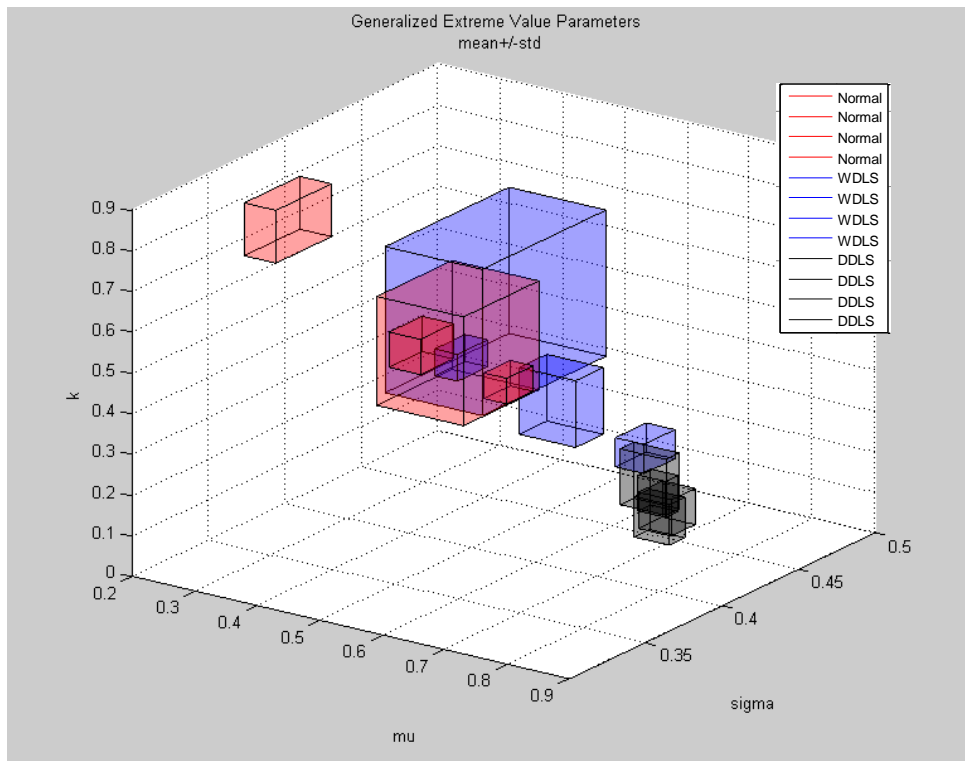


Figure III.3.18. Classification of Normal Fat Tissue, WDLs and DDLS. 4 tissue samples per tissue type are analyzed. Middle of the boxes represent the mean, the edges represent the standard deviation of the parameters k , σ , μ .

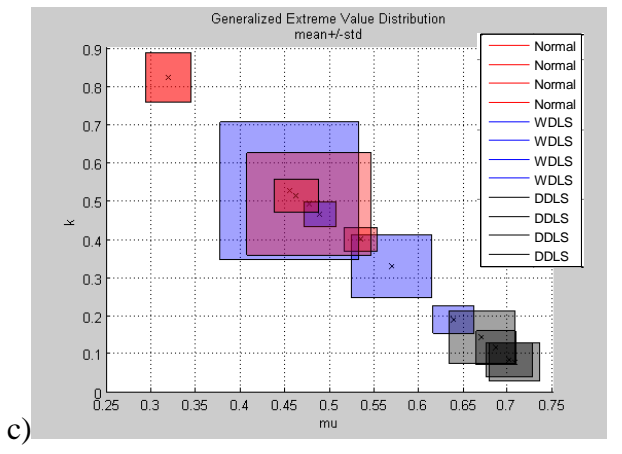
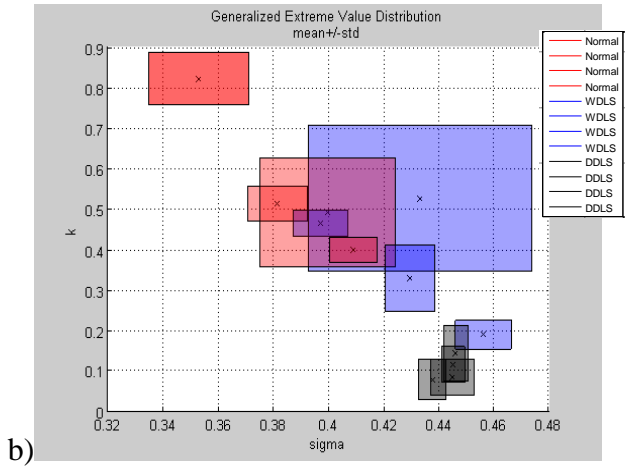
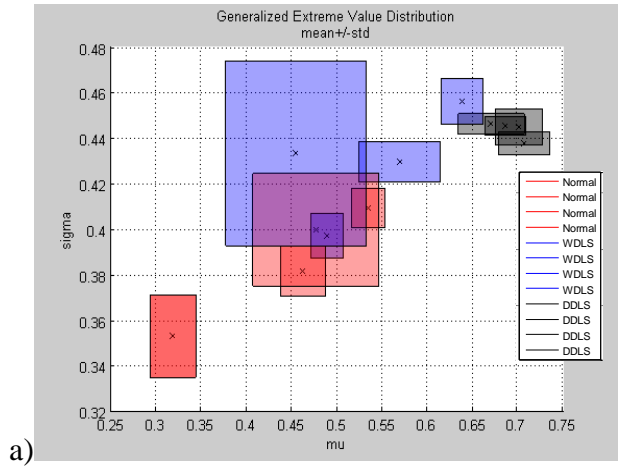


Figure III.3.19. Classification of Normal Fat Tissue, WDLs, DDLS. 4 tissue samples per tissue type are analyzed. Mean is the center, standard deviation is the edges of the boxes; a) μ - σ plane b) σ - k plane c) μ - k plane.

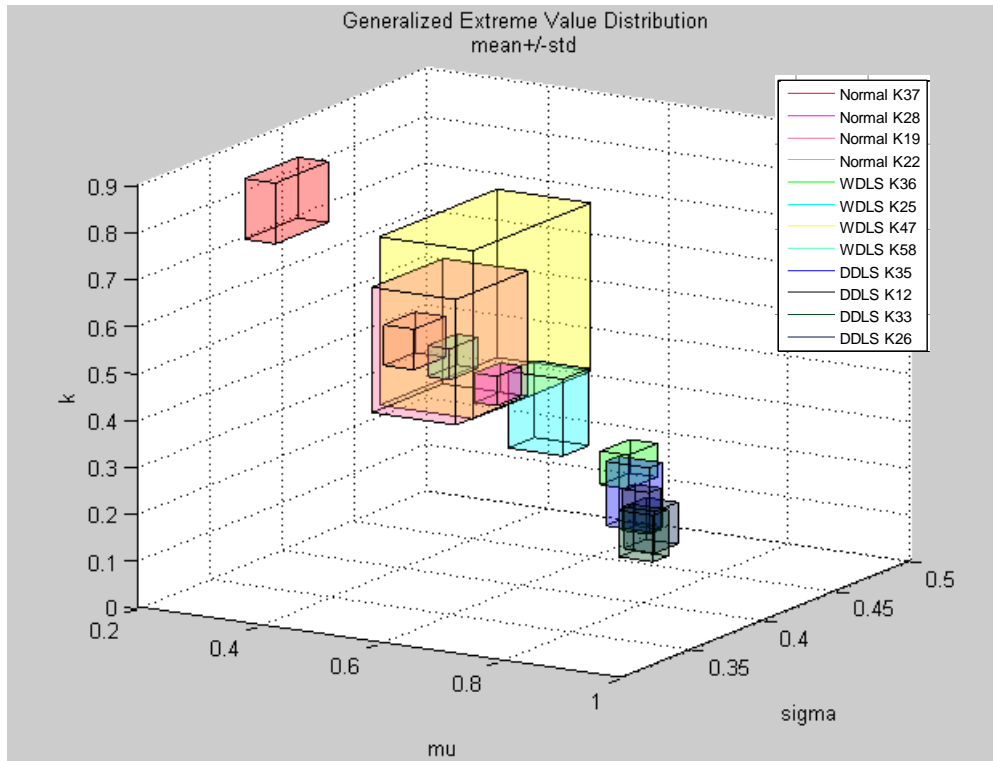
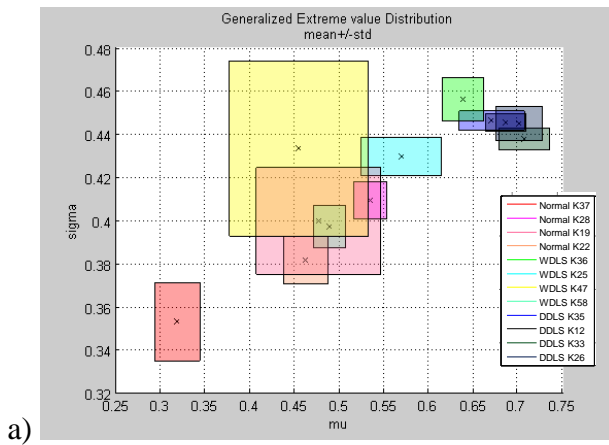
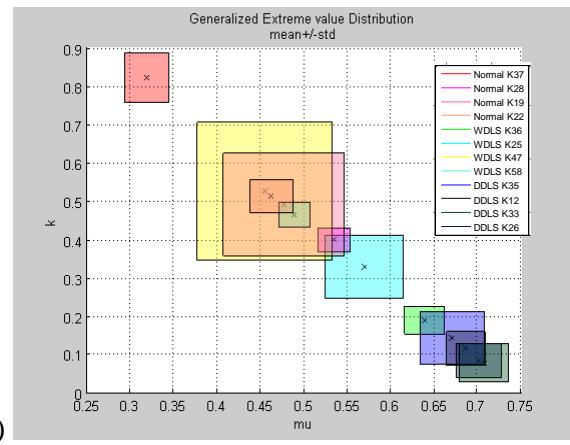


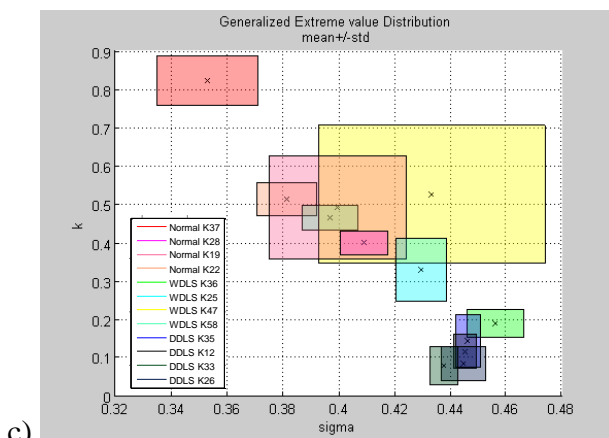
Figure III.3.20. Classification of Normal Fat Tissue, WDLs and DDLs. 4 tissue samples per tissue type are represented separately. Middle of the boxes represent the mean, the edges represent the standard deviation of the parameters k , σ , μ .



a)



b)



c)

Figure III.3.21. Classification of Normal Fat Tissue, WDLs, DDLs. 4 tissue samples per tissue type are represented separately. Mean is the center, standard deviation is the edges of the boxes.

a) μ - σ plane
b) σ - k plane
c) μ - k plane.

A clear tendency of all the three parameters (k , σ , μ) can be seen on the figures of each projection plane distinguishing Normal Fat Tissue, WDLS and DDLs.

There are more features to consider in the classification. Our aim was to differentiate Normal Fat Tissue, WDLS and DDLs. In addition the different subtypes show various pattern in case of WDLS and DDLs, and also the Normal Fat Tissue has a large scattered pattern for each parameter although the subtypes do not vary.

The DDLs subtypes, fibrotic (K35), myxoid (K33), spindle cellular (K12) and pleomorphic fibromyxoid (K26b) DDLs have closely the same parameters. Not only the parameters of the different subtypes are overlapped, but for each tissue sample, there is a little variation of the B-scans, yielding small standard deviation of each parameter. The missing adipose cells is a common feature of these DDLs subtypes, the tissue is mainly composed of smaller cells making it denser. The scattering properties detected with OCT reveal these characteristics, and our quantification method is able to confine this malignant cancer.

WDLS subtypes represent big variation in terms of all the 3 parameter range, and standard deviation per subtype. These results were expected from the histological findings and the OCT images, showing completely different morphology.

The most dense WDLS, the myxoid type (K36), tend to have similar characteristics than DDLs regarding the absolute value, and the standard deviation of the parameters.

The fibrous WDLS (K25) still contains adipose cells and is classified as Atypical Lipomatous Tumor with fibrotic changes. This feature is revealed in the parameter estimates. There is less scattering because adipose cells are present, so the parameters are shifted from the DDLs region, but it is still placed closely to the dense malignant tissue types due to the fibrous content.

K47 is also classified as Atypical Lipomatous Tumor, but with small mitotic changes, which is more or less dominant depending on the B-scans. This variation yields big standard deviation of the parameters calculated from the B-scans. σ parameter places this tissue type in the group of cancerous tissue regarding the absolute mean value and large standard deviation, however k and μ parameters do not distinguish it from healthy tissue. This corresponds to the t-test analysis explained below.

The final diagnosis of K58 as WDLS Lipomatous Tumor with mild atypia is based on molecular analysis. The structural analysis from OCT image or even from the histological staining is not evident for a non-pathologist to differentiate from Lipoma, benign tumor, or Normal Fat Tissue. The quantitative results of the structural analysis show the same results placing it to the Normal Fat Tissue region in the 3d coordinate system.

Normal Fat K28, K22 and K19 are placed in the same region; K28 and K22 with small standard deviation are well separated on each projection plane in the range of the K19 with larger standard deviation on each axis. The results on K37 are especially intriguing being farther from the Normal Fat Tissue group in each plane, and even more farther from the cancerous groups. The morphology of the tissues does not explain these differences. Each of them contains clusters of large adipose cells and fibrous connective tissue.

One reason of the differences can be the inter-patient variability, measuring different intensity pattern from patient to patient, which cannot be detected on the histological staining and OCT images. The problem can be rather the higher sensitivity of Normal Fat Tissue to our measurement technique and data analysis. However for cancerous tissue the tissue subtypes are different, the morphology supports well the parameters' mean and standard deviation values for each parameter, and there is not a scattered pattern, as in the case of Normal Fat Tissue,

especially regarding the mean parameter values of K37, and the bigger standard deviation of K19. The error analysis is explained in the next chapter.

A t-test was applied to the measurements to prove a statistically significant separation of the parameters between the tissue types at a 5% of significance level. The results show the clear distinction between Normal Fat Tissue and DDLS considering all the three parameters. Probabilities of failing diagnosing are: $P(k) = 0.29 \%$, $P(\sigma) = 0.36 \%$, $P(\mu) = 0.2 \%$. The classification between WDLS and DDLS is proved according to k and μ parameters, and sigma parameter is approved to show differences between Normal Fat Tissue and WDLS or DDLS. Probabilities of failing diagnosis between WDLS and DDLS are: $P(k) = 1.19 \%$, $P(\sigma) = 28.41 \%$, $P(\mu) = 1.08 \%$, and between WDLS and Normal Fat Tissue are: $P(k) = 18.12 \%$, $P(\sigma) = 4.73 \%$, $P(\mu) = 19.59 \%$.

III/3/b. Error analysis

The error analysis of the developed data analysis on the acquired OCT images includes the following factors: Error coming from not properly straightening the tissue surface (Figure III.3.22a), Saturation of the camera pixel-points (Figure III.3.22b), Obliqueness of the tissue surface during recording affects scattering measurements (Figure III.3.22c).

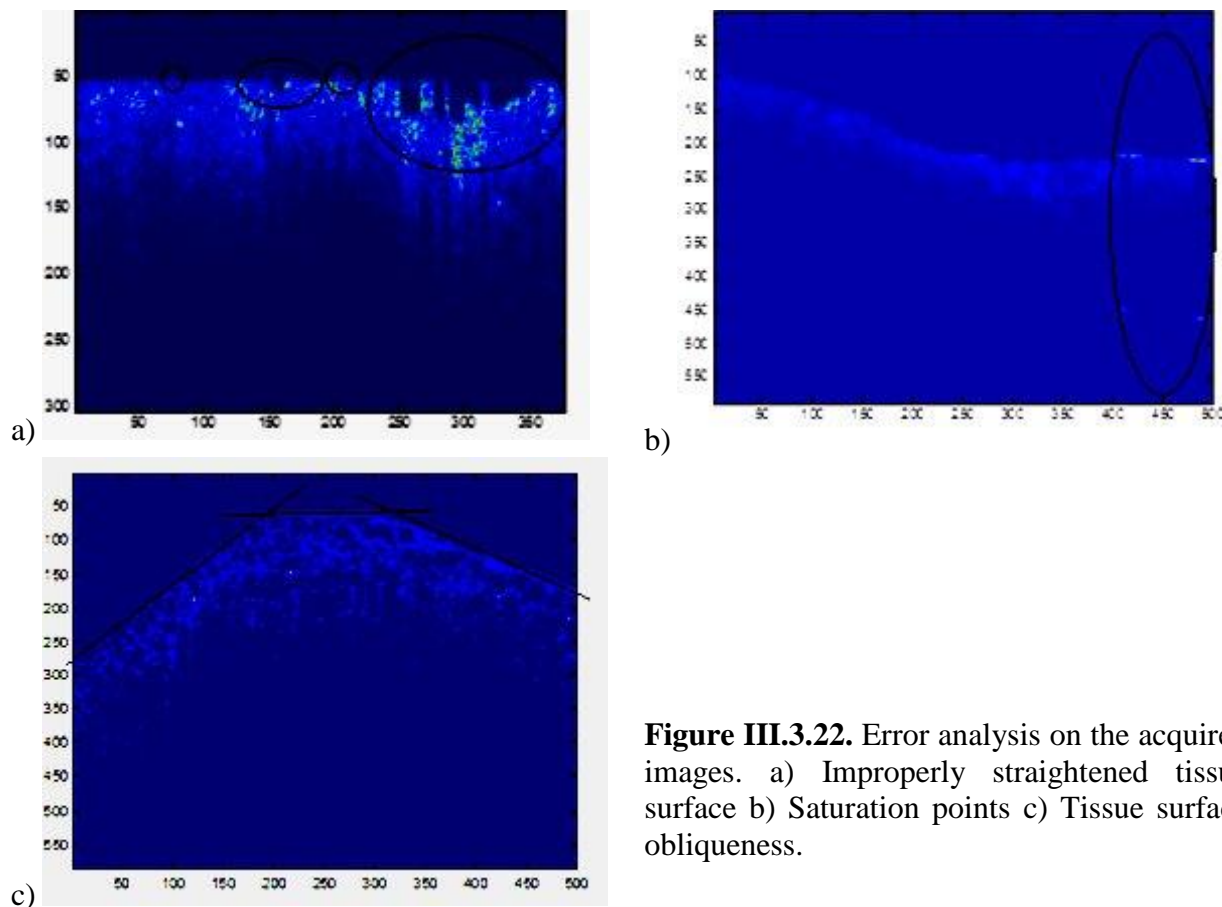


Figure III.3.22. Error analysis on the acquired images. a) Improperly straightened tissue surface b) Saturation points c) Tissue surface obliqueness.

The error analysis is applied on three B-scans per sample and shown in detail in **Appendix 3**. First the errors coming from not properly straightening the surface will be investigated. The digital straightening of the tissue surface is solved by using canny edge detector after removing the background noises with median filter. The computation was verified and corrected B-scan by B-scan, but errors can still be present.

To estimate a parameter error, the straightened surface was perturbed digitally. Each even A-line was shifted up by 10 pixel, and each odd line was shifted down, so each adjacent A-lines are shifted by 20 pixels. Three surface edge positions were applied on this perturbed image and the 40-pixel Region of Interest was considered (Figure III.3.23). First edge is at the original edge, so the tissue surface begins at the 11th pixel of each even A-line instead of the 1st one, and 10 pixel background is included in ROI for each odd A-line, so the 11th pixel-row will be the 1st pixel of the real tissue [$p0$]. Second edge is defined by the way that the original edge is shifted up by 10 pixel, so each even A-line begins at the correct surface edge, but each odd A-line includes first 20 pixel background, then the 21st pixel position will be the 1st pixel of the real surface [$p+10$]. At the third edge the original edge is shifted down by 10 pixel, so each odd A-line begins at the correct surface edge, but each even A-line begins at the 21st pixel of the real tissue, so 20-pixel deeper; the background is nowhere included in this case [$p-10$].

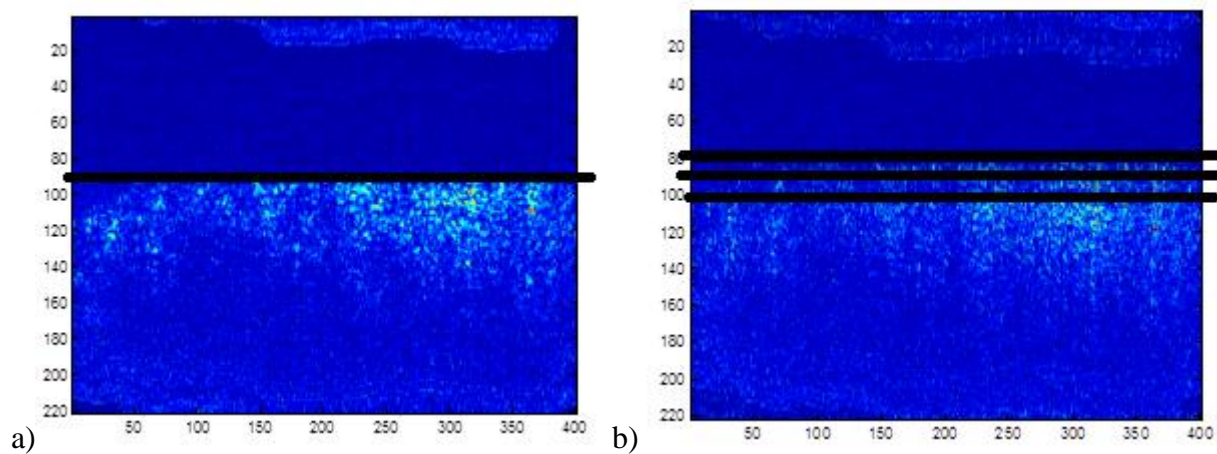


Figure III.3.23. a) Straightened Tissue Surface with marked edge b) The tissue surface edge is applied on the perturbed image at three positions.

The variation of the parameters k , σ and μ due to the wrong edges is summarized in Table III.3.2 (conclusion of **Appendix 3**).

Error of Perturbation			
μ	p-10 [pixel] = 1-11%		
	p0 [pixel] = 6-20%	except Normal Fat without K37 = 3-8%	
	p+10[pixel] = 14-38%	except Normal Fat without K37 = 3-8%	
σ	p-10 [pixel]: <10%		
	p0 [pixel]: <10%	except DDLS K35 = 16%, NFat K37 = 13%,	
	p+10[pixel]: <10%	except DDLS K35 & WDLS K58 & WDLS K47 = 12-16 % & Normal Fat K37 = 24%,	
k	DDLS	WDLS & Normal Fat K37	Normal Fat (except K37)

p-10 [pixel]:	>65%	5-26%	8-9%
p0 [pixel]:	>110%	10-80%	8-9%
p+10[pixel]:	>355%	31-170%	8-9%

Table III.3.2. Errors coming from not properly straightening the tissue surface.

The perturbation of the images gives an example how the parameters differ if the background is included in the ROI instead of the real tissue parts. Filling ROI with a ratio of 25 % by the background pixels [$p+10$] or with a ratio of 12.5 % [$p0$] can affect the parameters with a higher error ratio. In case the background is not included, but at some positions the ROI begins deeper in the tissue [$p-10$] gives also different results.

The hypothesis that the same tissue types with similar morphology should follow the same sensitivity is not true in each case. K37 Normal Fat Tissue sample usually shows different behavior considering all of the three parameters. One reason can be a different morphology which is cannot be detected at this resolution by the naked eye, but the quantitative results reveal this characteristic this way, or simply because the tissue surface has higher obliqueness during recording which affects the scattering coefficients, so this factor has a big effect on the results, especially in the case of Normal Fat Tissue. These results support the hypothesis supposed above why the absolute mean parameters of this tissue type differ from the group of the Normal Fat Tissue.

Regarding the location parameter (μ) WDLs and DDLS show similar behavior, Normal Fat Tissue is less affected except K37.

Regarding the scale parameter (σ) only the K37 shows higher sensitivity in the Normal Fat Tissue group. The error variation represents high sensitivity for K58 and K47 WDLs, which mean parameters are close to the Normal Tissue Group, since they are still composed of some large adipose cells, in addition their surface is oblique. In case of DDLS tissues, K35 is a little more affected. However it is a dense tissue, it represents a slightly steeper surface than the other DDLS subtypes, which can lead higher error sensitivity in the digital computation. To conclude the obliqueness of the tissue during recording affects the results, however it was corrected by the sensitivity roll-off curve. The reason can be the scattering process in the tissue which is dependent on the input angle of the light beam to which the sample is exposed. The error analysis of the surface obliqueness is computed below.

The shape parameter (k) changes significantly due to digital errors in surface straightening. Since the data analysis and ROI is defined on the variation of parameters μ , σ , k factor does not affect the optimization algorithm. In case the tissue is denser, and the scattering is stronger, the error on parameter k has bigger effect. The reason can be that scattering occurs only at cell boundaries, and in case the tissue type contains more adipose cells, which inner part intensity is similar to the background, the digital straightening error yields less variation. This also explains the less sensitivity of σ and μ parameters in the Normal Fat Tissue group.

Errors coming from the saturation of the pixel-points and from the tissue obliqueness during recording are shown in Table III.3.3 (conclusion of **Appendix 3**).

Pixel saturation occurs due to perpendicular light reflection. Recording certain A-lines the backreflected intensity is higher than the camera imaging range, and so all pixel-points become saturated, which can affect all the pixel-points in the A-line (Figure III.3.22b).

During data analysis the most A-lines with saturation was cut out from the image. However there were still some remaining saturated points with around less than 4 % ratio per B-

scan. The error analysis was analyzed in two ways. In the first case the saturation points were removed from the images, in the second case the same amount of saturation points was added.

On the OCT images the light intensity scattered back from the tissue volume with perpendicular surface is higher than with oblique surface. According to the obliqueness of the surface a factor was applied to enhance the intensity values on the oblique side. The calculation then was based on a stronger and weaker factor.

<i>Error of:</i>	<i>- Obliqueness</i>	<i>- Saturation</i>
μ & σ	<u>0-7%:</u> DDLS WDLS Normal Fat (except K37) <u>8-13%:</u> Normal Fat K37	<u>0-5%:</u> DDLS WDLS Normal Fat (except 37) <u>8-13%:</u> Normal Fat K37
k	<u>0-4%:</u> WDLS K36 Normal Fat except K37 <u>8-20%:</u> WDLS except K36 Normal Fat K37 <u>13-80%:</u> DDLS	<u>0-4%:</u> Normal Fat except K37 <u>4-24%:</u> WDLS NormalFat K37 <u>17-190%:</u> DDLS

Table III.3.3. Errors coming from saturation and surface obliqueness.

Each sample from tissue type shows similar characteristics considering both factors (obliqueness + saturation). We focus first on the parameters σ and μ as the significant factors in the quantification method. μ & σ follow similar behavior for obliqueness and saturation. Following our analysis by implementing some errors to the images and calculation, then to compute the outcome, neither the saturation, nor the obliqueness has significant effect in case of any tissue type. The only exception is the Normal Fat Tissue K37.

However our perturbation in saturation and intensity enhancement on the oblique surfaces does not affect significantly the parameters, there should be an effect of obliqueness, which is revealed in the sensitivity of edge detection algorithm straightening the tissue surface as explained above.

The parameter k is more sensitive to the error analysis. The densest tissue DDLS is the most sensitive, the next is WDLS, then the sensitivity of the Normal Fat Tissue is negligible. The only exception in these cases also is the K37 Normal Fat Tissue. The k factor of the obliqueness differs also in case of K36 WDLS type, probably because this tissue sample surface is almost completely perpendicular to the illuminating light.

In the case of these perturbations, the same conclusion can be deduced, that since the data analysis is based first on the variations of parameter μ - σ , the quantification method provides

accurate results. Although k factor shows high sensitivity, it was not used in the optimization algorithm to define ROI, and the results.

The data analysis can be improved in the future to avoid manual correction. The surface straightening algorithm should be more refined by filtering background and speckle noise, and provide more accurate tissue surface position. An algorithm removing saturation lines could be implemented by estimating the real intensity value of the saturated pixel from the surrounding pixels-points, or cutting out those A-lines by a thresholding algorithm. A mathematical model of the scattering process in the media could explain the effect of tissue boundary irregularity and obliqueness.

The data analysis can be broadened further to different Region of Interest, not only to the optimal one (40 pixels from tissue surface), by comparing them beginning at different position, and at different width.

The developed data analysis quantifies well the qualitative OCT images. The differences of the Generalized Extreme Value Distribution parameters (k, σ, μ) are the real feature of the tissue topological characteristics, slightly affected by digital computational errors. The accuracy of the parameters of the quantitative morphological description is at similar goodness as the qualitative OCT images. The quantitative method provides results independently from the measurement settings yielding absolute parameters to the tissue types and structural properties based on the backscattered intensity signal.

Conclusion

Presented is a model-based approach to the quantification of tissue with applications to health prognostics and diagnostics. In this approach, the mathematical models are calibrated using measured tissue information. The resulting model coefficients are used to accurately quantify the structural properties of the tissue sample. The importance of an adaptive model based approach is that the impact of measurement noise on tissue characterization is minimized during the least squares estimation process. In addition, the use of common model structure enables a more rigorous approach to accurate tissue property quantification than the existing imaging approaches. The method is independent of the sensing modality and improves the accuracy of cancer broad range of clinical and biomedical research applications.

The proposed method was applied to a dataset containing Spectral Domain Optical Coherence Tomography information obtained from images recorded on human Normal Fat Tissue vs. Well-differentiated (WD) and De-differentiated Liposarcoma (DDLs). This optical data records the response of tissue to a near infrared laser excitation revealing the subsurface morphology. The goal is to develop a mathematical model consistently capable of grading the structure of differentiate tissue types. The importance of this application centers on the accurate diagnosis at early stage of cancer, and most importantly the estimation of the tumor boundary. To date, the common image based OCT approach is incapable of consistently estimating the presences of the cancer based on tissue morphology. Thus any reliable patient diagnosis from these images is subjective and not unequivocal. Demonstrated was the filling of this need for rigorous objective method of data analysis. The outcome was the successful quantitative diagnostic method differentiating between healthy and cancerous tissue. The application of the model-based method focused images recorded on human Normal Fat Tissue vs. Well-differentiated (WD) and De-differentiated Liposarcoma (DDLs). As a demonstration, an accurate detection was found to identify and estimate healthy verses cancerous tissue.

Further applications of the method will allow detection tumor boundary, diagnose other type of cancer where structural analysis is required for diagnosis, or to monitor quantitatively tumor progression during cancer therapy. The analysis can be applied in real-time for diagnosis, and it is much simpler comparing to other quantifying method. This practical advantage gives the possibility to use in surgical evaluation. The analysis can be defined also for dynamic measurements looking the variation of structural properties in time and in space.

Bibliography

- [1] <http://www.cscn.nhs.uk/cancer-awareness/types-of-cancer.html>
- [2] N.G. Singer, A.I. Caplan, Mesenchymal stem cells: Mechanisms of inflammation, *Annual Review of Pathology*, 2011, 6:457–478.
- [3] J. Klijanienko, R. Lagacé, *Soft tissue tumors: a multidisciplinary, decisional, diagnostic approach*, 2011, John Wiley & sons, Inc., Hoboken, NJ, USA.
- [4] P.C.W. Hogendoorn, F. Collin, S. Daugaard, A.P. Dei Tos, C. Fisher, U. Schneider, R. Sciot, and Eortc, Changing concepts in the pathological basis of soft tissue and bone sarcoma treatment, *European Journal of Cancer*, 40(11), 1644–1654 (2004).
- [5] P.C.W. Hogendoorn, Pathology of soft tissue sarcomas with emphasis on molecular diagnostic techniques, *European Journal of Cancer*, 2003, S205–S210.
- [6] K. Thway, Pathology of soft tissue sarcoma, *Clinical Oncology (Royal College of Radiologists)*, 2009 Nov., 21(9), 695-705.
- [7] S. Ostlere, R. Graham, Imaging of soft tissue masses, *Imaging*, 2005, 17(3): 268-284.
- [8] M.J. Kransdorf, M.D. Murphey, *Imaging of soft tissue tumors*, 1997 by W.B. Saunders Company, Philadelphia, PA, USA.
- [9] M. Åkerman, H.A. Domanski, A. Rydholm, B. Carlén, *The Cytology of Soft Tissue Tumours*, 2003 by S. Karger AG, Basel, Switzerland.
- [10] M. Kind, N. Stock, J.M. Coindre, Histology and imaging of soft tissue sarcomas, *European Journal of Radiology*, 72 (2009) 6-15.
- [11] M.M Miettinen, *Modern soft tissue pathology; Tumors and Non-Neoplastic Conditions*, 2010, Cambridge University Press.
- [12] A. Rembielak, M. Green, A. Saleem, P. Price, Diagnostic and therapeutic imaging in oncology, *Medicine* 39 (12), 693-697, 2011.
- [13] P. Morris, A. Perkins, Diagnostic imaging, *Lancet*, 2012 Apr. 21, 379 (9825), 1525-33.
- [14] S. Singer, C.R. Antonescu, E. Riedel, and M.F. Brennan, Histologic subtype and margin of resection predict pattern of recurrence and survival for retroperitoneal liposarcoma, *Annals of Surgery*, 238(3), 358–370 (2003).
- [15] A.P.D. Tos, Liposarcoma: New Entities and Evolving Concepts, Review Article, *Annals of Diagnostic Pathology*, Vol 4, No 4 (August), 2000, 252-266.
- [16] A.N. Khan, M. Chandramohan, S. MacDonald, F.O. Alkubaidan, Liposarcoma Imaging. *eMedicine from WebMD, LLC* May 27, 2011.
- [17] W.D. Craig, J.C. Fanburg-Smith, L.R. Henry, R. Guerrero, J. H. Barton, Fat-containing Lesions of the Retroperitoneum: Radiologic-Pathologic Correlation, *RadioGraphics*, 2009; 29:261–290.
- [18] C.D.M. Fletcher M. Sundaram, A. Rydholm J.M. Coindre, S. Singer, *World Health Organization Classification of Soft Tissue Tumours, Soft tissue tumours: Epidemiology, clinical features, histopathological typing and grading*, International Agency for Research and Cancer Press, Lyon, 2006.
- [19] H. Brisse, D. Orbach, J. Klijanienko, J. Fréneaux, S. Neuenschwander, Imaging and diagnostic strategy of soft tissue tumors in children, *European Radiology*, 2006, 16:1147-64.
- [20] JF Lois, HJ Fischer, LS Deutsch, EC Stambuk, AS Gomes, Angiography in soft tissue sarcomas, *Cardiovascular and Interventional Radiology*, 1984, 7(6):309-16.

- [21] B. Andreoni, A. Chiappa, U. Pace, E. Bertani, F. Verweij, F. Orsi, G. Petralia, M. Tullii, M. Venturino, G. Pelosi, Surgical 'damage control' treatment of a large retroperitoneal liposarcoma encasing a horseshoe kidney, *Ecancermedicalscience*, 2008, 2:77.
- [22] J.F. Lois, H.J. Fischer, L-S. Deutsch, E.C. Stambuk, A.S. Gomes, Angiography in Soft Tissue Sarcomas, *Cardiovascular and Interventional Radiology*, 1984, 7(6):309-316.
- [23] W-C. Kuo, J. Kim, N.D. Shemonski, E.J. Chaney, D.R. Spillman, Jr., and S.A. Boppart, Real-time three-dimensional optical coherence tomography image-guided core-needle biopsy system, *Biomedical Optics Express*, 1 June 2012, Vol.3, No.6.
- [24] E.F. Carbajal, S.A. Baranov, V.G.R. Manne, E.D. Young, A.J.Lazar, D.C. Lev, R.E. Pollock, K.V. Larin, Revealing retroperitoneal liposarcoma morphology using optical coherence tomography, *Journal of Biomedical Optics*, 16(2). 2011.
- [25] G. Lahat, J. E. Madewell, D. A. Anaya, W. Qiao, D. Tuvin, R. S. Benjamin, D.C. Lev, R.E. Pollock, Computed Tomography Scan-Driven Selection of Treatment for Retroperitoneal Liposarcoma Histologic Subtypes, *Cancer* 115(5), 1081–1090 (2009).
- [26] D. Lev, S.A. Baranov, E.F. Carbajal, E.D. Young, R.E. Pollock, K.V. Larin, Differentiating retroperitoneal liposarcoma tumors with optical coherence tomography, *Advanced Biomedical and Clinical Diagnostic Systems IX*, (February 21, 2011), Proc. of SPIE Vol. 7890, 78900U.
- [27] E. Wardelmann, H.-U. Schildhaus, S. Merkelbach-Bruse, W. Hartmann, P. Reichardt, P. Hohenberger, R. Büttner, Soft tissue sarcoma: from molecular diagnosis to selection of treatment. Pathological diagnosis of soft tissue sarcoma amid molecular biology and targeted therapies, *Annals of Oncology* 21 (Issue Suppl. 7): vii265–vii269, 2010.
- [28] J.A. Bridge, A.M. Cushman-Vokoun, Molecular diagnostics of soft tissue tumors, *Archives of Pathology and Laboratory Medicine*, 2011 May, 135(5):588-601.
- [29] J. Czernin, M.R. Benz, M.S. Allen-Auerbach, Review, PET/CT imaging: The incremental value of assessing the glucose metabolic phenotype and the structure of cancers in a single examination, *European Journal of Radiology*, 73 (2010) 470–480.
- [30] B. Unal, Y.K. Bilgili, E.Batislam, S. Erdogan, Giant dedifferentiated liposarcoma: CT and MRI findings, *European Journal of Radiology Extra*, 51 (2004) 47-50.
- [31] C.D.M. Fletcher, K.K. Unni, F. Mertens, (Eds.), *World Health Organization Classification of Tumours. Pathology and Genetics of Tumours of Soft Tissue and Bone*, International Agency for Research and Cancer Press, Lyon 2002.
- [32] L.K. Meyer, T.P. Ciaraldi, R.R Henry, A.C. Wittgrove, S.A. Phillips, Adipose tissue depot and cell size dependency of adiponectin synthesis and secretion in human obesity, *Adipocyte* 2:4, 217–226; 2013, Landes Bioscience.
- [33] <http://medicineworld.org/stories/lead/12-2010/fat-cells-become-useful-stem-cells.html>
- [34] <http://www.vetmed.vt.edu/education/curriculum/vm8054/Labs/Lab5/Lab5.htm>
- [35] M.M. Miettinen, *Diagnostic soft tissue pathology*, 2003 Churchill Livingstone, Philadelphia, PA, USA.
- [36] M.K. Narul, R.Madan, O.P. Pathania, R. Anand, Primary Intra-Abdominal Synovial Sarcoma, *Applied Radiology*, 2007, 36(7):48A-48D.
- [37] F. Meloni, C.F. Feo, S. Profili, M.L. Cossu, G.B. Meloni, Omental Well-Differentiated Liposarcoma: US, CT and MR Findings, *International Journal of Biomedical Science*, September 2009, Vol. 5 No.3, 302-304.
- [38] X.H. Diao, S. Li, Y. Chen, Y. Pang, Y. Chen, Ultrasound for giant abdomen liposarcoma: one case report, *Quantitative Imaging in Medicine and Surgery*, 2013, 3(3):184-185.

- [39] W.-M. Chung, Y.M. Ting, R.A. Gagliardi, Ultrasonic diagnosis of retroperitoneal liposarcoma, *Journal of Clinical Ultrasound*, Vol. 6 (4), August 1978, 266-7.
- [40] E. Bastiaanneta, H. Groenb, P.L. Jagerc, D.C.P. Cobbenc, W.T.A. van der Graafd, W. Vaalburgc, H.J. Hoekstra, The value of FDG-PET in the detection, grading and response to therapy of soft tissue and bone sarcomas; a systematic review and meta-analysis, *Cancer Treatment Reviews*, 2004, 30, 83–101.
- [41] J.M. Boland, A.L. Folpe, The impact of advances in molecular genetics on the classification and diagnosis of liposarcoma, *Diagnostic histopathology*, 17:8, 2011.
- [42] J. Folkmann, S. Ryeom, Is Oncogene Addiction Angiogenesis-dependent?, *Cold Spring Harbor Symposia on Quantitative Biology*, 2005, 70:389-397.
- [43] D. Braas, E. Ahler, B. Tam, D. Nathanson, M. Riedinger, M.R. Benz, K.B. Smith, F.C. Eilber, O.N. Witte, W.D. Tap, H. Wu, H.R. Christofk, Metabolomics Strategy Reveals Subpopulation of Liposarcomas Sensitive to Gemcitabine Treatment, *Cancer Discovery*, 2012, 2(12), 1109-1117.
- [44] A.P. Dhawan, B. D'Alessandro, X. Fu, Optical Imaging Modalities for Biomedical Applications, *IEEE Reviews in Biomedical Engineering*, 2010, Vol. 3, 69-92.
- [45] C. Balas, Review of biomedical optical imaging—a powerful, non-invasive, non-ionizing technology for improving in vivo diagnosis, *Measurement Science and Technology*, 20 (2009) 104020.
- [46] <http://hyperphysics.phy-astr.gsu.edu/hbase/ems1.html#c1>
- [47] L. Schermelleh, R. Heintzmann, H. Leonhardt, A guide to super-resolution fluorescence microscopy, *Journal of Cell Biology*, 2010, Vol. 190, No. 2, 165–175.
- [48] J.R. Mourant, T. Fuselier, J. Boyer, T.M. Johnson, I.J. Bigio, Predictions and measurements of scattering and absorption over broad wavelength ranges in tissue phantoms, *Applied Optics*, 1 February 1997, Vol. 36, No. 4, 949-957.
- [49] *Biomedical Optical Imaging*, Edited by J.G. Fujimoto and D.L. Farkas, Oxford University Press, 2009.
- [50] www.snm.org/mi, SNM Center for Molecular Imaging and Translation, *Fact sheet produced by the SNM Molecular Imaging Center of Excellence for use of physicians*, 2011 February 23.
- [51] N.J. Everall, Confocal Raman microscopy: common errors and artefacts, Tutorial Review, *Analyst*, 2010, 135, 2512-2522.
- [52] V. Ntziachristos, Going deeper than microscopy: the optical imaging frontier in biology, *Nature Methods*, 2010 August, 7(8):603-14.
- [53] L. Alchab, G. Dupuis, C. Balleyguier, M-C. Mathieu, M-P. Fontaine-Aupart, R. Farcy, Towards an optical biopsy for the diagnosis of breast cancer in vivo by endogenous fluorescence spectroscopy, *Journal of Biophotonics*, 3, No. 5-6, 373-384 (2010).
- [54] K. Cui, X. Xu, H. Zhao, S.T.C. Wong, A quantitative study of factors affecting in vivo bioluminescence imaging, *Luminescence*, 2008, 23: 292–295.
- [55] L. Li, L.V. Wang, Optical coherence computed tomography, *Applied Physics Letters* 91, 141107 (2007).
- [56] A.H. Hielschera, A.Y. Bluestone, G.S. Abdoulaev, A.D. Klose, J. Lasker, M. Stewart, U. Netz, J. Beuthan, Near-infrared diffuse optical tomography, *Disease Markers*, 18 (2002) 313–337.
- [57] S.J. Erickson, A. Godavarty, Hand-held based near-infrared optical imaging devices: A review, *Medical Engineering & Physics*, 31 (2009) 495–509.

- [58] S.A. Boppart, Optical coherence tomography: Technology and applications for neuroimaging, *Psychophysiology*, 40 (2003), 529–541.
- [59] 6. W. Drexler and J. G. Fujimoto, *Optical Coherence Tomography: Technology and Applications*, 2008, Springer Berlin Heidelberg.
- [60] Mark Brezinski, *Optical Coherence Tomography, Principles and Applications*, 2006, Elsevier Inc., Oxford, UK.
- [61] M.G. Ghosn, V.T. Tuchin, K.V. Larin, Depth-resolved monitoring of glucose diffusion in tissues by using optical coherence tomography, *Optics Letters*, Vol. 31, No. 15, August 1, 2006.
- [62] M.G. Ghosn, E.F. Carbajal, N.A. Befruj, V.V. Tuchin, K.V. Larin, Differential permeability rate and percent clearing of glucose in different regions in rabbit sclera, *Journal of Biomedical Optics* 13(2), 021110 (March/April 2008).
- [63] T. Durduran, R. Choe, W.B. Baker, A.G. Yodh, Diffuse optics for tissue monitoring and tomography, *Reports on Progress in Physics*, 73 (2010) 076701.
- [64] N. Bosschaart, D.J. Faber, T.G. van Leeuwen, M.C.G. Aalders, In vivo low-coherence spectroscopic measurements of local hemoglobin absorption spectra in human skin, *Journal of Biomedical Optics*, October 2011, Vol. 16(10). 100504-1 – 100504-3.
- [65] J.G. Fujimoto, Optical Coherence Tomography, *Comptes Rendus de l'Académie des Sciences*, Paris, t. 2, Série IV, p. 1099-1111, 2001/ Applied Physics/ Biophysics/ Optical and Acoustical Imaging of Biological Media.
- [66] M.R. Hee, J.A. Izatt, J.M. Jacobson, J.G. Fujimoto, E.A. Swanson, Femtosecond transillumination optical coherence tomography, *Optics Letters*, Vol. 18, Issue 12, 950-952 (1993).
- [67] R.K. Wang, X. Xu, V.V. Tuchin, J.B. Elder, Concurrent enhancement of imaging depth and contrast for optical coherence tomography by hyperosmotic agents, *Journal of the Optical Society of America B: Optical Physics*, vol. 18, 948-953, July 2001.
- [68] V.V. Tuchin, *Optical Clearing of Tissues and Blood*, SPIE Press, 2006.
- [69] *Agiliad Medical: The next generation of product engineering: collaborative innovation*, September 18, 2012, Lights, Sound and Magnetism – the science behind next-generation medical technologies.
- [70] A. Devor, S. Sakadžić, V.J. Srinivasan, M.A. Yaseen, K. Nizar, P.A. Saisan, P. Tian, A.M. Dale, S.A. Vinogradov, M.A. Franceschini, D.A. Boas, Frontiers in optical imaging of cerebral blood flow and metabolism, Review Article, *Journal of Cerebral Blood Flow & Metabolism* (2012) 32, 1259–1276.
- [71] S.J. Kirkpatrick, R.K. Wang, D.D. Duncan, OCT-based elastography for large and small deformations, *Optics Express*, Vol. 14, Issue 24, pp. 11585-11597 (2006).
- [72] A.C. Sullivan, J.P. Hunt, A.L. Oldenburg, Fractal analysis for classification of breast carcinoma in Optical Coherence Tomography, *Journal of Biomedical Optics*, June 2011, 16(6), 066010.
- [73] S. Farsiu, S.J. Chiu, R.V. O'Connell, F.A. Folgar, E. Yuan, J.A. Izatt, C.A. Toth, Quantitative Classification of Eyes with and without Intermediate Age-related Macular Degeneration Using Optical Coherence Tomography, *Ophthalmology*, 2014 January, 121(1): 162-72.
- [74] C.L. Chen, H. Ishikawa, Y. Ling, G. Wollstein, R.A. Bilonick, J. Xu, J.G. Fujimoto, I.A. Sigal, L. Kagemann, J.S. Schuman, Signal Normalization Reduces Systematic Measurement Differences Between Spectral-Domain Optical Coherence Tomography

- Devices, *Investigative Ophthalmology & Visual Science*, 2013 November 5, 54(12):7317-22.
- [75] I.Y. Yanina; N.A. Trunina; V.V. Tuchin, Photoinduced cell morphology alterations quantified within adipose tissues by spectral optical coherence tomography, *Journal of Biomedical Optics*, 2013 November, 18(11) 111407.
- [76] Princeton Instruments, *Raman Spectroscopy Basics*, application note.
- [77] W. Min, C.W. Freudiger, S. Lu, X.S. Xie, Coherent Nonlinear Optical Imaging: Beyond Fluorescence Microscopy, *Annual Review of Physical Chemistry*, 2011, 62:507-530.
- [78] X. Xu, J. Cheng, M.J. Thrall, Z. Liu, X. Wang, S.T. Wong, Multimodal non-linear optical imaging for label-free differentiation of lung cancerous lesions from normal and desmoplastic tissues, *Biomedical Optics Express*, 2013 Nov 15, 4(12):2855-68.
- [79] E. Hecht, *Optics*, 4th ed. 2002, Pearson Education, Inc., publishing as Addison Wesley, San Francisco, CA, USA.
- [80] M. Born, E. Wolf, *Principles of Optics, Electromagnetic Theory of Propagation, Interference and Diffraction of Light*, 4th ed., 1970, Pergamon Press, Oxford, UK.
- [81] <http://micro.magnet.fsu.edu/primer/java/electromagnetic/>
- [82] W. Heisenberg, Über den anschaulichen Inhalt der quantentheoretischen Kinematik und Mechanik, 1927, *Zeitschrift für Physik* **43**, 172–198. English translation: J. Wheeler, H. Zurek, 1983, *Quantum Theory and Measurement*, Princeton University Press, Princeton.
- [83] D. Gabor, Theory of communication. *Journal of the Institute of Electrical Engineering*, 1946, **93**, 429–457.
- [84] Torsten Söderström, Petre Stoica, *System Identification*, 1989, Prentice Hall International (UK) Ltd.
- [85] A.F. Fercher, W. Drexler, C.K. Hitzenberger, T. Lasser, Optical coherence tomography—principles and applications, *Reports on Progress in Physics* 66 (2003) 239–303.
- [86] *Frequency Analysis* by R. B. Randall, 3rd Edition, 1st Print, 1987, Brüel & Kjaer.
- [87] *MATLAB – A Fundamental Tool for Scientific Computing and Engineering Applications – Volume I*, edited by Vasilios N. Katsikis, InTech, September 26, 2012.
- [88] www.k-wave.org; Documentation of MatLAB k-wave Toolbox
- [89] 1991 *RLE Progress Report* 147, Chapter Laser Medicine and Biomedical Imaging, RLE Groups, Laser Medicine and Medical Imaging Group, Optics and Quantum Electronics Group, Project Staff: A.D. Aguirre, J.G. Fujimoto
- [90] L. Vabre, A. Dubois, and A. C. Boccara, Thermal-light full-field optical coherence tomography, *Optics Letters*, April 1, 2002, Vol. 27, No. 7, 530-3.
- [91] A. Dubois, L. Vabre, A-C. Boccara, E. Beurepaire, High-resolution full-field optical coherence tomography with a Linnik microscope, *Applied Optics*, February 2002, Vol. 41, No.4, 805-812.
- [92] J.M. Schmitt, Optical Coherence Tomography (OCT): A Review, (Invited Paper), *IEEE Journal of Selected Topics in Quantum Electronics*, Vol. 5, No. 4, July/August 1999 1205-15.
- [93] A.M. Zysk, F.T. Nguyen, A.L. Oldenburg, D.L. Marks, S.A. Boppart, Optical coherence tomography: a review of clinical development from bench to bedside, *Journal of Biomedical Optics* 12(5), 051403 (September/October 2007).
- [94] J.G. Fujimoto, Optical coherence tomography, *Comptes Rendus de l'Académie des Sciences*, Paris, t. 2, Série IV, p. 1099–1111, 2001 /Applied physics /Biophysics/ Optical and Acoustical Imaging of Biological Media

- [95] R. K. Wang, X. Xu, V. V. Tuchin, and J. B. Elder, Concurrent enhancement of imaging depth and contrast for optical coherence tomography by hyperosmotic agents, *Journal of the Optical Society of America B Optical Physics*, Vol. 18: 948-953, July 2001.
- [96] A.L. Oldenburg, C. Xu, S.A. Boppart, Spectroscopic Optical Coherence Tomography and Microscopy, *IEEE Journal of selected topics in quantum electronics*, November/December 2007, Vol. 13, No. 6, 1629-40.
- [97] P. Lee, W. Gao, and X. Zhang, Performance of single-scattering model versus multiple-scattering model in the determination of optical properties of biological tissue with optical coherence tomography, *Applied Optics* 49, No. 18, 3538–3544 (2010).
- [98] P.H. Tomlins, R.K. Wang, Theory, developments and applications of optical coherence tomography, *Journal of Physics D: Applied Physics*, **38** (2005) 2519–2535.
- [99] <http://www.internationalcancertherapy.com/images/wavelength.jpg>
- [100] P. Jansz, S. Richardson, G. Wild, S. Hinckley, Modeling of Low Coherence Interferometry Using Broadband Multi-Gaussian Light Sources, *Photonic Sensors* (2012) Vol. 2, No. 3: 247–258.
- [101] J.A. Izatt, M.D. Kulkarni, K. Kobayashi, M.V. Sivak, J.K. Barton, and A.J. Welch, Optical coherence tomography for biodiagnostics, *Optics and Photonics News*, vol. 8, no. 5, pp. 41–47, 1997.
- [102] P. Jansz, G. Wild, S. Richardson, S. Hinckley, Low Coherence Interferometry Modelling using Combined Broadband Gaussian Light Sources, Third Asia Pacific Optical Sensors Conference, edited by John Canning, Gangding Peng, Proc. of SPIE Vol. 8351, 83510C, 2012.
- [103] Advanced Biophotonics: Tissue Optical Sectioning, edited by R.K. Wang, V.V Tuchin, CRC Press, Taylor & Francis Group, 2013.
- [104] *Lasers and Current Optical Techniques in Biology*, edited by G. Palumbo, R. Pratesi, 2004, The Royal Society of Chemistry, Cambridge, UK.
- [105] Ceyhun Akcay, Pascale Parrein, Jannick P. Rolland, Estimation of longitudinal resolution in optical coherence imaging, *Applied Optics*, Vol. 41, No. 25, 1 September 2002.
- [106] W. Drexler, Cellular and Functional Optical Coherence Tomography of the Human Retina, The Cogan Lecture, *Investigative Ophthalmology & Visual Science*, December 2007, Vol. 48, No. 12., 5340-51.
- [107] J.G. Fujimoto, Optical coherence tomography for ultrahigh resolution in vivo imaging, *Nature Biotechnology*, **21**, 1361–1367 (2003).
- [108] R. Ramsay, Photonic-crystal fiber characteristics benefit numerous applications, *Sensing & Measurement, SPIE Newsroom*, 17 November 2008.
- [109] T. Fuji, M. Miyata, S. Kawato, T. Hattori, H. Nakatsuka, *Linear propagation of light investigated with a white-light Michelson interferometer*, *Journal of the Optical Society of America B*, Vol. 14, No. 5, May 1997, 1074-8.
- [110] A.F. Fercher, C.K. Hitzenberger, M. Sticker, E. Moreno-Barriuso, R. Leitgeb, W. Drexler, H. Sattmann, A thermal light source technique for optical coherence tomography, *Optics Communications* 185 (2000) 57-64.
- [111] R.S. Quimby, *Photonics and Laser, An Introduction*, 2006, John Wiley & Sons, Inc., Hoboken, New Jersey, US.
- [112] <http://labman.phys.utk.edu/phys136/modules/m9/film.htm>
- [113] T. Wilson, Resolution and optical sectioning in the confocal microscope, *Journal of Microscopy*, 2011, Vol. 244, 113–121.

- [114] J.A. Izatt, M.D. Kulkarni, H-W. Wang, K. Kobayashi, M.V. Sivak, Jr., *Optical Coherence Tomography and Microscopy in Gastrointestinal Tissues*, IEEE Journal of Selected Topics in Quantum Electronics, Vol. 2, No. 4, December 1996, 1017-28.
- [115] O. Assayag, M. Antoine, B. Sigal-Zafrani, M. Riben, F. Harms, A. Burcheri, E. Dalimier, B. Le Conte de Poly, A-C. Boccara, Large Field, High Resolution Full Field Optical Coherence Tomography: A Pre-clinical study of human breast tissue and cancer assessment, *Technology in Cancer Research and Treatment*, 2013 Aug. 31. 12(4), 275-84.
- [116] G.J. Tearney, M.E. Brezinski, J.F. Southern, B.E. Bouma, M.R. Hee, J.G. Fujimoto, Determination of the refractive index of highly scattering human tissue by optical coherence tomography, November 1, 1995, *Optics Letters*, Vol. 20, No. 21, 2258-60.
- [117] S. Labiau, G. David, S. Gigan, A.C. Boccara, Defocus test and defocus correction in full-field optical coherence tomography, *Optics Letters*, May 15, 2009, Vol. 34, No. 10, 1576-8.
- [118] M.J. Cobb, X. Liu, X. Li, Continuous focus tracking for real-time optical coherence tomography, *Optics Letters*, vol. 30, no. 13, 1680-1682, 2005.
- [119] W. Drexler, U. Morgner, F.X. Kärtner, C. Pitris, S.A. Boppart, X.D. Li, E. P. Ippen, J. G. Fujimoto, In vivo ultrahigh-resolution optical coherence tomography, *Optics Letters*, vol. 24:17, 1221-1223, 1999.
- [120] L. Yu, B. Rao, J. Zhang, J. Su, Q. Wang, S. Guo, Z. Chen, Improved lateral resolution in optical coherence tomography by digital focusing using two-dimensional numerical diffraction method, *Optics Express*, 11 June 2007, Vol. 15, No. 12. 7634-7641.
- [121] Gaussian Beam Optics, Newport, Technical Reference and Fundamental Applications.
- [122] http://www.optique-ingenieur.org/en/courses/OPI_ang_M01_C01/co/Contenu_09.html
- [123] <http://www.psi.ch/swissfel/the-challenges-of-bio-imaging>
- [124] J. Vasco, P.J. Bártolo, B. Silva, C. Galo, Laser micromachining for mould manufacturing: II. Manufacture and testing of mould inserts, *Assembly Automation*, Vol. 27, No. 3, 231–239, 2007.
- [125] J.F. de Boer, B. Cense, B.H. Park, M.C. Pierce, G.J. Tearney, B.E. Bouma, Improved signal-to-noise ratio in spectral-domain compared with time-domain optical coherence tomography, *Optics Letters*, November 1 2003, Vol. 28, No. 21, 2067-9.
- [126] B. Grajciar, O. Ondráček, Dispersion compensation in Spectral Domain Optical Coherence Tomography. Downloaded from <http://www.vutbr.cz/>.
- [127] M. Ali, R. Parlapalli, *Signal Processing Overview of Optical Coherence Tomography Systems for Medical Imaging*, SPRABB9 – June 2010, White Paper, Texas Instruments.
- [128] light.ece.illinois.edu/ECE460/PDF/LCI.pdf
- [129] D.L. Marks, A.L. Oldenburg, J.J. Reynolds, S.A. Boppart, Autofocus algorithm for dispersion correction in optical coherence tomography, *Applied Optics*, 1 June 2003, Vol. 42, No. 16, 3038-46.
- [130] M. Gora, K. Karnowski, M. Szkulmowski, B.J. Kaluzny, R. Huber, A. Kowalczyk, M. Wojtkowski, Ultra-high-speed swept-source OCT imaging of the anterior segment of human eye at 200 kHz with adjustable imaging range, *Optics Express*, Vol.17, No.17, 2009, 14880-94.
- [131] Y. Yasuno, V.D. Madjarova, S. Makita, M. Akiba, A. Morosawa, C. Chong, T.Sakai, K-P. Chan, M. Itoh, T. Yatagai, Three-dimensional and high-speed swept-source optical

- coherence tomography for in vivo investigation of human anterior eye segments, *Optics Express*, Vol. 13, No. 26, 10652-10664, 26 December 2005.
- [132] M. Takeda, H. Ina, S. Kobayashi, Fourier-transform method of fringe-pattern analysis for computer-based topography and interferometry, *Journal of Optical Society of America*, Vol. 72, No. 1, 156-160, January 1982.
- [133] V. J. Srinivasan, D. C. Adler, Y. Chen, I. Gorczynska, R. Huber, J. S. Duker, J. S. Schuman, J. G. Fujimoto, Ultrahigh-Speed Optical Coherence Tomography for Three-Dimensional and En Face Imaging of the Retina and Optic Nerve Head, *Investigative Ophthalmology and Visual Science*, Vol. 49, No. 11, 5103-5110, November 2008.
- [134] K. Hsu, R. Huber, M. Wojtkowski, K. Taira, J. G. Fujimoto, Amplified, frequency swept lasers for frequency domain reflectometry and OCT imaging: design and scaling principles, *Optics Express*, Vol. 13, No. 9, 3513-28, 2 May 2005.
- [135] C.M. Eigenwillig, B.R. Biedermann, G. Palte, R. Huber, K-space linear Fourier domain mode locked laser and applications for optical coherence tomography, *Optics Express*, 9 June 2008, Vol. 16, No. 12, 8916-37.
- [136] T. Bajraszewski, M. Wojtkowski, M. Szkulmowski, A. Szkulmowska, R. Huber, A. Kowalczyk, Improved spectral optical coherence tomography using optical frequency comb, *Optics Express*, Vol. 16, No. 6, 4163-76, 17 March 2008.
- [137] B. Hofer, B. Považay, B. Hermann, A. Unterhuber, G. Matz, F. Hlawatsch, W. Drexler, Signal post processing in frequency domain OCT and OCM using a filter bank approach, *SPIE Proceedings* Vol. 6443. Three-Dimensional and Multidimensional Microscopy: Image Acquisition and Processing XIV, 64430O (14 February 2007)
- [138] S-W. Lee, H-W. Jeong, B-M. Kim, Y-C. Ahn, W. Jung, Z. Chen, Optimization for Axial Resolution, Depth Range, and Sensitivity of Spectral Domain Optical Coherence Tomography at 1.3 μm , *Journal of the Korean Physical Society*, Vol. 55, No. 6, December 2009, 2354-2360.
- [139] Dirk J. Faber, Freek J. van der Meer, Maurice C.G. Aalders, Quantitative measurement of attenuation coefficients of weakly scattering media using optical coherence tomography, *Optics Express*, September 2004. Vol. 12, No. 19, pp. 4353-4365.
- [140] L. Thrane, H.T. Yura, P.E. Andersen, Analysis of optical coherence tomography systems based on the extended Huygens-Fresnel principle, *Journal of Optical Society of America A*, Vol. 17, No. 3, 484-90, March 2000.
- [141] D.P. Popescu, C. Flueraru, Y. Mao, S. Chang, M.G. Sowa, Signal attenuation and box-counting fractal analysis of optical coherence tomography images of arterial tissue, *Biomedical Optics Express*, August 2010, Vol.1, No.1. 268-77.
- [142] J. W. Goodman, Some fundamental properties of speckle, *Journal of Optical Society of America*, 66, 1145-1150, 1976.
- [143] M.G. Ghosn, V.V. Tuchin, K.V. Larin, Depth-resolved monitoring of glucose diffusion in tissues by using optical coherence tomography, *Optics Letters*, Vol. 31, No. 15, August 2006. 2314-6.
- [144] M.G. Ghosn, E.F. Carbajal, N.A. Befrui, V.V. Tuchin, K.V. Larin, Differential permeability rate and percent clearing of glucose in different regions in rabbit sclera, *Journal of Biomedical Optics*, 13(2), 021110, March/April 2008.
- [145] M.G. Ghosn, M. Mashiattulla, S.H. Syed, M.A. Mohamed, K.V. Larin, J. D. Morrisett, Permeation of human plasma lipoproteins in human carotid endarterectomy tissues:

- measurement by optical coherence tomography, *Journal of Lipid Research*, Vol. 52, 1429-34, April 2011.
- [146] M.J. Yadlowsky, J.M. Schmitt, R.F. Bonner, Multiple scattering in optical coherence microscopy, *Applied Optics*, **34**, 5699–5707 (1995).
- [147] M. J. Yadlowsky, J. M. Schmitt, R.F. Bonner, Contrast and resolution in the optical coherence microscopy of dense biological tissue, in *Advances in Laser and Light Spectroscopy to Diagnose Cancer and other Diseases II*, R. R. Alfano, ed., *Proc. SPIE* **2387**, 193–203 (1995).
- [148] Y. Pan, R. Birngruber, R. Engelhardt, Contrast limits of coherence-gated imaging in scattering media, *Applied Optics* **36**, 2979–2983 (1997).
- [149] J.M. Schmitt, A. Knüttel, Model of optical coherence tomography of heterogeneous tissue, *Journal of Optical Society of America A* **14**, 1231–1242 (1997).
- [150] Y. Yang, T. Wang, N.C. Biswal, X. Wang, M. Sanders, M. Brewer, Q. Zhu, Optical scattering coefficient estimated by optical coherence tomography correlates with collagen content in ovarian tissue, *Journal of Biomedical Optics*, Vol. 16(9) 090504, September 2011.
- [151] F.J. van der Meer, D.J. Faber, D.M.B. Sassoon, M.C. Aalders, G. Pasterkamp, T.G. van Leeuwen, Localized Measurement of Optical Attenuation Coefficients of Atherosclerotic Plaque Constituents by Quantitative Optical Coherence Tomography, *IEEE Transactions on Medical Imaging*, 24 (10), 1369-1376 (2005).
- [152] J M Schmitt, A Knüttel, M Yadlowskyt and M A Eckhauss, Optical-coherence tomography of a dense tissue: statistics of attenuation and backscattering, *Physics in Medicine and Biology*, 39 (1994) 1705-1720.
- [153] J.M. Schmitt, A. Knüttel, R.F. Bonner, Measurement of optical properties of biological tissues by low-coherence reflectometry, *Applied Optics*, Vol. 32, No. 30, 6032-42, October 1993.
- [154] Ton G. van Leeuwen, Dirk J. Faber, and Maurice C. Aalders, Measurement of the Axial Point Spread Function in Scattering Media Using Single-Mode Fiber-Based Optical Coherence Tomography, *IEEE Journal of Selected Topics in Quantum Electronics*, Vol. 9, No. 2, March/April 2003, 227-233.
- [155] L. Scolaro, R.A. McLaughlin, B.R. Klyen, B.A. Wood, P.D. Robbins, C.M. Saunders, S.L. Jacques, D.D. Sampson, Parametric imaging of the local attenuation coefficient in human axillary lymph nodes assessed using optical coherence tomography, *Biomedical Optics Express*, February 2012, Vol. 3, No. 2, 366-378.
- [156] Wen Zhu, Nancy Zeng, Ning Wang, Sensitivity, Specificity, Accuracy, Associated Confidence Interval and ROC Analysis with Practical SAS® Implementations, *NESUG Conference Proceedings*, Health Care and Life Sciences, Noczember 14-17 2010, Baltimore, Maryland.
- [157] R.A. McLaughlin, L. Scolaro, Parametric imaging of cancer with optical coherence tomography, *Journal of Biomedical Optics*, 15(4), 046029 (July/August 2010)
- [158] K.K.M.B.D. Silva, A.V. Zvyagin, D.D. Sampson, Extended range, rapid scanning optical delay line for biomedical interferometric imaging, *Electronics Letters*, 19 August 1999, Vol. 35, No. 17, 1404-7.
- [159] S. Wang, N. Sudheendran, C-H. Liu, R.K. Manapuram, V.P. Zakharov, D.R. Ingram, A.J. Lazar, D.C. Lev, R.E. Pollock, K.V. Larin, Computational analysis of optical coherence

- tomography images for the detection of soft tissue sarcomas, *Proc. of SPIE* Vol. 8580, 85800 T, 2013, Dynamics and Fluctuations in Biomedical Photonics X.
- [160] M.A. Choma, M.V. Sarunic, C. Yang, J.A. Izatt, Sensitivity advantage of swept source and Fourier domain optical coherence tomography, *Optics Express*, 8 September 2003, Vol. 11, No. 18, 2183-9.
- [161] N.V. Iftimia, B.E. Bouma, M.B. Pitman, B.D. Goldberg, J.Bressner, G.J. Tearney, A portable, low coherence interferometry based instrument for fine needle aspiration biopsy guidance, *Review of Scientific Instruments* 76, 064301 (2005).
- [162] B.D. Goldberg, N.V. Iftimia, J. E. Bressner, M.B. Pitman, E. Halpern, B.E. Bouma, G.J. Tearney, Automated algorithm for differentiation of human breast tissue using low coherence interferometry for fine needle aspiration biopsy guidance, *Journal of Biomedical Optics*, 13(1), 014014 (January/February 2008).
- [163] M. Mujat, R.D. Ferguson, D.X. Hammer, C. Gittins, N. Iftimia, Automated algorithm for breast tissue differentiation in optical coherence tomography, *Journal of Biomedical Optics*, 14(3), 034040 (May/June 2009).
- [164] A.M. Zysk, S.A. Boppart, Computational methods for analysis of human breast tumor tissue in optical coherence tomography images, *Journal of Biomedical Optics* 11(5), 054015, (September/October 2006).
- [165] A.C. Sullivan, J.P. Hunt, A.L. Oldenburg, Fractal analysis for classification of breast carcinoma in Optical Coherence Tomography, *Journal of Biomedical Optics* 16(6), 066010-1/6 (June 2011).
- [166] K.W. Gossage, T.S. Tkaczyk, J. J. Rodriguez, J.K. Barton, Texture analysis of Optical Coherence Tomography images: feasibility for tissue classification, *Journal of Biomedical Optics* 8(3), 570–575 (July 2003).
- [167] K.W. Gossage, C.M. Smith, E.M. Kanter, L.P. Hariri, A.L. Stone, J.J. Rodriguez, S.K. Williams, J.K. Barton, Texture analysis of speckle in optical coherence tomography images of tissue phantoms, *Physics in Medicine and Biology*, 51 (2006) 1563-75.
- [168] A. Mcheil, H. Batatia, Segmentation of OCT skin images by classification of speckle statistical parameters, *IEEE 17th International Conference on Image Processing*, September 26-29, 2010, Hong Kong
- [169] D.D. Duncan, S.J. Kirkpatrick, R.K. Wang, Statistics of local speckle contrast, *Journal of Optical Society of America A*, Vol. 25, No. 1: 9-15, January 2008.
- [170] *Dynamic Laser Speckle and Applications*, Edited by Hector J. Rabal, Roberto A. Braga Jr., 2009, CRC Press, Taylor and Francis Group LLC.
- [171] Y. Huang, S. Gangaputra, K.E. Lee, A.R. Narkar, R. Klein, B.E.K. Klein, S.M. Meuer, R.P. Danis, Signal Quality Assessment of Retinal Optical Coherence Tomography Images, *Investigative Ophthalmology & Visual Science*, April 2012, Vol. 53, No. 4
- [172] C-L. Chen, H.i Ishikawa, G. Wollstein, Y. Ling, R.A. Bilonick, L. Kagemann, I.A. Sigal, J.S. Schuman, Individual A-Scan Signal Normalization Between Two Spectral Domain Optical Coherence Tomography Devices, *Investigative Ophthalmology & Visual Science, Multidisciplinary Ophthalmic Imaging*, May 2013, Vol. 54, No. 5, 3463-71.
- [173] K.A. Vermeer, J. van der Schoot, H.G. Lemij, J.F. de Boer, RPE-Normalized RNFL Attenuation Coefficient Maps Derived from Volumetric OCT Imaging for Glaucoma Assessment, *Investigative Ophthalmology & Visual Science, Glaucoma*, September 2012, Vol. 53, No. 10. 6102-8.

- [174] J. van der Schoot, K.A. Vermeer, J.F. de Boer, H.G. Lemij, The Effect of Glaucoma on the Optical Attenuation Coefficient of the Retinal Nerve Fiber Layer in Spectral Domain Optical Coherence Tomography Images, *Investigative Ophthalmology & Visual Science, Glaucoma*, April 2012, Vol. 53, No. 4. 2424-30.
- [175] A.M. Pavaskar, *Tools for creating wide-field views of the human retina using Optical Coherence Tomography*, Master's Thesis, Marquette University 2009.

Appendix

1. Lipoma_Liposarcoma
2. Parameters DataSets
3. Perturbation_Saturation_Obliqueness.

APPENDIX 1

Classification of Lipoma and Liposarcoma

Lipoma (Benign Fat Tissue Tumor)

Tumor Type	Comment/ Additional Elements/ Difference from Ordinary Lipoma	Regions of Chromosome with Genetic Changes
Lipoma (ordinary lipoma) Intra/intermuscular lipoma Fibrolipoma Myxoid lipoma/myxolipoma	Composed of mature adipose tissue Lipomas with deep locations Prominent fibrous septa Myxoid matrix	12q, 6p
Lipomas with heterologous elements Myolipoma Chondrolipoma Osteolipoma	Foci of mature smooth muscle Islands of mature cartilage Foci of metaplastic bone	
Angiolipoma	Capillaries with fibrin microthrombi, usually in young adults	None found
Angiomyolipoma	Immature, HMB45+ smooth muscle cells, in kidney or retroperitoneum	12q, 16p13
Chondroid lipoma	Epithelioid cartilage-like differentiation	11q13, 16p12-13
Myelolipoma	Fatty and hematopoietic marrow elements, in adrenal or retroperitoneum	
Spindle cell and pleomorphic lipoma	Lipoma with spindle cells or giant cells, posterior neck of older men. CD34 ⁺	16q
Hibernoma	Benign tumor with features of brown fat	11q13
Lipoblastoma	A childhood fatty tumor. Lobulated, myxoid composed of immature fat	8q
Atypical lipoma (atypical lipomatous tumor)	Lipoma with significant nuclear atypia	12q15

Table 8-1. Classification and Key Features of Benign Fatty Tumors [35]

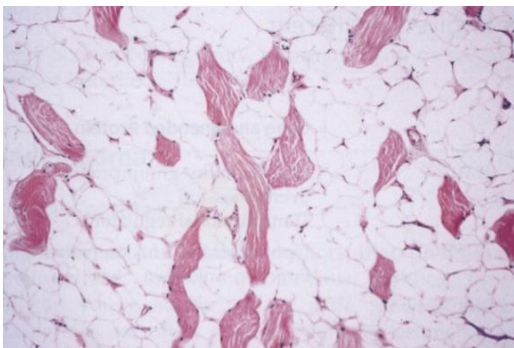


Figure 8-2. [35]

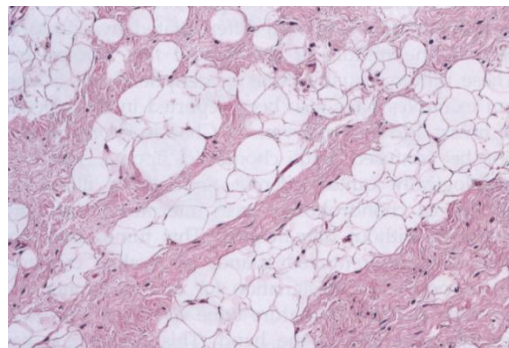


Figure 8-3. [35]

Intramuscular Lipoma,
Many of them grow between the muscle fibers
in a check board pattern.

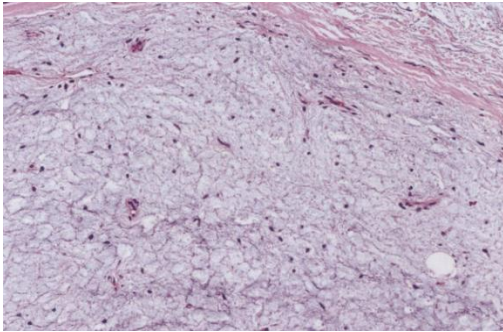


Figure 8-4. [35]

Myxoid lipoma shows abundant myxoid matrix and moderate vascularity. Only a single adipocyte is seen in this field.

Fibrolipoma,
Lipomas with prominent fibrous septa

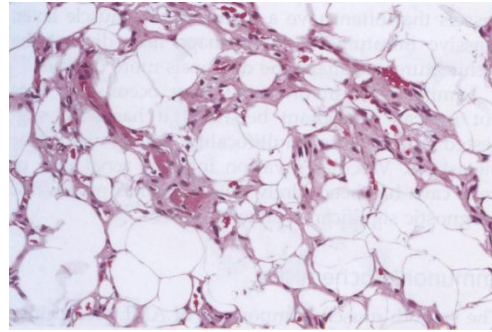


Figure 8-5. [35]

Angiolipoma typically contains peripheral streaks of thick-walled capillaries filled with erythrocytes and often fibrin microthrombi.

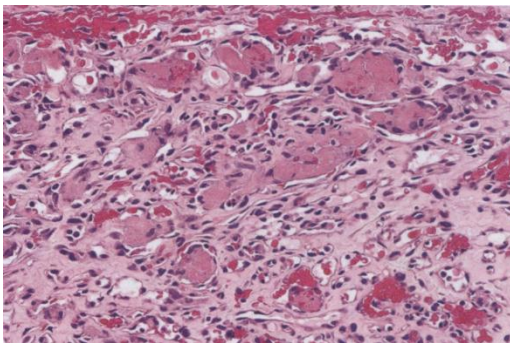


Figure 8-6. [35]

Cellular angiolipoma shows a dominant vascular component, and prominent fibrin thrombosis is present.

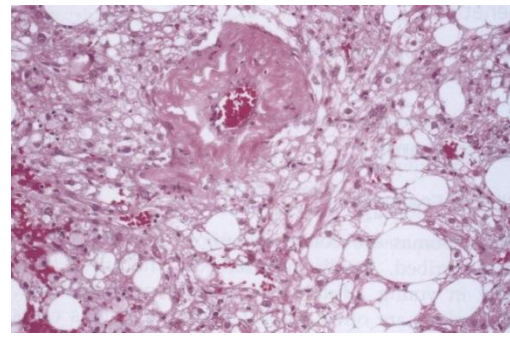


Figure 8-8. [35]

Typical angiomyolipoma with thick-walled blood vessels, a clear cytoplasmic smooth muscle component, and a mature fatty component.

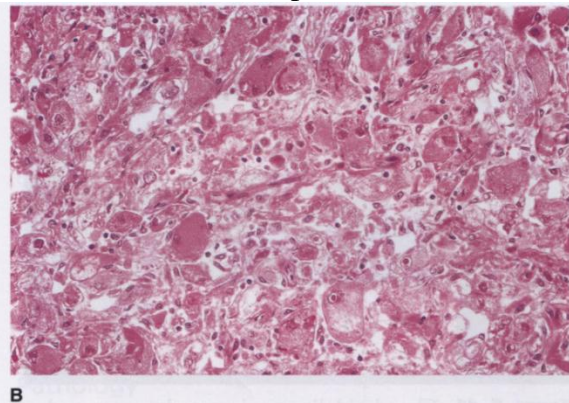
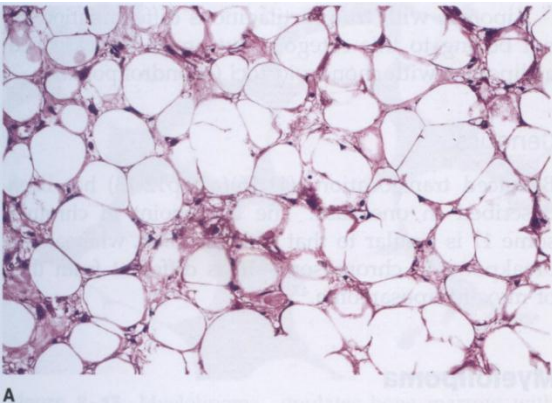


Figure 8-9. [35]

Histologic variants of angiomyolipoma include (A) tumors dominated by fat with small streaks of smooth muscle, and (B) rare variants primarily composed of epithelioid cells with eosinophilic cytoplasm.

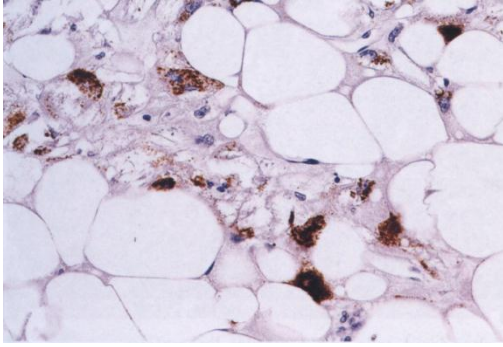


Figure 8-10. [35]
Angiomyolipoma contains varying numbers of HMB45⁺ epithelioid muscle cells.

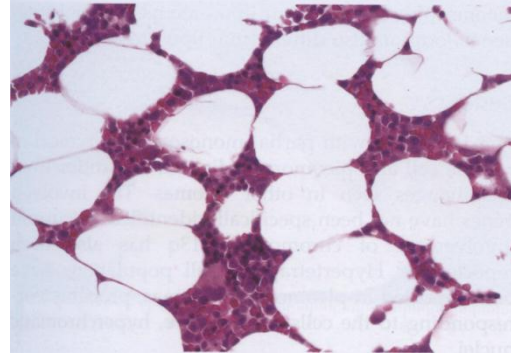


Figure 8-13. [35]
Myelolipoma simulates bone marrow with fatty and hematopoietic elements.

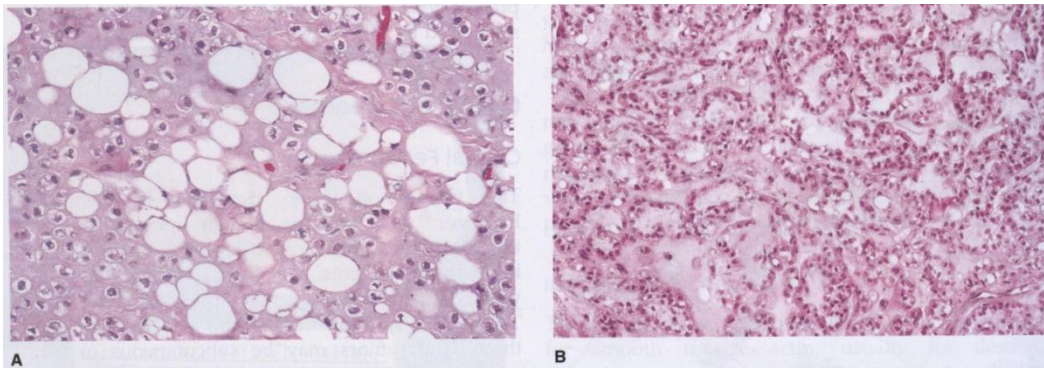


Figure 8-12. [35]
A, Typical chondroid lipoma contains epithelioid chondroid cells and a mature lipomatous component. B, Chondroid lipomas may have a trabecular or alveolar pattern resembling extraskeletal myxoid chondrosarcoma.

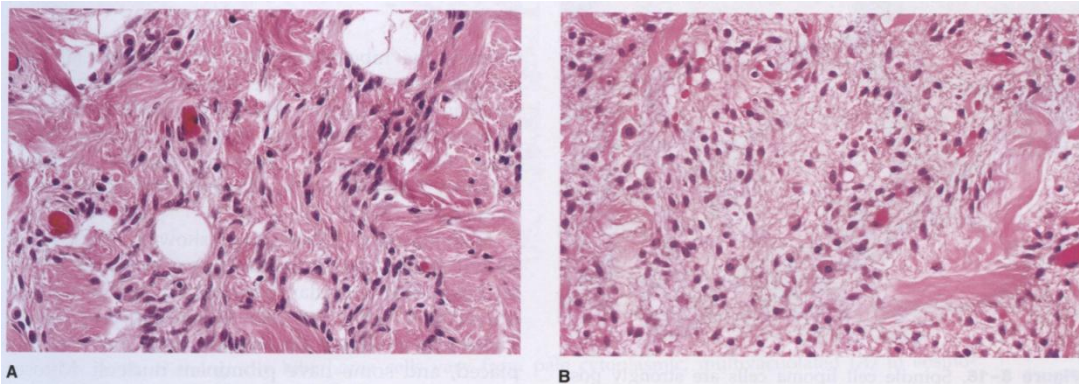


Figure 8-14. [35]
Spindle cell lipomas with different appearances. A, Spindle cell component in a coarse collagenous background. B, Cellular spindle cell pattern in a myxoid background.

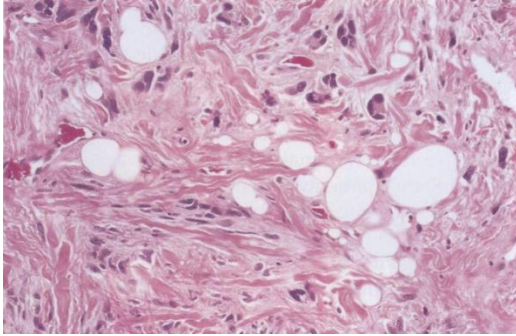


Figure 8-15. [35]

Pleomorphic lipoma resembles spindle cell lipoma but has floret-like giant cells.

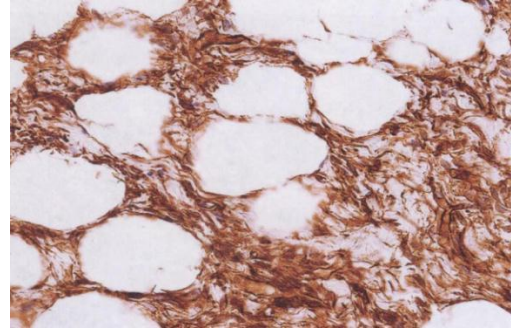


Figure 8-16. [35]

Spindle cell lipoma cells are strongly positive for CD34.

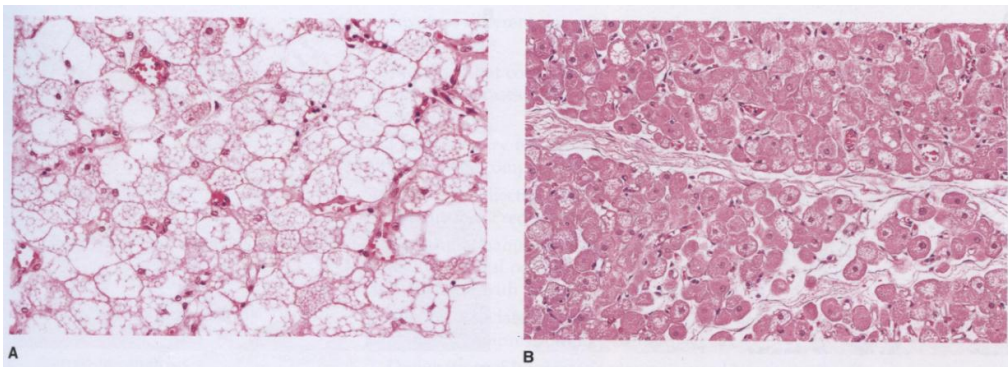


Figure 8-18. [35]

Histologically hibernoma cells vary from pale cytoplasmic, multivacuolated (A) to eosinophilic cells with granular cytoplasm (B).

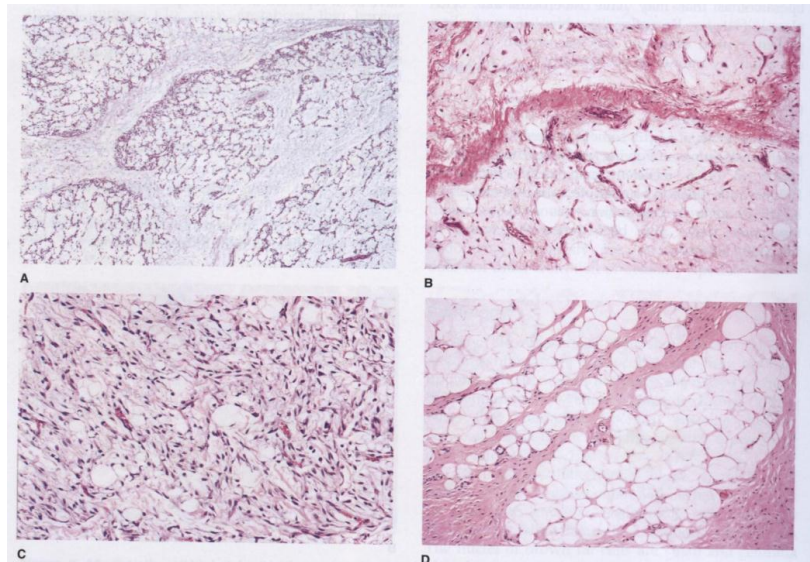


Figure 8-20. [35]

Histologically lipoblastomas typically have microlobulation (A), and vary in maturation. B, immature lipoblastoma with myxoid features and high vascularity. C, Lipoblastoma with spindle cell features. D, Mature lipoma-like lipoblastoma lobulated by fibrous septa.

Liposarcoma (Malignant fat tissue tumor)

Type	Estimated Frequency (%)	Age at Presentation	Typical Sites	Behavior	Regions of chromosome with Genetics changes
Atypical Lipoma/ Well-Differentiated	>50	Middle-aged to old	Retro-peritoneum, extremities	Local recurrence and risk of dedifferentiation	12q13-15 amplification
De-differentiated LS	5	Middle-aged to old	Retro-peritoneum, extremities	Risk for metastasis, especially with high-grade dedifferentiation	12q13-15 amplification
Myxoid/ round cell LS	30-40	Adult, often <40 years, rare in childhood	Thigh, very rare in retro-peritoneum	Recurrence common. Metastatic rate 30%-40% in long-term follow-up	t(12;16)
Pleomorphic LS	<5	Old adults	Extremities, retro-peritoneum	High risk for recurrence and metastasis	Complex, poorly understood

Table 15.1: Overview of Liposarcoma Types and Their clinicopathologic Features [35, 11]

1. Well-Differentiated Liposarcoma

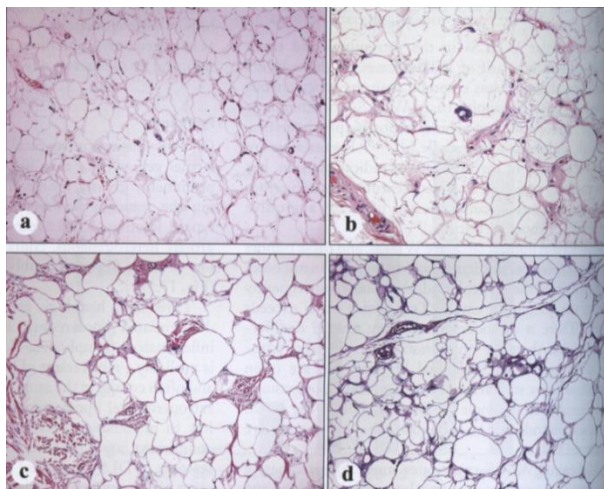


Figure 15.6. [11]

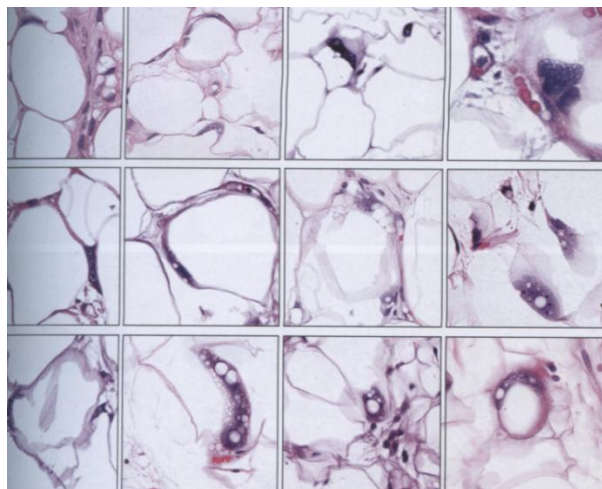


Figure 15.7. [11]

Atypical lipoma/lipoma-like well-differentiated liposarcoma shows significant variation in adipocyte size, and focal nuclear atypia is present. Note also increased cellularity in A, representing histiocytic infiltration. M: 4-10x

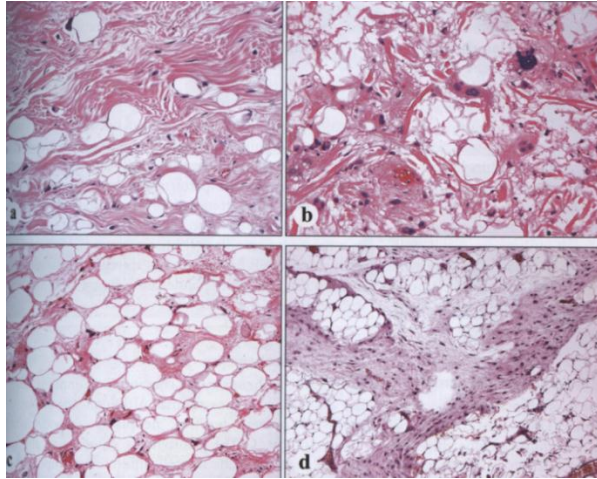


Figure 15.8. [11]

Atypical lipoma/lipoma-like, well-differentiated liposarcoma with stromal sclerosis and expanded, hypercellular fibrous septa.

Examples of atypical adipocytes in *atypical lipoma/well-differentiated liposarcoma*. Note enlarged nuclei, hyperchromasia, and intranuclear vacuoles in the atypical cells.

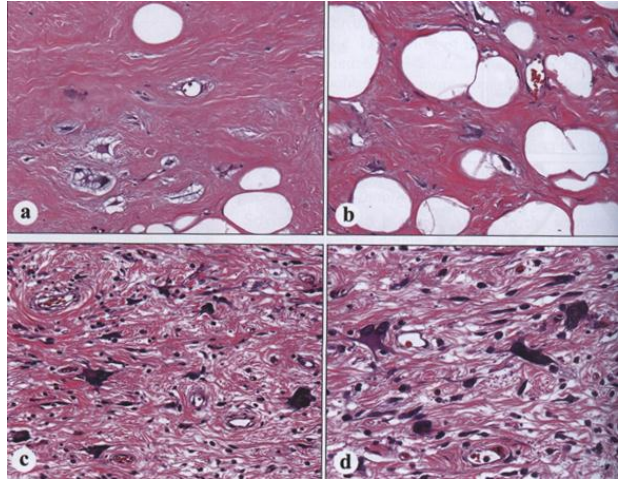


Figure 15.9. [11]

Sclerosing well-differentiated liposarcoma. Although adipocytes are scant or absent, this pattern with low cellularity and abundant collagenous matrix is not considered dedifferentiation

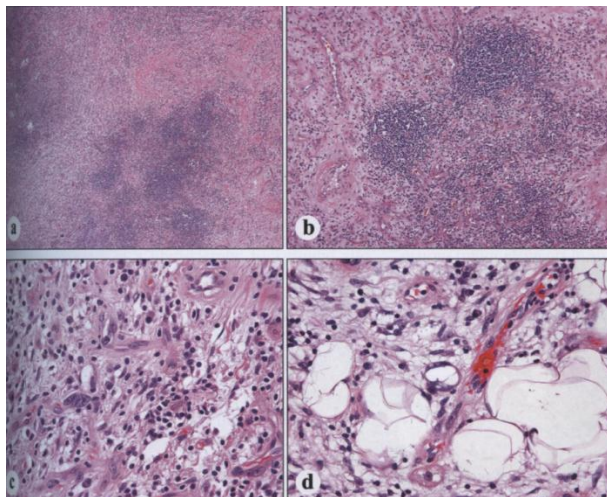


Figure 15.10. [11]

Inflammatory well-differentiated liposarcoma contains lymphoplasmacytic infiltration and fibrosclerosing stroma. Foci of atypical lipomatous component are present.

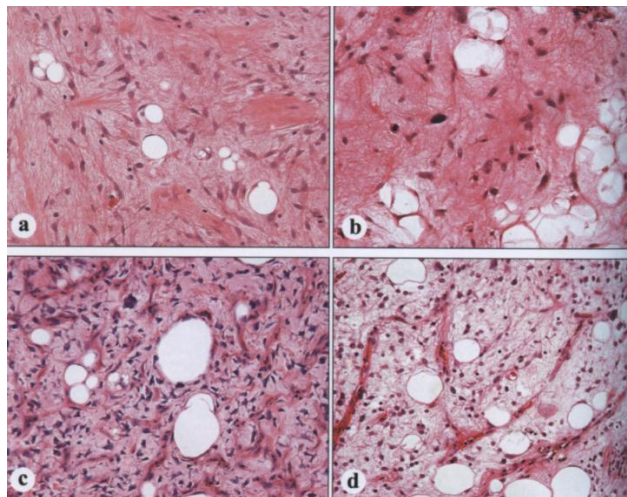


Figure 15.12. [11]

Spectrum of *well-differentiated liposarcoma of the retroperitoneum with myxoid features*. Note the focal presence of multivacuolated lipoblasts (A,C), and prominent capillaries with some resemblance to myxoid liposarcoma (C,D).

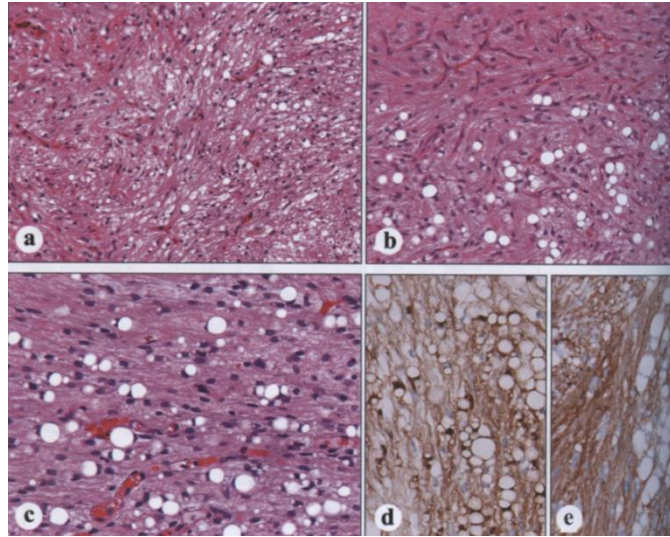


Figure 15.13. [11]

(A-C) *Spindle cell liposarcoma* is composed of mildly atypical spindled cells admixed with atypical, mainly univacuolar adipocytes. Note a prominent capillary pattern. (D) Significant S100 protein positivity is present in both adipocytes and the nonlipogenic spindle cells. (E) The spindle cells are positive for CD34.

2. De-Differentiated Liposarcoma

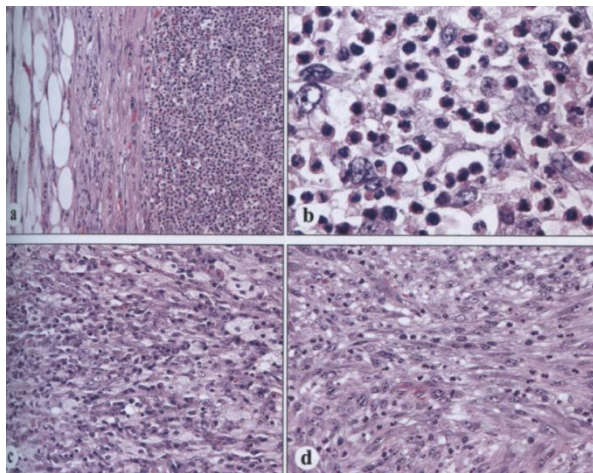


Figure 15.17. [11]

Example of *dedifferentiated liposarcoma resembling inflammatory malignant fibrous histiocytoma*. (A) Low magnification shows sharp demarcation between the components. (B) Scattered atypical cells are present among neutrophils. (C) Abundant xantoma cells and plasma cells obscure the tumor cells. (D) Spindle cell sarcomatous pattern resembling myofibroblastic sarcoma.

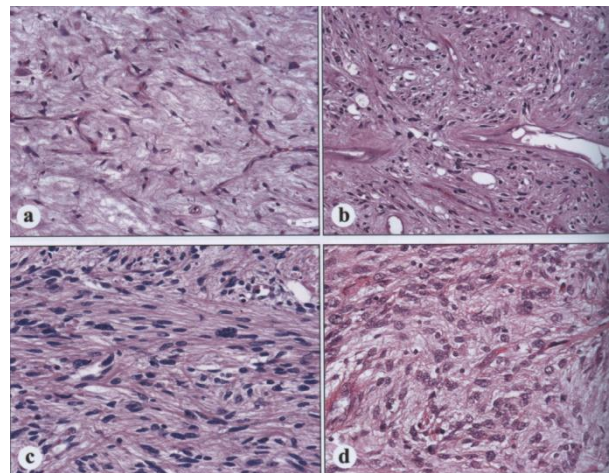


Figure 15.18. [11]

Four examples of *dedifferentiated liposarcoma simulating different sarcoma types*: (A) Myxofibrosarcoma. (B) Solitary fibrous tumor. (C) Fibrosarcoma. (D) Gastrointestinal stromal tumor.

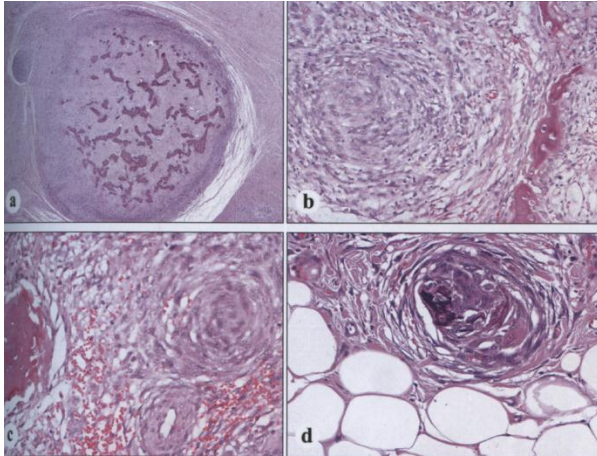


Figure 15.19. [11] (rare example)
Dedifferentiated liposarcoma with concentric perivascular spindle cells resembling meningothelial whorls. (A) Such nodules are often associated with osseous differentiation. (B) Meningothelial nodule at 10 o'clock on side of an area with bone formation. (C,D). The meningothelial nodule is intimately associated with bone formation.

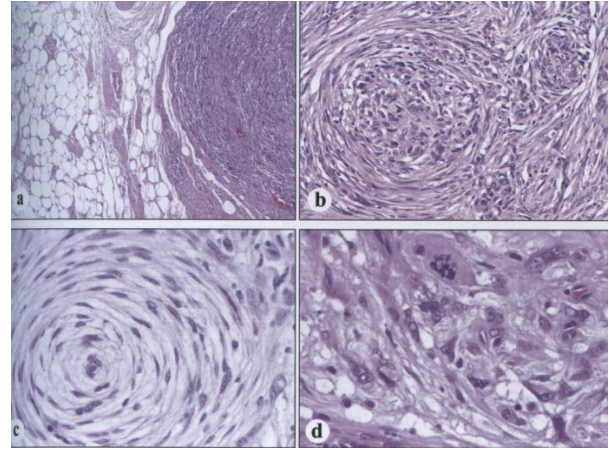


Figure 15.20. [11] (rare example)
Dedifferentiated liposarcoma with meningotheial-like whorls. (A) Abrupt demarcation between the well-differentiated and dedifferentiated components. (B) In some cases, meningothelial whorls are composed of more highly cellular oval cells. (C) Delicate spindle cells forming a distinct whorl composed on concentric lamellae of spindle cells. (D) An atypical mitosis in a dedifferentiated liposarcoma with meningothelial whorls.

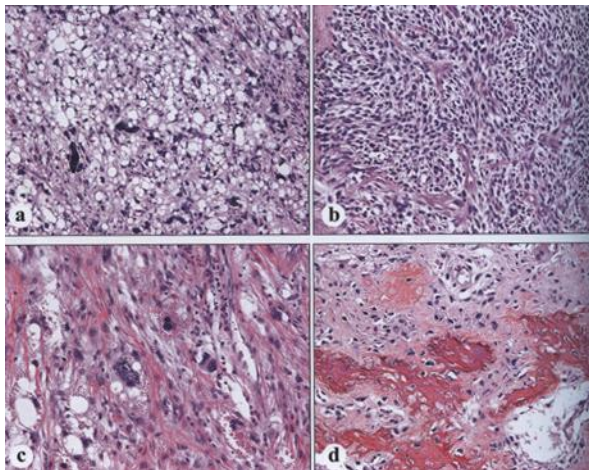


Figure 15.21. [11]
 Different patterns in dedifferentiated liposarcoma. (A) A pleomorphic liposarcomatous component. (B) A mildly pleomorphic spindle cell sarcoma. (C) Pleomorphic component with large cells containing eosinophilic hyaline globules. (D) Osteosarcomatous differentiation.

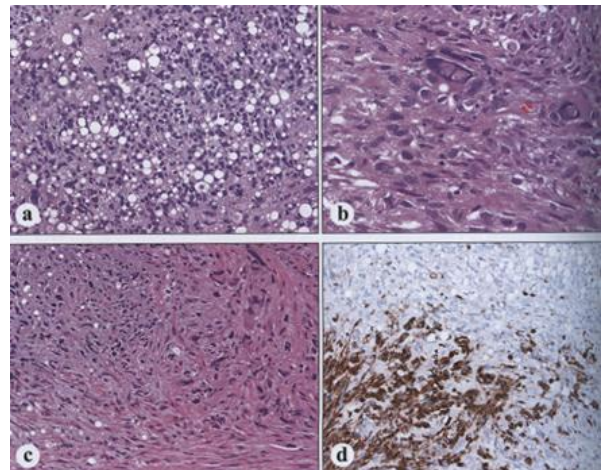


Figure 15.22. [11]
Dedifferentiated liposarcoma with leiomyosarcomatous differentiation. (A) Pleomorphic liposarcoma component. (B) A pleomorphic MFH-like component without specific differentiation. (C) A leiomyosarcomatous component is distinguished by its eosinophilic tinctorial quality. (D) This component is strongly positive for heavy caldesmon.

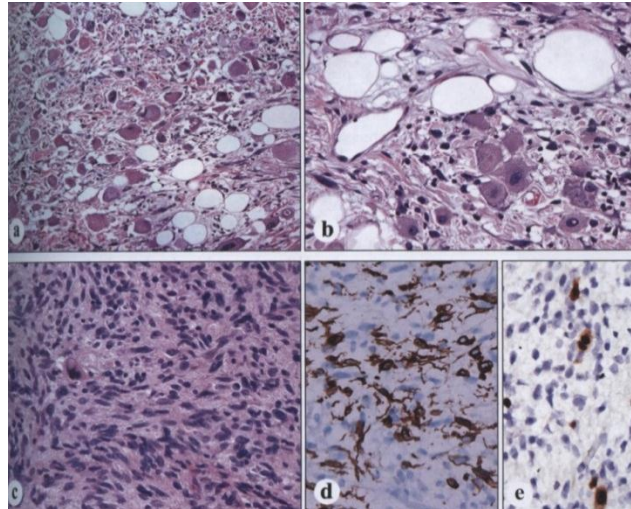


Figure 15.23. [11]

Two examples of *dedifferentiated liposarcoma with rhabdomyosarcomatous differentiation*.

(A,B) An example with well-differentiated rhabdomyoblasts admixed with a lipomatous component. (C) A histologically less obvious example with scattered large rhabdomyoblasts. (D) The number of desmin-positive cells is larger than expected based on HE stain. (E) Myogenin-positive nuclei confirm skeletal muscle differentiation.

3. *Myxoid Liposarcoma (Including Round Cell Liposarcoma)*

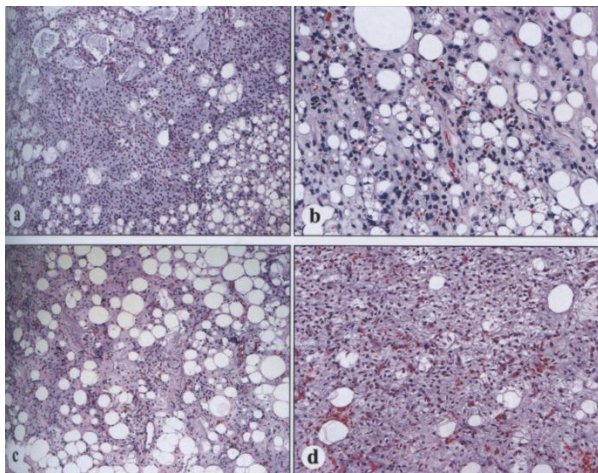


Figure 15.27. [11]

Low magnification of *myxoid liposarcoma* showing variable numbers of adipocytes and a prominent capillary pattern.

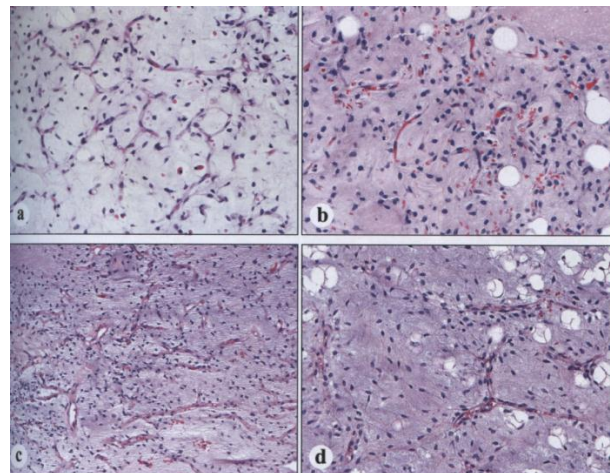


Figure 15.28. [11]

Myxoid liposarcoma with relatively low cellularity shows evenly dispersed, uniform oval tumor cells and a prominent, branching capillary pattern with variable numbers of nonatypical adipocytes.

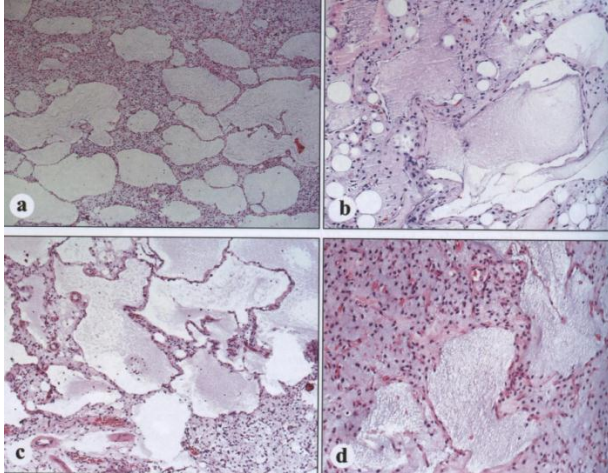


Figure 15.29. [11]

Lymphangioma-like or pulmonary edema-like pattern in myxoid liposarcoma containing acellular spaces filled with mucoid material.

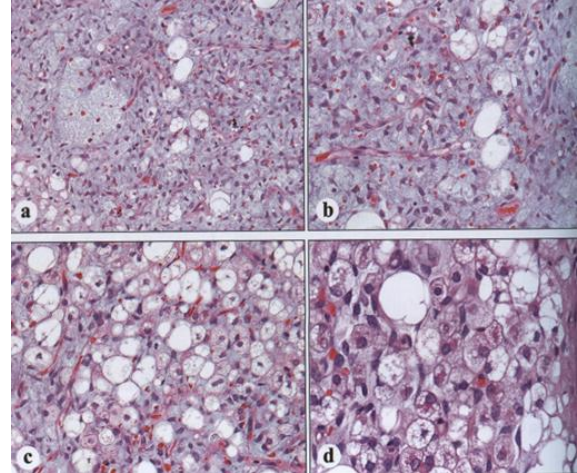


Figure 15.30. [11]

Hibernoma-like pattern in myxoid liposarcoma. Note multivacuolated hibernoma-like cells. White fatlike cells and a prominent, branching capillary pattern are also present.

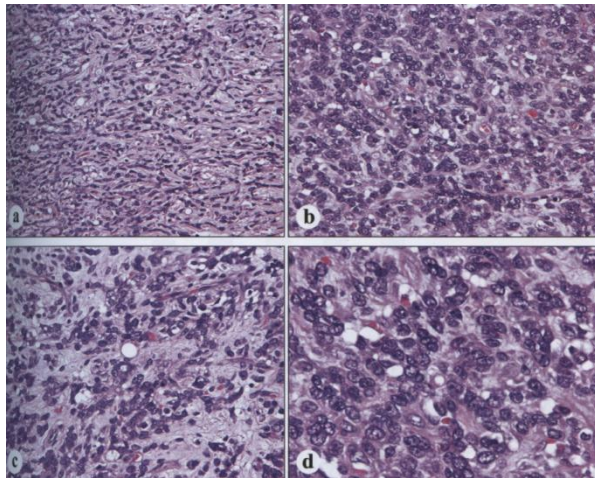


Figure 15.31. [11]

Myxoid liposarcoma with highly cellular round cell liposarcoma pattern containing few cells with adipocytic differentiation. This tumor had also areas typical of low-grade liposarcoma. (A) A trabecular pattern. (B-D) Dense round cell population and a scant adipocytic component can create an illusion of lymphoma.

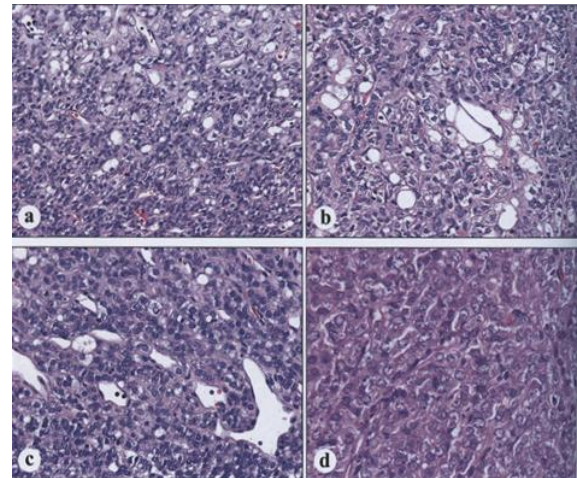


Figure 15.32. [11]

Myxoid liposarcoma with round-cell liposarcoma pattern can show variable collagenous matrix (A,B), a hemangiopericytoma-like vascular pattern (C), and a solid cellular pattern resembling round cell sarcomas or lymphoma (D).

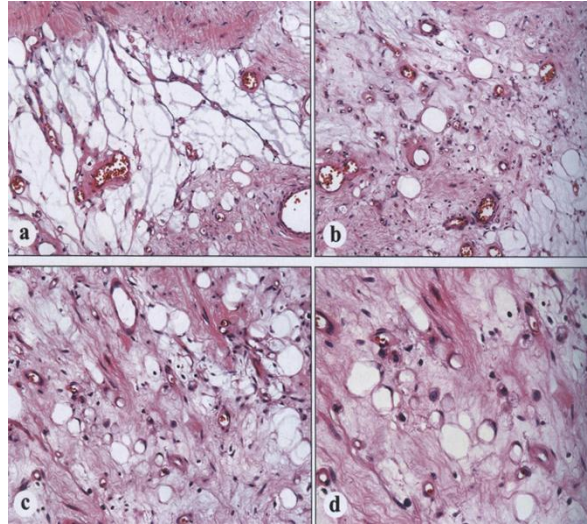


Figure 15.33. [11]

Myxoid liposarcoma following radiation therapy typically shows hyalinized vessels and low cellularity with scattered fat cells. These features are no longer diagnostic of myxoid liposarcoma, although the pretreatment biopsy showed typical features.

4. Pleomorphic Liposarcoma

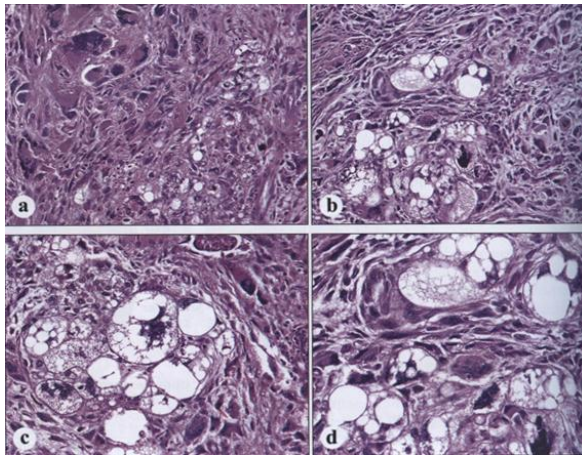


Figure 15.37 [11]

The most common variant of pleomorphic liposarcomas contains multivacuolated, highly atypical tumor cells and undifferentiated large cells similar to those seen in MFH.

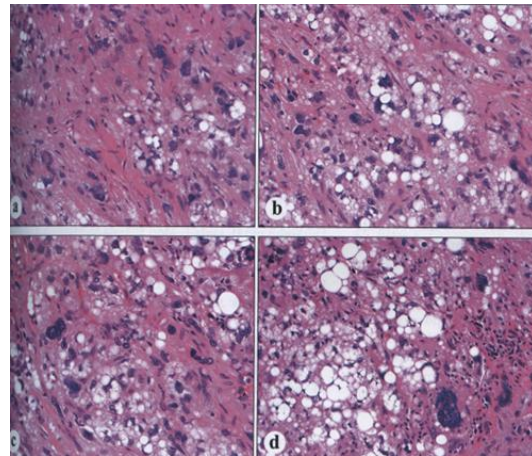


Figure 15.38 [11]

Pleomorphic liposarcoma with markedly atypical nuclei and high cellularity.

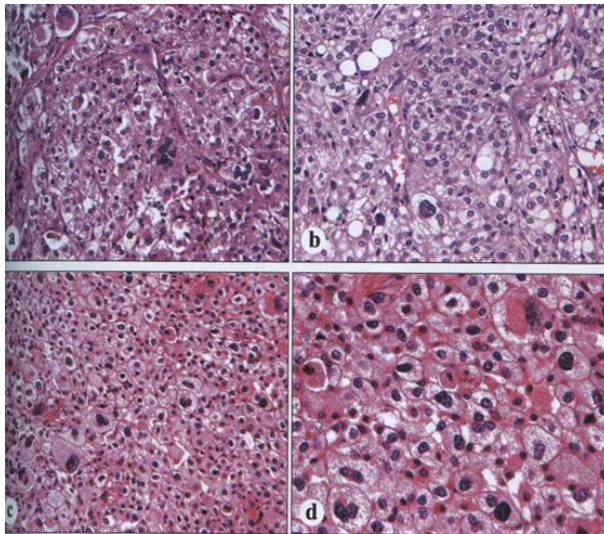


Figure 15.39 [11]

Pleomorphic liposarcoma with epithelioid features. Note distinct cell borders creating a resemblance to adrenal cortical or renal cell carcinoma. Adipocytic differentiation is diagnostic.

References:

[35]

Markku Miettinen, *Diagnostic soft tissue pathology*, 2003 Churchill Livingstone

[11]

Markku M Miettinen, *Modern soft tissue pathology; tumors and non-neoplastic conditions*, 2010.

APPENDIX 2

Generalized Extreme Value Parameters B-scan per B-scan

STD/MEAN

	Normal Fat			WDLS			DDL5		
	K37			K36			K35		
	k	σ	μ	k	σ	μ	k	σ	μ
1	0.2422	0.1879	1.1845	0.1947	0.0647	0.6906	0.0986	0.0575	0.7210
2	0.0445	0.2531	1.2103	0.3730	0.0763	0.6893	-0.3308	0.0662	0.7637
3	0.1095	0.2683	1.2927	0.4392	0.0591	0.7036	-0.0467	0.0501	0.7657
4	-0.0183	0.2225	1.3041	0.1277	0.0723	0.7689	-0.0591	0.0558	0.7817
5	0.4887	0.2941	1.2895	0.1970	0.0629	0.7545	0.0137	0.0547	0.7741
6	-0.1151	0.2720	1.2576	-0.1391	0.0620	0.7052	0.0462	0.0679	0.7803
7	-0.5264	0.2718	1.3457	-0.0413	0.0513	0.6776	-0.1201	0.0471	0.7523
8	-0.0781	0.2150	1.3386	0.2775	0.0393	0.6891	-0.0708	0.0683	0.7747
9	0.0337	0.2013	1.2446	0.0547	0.0511	0.6827	-0.1091	0.0633	0.7681
10	0.3170	0.2714	1.2956	-0.1871	0.0646	0.6945	0.1404	0.0448	0.7511
11	0.2128	0.2092	1.2210	-0.1326	0.0508	0.7147	-0.0274	0.0480	0.7435
12	-0.0217	0.1861	1.2195	0.0006	0.0719	0.7317	0.0001	0.0590	0.7394
13	-0.3535	0.2215	1.4275	0.1827	0.0716	0.7257	0.0854	0.0477	0.7361
14	-0.5094	0.2602	1.3872	0.2572	0.0508	0.7332	0.0610	0.0571	0.7455
15	-0.2536	0.1608	1.3018	-0.1113	0.0734	0.7473	0.1759	0.0477	0.7367
16	0.5093	0.1968	1.2074	0.5371	0.0594	0.7399	0.1480	0.0538	0.7445
17	-0.0927	0.2095	1.2847	-0.2657	0.0407	0.7683	0.0680	0.0384	0.7435
18	-0.1121	0.1959	1.2758	-0.1571	0.0414	0.7639	0.1266	0.0621	0.7613
19	-0.0329	0.2254	1.3530	-0.3641	0.0490	0.7800	0.0596	0.0494	0.7528
20	-0.1472	0.1950	1.3398	-0.1294	0.0544	0.7681	0.0027	0.0757	0.7358
21	-0.1728	0.2194	1.2982	0.6348	0.0454	0.7583	-0.0497	0.0674	0.7754
22	-0.1581	0.1653	1.2206	-0.2165	0.0615	0.7448	0.1843	0.0419	0.7659
23	-0.0148	0.1648	1.2243	0.1927	0.0796	0.7346	0.1435	0.0578	0.7911
24	0.3216	0.2270	1.2892	-0.0745	0.0582	0.7244	-0.0340	0.0680	0.7852
25	0.0908	0.1581	1.2203	0.1852	0.0816	0.7235	0.0239	0.0611	0.7660
26	0.0556	0.2061	1.2693	-0.0037	0.0720	0.6922	0.0504	0.0607	0.7695
27	0.0941	0.1997	1.2139	0.0238	0.0676	0.7321	0.1645	0.0550	0.7621
28	-0.4581	0.2737	1.4550	-0.2036	0.0467	0.7501	-0.0493	0.0660	0.7913
29	0.2258	0.3260	1.3469	0.1519	0.0467	0.7393	0.2601	0.0605	0.7469
30	0.1383	0.2407	1.2871	0.0977	0.0524	0.7330	0.1438	0.0684	0.7080
31	-0.1529	0.2263	1.3008	-0.3725	0.0595	0.7327	0.0300	0.0501	0.6973
32	-0.3621	0.2535	1.3568	0.5903	0.0607	0.6996	-0.0697	0.0713	0.6686
33	0.3052	0.2014	1.1797	0.4688	0.0425	0.6894	0.0846	0.0415	0.6763
34	0.0896	0.1660	1.1641	0.1631	0.0415	0.6822	0.0242	0.0416	0.6562
35	0.1775	0.1226	1.1261	-0.2060	0.0406	0.6969	0.1825	0.0381	0.6337
36	0.2432	0.1700	1.2062	0.4789	0.0331	0.6879	0.2667	0.0319	0.6141
37	-0.0302	0.1661	1.2829	-0.7166	0.0426	0.7145	0.4487	0.0387	0.6005
38	-0.1960	0.1609	1.2704	0.2525	0.0534	0.7098	0.0275	0.0547	0.6125
39	0.0284	0.1372	1.3305	-0.1771	0.0568	0.7289	0.2129	0.0344	0.6139

40	0.3744	0.1267	1.2403	0.0130	0.0553	0.7375	0.1727	0.0377	0.6299
41	-0.1263	0.1931	1.3530	-0.1822	0.0587	0.7760	-0.0652	0.0491	0.6507
42	0.0062	0.1753	1.2754	-0.2486	0.0555	0.7843	0.1396	0.0363	0.6322
43	0.2766	0.1675	1.3012	0.2822	0.0820	0.8383	-0.1211	0.0554	0.6309
44	-0.0891	0.1909	1.2588	0.2720	0.0573	0.8066	0.1687	0.0300	0.6607
45	0.3008	0.2587	1.3194	0.2409	0.0811	0.7689	0.1364	0.0519	0.6278
46	0.1079	0.1580	1.2600	-0.0992	0.0408	0.7422	0.1328	0.0481	0.6159
47	0.1352	0.2277	1.2885	-0.0990	0.0419	0.7040	0.1116	0.0591	0.6281
48	0.1032	0.2534	1.3387	0.0301	0.0503	0.6633	0.2941	0.0432	0.6342
49	-0.1246	0.2770	1.3869	-0.1588	0.0347	0.7127	0.4962	0.0404	0.6465
50	0.1690	0.2047	1.2280	-0.1818	0.0569	0.7218	0.0960	0.0639	0.6613
51	0.1800	0.2309	1.2478	-0.0675	0.0539	0.7329	-0.0967	0.0577	0.6739
52	-0.0288	0.1829	1.3211	0.0396	0.0600	0.7691	0.1799	0.0544	0.6524
53	-0.0016	0.1384	1.2021	-0.0238	0.0574	0.7527	-0.0299	0.0412	0.6480
54	0.1503	0.1731	1.2349	0.1961	0.0570	0.7474	-0.0961	0.0457	0.6535
55	-0.0289	0.1819	1.2083	0.1932	0.0500	0.7599	-0.0199	0.0598	0.6657
56	0.1984	0.2075	1.1786	0.0505	0.0633	0.7422	0.2146	0.0616	0.6534
57	-0.0815	0.2026	1.2126	-0.0952	0.0664	0.7503	0.1011	0.0651	0.6906
58	0.2872	0.2060	1.2631	-0.2584	0.0403	0.7868	0.1339	0.0792	0.7153
59	0.0433	0.1685	1.2884	-0.1133	0.0561	0.7387	0.1285	0.0762	0.6819
60	0.5214	0.1435	1.2137	-0.1946	0.0493	0.7462	0.1577	0.0645	0.6777
61	0.0834	0.2829	1.3696	-0.2413	0.0745	0.7667	-0.0018	0.0788	0.6860
62	0.4151	0.2145	1.2850	-0.4736	0.0495	0.7588	0.1892	0.0743	0.6883
63	-0.0264	0.1892	1.3251	0.1787	0.0518	0.7803	-0.0935	0.0847	0.7069
64	0.0476	0.2263	1.2884	-0.2433	0.0453	0.7189	0.2600	0.0538	0.6830
65	-0.1425	0.1878	1.2505	-0.0895	0.0391	0.7244	0.1974	0.0693	0.6731
66	0.2280	0.1878	1.2068	-0.0648	0.0549	0.6964	0.2158	0.0652	0.6794
67	-0.2148	0.1897	1.2201	-0.0341	0.0460	0.6773	-0.0022	0.0849	0.6519
68	-0.0354	0.1618	1.2396	-0.0338	0.0448	0.7336	0.1247	0.0583	0.6350
69	-0.0403	0.1894	1.2812	-0.0939	0.0582	0.7260	0.2979	0.0532	0.6412
70	0.0447	0.1653	1.2132	-0.0565	0.0421	0.7113	-0.0591	0.0514	0.6329
71	-0.0420	0.1929	1.2416	-0.0318	0.0493	0.7108	-0.1168	0.0365	0.6149
72	0.2237	0.2396	1.3230	-0.0495	0.0354	0.7030	0.3241	0.0258	0.5924
73	0.0792	0.1597	1.2363	-0.0570	0.0572	0.7161	-0.0339	0.0407	0.5818
74	0.5518	0.1346	1.2671	-0.0068	0.0462	0.7358	0.1742	0.0404	0.6101
75	0.1179	0.1817	1.2308	-0.2136	0.0593	0.7096	0.6404	0.0473	0.6044
76	-0.1640	0.1265	1.2038	0.1774	0.0424	0.6991	0.3181	0.0538	0.6016
77	0.1701	0.1418	1.1994	0.0086	0.0520	0.7149	0.9047	0.0694	0.6144
78	0.0203	0.1442	1.1384	0.0021	0.0451	0.7106	0.3404	0.0569	0.6214
79	-0.3157	0.1956	1.2357	0.1960	0.0437	0.6958	-0.0277	0.0470	0.5957
80	-0.2642	0.2119	1.2492	0.0896	0.0348	0.6795	0.0355	0.0537	0.5913
81	-0.2187	0.2270	1.2765	0.2199	0.0453	0.6846	0.0779	0.0477	0.5988
82	0.0230	0.1914	1.1384	-0.2857	0.0619	0.7067	0.2359	0.0369	0.5879
83	0.1163	0.2285	1.2291	-0.3910	0.0578	0.6945	0.1744	0.0347	0.5884
84	0.1917	0.2077	1.1702	-0.6554	0.0690	0.7249	0.1476	0.0378	0.5850
85	0.1238	0.2647	1.3261	-0.1033	0.0688	0.7295	0.1328	0.0414	0.6057
86	0.3670	0.1086	1.1569	0.2061	0.0655	0.7021	0.0754	0.0367	0.6061

87	-0.0118	0.1580	1.1766	0.1780	0.0791	0.7368	0.1148	0.0406	0.6397
88	0.2077	0.1715	1.1941	0.0477	0.0566	0.7251	0.1771	0.0491	0.6319
89	0.1371	0.2066	1.2378	0.3391	0.0442	0.7331	0.0870	0.0461	0.6282
90	0.0000	0.2457	1.2393	0.2920	0.0529	0.7296	0.0715	0.0434	0.6387
91	0.0193	0.1990	1.2596	0.1588	0.0523	0.7060	0.2485	0.0423	0.6283
92	-0.2822	0.1836	1.2230	-0.0072	0.0548	0.7416	0.0728	0.0396	0.6384
93	0.3768	0.2406	1.2886	-0.0673	0.0438	0.7216	-0.1191	0.0388	0.6306
94	-0.0650	0.4112	1.4717	-0.0656	0.0486	0.7153	0.2469	0.0361	0.6119
95	-0.0584	0.2977	1.2673	-0.2121	0.0385	0.7196	0.0963	0.0470	0.6098
96	0.0653	0.2569	1.2887	0.2377	0.0434	0.7039	-0.0090	0.0371	0.6208
97	-0.0192	0.2709	1.2355	-0.1604	0.0449	0.6794	0.3758	0.0247	0.6089
98	-0.1277	0.2937	1.3151	0.1387	0.0381	0.6682	0.0931	0.0423	0.6129
99	-0.2030	0.2478	1.2754	-0.2576	0.0406	0.6643	-0.2266	0.0347	0.6230
100	0.1114	0.3813	1.3556	-0.2518	0.0430	0.6882	0.1203	0.0461	0.6175
101	-0.1944	0.3807	1.4416	-0.0314	0.0342	0.6546	0.1521	0.0417	0.6210
102	-0.3464	0.2390	1.2839	-0.1193	0.0310	0.6510	0.2388	0.0301	0.6202
103	-0.2629	0.2135	1.2648	0.1193	0.0362	0.6648	0.0349	0.0300	0.5962
104	-0.5720	0.2108	1.2726	-0.1806	0.0450	0.6530	0.0590	0.0393	0.6103
105	-0.0287	0.1831	1.2159	-0.1585	0.0553	0.6315	-0.0545	0.0481	0.6192
106	-0.5690	0.2514	1.3323	-0.0967	0.0412	0.6679	0.0335	0.0352	0.5989
107	-0.3548	0.2479	1.3065	0.1020	0.0474	0.6779	0.1449	0.0370	0.5926
108	-0.0343	0.2599	1.2606	-0.1565	0.0650	0.6938	0.3162	0.0332	0.5835
109	0.0275	0.2835	1.2654	-0.1287	0.0671	0.6834	0.0020	0.0325	0.6122
110	-0.3541	0.1908	1.2047	-0.1448	0.0646	0.6768	0.0700	0.0290	0.5883
111	-0.1410	0.2009	1.1830	-0.2851	0.0542	0.6943	-0.0459	0.0342	0.5951
112	-0.0920	0.2218	1.2653	-0.0485	0.0592	0.7169	0.1687	0.0320	0.6079
113	0.2911	0.2897	1.2839	0.0220	0.0420	0.7015	0.0245	0.0287	0.6033
114	0.2872	0.1949	1.2315	-0.2024	0.0372	0.6675	-0.2642	0.0485	0.6197
115	0.4753	0.1368	1.2566	-0.0332	0.0393	0.6498	-0.1438	0.0601	0.6182
116	-0.0715	0.2251	1.2831	0.0402	0.0423	0.6882	0.1297	0.0424	0.6281
117	0.1042	0.2723	1.3165	0.1605	0.0475	0.7028	-0.0366	0.0593	0.6267
118	-0.1181	0.2422	1.3530	-0.7296	0.0554	0.6999	-0.0571	0.0460	0.6365
119	0.0540	0.1873	1.2731	-0.1048	0.0616	0.6965	0.3834	0.0475	0.6337
120	-0.2252	0.1144	1.2244	-0.1518	0.0593	0.6980	-0.1504	0.0711	0.6383
121	0.1188	0.2489	1.2355	0.0111	0.0329	0.6807	-0.0956	0.0703	0.6334
122	-0.0936	0.2410	1.3393	0.1242	0.0448	0.6797	-0.0272	0.0591	0.6277
123	0.1722	0.1910	1.3003	0.0604	0.0516	0.6629	0.3223	0.0553	0.5999
124	0.1351	0.1961	1.3322	-0.1603	0.0522	0.6806	0.2127	0.0525	0.6257
125	-0.0256	0.1903	1.2769	-0.1639	0.0445	0.6529	0.3684	0.0441	0.6284
126	-0.3156	0.1239	1.2612	-0.4902	0.0746	0.6757	0.2770	0.0374	0.6001
127	0.0991	0.1659	1.2818	0.0338	0.0538	0.6863	-0.2241	0.0374	0.6172
128	-0.2135	0.2211	1.3465	-0.1750	0.0452	0.6684	-0.1713	0.0404	0.6194
129	-0.2018	0.1308	1.2537	-0.1944	0.0482	0.6347	-0.1055	0.0453	0.6282
130	-0.2738	0.1317	1.1918	-0.2213	0.0663	0.6563	0.1597	0.0451	0.6038
131	0.0931	0.1869	1.3498	-0.1394	0.0550	0.6633	0.1783	0.0369	0.6230
132	-0.1391	0.1440	1.3260	0.0165	0.0464	0.6676	-0.0637	0.0451	0.6127
133	0.2049	0.1471	1.3241	-0.1644	0.0687	0.6754	-0.1259	0.0501	0.6088

134	-0.1290	0.1517	1.2664	-0.3567	0.0573	0.6851	-0.0641	0.0648	0.6089
135	-0.4373	0.1967	1.2783	-0.1150	0.0374	0.6784	0.2594	0.0595	0.5782
136	-0.2683	0.1333	1.3040	0.0670	0.0412	0.6875	0.0953	0.0599	0.6097
137	0.0765	0.1286	1.3270	0.1662	0.0596	0.7028	0.2021	0.0631	0.6140
138	0.1941	0.3029	1.4236	0.2399	0.0531	0.6772	0.0065	0.0593	0.6270
139	-0.0626	0.2241	1.3999	0.0950	0.0339	0.6853	-0.0643	0.0536	0.6157
140	-0.5387	0.1884	1.3278	0.0372	0.0511	0.6723	-0.0285	0.0373	0.6265
141	-0.3263	0.2130	1.2815	-0.0682	0.0425	0.6892	-0.1947	0.0492	0.6064
142	0.0076	0.1846	1.2701	0.3771	0.0455	0.6958	0.2058	0.0351	0.6138
143	-0.3112	0.2178	1.3953	0.9543	0.0553	0.7084	0.0059	0.0495	0.6030
144	-0.1892	0.1451	1.2420	0.6511	0.0530	0.6732	0.4027	0.0409	0.5971
145	0.1456	0.1788	1.2017	0.0461	0.0520	0.6790	0.0572	0.0352	0.6054
146	-0.0506	0.2765	1.3088	-0.0313	0.0516	0.6792	0.0884	0.0342	0.6058
147	-0.3078	0.2192	1.3471	0.0817	0.0573	0.6809	0.1577	0.0261	0.6034
148	-0.1653	0.1793	1.2187	-0.1707	0.0452	0.6788	-0.1567	0.0415	0.6115
149	-0.0454	0.1776	1.2056	-0.1400	0.0524	0.6672	-0.0490	0.0383	0.6338
150	-0.2506	0.1674	1.2121	0.1373	0.0451	0.6945	-0.1059	0.0410	0.6477
151	-0.3585	0.1443	1.2173	-0.3473	0.0432	0.6702	-0.1273	0.0556	0.6265
152	-0.3060	0.2117	1.2583	-0.0370	0.0398	0.6773	0.0391	0.0479	0.6094
153	-0.3051	0.2064	1.2956	0.1070	0.0264	0.6721	0.1669	0.0437	0.6219
154	0.1549	0.2980	1.3223	-0.0701	0.0417	0.6765	0.2936	0.0456	0.5740
155	-0.0067	0.2641	1.2951	0.0999	0.0651	0.6921	0.1886	0.0430	0.5964
156	-0.0597	0.2689	1.2601	-0.0220	0.0582	0.7135	0.0796	0.0433	0.5939
157	-0.2616	0.1898	1.2884	-0.1287	0.0521	0.7167	0.0473	0.0363	0.6067
158	-0.0504	0.1561	1.2024	0.0794	0.0699	0.7527	0.0886	0.0532	0.6034
159	0.0631	0.2352	1.2843	0.1193	0.0655	0.7449	0.0004	0.0378	0.6109
160	-0.2244	0.2958	1.3432	-0.5328	0.0976	0.7559	-0.0091	0.0488	0.6407
161	-0.0391	0.2554	1.3776						
162	0.1133	0.1751	1.2261						
163	-0.4437	0.2844	1.4032						
164	0.0504	0.3223	1.3217						
165	-0.1478	0.1351	1.2444						
166	-0.1796	0.1901	1.2745						
167	-0.2061	0.2314	1.2196						
168	-0.0673	0.1768	1.2378						
169	-0.3022	0.1784	1.2951						
170	0.2491	0.2546	1.3583						
171	-0.0461	0.1400	1.1891						
172	0.1315	0.2322	1.2683						
173	-0.0292	0.3083	1.2774						
174	0.2960	0.2649	1.2925						
175	0.1018	0.2947	1.3357						
176	0.3759	0.3210	1.3099						
177	0.0893	0.3065	1.3732						
178	0.3068	0.2414	1.2773						
179	0.1628	0.3953	1.4213						

180	-0.1177	0.3283	1.3795						
181	0.3368	0.3378	1.3602						
182	0.0807	0.2322	1.2618						
183	0.2885	0.1642	1.2701						
184	0.3843	0.2769	1.2716						
185	0.3876	0.3020	1.4265						
186	0.1598	0.2518	1.2882						
187	-0.2587	0.2884	1.4189						
188	0.0895	0.3586	1.3773						
189	-0.2272	0.2904	1.3767						
190	0.1986	0.2203	1.4040						
191	0.2126	0.1560	1.3208						
192	0.2914	0.1504	1.1734						
193	0.0877	0.1750	1.2449						
194	-0.1060	0.2143	1.2565						
195	-0.0682	0.2963	1.3450						
196	-0.6322	0.2425	1.3793						
197	0.2791	0.2690	1.3255						
198	0.3570	0.1714	1.2918						
199	0.3613	0.1098	1.1802						
200	0.4194	0.1642	1.1774						
mean	0.0007	0.2151	1.2796	-0.0128	0.0529	0.7093	0.0857	0.0493	0.6502
std +/-	0.2347	0.0579	0.0659	0.2443	0.0120	0.0359	0.1673	0.0128	0.0584
std/m.	319.0928	0.2690	0.0515	-19.0613	0.2274	0.0507	1.9510	0.2591	0.0898

Generalized Extreme Value Parameters B-scan per B-scan

Intensity values normalized by mean

	Normal Fat			WDLS			DLS		
	K37			K36			K35		
	k	σ	μ	k	σ	μ	k	σ	μ
1	0.7060	0.3789	0.3597	0.2068	0.4426	0.6390	0.2329	0.4418	0.6251
2	0.7114	0.3742	0.3600	0.2001	0.4435	0.6390	0.2739	0.4374	0.6053
3	0.7674	0.3565	0.3351	0.2239	0.4451	0.6262	0.2685	0.4435	0.6030
4	0.7720	0.3585	0.3355	0.2631	0.4397	0.6058	0.2800	0.4430	0.5957
5	0.7954	0.3449	0.3153	0.2640	0.4426	0.6048	0.2759	0.4382	0.6013
6	0.7399	0.3714	0.3468	0.1998	0.4464	0.6412	0.2744	0.4427	0.5977
7	0.8141	0.3549	0.3208	0.1577	0.4538	0.6591	0.2522	0.4480	0.6107
8	0.8103	0.3525	0.3193	0.1801	0.4512	0.6485	0.2764	0.4399	0.6003
9	0.7792	0.3636	0.3354	0.1765	0.4484	0.6524	0.2731	0.4462	0.5994
10	0.8697	0.3359	0.2950	0.1794	0.4461	0.6522	0.2671	0.4456	0.6038
11	0.8619	0.3477	0.3073	0.1800	0.4606	0.6413	0.2539	0.4477	0.6104
12	0.7935	0.3649	0.3336	0.1983	0.4655	0.6261	0.2378	0.4471	0.6182
13	0.8336	0.3402	0.3107	0.1986	0.4711	0.6216	0.2475	0.4471	0.6143
14	0.9007	0.3317	0.2900	0.2001	0.4699	0.6217	0.2575	0.4484	0.6065
15	0.8636	0.3436	0.3050	0.1953	0.4760	0.6198	0.2457	0.4422	0.6173
16	0.8309	0.3520	0.3126	0.2164	0.4700	0.6106	0.2475	0.4504	0.6091
17	0.8263	0.3540	0.3170	0.2211	0.4699	0.6107	0.2365	0.4435	0.6218
18	0.8570	0.3499	0.3077	0.2241	0.4652	0.6123	0.2675	0.4473	0.5992
19	0.8511	0.3407	0.3050	0.2450	0.4662	0.5998	0.2605	0.4392	0.6107
20	0.8720	0.3402	0.3032	0.2364	0.4677	0.6031	0.2564	0.4423	0.6110
21	0.8185	0.3546	0.3194	0.2519	0.4529	0.6010	0.2926	0.4375	0.5930
22	0.7964	0.3690	0.3342	0.2205	0.4510	0.6247	0.2919	0.4370	0.5953
23	0.7902	0.3641	0.3351	0.2392	0.4416	0.6189	0.3025	0.4355	0.5871
24	0.8151	0.3496	0.3176	0.2107	0.4496	0.6318	0.2985	0.4393	0.5876
25	0.8123	0.3637	0.3268	0.2201	0.4461	0.6270	0.2791	0.4430	0.5973
26	0.8509	0.3502	0.3080	0.1857	0.4524	0.6440	0.2870	0.4450	0.5912
27	0.7657	0.3684	0.3397	0.2325	0.4512	0.6182	0.2783	0.4413	0.5985
28	0.7926	0.3531	0.3222	0.2087	0.4661	0.6207	0.2890	0.4399	0.5916
29	0.8962	0.3311	0.2866	0.2027	0.4701	0.6207	0.2556	0.4400	0.6113
30	0.8442	0.3493	0.3082	0.2079	0.4668	0.6209	0.2291	0.4434	0.6263
31	0.8518	0.3461	0.3087	0.2025	0.4584	0.6307	0.2017	0.4536	0.6360
32	0.8517	0.3480	0.3084	0.2024	0.4489	0.6305	0.1616	0.4556	0.6558
33	0.7911	0.3669	0.3313	0.1917	0.4471	0.6436	0.1660	0.4538	0.6547
34	0.8146	0.3648	0.3283	0.1796	0.4527	0.6483	0.1495	0.4480	0.6679
35	0.7218	0.3920	0.3621	0.1768	0.4529	0.6497	0.1251	0.4491	0.6799
36	0.7209	0.3729	0.3571	0.1749	0.4563	0.6466	0.0957	0.4534	0.6920
37	0.8057	0.3562	0.3230	0.1682	0.4608	0.6484	0.1129	0.4495	0.6857
38	0.8172	0.3591	0.3221	0.1827	0.4614	0.6382	0.1053	0.4508	0.6890
39	0.8533	0.3457	0.3046	0.1896	0.4722	0.6276	0.0873	0.4561	0.6944

40	0.8142	0.3582	0.3231	0.2145	0.4736	0.6125	0.1179	0.4502	0.6828
41	0.8996	0.3318	0.2894	0.2317	0.4755	0.5996	0.1338	0.4483	0.6756
42	0.8204	0.3531	0.3199	0.2233	0.4850	0.5975	0.1118	0.4475	0.6876
43	0.8225	0.3486	0.3148	0.3055	0.4697	0.5535	0.1135	0.4480	0.6866
44	0.8528	0.3503	0.3111	0.2663	0.4711	0.5796	0.1404	0.4506	0.6706
45	0.8377	0.3452	0.3073	0.2362	0.4689	0.5987	0.1235	0.4514	0.6791
46	0.8253	0.3587	0.3206	0.2001	0.4739	0.6209	0.1084	0.4491	0.6884
47	0.8720	0.3446	0.2999	0.1896	0.4547	0.6416	0.1335	0.4433	0.6793
48	0.8744	0.3419	0.3006	0.1549	0.4547	0.6604	0.1404	0.4455	0.6739
49	0.8979	0.3344	0.2892	0.1880	0.4642	0.6358	0.1611	0.4449	0.6633
50	0.7757	0.3694	0.3343	0.1869	0.4678	0.6328	0.1547	0.4519	0.6613
51	0.7712	0.3671	0.3398	0.2082	0.4591	0.6261	0.1682	0.4375	0.6643
52	0.7485	0.3679	0.3432	0.2352	0.4629	0.6065	0.1556	0.4456	0.6656
53	0.7880	0.3678	0.3395	0.2442	0.4585	0.6066	0.1345	0.4456	0.6773
54	0.8054	0.3624	0.3284	0.2435	0.4580	0.6063	0.1431	0.4402	0.6764
55	0.7639	0.3717	0.3455	0.2440	0.4552	0.6074	0.1599	0.4411	0.6662
56	0.7136	0.3817	0.3616	0.2365	0.4565	0.6118	0.1609	0.4464	0.6619
57	0.7334	0.3811	0.3554	0.2478	0.4504	0.6100	0.2083	0.4417	0.6394
58	0.7447	0.3721	0.3442	0.2630	0.4605	0.5944	0.2204	0.4435	0.6288
59	0.7827	0.3623	0.3331	0.2453	0.4561	0.6099	0.2102	0.4481	0.6340
60	0.8106	0.3554	0.3234	0.2206	0.4635	0.6173	0.1999	0.4487	0.6397
61	0.8803	0.3282	0.2917	0.2333	0.4701	0.6033	0.2163	0.4505	0.6301
62	0.8856	0.3398	0.2962	0.2096	0.4771	0.6130	0.2260	0.4418	0.6296
63	0.8776	0.3411	0.2988	0.2451	0.4650	0.5984	0.2227	0.4428	0.6305
64	0.8239	0.3551	0.3173	0.1735	0.4658	0.6412	0.1976	0.4478	0.6412
65	0.7512	0.3690	0.3468	0.1893	0.4722	0.6288	0.1936	0.4443	0.6454
66	0.7392	0.3741	0.3513	0.1863	0.4591	0.6403	0.1924	0.4408	0.6477
67	0.7136	0.3844	0.3632	0.1550	0.4550	0.6597	0.1602	0.4468	0.6622
68	0.7518	0.3711	0.3474	0.2204	0.4490	0.6275	0.1453	0.4448	0.6722
69	0.7124	0.3764	0.3582	0.2041	0.4610	0.6277	0.1341	0.4459	0.6765
70	0.6895	0.3878	0.3713	0.1674	0.4724	0.6405	0.1257	0.4444	0.6830
71	0.8288	0.3589	0.3217	0.1651	0.4758	0.6389	0.0845	0.4480	0.7012
72	0.8730	0.3410	0.2992	0.1445	0.4782	0.6488	0.0784	0.4439	0.7070
73	0.8601	0.3542	0.3104	0.1611	0.4864	0.6336	0.0603	0.4438	0.7156
74	0.8863	0.3369	0.2954	0.1877	0.4794	0.6232	0.0990	0.4462	0.6952
75	0.7772	0.3662	0.3373	0.1667	0.4759	0.6383	0.1140	0.4448	0.6871
76	0.7168	0.3832	0.3642	0.1992	0.4569	0.6346	0.1028	0.4485	0.6913
77	0.7318	0.3762	0.3552	0.1971	0.4591	0.6332	0.1418	0.4411	0.6721
78	0.6862	0.3942	0.3758	0.2056	0.4541	0.6330	0.1274	0.4506	0.6764
79	0.6532	0.3931	0.3824	0.1861	0.4542	0.6431	0.0743	0.4468	0.7071
80	0.6318	0.3909	0.3911	0.1527	0.4578	0.6591	0.0756	0.4489	0.7051
81	0.6695	0.3870	0.3736	0.1878	0.4542	0.6429	0.0814	0.4532	0.6993
82	0.6593	0.3924	0.3840	0.1817	0.4506	0.6477	0.0661	0.4492	0.7096
83	0.6799	0.3838	0.3730	0.1745	0.4499	0.6529	0.0730	0.4437	0.7097
84	0.7791	0.3666	0.3380	0.1804	0.4594	0.6419	0.0473	0.4584	0.7126
85	0.8011	0.3466	0.3203	0.2107	0.4569	0.6261	0.0820	0.4558	0.6973
86	0.6900	0.3893	0.3715	0.1784	0.4604	0.6405	0.0812	0.4527	0.6997

87	0.7499	0.3805	0.3510	0.2231	0.4622	0.6127	0.1245	0.4455	0.6824
88	0.7139	0.3838	0.3589	0.1957	0.4650	0.6284	0.1331	0.4434	0.6795
89	0.8030	0.3606	0.3260	0.2200	0.4565	0.6203	0.1110	0.4508	0.6859
90	0.7582	0.3711	0.3409	0.2282	0.4522	0.6195	0.1291	0.4478	0.6787
91	0.7641	0.3656	0.3348	0.2072	0.4529	0.6323	0.1255	0.4462	0.6815
92	0.6745	0.3935	0.3734	0.2382	0.4558	0.6125	0.1233	0.4496	0.6805
93	0.8102	0.3542	0.3178	0.2102	0.4562	0.6289	0.1105	0.4458	0.6897
94	0.9022	0.3179	0.2780	0.2101	0.4534	0.6311	0.0964	0.4557	0.6901
95	0.8367	0.3526	0.3131	0.2011	0.4548	0.6350	0.1013	0.4466	0.6938
96	0.8261	0.3492	0.3158	0.1892	0.4497	0.6438	0.0929	0.4508	0.6952
97	0.8014	0.3556	0.3240	0.1481	0.4551	0.6634	0.0872	0.4560	0.6946
98	0.7692	0.3617	0.3326	0.1330	0.4629	0.6658	0.1008	0.4474	0.6936
99	0.8000	0.3674	0.3279	0.1182	0.4686	0.6702	0.0905	0.4471	0.6989
100	0.8680	0.3373	0.2933	0.1494	0.4655	0.6555	0.1013	0.4534	0.6892
101	0.8754	0.3328	0.2913	0.1357	0.4521	0.6726	0.0997	0.4574	0.6874
102	0.8315	0.3565	0.3161	0.1210	0.4551	0.6781	0.1009	0.4542	0.6888
103	0.8159	0.3595	0.3259	0.1409	0.4557	0.6668	0.0674	0.4482	0.7093
104	0.8142	0.3650	0.3251	0.1351	0.4513	0.6734	0.0894	0.4473	0.6993
105	0.7700	0.3728	0.3408	0.1149	0.4505	0.6843	0.0992	0.4481	0.6938
106	0.8444	0.3539	0.3131	0.1527	0.4514	0.6640	0.0702	0.4512	0.7060
107	0.8947	0.3425	0.2961	0.1489	0.4635	0.6567	0.0690	0.4527	0.7057
108	0.8840	0.3447	0.2998	0.1516	0.4636	0.6543	0.0611	0.4511	0.7106
109	0.8717	0.3434	0.3004	0.1548	0.4665	0.6514	0.0836	0.4502	0.7002
110	0.8134	0.3655	0.3285	0.1639	0.4568	0.6538	0.0507	0.4522	0.7147
111	0.7176	0.3882	0.3620	0.1741	0.4513	0.6520	0.0657	0.4485	0.7100
112	0.8285	0.3557	0.3180	0.1998	0.4520	0.6361	0.0916	0.4466	0.6987
113	0.9521	0.3246	0.2732	0.1848	0.4511	0.6459	0.0773	0.4462	0.7060
114	0.8346	0.3525	0.3145	0.1400	0.4559	0.6677	0.0956	0.4458	0.6972
115	0.8668	0.3416	0.3006	0.1358	0.4516	0.6731	0.1076	0.4438	0.6925
116	0.8244	0.3558	0.3167	0.1817	0.4500	0.6493	0.1165	0.4498	0.6839
117	0.8913	0.3345	0.2932	0.2132	0.4480	0.6331	0.1119	0.4440	0.6899
118	0.8557	0.3412	0.3033	0.1707	0.4452	0.6582	0.1233	0.4426	0.6851
119	0.8388	0.3505	0.3131	0.1942	0.4463	0.6446	0.1411	0.4441	0.6745
120	0.7545	0.3780	0.3465	0.1747	0.4478	0.6533	0.1331	0.4469	0.6770
121	0.7978	0.3616	0.3251	0.1548	0.4529	0.6612	0.1361	0.4430	0.6782
122	0.8727	0.3380	0.2959	0.1675	0.4499	0.6565	0.1309	0.4416	0.6821
123	0.9039	0.3346	0.2879	0.1457	0.4515	0.6669	0.1210	0.4415	0.6872
124	0.8265	0.3422	0.3102	0.1645	0.4494	0.6587	0.1287	0.4411	0.6831
125	0.7807	0.3591	0.3318	0.1317	0.4472	0.6777	0.1382	0.4396	0.6792
126	0.7573	0.3668	0.3432	0.1571	0.4492	0.6629	0.0944	0.4402	0.7015
127	0.8598	0.3487	0.3055	0.1647	0.4518	0.6558	0.0951	0.4449	0.6981
128	0.9092	0.3364	0.2901	0.1363	0.4551	0.6696	0.0942	0.4472	0.6970
129	0.7565	0.3653	0.3416	0.1050	0.4535	0.6873	0.1154	0.4380	0.6923
130	0.7607	0.3682	0.3468	0.1447	0.4478	0.6704	0.0999	0.4412	0.6982
131	0.9175	0.3195	0.2805	0.1511	0.4493	0.6662	0.1176	0.4439	0.6875
132	0.9529	0.3245	0.2760	0.1560	0.4482	0.6641	0.0888	0.4489	0.6985
133	0.8634	0.3339	0.2987	0.1548	0.4505	0.6625	0.0843	0.4459	0.7027

134	0.7690	0.3546	0.3375	0.1520	0.4508	0.6638	0.1027	0.4459	0.6935
135	0.8727	0.3508	0.3055	0.1535	0.4470	0.6659	0.0888	0.4464	0.7003
136	0.8196	0.3475	0.3208	0.1761	0.4520	0.6504	0.1079	0.4476	0.6897
137	0.8635	0.3326	0.3022	0.2123	0.4475	0.6331	0.1281	0.4441	0.6816
138	0.9442	0.3127	0.2695	0.1725	0.4500	0.6529	0.1225	0.4474	0.6823
139	0.9478	0.3117	0.2697	0.1737	0.4484	0.6544	0.1066	0.4451	0.6921
140	0.9285	0.3335	0.2835	0.1607	0.4516	0.6590	0.1095	0.4410	0.6933
141	0.8444	0.3417	0.3117	0.1767	0.4470	0.6538	0.0848	0.4441	0.7038
142	0.8640	0.3436	0.3041	0.1973	0.4466	0.6406	0.1050	0.4426	0.6946
143	0.9124	0.3254	0.2809	0.2430	0.4349	0.6056	0.0902	0.4450	0.7004
144	0.7920	0.3650	0.3328	0.1824	0.4438	0.6443	0.1035	0.4424	0.6955
145	0.7704	0.3672	0.3398	0.1659	0.4474	0.6587	0.0875	0.4465	0.7008
146	0.8990	0.3298	0.2870	0.1683	0.4465	0.6583	0.0876	0.4478	0.6999
147	0.9571	0.3196	0.2731	0.1807	0.4423	0.6541	0.0816	0.4469	0.7034
148	0.8397	0.3574	0.3170	0.1683	0.4415	0.6621	0.0903	0.4479	0.6985
149	0.7951	0.3680	0.3325	0.1559	0.4424	0.6680	0.1156	0.4496	0.6846
150	0.8012	0.3688	0.3333	0.1839	0.4410	0.6528	0.1330	0.4470	0.6775
151	0.7994	0.3657	0.3369	0.1539	0.4422	0.6696	0.1177	0.4428	0.6880
152	0.7934	0.3618	0.3337	0.1693	0.4496	0.6565	0.1014	0.4455	0.6946
153	0.8309	0.3472	0.3176	0.1567	0.4478	0.6642	0.1156	0.4436	0.6885
154	0.8736	0.3340	0.2953	0.1631	0.4498	0.6594	0.0719	0.4461	0.7087
155	0.8236	0.3519	0.3151	0.1984	0.4416	0.6447	0.0938	0.4457	0.6982
156	0.8451	0.3467	0.3112	0.2142	0.4473	0.6322	0.0751	0.4485	0.7056
157	0.8290	0.3544	0.3169	0.2146	0.4493	0.6313	0.0815	0.4475	0.7031
158	0.8523	0.3512	0.3143	0.2564	0.4436	0.6090	0.1030	0.4445	0.6944
159	0.8765	0.3377	0.3005	0.2456	0.4439	0.6149	0.0980	0.4419	0.6987
160	0.8322	0.3448	0.3103	0.2311	0.4478	0.6203	0.1257	0.4434	0.6832
161	0.8679	0.3399	0.2972						
162	0.8794	0.3471	0.3021						
163	0.8932	0.3300	0.2927						
164	0.8816	0.3338	0.2959						
165	0.8172	0.3627	0.3254						
166	0.8368	0.3555	0.3158						
167	0.8013	0.3606	0.3313						
168	0.8165	0.3603	0.3267						
169	0.8784	0.3434	0.3035						
170	0.8639	0.3380	0.2941						
171	0.7885	0.3735	0.3375						
172	0.7974	0.3622	0.3288						
173	0.7466	0.3668	0.3414						
174	0.8102	0.3459	0.3159						
175	0.8236	0.3448	0.3122						
176	0.8908	0.3265	0.2874						
177	0.8618	0.3298	0.2960						
178	0.8267	0.3451	0.3134						
179	0.9710	0.3028	0.2566						

180	0.9162	0.3250	0.2799						
181	0.9107	0.3183	0.2767						
182	0.8254	0.3528	0.3201						
183	0.8657	0.3404	0.3035						
184	0.9046	0.3294	0.2811						
185	0.9117	0.3164	0.2766						
186	0.8509	0.3429	0.3070						
187	0.8406	0.3435	0.3058						
188	0.8942	0.3297	0.2839						
189	0.9338	0.3229	0.2771						
190	0.8654	0.3265	0.2907						
191	0.8334	0.3400	0.3107						
192	0.7918	0.3657	0.3353						
193	0.8175	0.3593	0.3232						
194	0.8452	0.3495	0.3109						
195	0.8916	0.3348	0.2925						
196	0.8996	0.3361	0.2909						
197	0.8085	0.3499	0.3178						
198	0.8429	0.3489	0.3092						
199	0.7892	0.3664	0.3335						
200	0.7343	0.3722	0.3532						
mean	0.8209	0.3532	0.3191	0.1905	0.4561	0.6381	0.1447	0.4462	0.6700
std +/-	0.0647	0.0181	0.0254	0.0358	0.0100	0.0229	0.0684	0.0044	0.0364
std/m.	0.0789	0.0513	0.0796	0.1878	0.0220	0.0359	0.4728	0.0099	0.0543

Normal Fat									
	K28			K19			K22		
	k	σ	μ	k	σ	μ	k	σ	μ
1	0.4500	0.3917	0.5017	0.4746	0.3975	0.4836	0.5919	0.3574	0.4093
2	0.3999	0.4077	0.5358	0.4682	0.4042	0.4873	0.5515	0.3751	0.4355
3	0.4279	0.4022	0.5187	0.5171	0.3904	0.4604	0.5424	0.3796	0.4474
4	0.4432	0.3971	0.5073	0.4652	0.4023	0.4934	0.5071	0.3887	0.4675
5	0.4570	0.3939	0.5042	0.4959	0.3966	0.4715	0.5052	0.3942	0.4678
6	0.4537	0.3859	0.4933	0.4815	0.4000	0.4802	0.5493	0.3804	0.4447
7	0.3805	0.4187	0.5458	0.4742	0.4031	0.4872	0.5729	0.3684	0.4276
8	0.4152	0.4036	0.5273	0.4864	0.3967	0.4773	0.5637	0.3769	0.4410
9	0.3446	0.4236	0.5662	0.4432	0.4090	0.5078	0.5411	0.3810	0.4505
10	0.3707	0.4159	0.5511	0.4427	0.4086	0.5052	0.5080	0.3945	0.4691
11	0.3966	0.4118	0.5352	0.4957	0.3950	0.4719	0.5026	0.3852	0.4700
12	0.4397	0.4045	0.5139	0.4861	0.4018	0.4852	0.4943	0.3883	0.4705
13	0.4241	0.4038	0.5155	0.5012	0.3923	0.4740	0.5380	0.3619	0.4333
14	0.4326	0.4043	0.5171	0.4630	0.4016	0.4918	0.5379	0.3766	0.4472
15	0.4030	0.4109	0.5365	0.5259	0.3913	0.4603	0.5459	0.3727	0.4486
16	0.4050	0.4115	0.5318	0.5548	0.3844	0.4362	0.4764	0.3931	0.4850
17	0.4241	0.4090	0.5194	0.5720	0.3667	0.4203	0.5320	0.3819	0.4533
18	0.4410	0.4022	0.5139	0.6038	0.3666	0.4096	0.4846	0.3916	0.4822
19	0.4528	0.3982	0.5039	0.5484	0.3881	0.4428	0.5220	0.3781	0.4554
20	0.4283	0.4077	0.5234	0.5377	0.3872	0.4513	0.5365	0.3718	0.4430
21	0.4031	0.4142	0.5383	0.3403	0.4252	0.5539	0.4840	0.3839	0.4744
22	0.4086	0.4135	0.5319	0.3087	0.4315	0.5764	0.5162	0.3799	0.4537
23	0.4347	0.4063	0.5204	0.3103	0.4315	0.5763	0.5306	0.3687	0.4440
24	0.4260	0.4051	0.5221	0.2974	0.4299	0.5815	0.4768	0.4008	0.4884
25	0.4093	0.4062	0.5283	0.2913	0.4310	0.5816	0.4647	0.3945	0.4940
26	0.4315	0.3955	0.5133	0.3498	0.4287	0.5508	0.5077	0.3837	0.4650
27	0.3972	0.4040	0.5320	0.3138	0.4378	0.5711	0.5200	0.3828	0.4688
28	0.3708	0.4149	0.5547	0.3405	0.4265	0.5543	0.4949	0.3823	0.4764
29	0.3676	0.4148	0.5561	0.2346	0.4469	0.6149	0.5089	0.3873	0.4741
30	0.4004	0.4086	0.5360	0.2505	0.4450	0.6050	0.5079	0.3844	0.4670
31	0.3886	0.4054	0.5396	0.2938	0.4355	0.5780	0.5146	0.3852	0.4665
32	0.3708	0.4059	0.5481	0.3092	0.4367	0.5770	0.5391	0.3714	0.4491
33	0.3713	0.4082	0.5503	0.3397	0.4266	0.5573	0.5209	0.3794	0.4564
34	0.3903	0.4033	0.5428	0.3265	0.4279	0.5646	0.5070	0.3787	0.4660
35	0.3722	0.4107	0.5439	0.3796	0.4261	0.5367	0.5453	0.3733	0.4433
36	0.3465	0.4195	0.5635	0.3896	0.4284	0.5206	0.5498	0.3800	0.4443
37	0.3491	0.4182	0.5656	0.4152	0.4094	0.5078	0.5330	0.3839	0.4550
38	0.3777	0.4115	0.5488	0.4424	0.4131	0.4909	0.5546	0.3768	0.4447
39	0.3184	0.4255	0.5789	0.3867	0.4243	0.5247	0.5306	0.3822	0.4566
40	0.3932	0.4121	0.5373	0.3578	0.4251	0.5433	0.5173	0.3870	0.4641
41	0.3667	0.4165	0.5496	0.5899	0.3894	0.4243	0.5824	0.3625	0.4209

42	0.4160	0.4100	0.5224	0.6464	0.3624	0.3890	0.5503	0.3783	0.4443
43	0.4059	0.4086	0.5306	0.6296	0.3729	0.4051	0.5529	0.3676	0.4379
44	0.3703	0.4118	0.5521	0.5875	0.3917	0.4281	0.2918	0.4225	0.5859
45	0.4297	0.3943	0.5138	0.5564	0.3983	0.4467	0.4260	0.3937	0.4976
46	0.4089	0.4094	0.5307	0.5876	0.3867	0.4276	0.4982	0.3829	0.4683
47	0.3878	0.4099	0.5395	0.6588	0.3699	0.3927	0.4967	0.3880	0.4728
48	0.3685	0.4153	0.5511	0.6118	0.3819	0.4140	0.5297	0.3693	0.4453
49	0.4010	0.4063	0.5291	0.6009	0.3815	0.4145	0.5153	0.3802	0.4627
50	0.3624	0.4213	0.5569	0.6219	0.3707	0.4040	0.5052	0.3819	0.4645
51	0.3502	0.4233	0.5633	0.6247	0.3778	0.4090	0.5045	0.3770	0.4649
52	0.3479	0.4251	0.5657	0.6810	0.3684	0.3830	0.5453	0.3632	0.4408
53	0.3776	0.4189	0.5485	0.6840	0.3653	0.3830	0.4801	0.3918	0.4817
54	0.3939	0.4058	0.5355	0.6381	0.3760	0.4059	0.4876	0.3802	0.4729
55	0.4117	0.3991	0.5276	0.6702	0.3719	0.3896	0.4989	0.3731	0.4642
56	0.4213	0.4065	0.5226	0.6623	0.3730	0.3898	0.4861	0.3913	0.4825
57	0.4079	0.4069	0.5329	0.6465	0.3765	0.3967	0.5096	0.3782	0.4684
58	0.4022	0.4117	0.5380	0.6885	0.3646	0.3805	0.4781	0.3854	0.4844
59	0.4217	0.4168	0.5212	0.6979	0.3674	0.3768	0.4401	0.4026	0.5088
60	0.4039	0.4275	0.5285	0.6896	0.3689	0.3839	0.4827	0.3877	0.4827
mean	0.3995	0.4092	0.5346	0.4915	0.3998	0.4768	0.5131	0.3817	0.4625
std +/-	0.0313	0.0086	0.0183	0.1334	0.0245	0.0694	0.0432	0.0108	0.0250
std/m.	0.0784	0.0210	0.0342	0.2715	0.0614	0.1455	0.0842	0.0282	0.0540

WDLS									
K25			K47			K58			
	k	σ	μ	k	σ	μ	k	σ	μ
1	0.2682	0.4318	0.6098	0.4915	0.4513	0.4656	0.4818	0.3777	0.4732
2	0.2567	0.4365	0.6111	0.4130	0.4158	0.4909	0.4852	0.3801	0.4707
3	0.3209	0.4289	0.5786	0.5333	0.4393	0.4469	0.4574	0.3968	0.4955
4	0.2746	0.4376	0.6013	0.5700	0.4314	0.4325	0.4472	0.3976	0.5003
5	0.2883	0.4331	0.5933	0.5290	0.4392	0.4511	0.4443	0.3916	0.4980
6	0.3089	0.4282	0.5815	0.5704	0.4325	0.4335	0.4611	0.3885	0.4898
7	0.2871	0.4404	0.5911	0.6382	0.4215	0.4088	0.4536	0.3915	0.4998
8	0.3080	0.4360	0.5789	0.6976	0.4072	0.3876	0.4712	0.3930	0.4895
9	0.3211	0.4365	0.5749	0.7043	0.4035	0.3843	0.4941	0.3911	0.4733
10	0.3200	0.4336	0.5743	0.7022	0.4023	0.3852	0.5009	0.3797	0.4614
11	0.3553	0.4253	0.5571	0.6300	0.4203	0.4116	0.4724	0.3843	0.4797
12	0.3178	0.4297	0.5800	0.5835	0.4318	0.4305	0.4704	0.3818	0.4808
13	0.3453	0.4246	0.5644	0.5716	0.4295	0.4307	0.4559	0.3874	0.4927
14	0.2946	0.4358	0.5911	0.6533	0.4143	0.4004	0.4289	0.3960	0.5101
15	0.3028	0.4381	0.5833	0.6381	0.4221	0.4071	0.4073	0.4037	0.5241
16	0.3451	0.4263	0.5648	0.6767	0.4115	0.3921	0.4207	0.4022	0.5174
17	0.3381	0.4251	0.5667	0.5186	0.4427	0.4526	0.4485	0.3939	0.4950
18	0.3677	0.4281	0.5509	0.4774	0.4523	0.4740	0.4612	0.3947	0.4890
19	0.3268	0.4298	0.5721	0.5195	0.4486	0.4553	0.4847	0.3898	0.4766
20	0.3193	0.4338	0.5741	0.4797	0.4544	0.4686	0.4645	0.3931	0.4890
21	0.3356	0.4345	0.5686	0.6609	0.3501	0.3698	0.4404	0.4009	0.4937
22	0.3672	0.4302	0.5501	0.6257	0.3697	0.3934	0.4254	0.3979	0.4938
23	0.3698	0.4291	0.5469	0.6158	0.3635	0.3976	0.4198	0.4013	0.4973
24	0.3671	0.4263	0.5475	0.7657	0.3761	0.3532	0.4162	0.4048	0.5071
25	0.3690	0.4298	0.5448	0.8253	0.3602	0.3336	0.3993	0.4128	0.5254
26	0.3623	0.4192	0.5438	0.7726	0.3796	0.3535	0.4320	0.4039	0.5078
27	0.3615	0.4253	0.5527	0.7583	0.3815	0.3587	0.4511	0.3968	0.4916
28	0.3368	0.4369	0.5638	0.8064	0.3652	0.3377	0.4749	0.3891	0.4804
29	0.3425	0.4380	0.5626	0.8266	0.3646	0.3329	0.4826	0.3860	0.4748
30	0.3858	0.4247	0.5383	0.7801	0.3823	0.3539	0.4822	0.3884	0.4783
31	0.3954	0.4126	0.5365	0.8306	0.3702	0.3346	0.4533	0.3974	0.4907
32	0.3466	0.4252	0.5599	0.7704	0.3840	0.3551	0.4333	0.3996	0.5001
33	0.3723	0.4236	0.5436	0.6794	0.4108	0.3909	0.4285	0.3993	0.5028
34	0.3813	0.4250	0.5385	0.6296	0.4215	0.4093	0.4495	0.3957	0.4976
35	0.3987	0.4200	0.5276	0.5945	0.4268	0.4231	0.4449	0.3974	0.5003
36	0.3030	0.4374	0.5845	0.5616	0.4349	0.4368	0.4602	0.3909	0.4948
37	0.3552	0.4258	0.5550	0.5431	0.4393	0.4453	0.4474	0.3953	0.5024
38	0.2997	0.4355	0.5867	0.5210	0.4478	0.4543	0.4217	0.4074	0.5178
39	0.3449	0.4310	0.5579	0.6496	0.4027	0.4009	0.4338	0.3992	0.5135
40	0.2780	0.4453	0.5940	0.5482	0.4415	0.4394	0.4517	0.3908	0.4962
41	0.4263	0.4175	0.5204	0.3757	0.4731	0.5137	0.4829	0.4013	0.4820

42	0.4643	0.4120	0.4999	0.3128	0.4828	0.5446	0.4314	0.4203	0.5141
43	0.4535	0.4162	0.5041	0.3294	0.4856	0.5343	0.4364	0.4235	0.5103
44	0.4662	0.4104	0.4942	0.3177	0.4916	0.5369	0.4552	0.4108	0.4971
45	0.4487	0.4139	0.5060	0.2539	0.4830	0.5825	0.4681	0.4092	0.4860
46	0.4645	0.4150	0.4993	0.3180	0.4745	0.5453	0.4852	0.4008	0.4759
47	0.4470	0.4222	0.5023	0.3546	0.4777	0.5245	0.4703	0.4109	0.4885
48	0.4013	0.4328	0.5260	0.2887	0.4867	0.5591	0.4673	0.4130	0.4943
49	0.4149	0.4162	0.5136	0.2733	0.4798	0.5718	0.4887	0.4092	0.4833
50	0.4230	0.4228	0.5143	0.2549	0.4778	0.5843	0.5034	0.4033	0.4736
51	0.3150	0.4285	0.5742	0.3002	0.4643	0.5656	0.5219	0.4004	0.4605
52	0.3228	0.4187	0.5675	0.3083	0.4657	0.5599	0.5386	0.3905	0.4474
53	0.2678	0.4363	0.5976	0.3123	0.4640	0.5601	0.4938	0.4065	0.4784
54	0.2283	0.4405	0.6195	0.3015	0.4703	0.5620	0.4789	0.4068	0.4836
55	0.1689	0.4410	0.6603	0.2997	0.4820	0.5510	0.4879	0.3995	0.4870
56	0.1669	0.4332	0.6624	0.3216	0.4785	0.5387	0.4956	0.4016	0.4799
57	0.1623	0.4437	0.6602	0.3266	0.4768	0.5364	0.5028	0.3967	0.4745
58	0.1694	0.4447	0.6556	0.3205	0.4792	0.5413	0.5113	0.3894	0.4630
59	0.0972	0.4448	0.6968	0.2795	0.4848	0.5628	0.5477	0.3811	0.4430
60	0.1307	0.4451	0.6776	0.3269	0.4768	0.5404	0.5496	0.3815	0.4390
mean	0.3296	0.4295	0.5692	0.5256	0.4333	0.4550	0.4646	0.3971	0.4889
std +/-	0.0818	0.0090	0.0450	0.1792	0.0405	0.0776	0.0330	0.0098	0.0182
std/m.	0.2482	0.0209	0.0791	0.3410	0.0934	0.1705	0.0710	0.0248	0.0372

	DDL5								
	K12			K33			K26b		
	k	σ	μ	k	σ	μ	k	σ	μ
1	0.0677	0.4488	0.7088	0.0401	0.4385	0.7292	0.2002	0.4405	0.6294
2	0.0713	0.4487	0.7071	0.0441	0.4443	0.7236	0.1333	0.4472	0.6726
3	0.0838	0.4499	0.7003	0.0197	0.4417	0.7359	0.1346	0.4527	0.6718
4	0.0646	0.4431	0.7140	0.0482	0.4422	0.7229	0.1213	0.4475	0.6806
5	0.0604	0.4408	0.7175	0.0598	0.4418	0.7179	0.1339	0.4418	0.6777
6	0.0889	0.4493	0.6983	0.0511	0.4410	0.7226	0.1136	0.4449	0.6884
7	0.0769	0.4468	0.7058	0.0454	0.4430	0.7243	0.0701	0.4462	0.7095
8	0.0897	0.4459	0.7001	0.0562	0.4390	0.7213	0.0426	0.4516	0.7187
9	0.0662	0.4474	0.7105	0.0484	0.4357	0.7270	0.0564	0.4447	0.7170
10	0.0625	0.4531	0.7086	0.0537	0.4385	0.7229	0.0490	0.4481	0.7182
11	0.0808	0.4491	0.7023	0.0213	0.4422	0.7354	0.0396	0.4448	0.7250
12	0.0689	0.4495	0.7079	0.0193	0.4464	0.7326	0.0378	0.4524	0.7210
13	0.0659	0.4495	0.7091	0.0419	0.4400	0.7272	0.1074	0.4390	0.6923
14	0.0594	0.4474	0.7137	0.0715	0.4392	0.7137	0.0687	0.4454	0.7108
15	0.0480	0.4522	0.7159	0.0705	0.4382	0.7149	0.0543	0.4485	0.7156
16	0.0724	0.4503	0.7056	0.0636	0.4424	0.7154	0.0473	0.4477	0.7194
17	0.0617	0.4471	0.7128	0.0385	0.4463	0.7246	0.0380	0.4464	0.7244
18	0.0991	0.4412	0.6985	0.0373	0.4420	0.7279	0.0865	0.4425	0.7039
19	0.1026	0.4464	0.6933	0.0447	0.4425	0.7245	0.0263	0.4424	0.7324
20	0.0863	0.4471	0.7010	0.0730	0.4418	0.7113	0.0322	0.4405	0.7309
21	0.0638	0.4461	0.7125	0.0890	0.4370	0.7058	0.0388	0.4424	0.7266
22	0.0768	0.4482	0.7048	0.0583	0.4383	0.7208	0.0271	0.4400	0.7334
23	0.1175	0.4484	0.6847	0.0413	0.4409	0.7270	0.0507	0.4432	0.7211
24	0.1352	0.4440	0.6785	0.0358	0.4401	0.7306	0.0541	0.4385	0.7223
25	0.1436	0.4456	0.6731	0.0386	0.4405	0.7292	0.0624	0.4378	0.7189
26	0.1671	0.4419	0.6605	0.1112	0.4331	0.6944	0.0650	0.4384	0.7173
27	0.1586	0.4450	0.6646	0.1474	0.4272	0.6738	0.0543	0.4374	0.7233
28	0.1648	0.4413	0.6621	0.1136	0.4372	0.6896	0.1035	0.4308	0.6995
29	0.1514	0.4454	0.6686	0.1596	0.4281	0.6611	0.1111	0.4283	0.6962
30	0.2120	0.4404	0.6373	0.1385	0.4320	0.6750	0.0747	0.4302	0.7179
31	0.1722	0.4441	0.6564	0.1751	0.4284	0.6490	0.0277	0.4419	0.7329
32	0.1131	0.4519	0.6846	0.1366	0.4317	0.6785	0.0325	0.4372	0.7330
33	0.1245	0.4503	0.6798	0.1394	0.4363	0.6696	0.0062	0.4415	0.7425
34	0.1705	0.4444	0.6592	0.1693	0.4412	0.6412	0.0324	0.4385	0.7328
35	0.1483	0.4473	0.6690	0.1376	0.4379	0.6698	0.0444	0.4391	0.7273
36	0.1452	0.4427	0.6739	0.1347	0.4337	0.6740	0.0555	0.4391	0.7221
37	0.1449	0.4493	0.6699	0.1732	0.4320	0.6424	0.0854	0.4353	0.7084
38	0.1665	0.4472	0.6595	0.1625	0.4318	0.6510	0.1000	0.4361	0.6966
39	0.1480	0.4479	0.6683	0.1347	0.4380	0.6789	0.0706	0.4366	0.7157
40	0.1299	0.4518	0.6757	0.0732	0.4365	0.7140	0.1088	0.4364	0.6945
41	0.1730	0.4420	0.6545	0.0624	0.4370	0.7196	0.1029	0.4332	0.7006

42	0.1410	0.4359	0.6799	0.0386	0.4355	0.7326	0.1254	0.4385	0.6840
43	0.1131	0.4470	0.6873	0.0252	0.4429	0.7333	0.0884	0.4434	0.7022
44	0.1638	0.4370	0.6656	0.0307	0.4404	0.7319	0.1066	0.4462	0.6898
45	0.1486	0.4401	0.6725	0.0010	0.4430	0.7431	0.1426	0.4417	0.6679
46	0.1748	0.4375	0.6592	-0.0077	0.4464	0.7449	0.0361	0.4550	0.7204
47	0.1508	0.4452	0.6680	0.0308	0.4366	0.7346	0.0672	0.4551	0.7054
48	0.1970	0.4410	0.6442	0.0412	0.4407	0.7279	0.0878	0.4553	0.6948
49	0.1861	0.4444	0.6480	0.0754	0.4321	0.7154	0.1437	0.4466	0.6681
50	0.1793	0.4389	0.6552	0.0936	0.4275	0.7074	0.1371	0.4464	0.6722
51	0.1718	0.4382	0.6599	0.0595	0.4353	0.7227	0.1224	0.4525	0.6772
52	0.1436	0.4397	0.6758	0.0656	0.4402	0.7163	0.1043	0.4565	0.6848
53	0.1121	0.4440	0.6888	0.1245	0.4326	0.6821	0.1215	0.4542	0.6768
54	0.1013	0.4468	0.6932	0.1543	0.4297	0.6604	0.0851	0.4614	0.6921
55	0.0684	0.4426	0.7126	0.1657	0.4293	0.6568	0.0998	0.4583	0.6865
56	0.0776	0.4435	0.7076	0.1513	0.4296	0.6693	0.1209	0.4594	0.6735
57	0.0580	0.4411	0.7184	0.1193	0.4318	0.6913	0.1456	0.4612	0.6579
58	0.0879	0.4468	0.7004	0.0794	0.4402	0.7091	0.1692	0.4539	0.6453
59	0.0991	0.4450	0.6957	0.0698	0.4393	0.7144	0.1621	0.4554	0.6485
60	0.1367	0.4395	0.6799	0.0521	0.4425	0.7210	0.1776	0.4493	0.6437
mean	0.1169	0.4452	0.6857	0.0792	0.4377	0.7064	0.0857	0.4448	0.7006
std +/-	0.0441	0.0041	0.0220	0.0496	0.0050	0.0282	0.0444	0.0079	0.0262
std/m.	0.3774	0.0092	0.0321	0.6266	0.0115	0.0400	0.5176	0.0177	0.0374

APPENDIX 3

Explanation of the data analysis

Error analysis of the parameters on one B-scan from each measurement.

The problems can arise from

- 1 - Digital error from straightening the image -> the mean intensity value at each depth position and distribution can be affected
- 2 - Saturation points on the images -> these pixel points give erroneous intensity values
- 3 - surface scattering effect -> the obliqueness of the surface has effect on the intensity values

Explanation of the notes

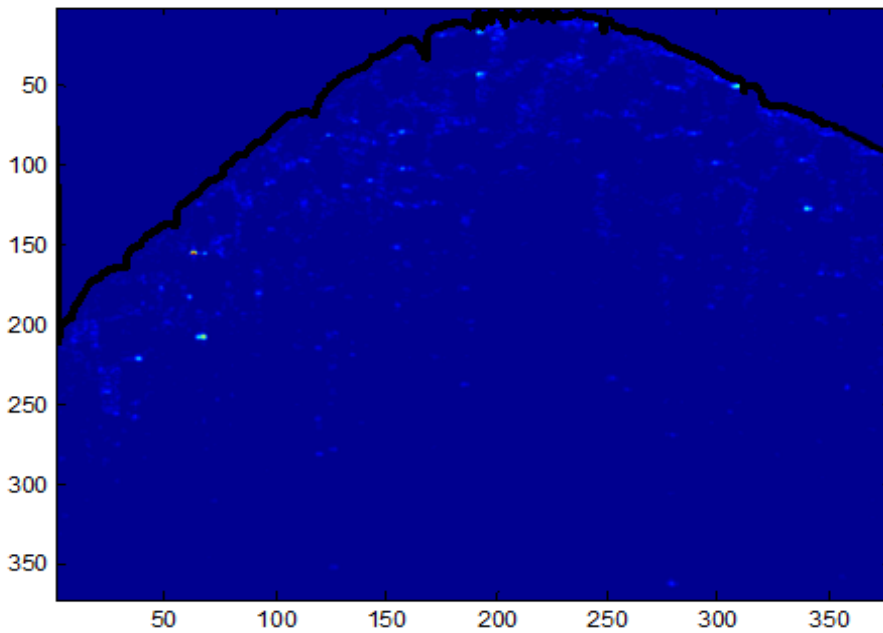
- normal* tissue PDF is calculated the way as represented on the images, 40 pixel depth
- 1 - perturbation : I shifted each second column up to 10 px and second+1 down to 10 px
 - p+10* tissue surface is considered 10 px down from the original tissue surface
 - p0* tissue surface is considered at the original tissue surface
 - p-10* tissue surface is considered 10 px up of the original tissue surface
 - 2 - saturation
 - ws* tissue PDF is calculated without the saturation lines, in these cases it was 4%
 - ms* tissue PDF is calculated adding more saturation lines, 4%
 - 3 - surface obliqueness : after fitting the surface (black line) derivative of the fit is calculated
 - deriv* each column intensity values were enhanced according to the obliqueness
 - deriv/2* I applied smaller factor on the surface obliqueness

NF K37		sheet9	Vol2			
	k	sigma	mu	$(k_p - k_n)/k_n$	$(s_p - s_n)/s_n$	$(m_p - m_n)/m_n$
<i>normal</i>	0.8962	0.3311	0.2866			
<i>p+10</i>	0.8735	0.3297	0.2892	-2.53%	-0.41%	0.89%
<i>p0</i>	0.9660	0.3027	0.2585	7.79%	-8.59%	-9.83%
<i>p-10</i>	1.0824	0.2688	0.2181	20.78%	-18.81%	-23.92%

	k	sigma	mu	$(k_s - k_n)/k_n$	$(s_s - s_n)/s_n$	$(m_s - m_n)/m_n$
<i>normal</i>	0.8962	0.3311	0.2866			
<i>ws</i>						
<i>ms</i>	0.9550	0.3087	0.2539	6.56%	-6.76%	-11.41%

saturation lines: only add
 col 35, raw 7 over 367 cols
35/367 = 0.095368 9.5%

	k	sigma	mu	$(k_d - k_n)/k_n$	$(s_d - s_n)/s_n$	$(m_d - m_n)/m_n$
<i>normal</i>	0.8962	0.3311	0.2866			
<i>deriv/2</i>	0.9206	0.3211	0.2745	2.72%	-3.01%	-4.22%
<i>deriv</i>	0.9660	0.3017	0.2515	7.78%	-8.88%	-12.26%



Here each B-scan was corrected line by line

NF K37

sheet14

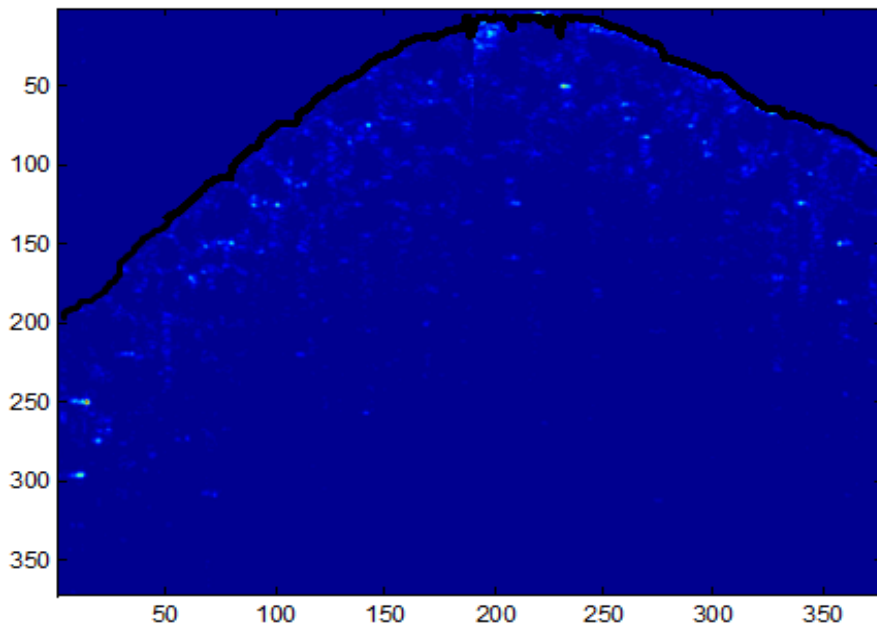
Vol2

	k	sigma	mu	$(k_p - k_n)/k_n$	$(s_p - s_n)/s_n$	$(m_p - m_n)/m_n$
<i>normal</i>	0.8146	0.3648	0.3283			
<i>p+10</i>	0.8570	0.3469	0.3086	5.21%	-4.90%	-6.00%
<i>p0</i>	0.9623	0.3179	0.2702	18.13%	-12.85%	-17.69%
<i>p-10</i>	1.0667	0.2884	0.2335	30.94%	-20.95%	-28.88%

	k	sigma	mu	$(k_s - k_n)/k_n$	$(s_s - s_n)/s_n$	$(m_s - m_n)/m_n$
<i>normal</i>	0.8146	0.3648	0.3283			
<i>ws</i>						
<i>ms</i>	0.8931	0.3361	0.2867	9.63%	-7.86%	-12.66%

saturation lines: only add
 col 35, raw 7 over 367 cols
35/367 = 0.095368 9.5%

	k	sigma	mu	$(k_d - k_n)/k_n$	$(s_d - s_n)/s_n$	$(m_d - m_n)/m_n$
<i>normal</i>	0.8146	0.3648	0.3283			
<i>deriv/2</i>	0.8154	0.3628	0.3264	0.10%	-0.56%	-0.58%
<i>deriv</i>	0.8269	0.3559	0.3177	1.51%	-2.43%	-3.23%



Here each B-scan was corrected line by line

NF K37

sheet15

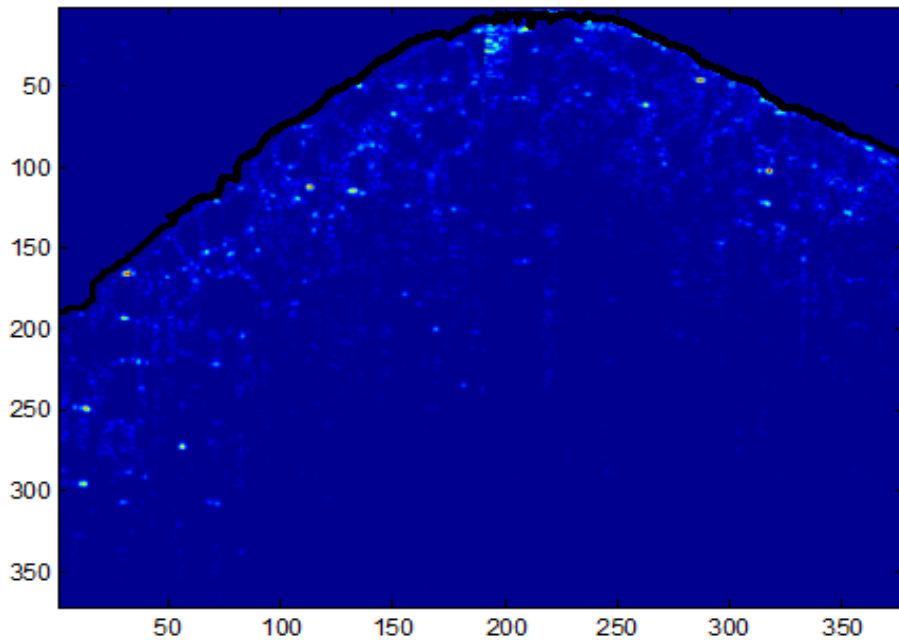
Vol2

	k	sigma	mu	$(k_p - k_n)/k_n \quad (s_p - s_n)/s_n \quad (m_p - m_n)/m_n$		
<i>normal</i>	0.7218	0.3920	0.3621			
<i>p+10</i>	0.7053	0.3888	0.3657	-2.28%	-0.81%	1.01%
<i>p0</i>	0.8883	0.3408	0.2972	23.06%	-13.06%	-17.91%
<i>p-10</i>	1.0509	0.2984	0.2432	45.59%	-23.86%	-32.83%

	k	sigma	mu	$(k_s - k_n)/k_n \quad (s_s - s_n)/s_n \quad (m_s - m_n)/m_n$		
<i>normal</i>	0.7218	0.3920	0.3621			
<i>ws</i>						
<i>ms</i>	0.7892	0.3677	0.3237	9.34%	-6.19%	-10.59%

saturation lines: only add
 col 35, raw 7 over 367 cols
35/367 = 0.095368 9.5%

	k	sigma	mu	$(k_d - k_n)/k_n \quad (s_d - s_n)/s_n \quad (m_d - m_n)/m_n$		
<i>normal</i>	0.7218	0.3920	0.3621			
<i>deriv/2</i>	0.7341	0.3878	0.3565	1.70%	-1.06%	-1.54%
<i>deriv</i>	0.7640	0.3770	0.3416	5.85%	-3.82%	-5.66%



Here each B-scan was corrected line by line

NF K28

sheet1

Vol1

	k	sigma	mu	$(k_p - k_n)/k_n$	$(s_p - s_n)/s_n$	$(m_p - m_n)/m_n$
<i>normal</i>	0.4588	0.3891	0.4957			
<i>p+10</i>	0.4823	0.3875	0.4757	5.12%	-0.42%	-4.05%
<i>p0</i>	0.4835	0.3863	0.4740	5.38%	-0.73%	-4.38%
<i>p-10</i>	0.4835	0.3863	0.4740	5.38%	-0.73%	-4.38%

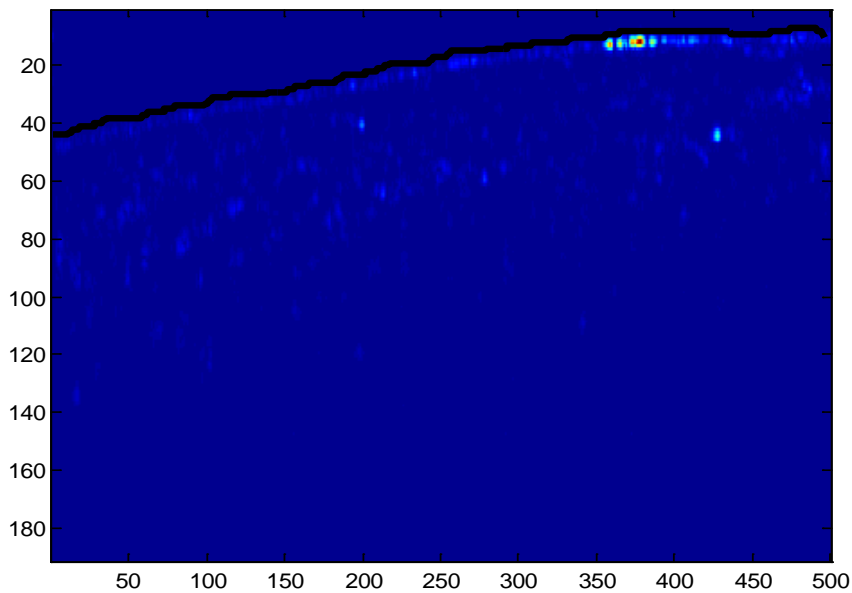
	k	sigma	mu	$(k_s - k_n)/k_n$	$(s_s - s_n)/s_n$	$(m_s - m_n)/m_n$
<i>normal</i>	0.4588	0.3891	0.4957			
<i>ws</i>	0.4345	0.3977	0.5132	-5.31%	2.20%	3.52%
<i>ms</i>	0.4779	0.3866	0.4845	4.15%	-0.64%	-2.27%

saturation lines: remove or add

4+3+2+10+2 = 21 over 496

21/496 = **0.042339** 4.2%

	k	sigma	mu	$(k_d - k_n)/k_n$	$(s_d - s_n)/s_n$	$(m_d - m_n)/m_n$
<i>normal</i>	0.4588	0.3891	0.4957			
<i>deriv/2</i>	0.4575	0.3897	0.4968	-0.29%	0.15%	0.21%
<i>deriv</i>	0.4567	0.3903	0.4975	-0.46%	0.29%	0.35%



NF K28

sheet2

Vol1

	k	sigma	mu	$(k_p - k_n)/k_n$	$(s_p - s_n)/s_n$	$(m_p - m_n)/m_n$
<i>normal</i>	0.4321	0.3993	0.5162			
<i>p+10</i>	0.4547	0.3969	0.4944	5.21%	-0.59%	-4.21%
<i>p0</i>	0.4641	0.3933	0.4895	7.40%	-1.49%	-5.16%
<i>p-10</i>	0.4641	0.3933	0.4895	7.40%	-1.49%	-5.16%

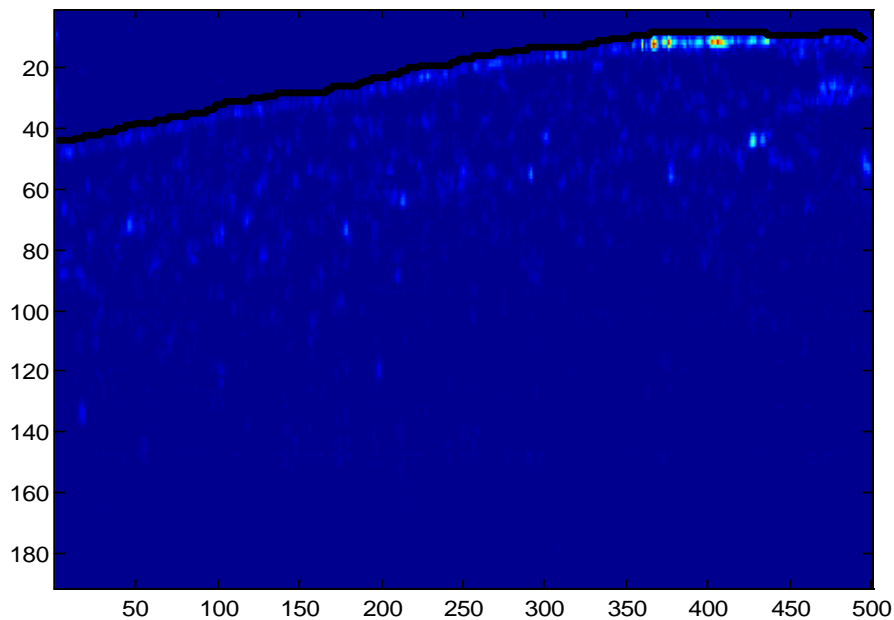
	k	sigma	mu	$(k_s - k_n)/k_n$	$(s_s - s_n)/s_n$	$(m_s - m_n)/m_n$
<i>normal</i>	0.4321	0.3993	0.5162			
<i>ws</i>	0.4100	0.4037	0.5296	-5.12%	1.11%	2.60%
<i>ms</i>	0.4484	0.3995	0.5079	3.76%	0.05%	-1.60%

saturation lines: remove or add

2+5+8+12+4= 31 over 496

31/496 = 0.0625 6.2%

	k	sigma	mu	$(k_d - k_n)/k_n$	$(s_d - s_n)/s_n$	$(m_d - m_n)/m_n$
<i>normal</i>	0.4321	0.3993	0.5162			
<i>deriv/2</i>	0.4295	0.4004	0.5179	-0.61%	0.28%	0.33%
<i>deriv</i>	0.4273	0.4016	0.5193	-1.12%	0.58%	0.61%



NF K28

sheet3

Vol1

	k	sigma	mu	$(k_p - k_n)/k_n \quad (s_p - s_n)/s_n \quad (m_p - m_n)/m_n$		
<i>normal</i>	0.4478	0.3972	0.5073			
<i>p+10</i>	0.4865	0.3935	0.4779	8.64%	-0.93%	-5.79%
<i>p0</i>	0.4840	0.3897	0.4762	8.08%	-1.88%	-6.13%
<i>p-10</i>	0.4840	0.3897	0.4762	8.08%	-1.88%	-6.13%

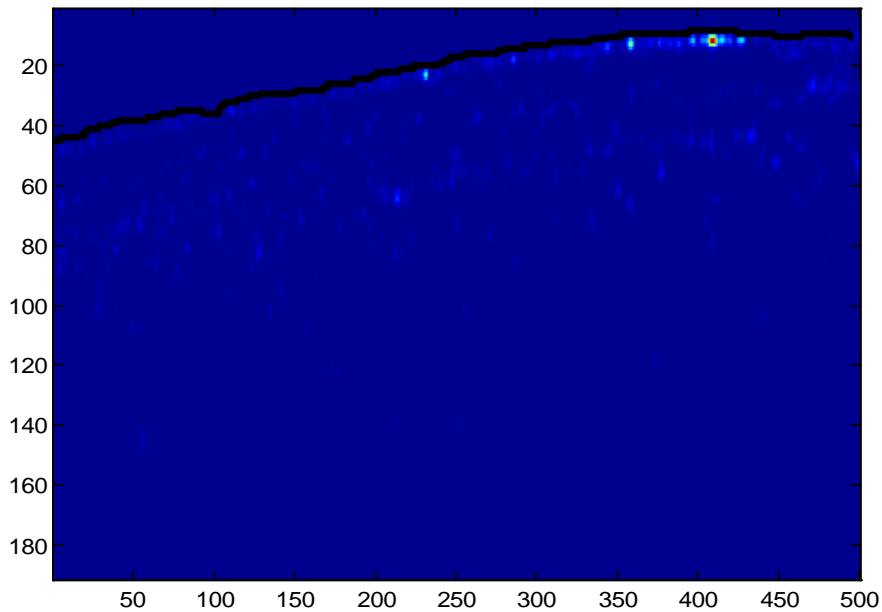
	k	sigma	mu	$(k_s - k_n)/k_n \quad (s_s - s_n)/s_n \quad (m_s - m_n)/m_n$		
<i>normal</i>	0.4478	0.3972	0.5073			
<i>ws</i>	0.4264	0.4045	0.5220	-4.78%	1.85%	2.89%
<i>ms</i>	0.4663	0.3929	0.4960	4.12%	-1.07%	-2.22%

saturation lines: remove or add

2+3+7=12 over 496

12/496 = **0.024194** 2.4%

	k	sigma	mu	$(k_d - k_n)/k_n \quad (s_d - s_n)/s_n \quad (m_d - m_n)/m_n$		
<i>normal</i>	0.4478	0.3972	0.5073			
<i>deriv/2</i>	0.4467	0.3979	0.5083	-0.25%	0.18%	0.20%
<i>deriv</i>	0.4461	0.3986	0.5089	-0.39%	0.37%	0.32%



NF K19

sheet1

vol3

	k	sigma	mu	$(k_p - k_n)/k_n$	$(s_p - s_n)/s_n$	$(m_p - m_n)/m_n$
<i>normal</i>	0.5899	0.3894	0.4243			
<i>p+10</i>	0.6166	0.3769	0.4101	4.52%	-3.22%	-3.36%
<i>p0</i>	0.6291	0.3677	0.4014	6.63%	-5.56%	-5.40%
<i>p-10</i>	0.6028	0.3760	0.4156	2.18%	-3.44%	-2.05%

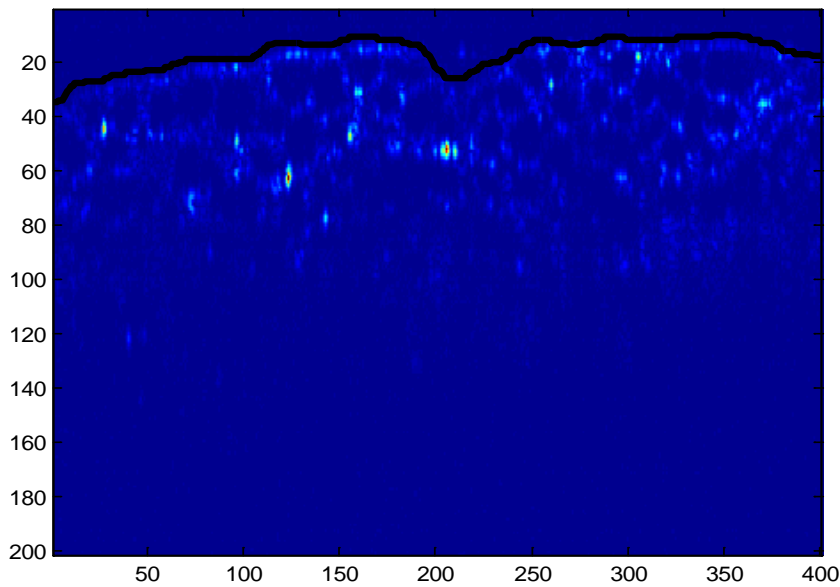
	k	sigma	mu	$(k_s - k_n)/k_n$	$(s_s - s_n)/s_n$	$(m_s - m_n)/m_n$
<i>normal</i>	0.5899	0.3894	0.4243			
<i>ws</i>	0.5809	0.3948	0.4326	-1.54%	1.38%	1.94%
<i>ms</i>	0.5986	0.3855	0.4175	1.46%	-1.00%	-1.62%

saturation lines: remove or add

3+5 = 8 over 401

8/401 = 0.01995 2.0%

	k	sigma	mu	$(k_d - k_n)/k_n$	$(s_d - s_n)/s_n$	$(m_d - m_n)/m_n$
<i>normal</i>	0.5899	0.3894	0.4243			
<i>deriv/2</i>	0.5890	0.3897	0.4248	-0.15%	0.09%	0.11%
<i>deriv</i>	0.5883	0.3900	0.4251	-0.27%	0.17%	0.19%



NF K19

sheet2

vol2

	k	sigma	mu	$(k_p - k_n)/k_n$	$(s_p - s_n)/s_n$	$(m_p - m_n)/m_n$
<i>normal</i>	0.5853	0.3717	0.4223			
<i>p+10</i>	0.5778	0.3704	0.4253	-1.28%	-0.33%	0.72%
<i>p0</i>	0.6025	0.3580	0.4087	2.94%	-3.69%	-3.23%
<i>p-10</i>	0.6351	0.3527	0.3913	8.52%	-5.12%	-7.35%

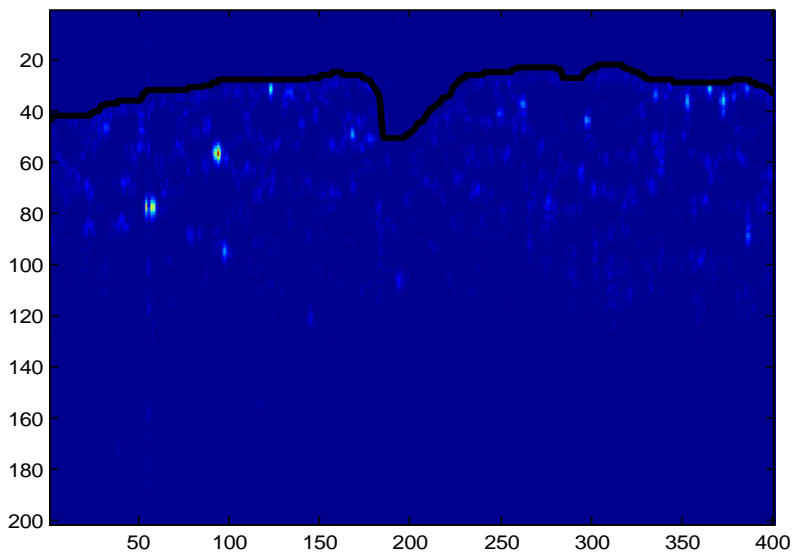
	k	sigma	mu	$(k_s - k_n)/k_n$	$(s_s - s_n)/s_n$	$(m_s - m_n)/m_n$
<i>normal</i>	0.5853	0.3717	0.4223			
<i>ws</i>	0.5746	0.3813	0.4354	-1.83%	2.59%	3.09%
<i>ms</i>	0.5974	0.3641	0.4108	2.07%	-2.03%	-2.73%

saturation lines: remove or add

5+3= 8 over 401

8/401 = 0.01995 2.0%

	k	sigma	mu	$(k_d - k_n)/k_n$	$(s_d - s_n)/s_n$	$(m_d - m_n)/m_n$
<i>normal</i>	0.5853	0.3717	0.4223			
<i>deriv/2</i>	0.5871	0.3715	0.4213	0.31%	-0.06%	-0.23%
<i>deriv</i>	0.5893	0.3712	0.4201	0.69%	-0.14%	-0.51%



NF K19

sheet3

vol3

	k	sigma	mu	$(k_p - k_n)/k_n \quad (s_p - s_n)/s_n \quad (m_p - m_n)/m_n$		
<i>normal</i>	0.6296	0.3729	0.4051			
<i>p+10</i>	0.6374	0.3611	0.3966	1.24%	-3.15%	-2.09%
<i>p0</i>	0.6315	0.3614	0.4011	0.31%	-3.07%	-0.98%
<i>p-10</i>	0.6188	0.3638	0.4038	-1.71%	-2.44%	-0.32%

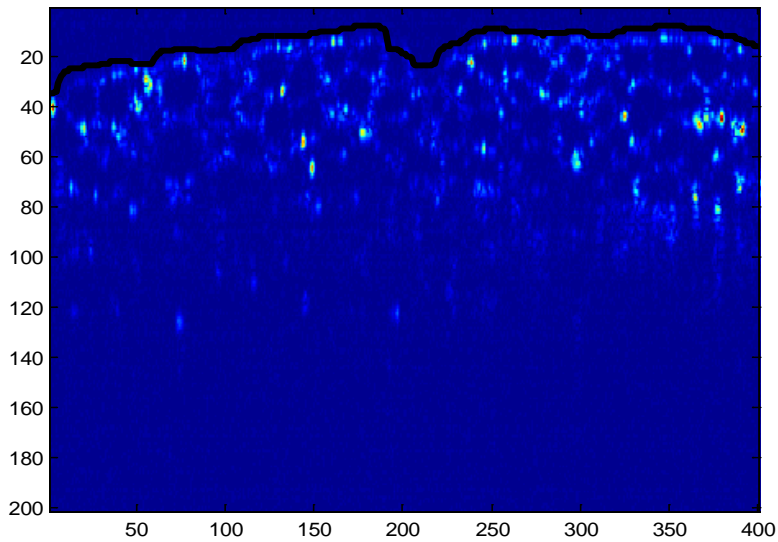
	k	sigma	mu	$(k_s - k_n)/k_n \quad (s_s - s_n)/s_n \quad (m_s - m_n)/m_n$		
<i>normal</i>	0.6296	0.3729	0.4051			
<i>ws</i>	0.6296	0.3729	0.4051	0.00%	0.00%	0.00%
<i>ms</i>	0.6521	0.3581	0.3853	3.58%	-3.98%	-4.89%

saturation lines: no remove | only add

8+8 = 16 over 401

16/401 = 0.0399 4.0%

	k	sigma	mu	$(k_d - k_n)/k_n \quad (s_d - s_n)/s_n \quad (m_d - m_n)/m_n$		
<i>normal</i>	0.6296	0.3729	0.4051			
<i>deriv/2</i>	0.6297	0.3729	0.4051	0.01%	0.00%	-0.01%
<i>deriv</i>	0.6300	0.3728	0.4049	0.07%	-0.01%	-0.06%



Normal Fat K22

sheet 10 vol1

	k	sigma	mu	$(k_p - k_n)/k_n$	$(s_p - s_n)/s_n$	$(m_p - m_n)/m_n$
<i>normal</i>	0.5303	0.3875	0.4561			
<i>p+10</i>	0.5415	0.3746	0.4456	2.10%	-3.32%	-2.31%
<i>p0</i>	0.5376	0.3763	0.4503	1.38%	-2.90%	-1.28%
<i>p-10</i>	0.5264	0.3767	0.4485	-0.74%	-2.78%	-1.68%

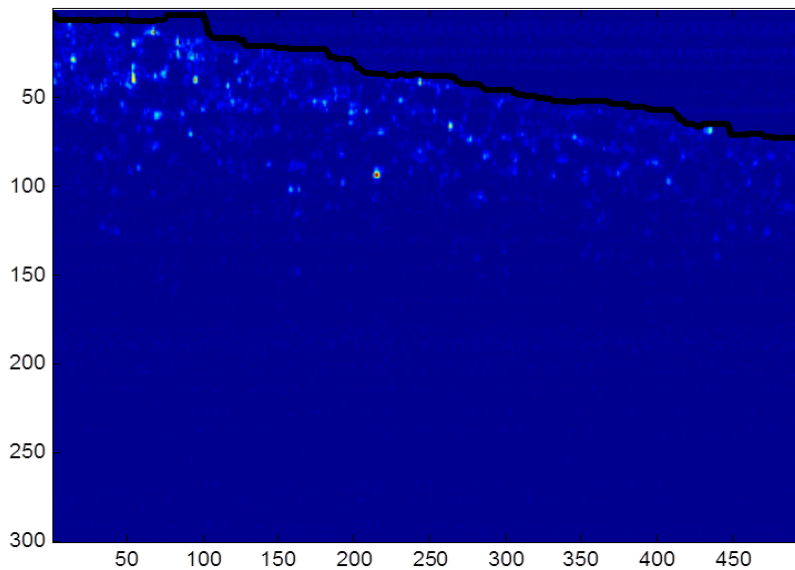
	k	sigma	mu	$(k_s - k_n)/k_n$	$(s_s - s_n)/s_n$	$(m_s - m_n)/m_n$
<i>normal</i>	0.5303	0.3875	0.4561			
<i>ws</i>	0.5316	0.3874	0.4556	0.24%	-0.03%	-0.11%
<i>ms</i>	0.5290	0.3876	0.4567	-0.25%	0.03%	0.12%

saturation lines: remove or add

4over 496

4/496 = 0.0081 1.0%

	k	sigma	mu	$(k_d - k_n)/k_n$	$(s_d - s_n)/s_n$	$(m_d - m_n)/m_n$
<i>normal</i>	0.5303	0.3875	0.4561			
<i>deriv/2</i>	0.5245	0.3891	0.4600	-1.11%	0.41%	0.84%
<i>deriv</i>	0.5195	0.3904	0.4632	-2.05%	0.76%	1.56%



Normal Fat K22

sheet 11 vol1

	k	sigma	mu	$(k_p - k_n)/k_n$	$(s_p - s_n)/s_n$	$(m_p - m_n)/m_n$
<i>normal</i>	0.5066	0.3933	0.4721			
<i>p+10</i>	0.5224	0.3803	0.4583	3.13%	-3.30%	-2.92%
<i>p0</i>	0.5145	0.3828	0.4636	1.56%	-2.68%	-1.80%
<i>p-10</i>	0.5240	0.3916	0.4672	3.44%	-0.43%	-1.04%

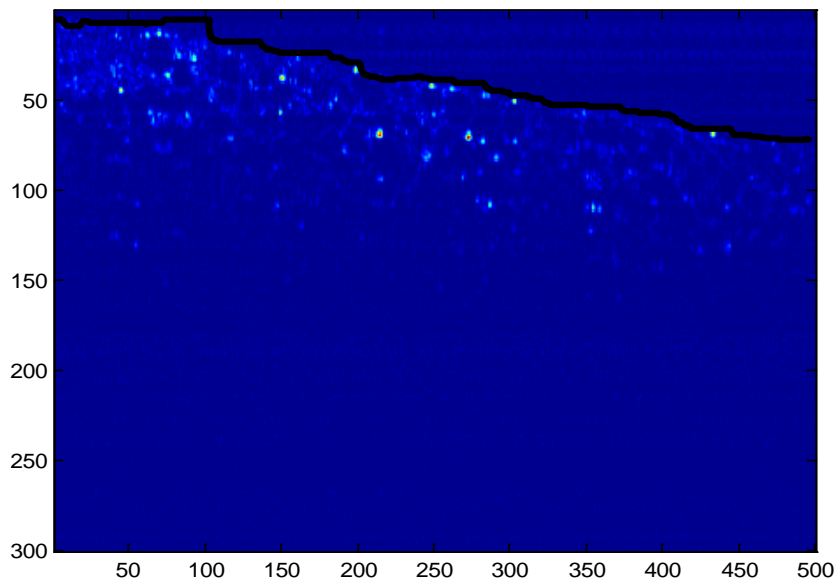
	k	sigma	mu	$(k_s - k_n)/k_n$	$(s_s - s_n)/s_n$	$(m_s - m_n)/m_n$
<i>normal</i>	0.5066	0.3933	0.4721			
<i>ws</i>	0.4955	0.3984	0.4810	-2.19%	1.28%	1.89%
<i>ms</i>	0.5174	0.3895	0.4644	2.13%	-0.96%	-1.64%

saturation lines: remove or add

4+3= 7 over 496

7/496 = 0.0141 1.4%

	k	sigma	mu	$(k_d - k_n)/k_n$	$(s_d - s_n)/s_n$	$(m_d - m_n)/m_n$
<i>normal</i>	0.5066	0.3933	0.4721			
<i>deriv/2</i>	0.4972	0.3947	0.4767	-1.84%	0.34%	0.98%
<i>deriv</i>	0.4888	0.3957	0.4807	-3.50%	0.60%	1.82%



Normal Fat K22

sheet 20 vol1

	k	sigma	mu	$(k_p - k_n)/k_n$	$(s_p - s_n)/s_n$	$(m_p - m_n)/m_n$
<i>normal</i>	0.5665	0.3612	0.4231			
<i>p+10</i>	0.5581	0.3591	0.4259	-1.49%	-0.59%	0.64%
<i>p0</i>	0.5580	0.3595	0.4273	-1.49%	-0.47%	0.97%
<i>p-10</i>	0.6184	0.3669	0.4145	9.18%	1.59%	-2.05%

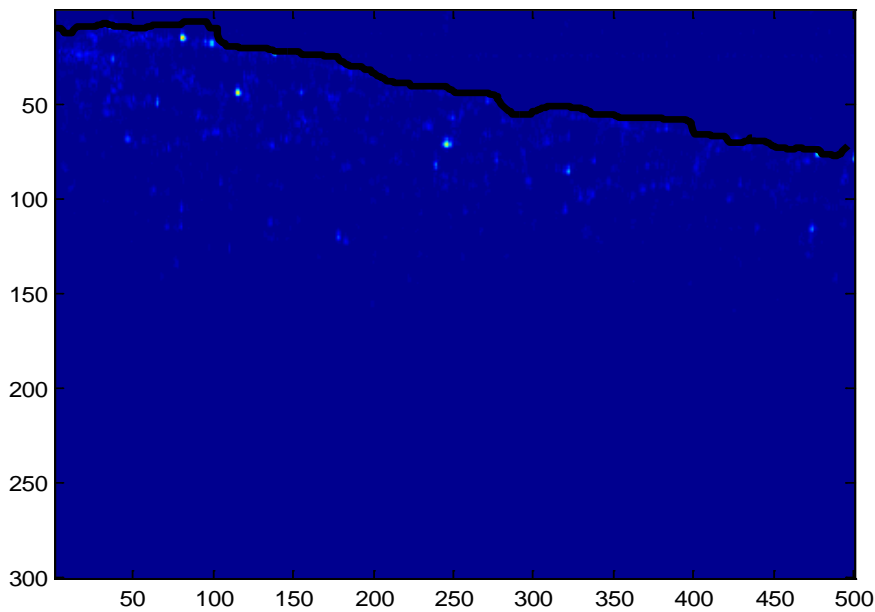
	k	sigma	mu	$(k_s - k_n)/k_n$	$(s_s - s_n)/s_n$	$(m_s - m_n)/m_n$
<i>normal</i>	0.5665	0.3612	0.4231			
<i>ws</i>	0.5461	0.3781	0.4473	-3.60%	4.68%	5.70%
<i>ms</i>	0.5869	0.3494	0.4038	3.60%	-3.28%	-4.57%

saturation lines: remove or add

7+3+2 = 12 over 496

12/496 = 0.024194 2.4%

	k	sigma	mu	$(k_d - k_n)/k_n$	$(s_d - s_n)/s_n$	$(m_d - m_n)/m_n$
<i>normal</i>	0.5665	0.3612	0.4231			
<i>deriv/2</i>	0.5622	0.3628	0.4258	-0.75%	0.43%	0.62%
<i>deriv</i>	0.5586	0.3643	0.4279	-1.39%	0.85%	1.12%



WDLS K36 sheet5 Vol1

	k	sigma	mu	$(k_p - k_n)/k_n$	$(s_p - s_n)/s_n$	$(m_p - m_n)/m_n$
<i>normal</i>	0.2595	0.4437	0.6061			
<i>p+10</i>	0.2494	0.4466	0.6100	-3.89%	0.65%	0.65%
<i>p0</i>	0.3638	0.4713	0.5173	40.19%	6.21%	-14.64%
<i>p-10</i>	0.5922	0.4356	0.4120	128.20%	-1.83%	-32.02%

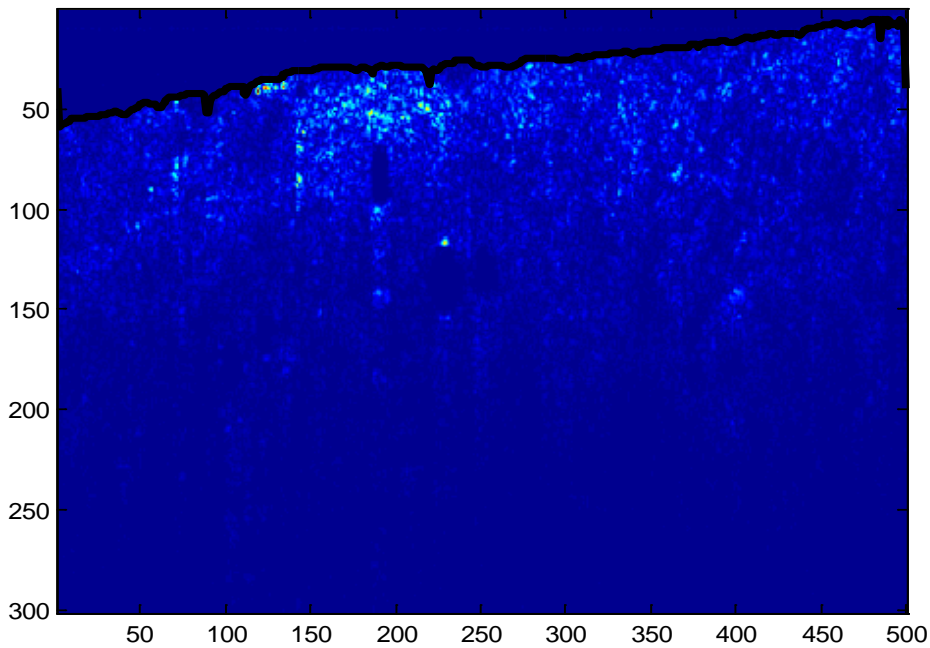
	k	sigma	mu	$(k_s - k_n)/k_n$	$(s_s - s_n)/s_n$	$(m_s - m_n)/m_n$
<i>normal</i>	0.2595	0.4437	0.6061			
<i>ws</i>	0.2409	0.4473	0.6158	-7.18%	0.80%	1.61%
<i>ms</i>	0.2768	0.4406	0.5970	6.65%	-0.71%	-1.50%

saturation lines: remove or add

$$5+3+2+3+3 = 16 \text{ over } 500$$

$$16/500 = 0.032 \quad 3.2\%$$

	k	sigma	mu	$(k_d - k_n)/k_n$	$(s_d - s_n)/s_n$	$(m_d - m_n)/m_n$
<i>normal</i>	0.2595	0.4437	0.6061			
<i>deriv/2</i>	0.2615	0.4433	0.6051	0.75%	-0.10%	-0.16%
<i>deriv</i>	0.2637	0.4428	0.6039	1.62%	-0.20%	-0.35%



WDLS K36 sheet6 Vol1

	k	sigma	mu	$(k_p - k_n)/k_n$	$(s_p - s_n)/s_n$	$(m_p - m_n)/m_n$
<i>normal</i>	0.2059	0.4470	0.6373			
<i>p+10</i>	0.2116	0.4491	0.6316	2.76%	0.46%	-0.89%
<i>p0</i>	0.3093	0.4826	0.5441	50.24%	7.95%	-14.63%
<i>p-10</i>	0.5164	0.4570	0.4430	150.83%	2.24%	-30.49%

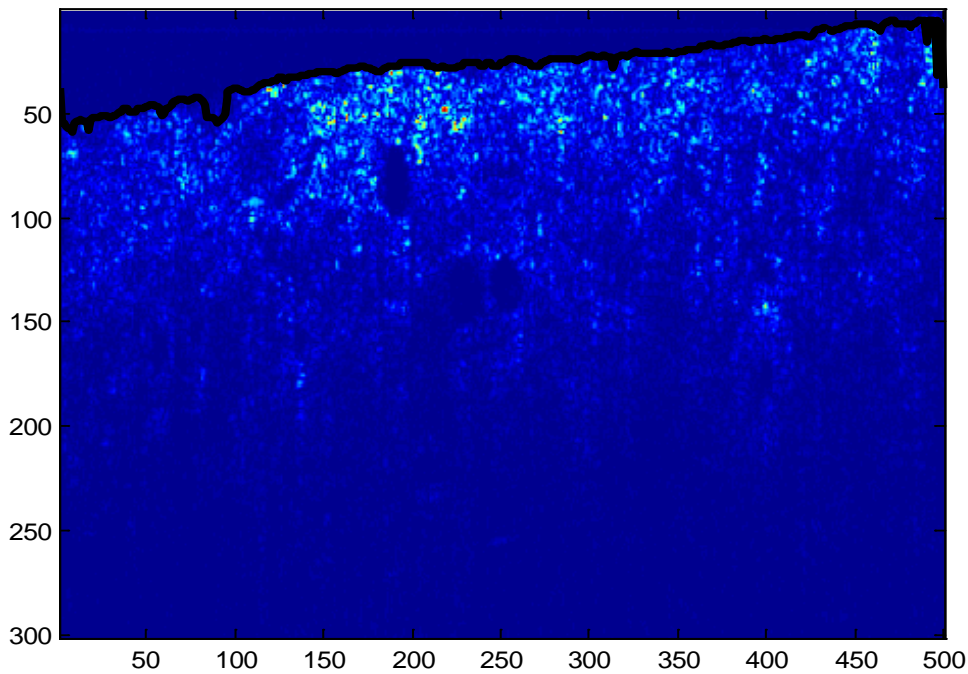
	k	sigma	mu	$(k_s - k_n)/k_n$	$(s_s - s_n)/s_n$	$(m_s - m_n)/m_n$
<i>normal</i>	0.2059	0.4470	0.6373			
<i>ws</i>	0.2067	0.4478	0.6367	0.41%	0.18%	-0.10%
<i>ms</i>	0.2049	0.4463	0.6380	-0.48%	-0.17%	0.11%

saturation lines: remove or add

4+3+3 = 10 over 500

10/500 **0.02** **2.0%**

	k	sigma	mu	$(k_d - k_n)/k_n$	$(s_d - s_n)/s_n$	$(m_d - m_n)/m_n$
<i>normal</i>	0.2059	0.4470	0.6373			
<i>deriv/2</i>	0.2069	0.4469	0.6368	0.52%	-0.03%	-0.08%
<i>deriv</i>	0.2083	0.4467	0.6361	1.17%	-0.07%	-0.19%



WDLS K36 sheet7

Vol1

	k	sigma	mu	$(k_p - k_n)/k_n \quad (s_p - s_n)/s_n \quad (m_p - m_n)/m_n$		
<i>normal</i>	0.1797	0.4530	0.6477			
<i>p+10</i>	0.1984	0.4556	0.6340	10.45%	0.57%	-2.11%
<i>p0</i>	0.2953	0.4865	0.5512	64.37%	7.41%	-14.91%
<i>p-10</i>	0.4855	0.4665	0.4565	170.19%	2.98%	-29.52%

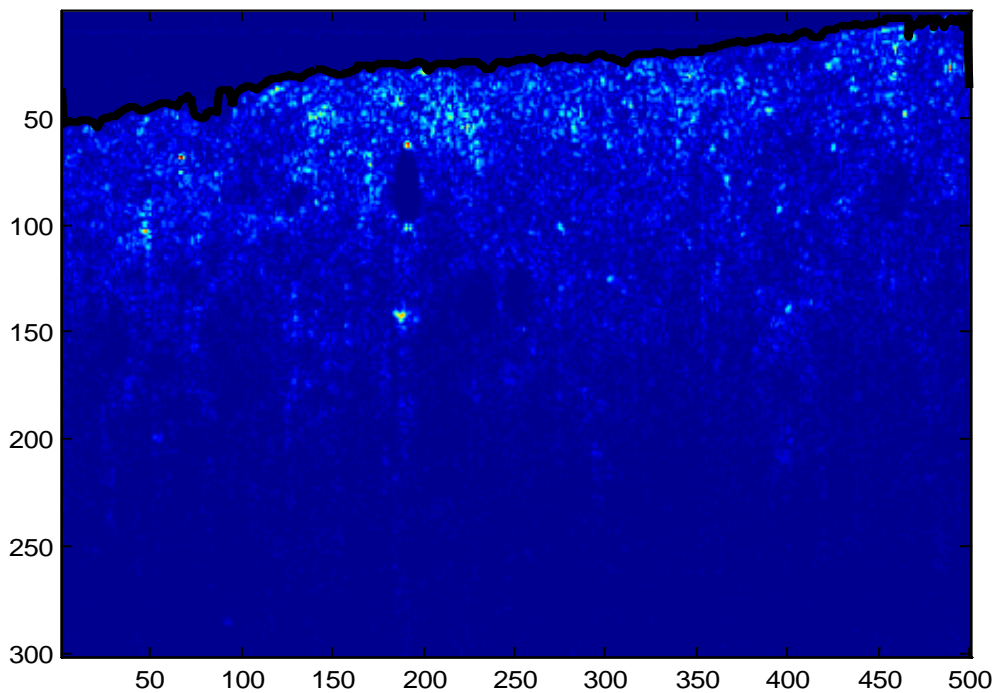
	k	sigma	mu	$(k_s - k_n)/k_n \quad (s_s - s_n)/s_n \quad (m_s - m_n)/m_n$		
<i>normal</i>	0.1797	0.4530	0.6477			
<i>ws</i>	0.1761	0.4536	0.6495	-1.97%	0.13%	0.27%
<i>ms</i>	0.1827	0.4525	0.6461	1.68%	-0.10%	-0.24%

saturation lines: remove or add

5+2+2 = 9 over 500

9/500 = **0.018** 1.8%

	k	sigma	mu	$(k_d - k_n)/k_n \quad (s_d - s_n)/s_n \quad (m_d - m_n)/m_n$		
<i>normal</i>	0.1797	0.4530	0.6477			
<i>deriv/2</i>	0.1807	0.4530	0.6471	0.56%	0.02%	-0.10%
<i>deriv</i>	0.1820	0.4531	0.6463	1.29%	0.04%	-0.22%



WDLS K25 sheet1

Vol1

	k	sigma	mu	$(k_p - k_n)/k_n$	$(s_p - s_n)/s_n$	$(m_p - m_n)/m_n$
<i>normal</i>	0.2641	0.4331	0.6110			
<i>p+10</i>	0.2818	0.4293	0.6012	6.72%	-0.86%	-1.60%
<i>p0</i>	0.3189	0.4236	0.5825	20.75%	-2.18%	-4.66%
<i>p-10</i>	0.3898	0.4166	0.5435	47.58%	-3.81%	-11.05%

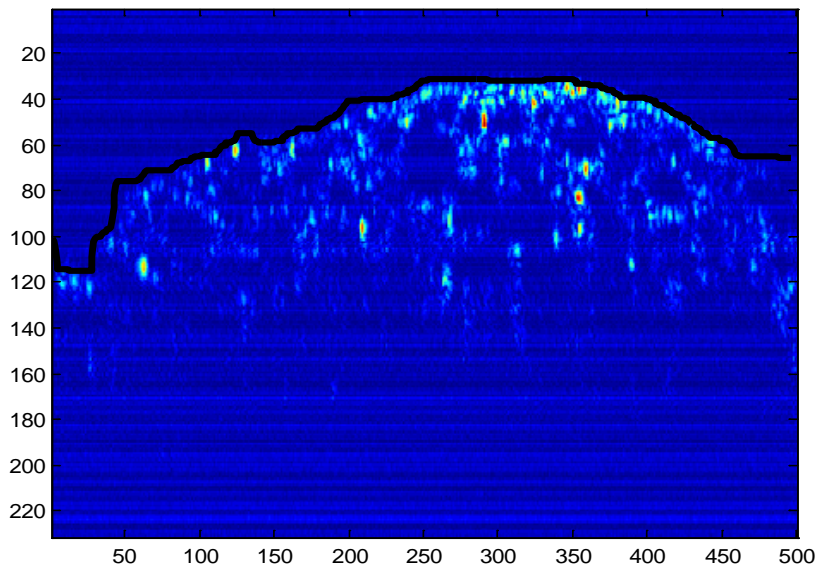
	k	sigma	mu	$(k_s - k_n)/k_n$	$(s_s - s_n)/s_n$	$(m_s - m_n)/m_n$
<i>normal</i>	0.2641	0.4331	0.6110			
<i>ws</i>	0.2331	0.4397	0.6269	-11.74%	1.53%	2.60%
<i>ms</i>	0.2916	0.4271	0.5965	10.44%	-1.37%	-2.37%

saturation lines: remove or add

5+5+3+4=17 over 496

17/496 = **0.034274** 3.4%

	k	sigma	mu	$(k_d - k_n)/k_n$	$(s_d - s_n)/s_n$	$(m_d - m_n)/m_n$
<i>normal</i>	0.2641	0.4331	0.6110			
<i>deriv/2</i>	0.2549	0.4349	0.6159	-3.46%	0.41%	0.79%
<i>deriv</i>	0.2689	0.4350	0.6075	1.82%	0.44%	-0.58%



WDLS K25 sheet5 Vol6

	k	sigma	mu	$(k_p - k_n)/k_n$	$(s_p - s_n)/s_n$	$(m_p - m_n)/m_n$
<i>normal</i>	0.3095	0.4436	0.5772			
<i>p+10</i>	0.3071	0.4370	0.5801	-0.77%	-1.48%	0.50%
<i>p0</i>	0.3723	0.4237	0.5480	20.30%	-4.49%	-5.06%
<i>p-10</i>	0.4095	0.4205	0.5304	32.33%	-5.20%	-8.10%

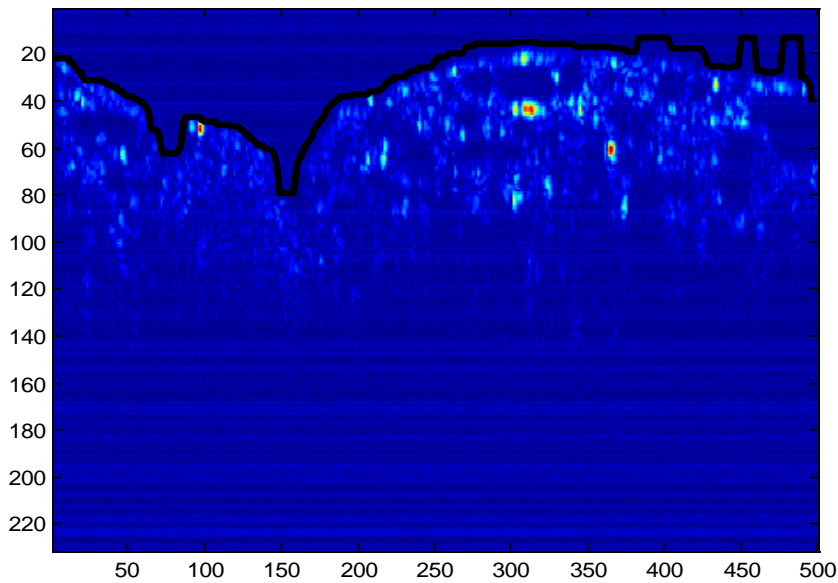
	k	sigma	mu	$(k_s - k_n)/k_n$	$(s_s - s_n)/s_n$	$(m_s - m_n)/m_n$
<i>normal</i>	0.3095	0.4436	0.5772			
<i>ws</i>	0.2831	0.4505	0.5911	-8.51%	1.55%	2.41%
<i>ms</i>	0.3324	0.4378	0.5648	7.42%	-1.32%	-2.15%

saturation lines: remove or add

3+4+7 = 14 over 496

14/496 = **0.028226** 2.8%

	k	sigma	mu	$(k_d - k_n)/k_n$	$(s_d - s_n)/s_n$	$(m_d - m_n)/m_n$
<i>normal</i>	0.3095	0.4436	0.5772			
<i>deriv/2</i>	0.3292	0.4386	0.5678	6.38%	-1.13%	-1.62%
<i>deriv</i>	0.3721	0.4296	0.5459	20.25%	-3.16%	-5.42%



WDLS K25 sheet20 Vol7

	k	sigma	mu	$(k_p - k_n)/k_n \quad (s_p - s_n)/s_n \quad (m_p - m_n)/m_n$		
<i>normal</i>	0.1601	0.4494	0.6585			
<i>p+10</i>	0.2014	0.4440	0.6404	25.82%	-1.20%	-2.75%
<i>p0</i>	0.2851	0.4487	0.5895	78.10%	-0.16%	-10.48%
<i>p-10</i>	0.4297	0.4283	0.5143	168.39%	-4.69%	-21.90%

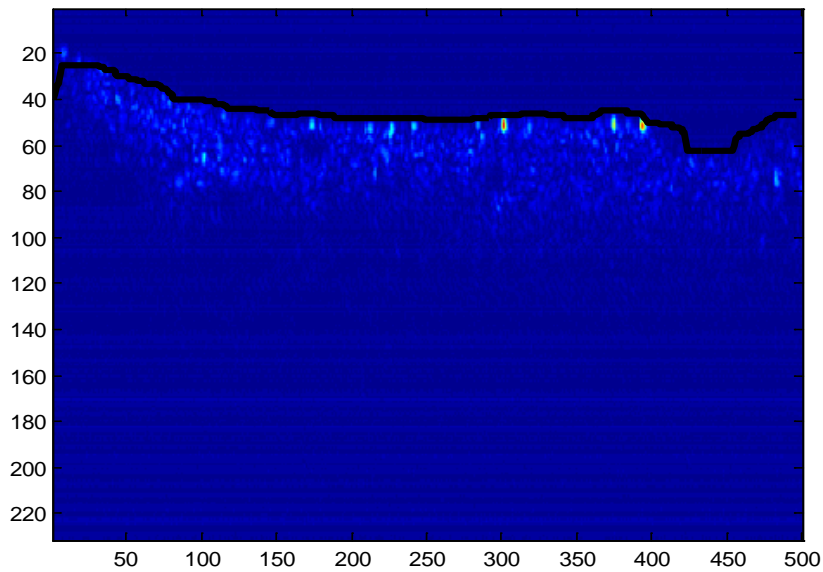
	k	sigma	mu	$(k_s - k_n)/k_n \quad (s_s - s_n)/s_n \quad (m_s - m_n)/m_n$		
<i>normal</i>	0.1601	0.4494	0.6585			
<i>ws</i>	0.1218	0.4561	0.6769	-23.90%	1.49%	2.79%
<i>ms</i>	0.1855	0.4459	0.6449	15.85%	-0.76%	-2.06%

saturation lines: remove or add

4+4+3 = 11 over 496

11/496 = **0.022177** 2.2%

	k	sigma	mu	$(k_d - k_n)/k_n \quad (s_d - s_n)/s_n \quad (m_d - m_n)/m_n$		
<i>normal</i>	0.1601	0.4494	0.6585			
<i>deriv/2</i>	0.1606	0.4492	0.6584	0.31%	-0.04%	-0.01%
<i>deriv</i>	0.1617	0.4490	0.6580	1.00%	-0.09%	-0.07%



	k	sigma	mu	$(k_p - k_n)/k_n$	$(s_p - s_n)/s_n$	$(m_p - m_n)/m_n$
<i>normal</i>	0.6453	0.4083	0.4006			
<i>p+10</i>	0.7321	0.3828	0.3664	13.46%	-6.25%	-8.54%
<i>p0</i>	0.7696	0.3705	0.3504	19.26%	-9.26%	-12.54%
<i>p-10</i>	0.7985	0.3586	0.3391	23.73%	-12.18%	-15.36%

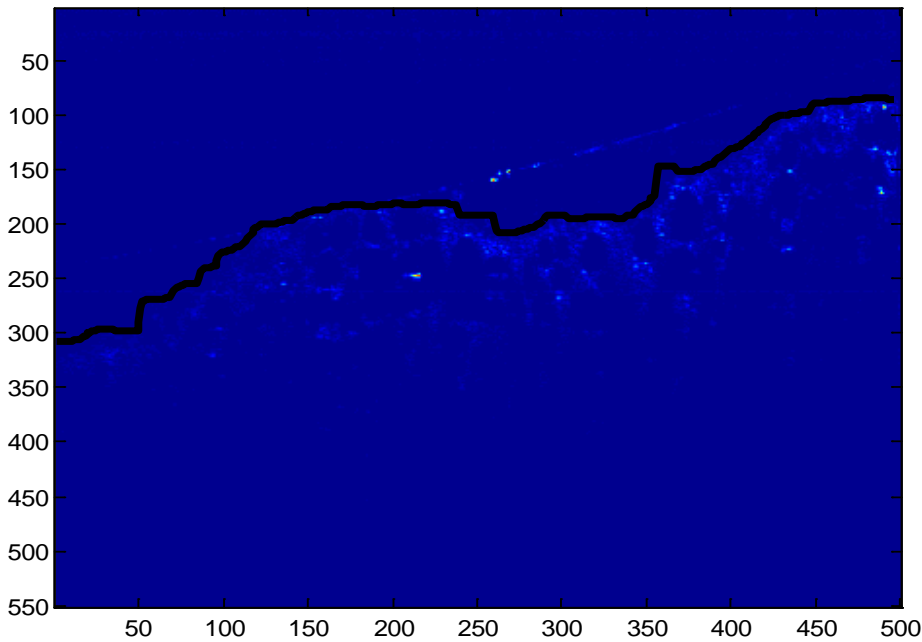
	k	sigma	mu	$(k_s - k_n)/k_n$	$(s_s - s_n)/s_n$	$(m_s - m_n)/m_n$
<i>normal</i>	0.6453	0.4083	0.4006			
<i>ws</i>	0.6480	0.4083	0.3993	0.41%	-0.01%	-0.32%
<i>ms</i>	0.6426	0.4083	0.4019	-0.42%	0.01%	0.33%

saturation lines: remove or add

6 over 496

6/496 = 0.012097 1.2%

	k	sigma	mu	$(k_d - k_n)/k_n$	$(s_d - s_n)/s_n$	$(m_d - m_n)/m_n$
<i>normal</i>	0.6453	0.4083	0.4006			
<i>deriv/2</i>	0.6466	0.4115	0.3989	0.20%	0.77%	-0.42%
<i>deriv</i>	0.6780	0.4068	0.3838	5.07%	-0.38%	-4.19%



	k	sigma	mu	$(k_p - k_n)/k_n$	$(s_p - s_n)/s_n$	$(m_p - m_n)/m_n$
<i>normal</i>	0.7789	0.3755	0.3509			
<i>p+10</i>	0.7886	0.3687	0.3468	1.24%	-1.80%	-1.17%
<i>p0</i>	0.8327	0.3521	0.3278	6.90%	-6.23%	-6.58%
<i>p-10</i>	0.8509	0.3371	0.3157	9.23%	-10.23%	-10.04%

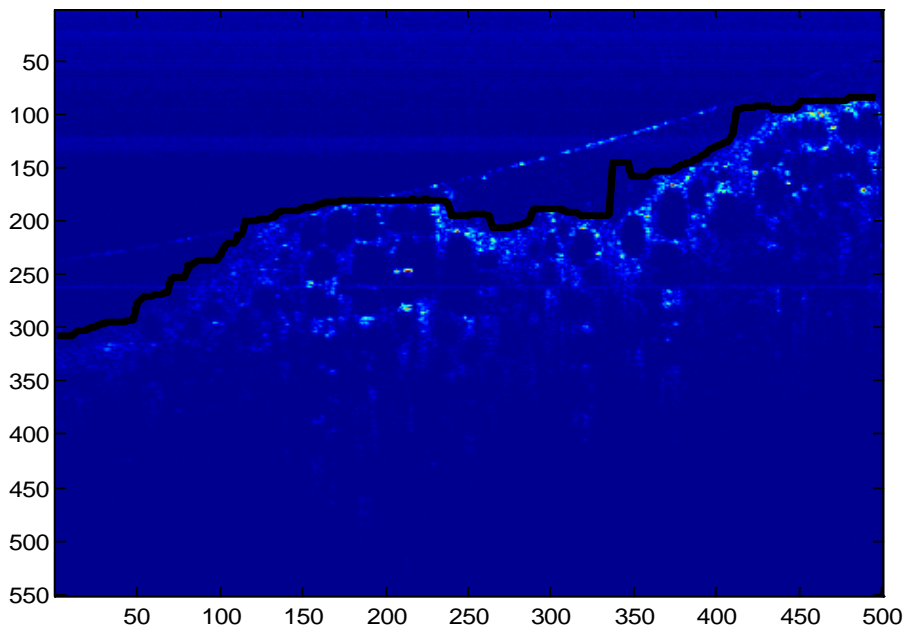
	k	sigma	mu	$(k_s - k_n)/k_n$	$(s_s - s_n)/s_n$	$(m_s - m_n)/m_n$
<i>normal</i>	0.7789	0.3755	0.3509			
<i>ws</i>	0.7603	0.3802	0.3575	-2.39%	1.25%	1.89%
<i>ms</i>	0.7970	0.3708	0.3445	2.32%	-1.24%	-1.83%

saturation lines: remove or add

3+6 =9 over 496

9/496 = 0.0181 1.8%

	k	sigma	mu	$(k_d - k_n)/k_n$	$(s_d - s_n)/s_n$	$(m_d - m_n)/m_n$
<i>normal</i>	0.7789	0.3755	0.3509			
<i>deriv/2</i>	0.7872	0.3794	0.3490	1.06%	1.04%	-0.54%
<i>deriv</i>	0.8257	0.3761	0.3355	6.01%	0.17%	-4.40%



	k	sigma	mu	$(k_p - k_n)/k_n$	$(s_p - s_n)/s_n$	$(m_p - m_n)/m_n$
<i>normal</i>	0.4287	0.4577	0.4953			
<i>p+10</i>	0.4842	0.4457	0.4685	12.94%	-2.62%	-5.41%
<i>p0</i>	0.6037	0.4185	0.4231	40.83%	-8.56%	-14.60%
<i>p-10</i>	0.7106	0.3864	0.3845	65.76%	-15.56%	-22.38%

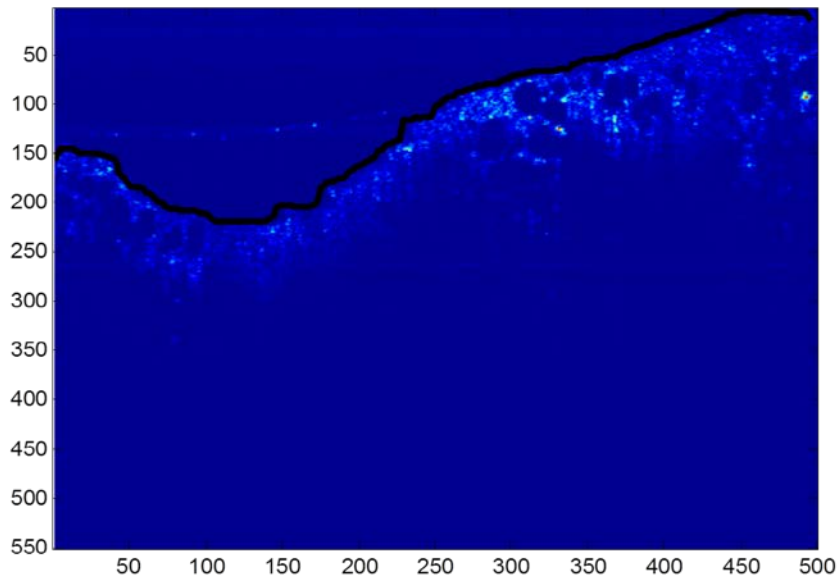
	k	sigma	mu	$(k_s - k_n)/k_n$	$(s_s - s_n)/s_n$	$(m_s - m_n)/m_n$
<i>normal</i>	0.4287	0.4577	0.4953			
<i>ws</i>	0.4044	0.4642	0.5068	-5.67%	1.42%	2.32%
<i>ms</i>	0.4515	0.4517	0.4847	5.31%	-1.31%	-2.16%

saturation lines: remove or add

3+2+8+6= 19 over 496

19/496 = 0.038306 3.8%

	k	sigma	mu	$(k_d - k_n)/k_n$	$(s_d - s_n)/s_n$	$(m_d - m_n)/m_n$
<i>normal</i>	0.4287	0.4577	0.4953			
<i>deriv/2</i>	0.4567	0.4536	0.4826	6.54%	-0.88%	-2.58%
<i>deriv</i>	0.5016	0.4476	0.4616	17.02%	-2.21%	-6.81%



WDLS K58 sheet9 Vol1 or 25

	k	sigma	mu	$(k_p - k_n)/k_n$	$(s_p - s_n)/s_n$	$(m_p - m_n)/m_n$
<i>normal</i>	0.5226	0.3808	0.4447			
<i>p+10</i>	0.5968	0.3527	0.3990	14.18%	-7.36%	-10.27%
<i>p0</i>	0.5157	0.3731	0.4413	-1.33%	-2.02%	-0.75%
<i>p-10</i>	0.5484	0.3704	0.4045	4.92%	-2.72%	-9.03%

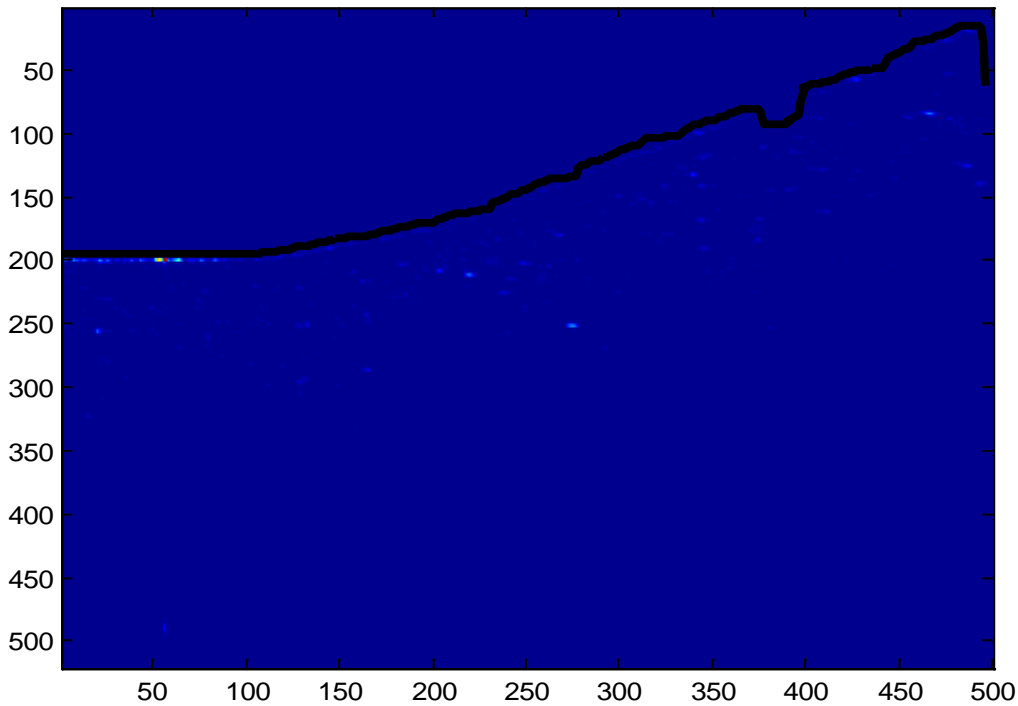
	k	sigma	mu	$(k_s - k_n)/k_n$	$(s_s - s_n)/s_n$	$(m_s - m_n)/m_n$
<i>normal</i>	0.5226	0.3808	0.4447			
<i>ws</i>	0.5116	0.3871	0.4586	-2.12%	1.66%	3.12%
<i>ms</i>	0.5341	0.3768	0.4336	2.19%	-1.05%	-2.50%

saturation lines: remove or add

7+3 = 10 over 496

10/496 = **0.020161** 2.0%

	k	sigma	mu	$(k_d - k_n)/k_n$	$(s_d - s_n)/s_n$	$(m_d - m_n)/m_n$
<i>normal</i>	0.5226	0.3808	0.4447			
<i>deriv/2</i>	0.5209	0.3805	0.4500	-0.33%	-0.07%	1.19%
<i>deriv</i>	0.5840	0.3730	0.4186	11.74%	-2.05%	-5.86%



WDLS K58 sheet10 Vol2 or 24

	k	sigma	mu	$(k_p - k_n)/k_n$	$(s_p - s_n)/s_n$	$(m_p - m_n)/m_n$
<i>normal</i>	0.5106	0.3881	0.4491			
<i>p+10</i>	0.5497	0.3685	0.4235	7.66%	-5.06%	-5.69%
<i>p0</i>	0.5188	0.3744	0.4372	1.60%	-3.53%	-2.64%
<i>p-10</i>	0.5935	0.3598	0.3796	16.23%	-7.29%	-15.46%

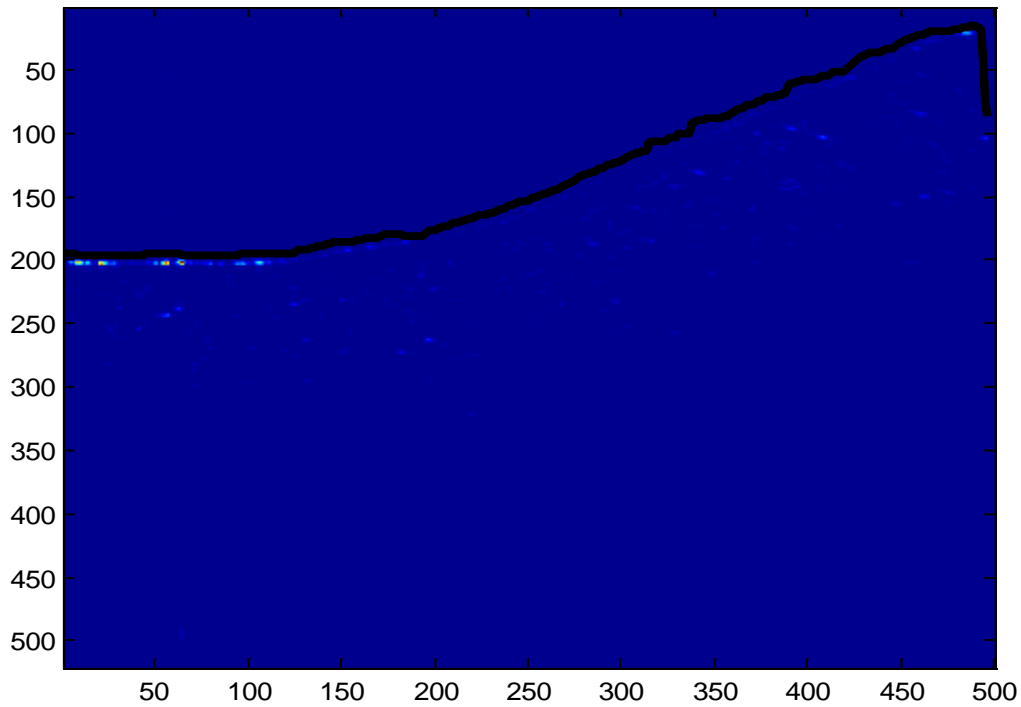
	k	sigma	mu	$(k_s - k_n)/k_n$	$(s_s - s_n)/s_n$	$(m_s - m_n)/m_n$
<i>normal</i>	0.5106	0.3881	0.4491			
<i>ws</i>	0.4926	0.3940	0.4675	-3.52%	1.51%	4.11%
<i>ms</i>	0.5292	0.3843	0.4341	3.64%	-0.99%	-3.34%

saturation lines: remove or add

4+3+3+3 = 13 over 496

13/496 **0.02621** 2.6%

	k	sigma	mu	$(k_d - k_n)/k_n$	$(s_d - s_n)/s_n$	$(m_d - m_n)/m_n$
<i>normal</i>	0.5106	0.3881	0.4491			
<i>deriv/2</i>	0.4916	0.3916	0.4653	-3.73%	0.90%	3.61%
<i>deriv</i>	0.5286	0.3897	0.4497	3.52%	0.40%	0.14%



WDLS K58 sheet3 Vol2 or 24

	k	sigma	mu	$(k_p - k_n)/k_n (s_p - s_n)/s_n (m_p - m_n)/m_n$		
<i>normal</i>	0.4519	0.4057	0.4747			
<i>p+10</i>	0.5114	0.3837	0.4439	13.16%	-5.40%	-6.49%
<i>p0</i>	0.4985	0.3740	0.4402	10.29%	-7.80%	-7.26%
<i>p-10</i>	0.5929	0.3493	0.3695	31.19%	-13.90%	-22.15%

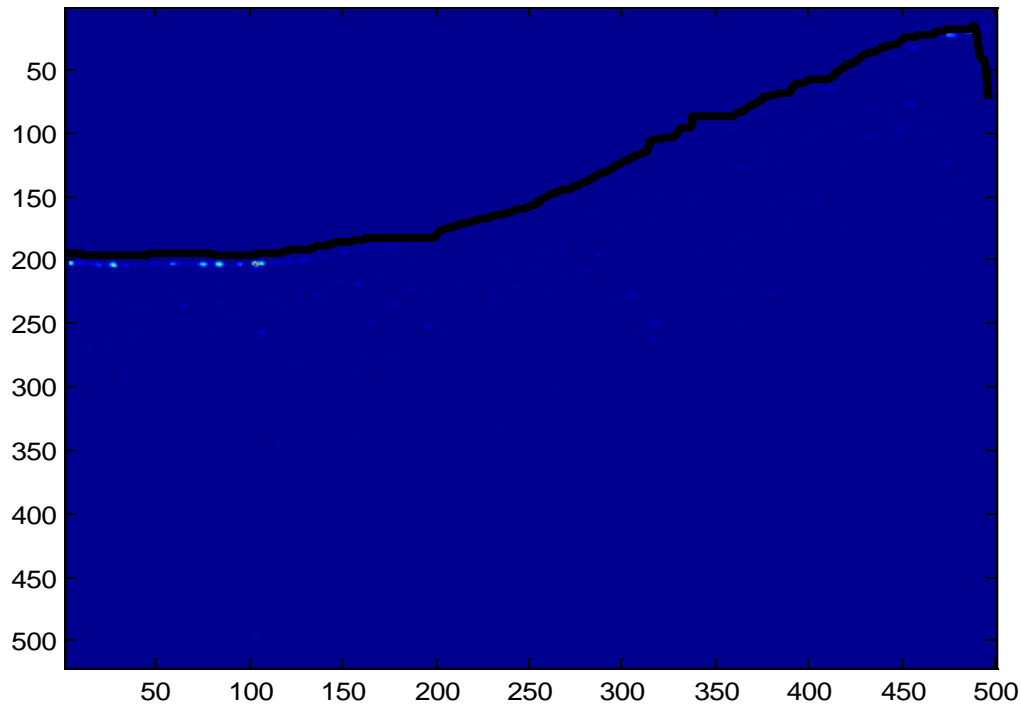
	k	sigma	mu	$(k_s - k_n)/k_n (s_s - s_n)/s_n (m_s - m_n)/m_n$		
<i>normal</i>	0.4519	0.4057	0.4747			
<i>ws</i>	0.4450	0.4089	0.4838	-1.53%	0.79%	1.93%
<i>ms</i>	0.4596	0.4028	0.4662	1.70%	-0.71%	-1.78%

saturation lines: remove or add

3+2 =5 over 496

5/496 = **0.010081** 1.0%

	k	sigma	mu	$(k_d - k_n)/k_n (s_d - s_n)/s_n (m_d - m_n)/m_n$		
<i>normal</i>	0.4519	0.4057	0.4747			
<i>deriv/2</i>	0.4326	0.4104	0.4936	-4.29%	1.17%	3.99%
<i>deriv</i>	0.4794	0.4082	0.4781	6.08%	0.62%	0.72%



DDLS K35 sheet1 Vol7

	k	sigma	mu	$(k_p - k_n)/k_n$	$(s_p - s_n)/s_n$	$(m_p - m_n)/m_n$
<i>normal</i>	0.1303	0.4492	0.6768			
<i>p+10</i>	0.2324	0.4521	0.6174	78.27%	0.64%	-8.78%
<i>p0</i>	0.2572	0.5099	0.5563	97.29%	13.51%	-17.81%
<i>p-10</i>	0.5178	0.4911	0.4192	297.26%	9.33%	-38.07%

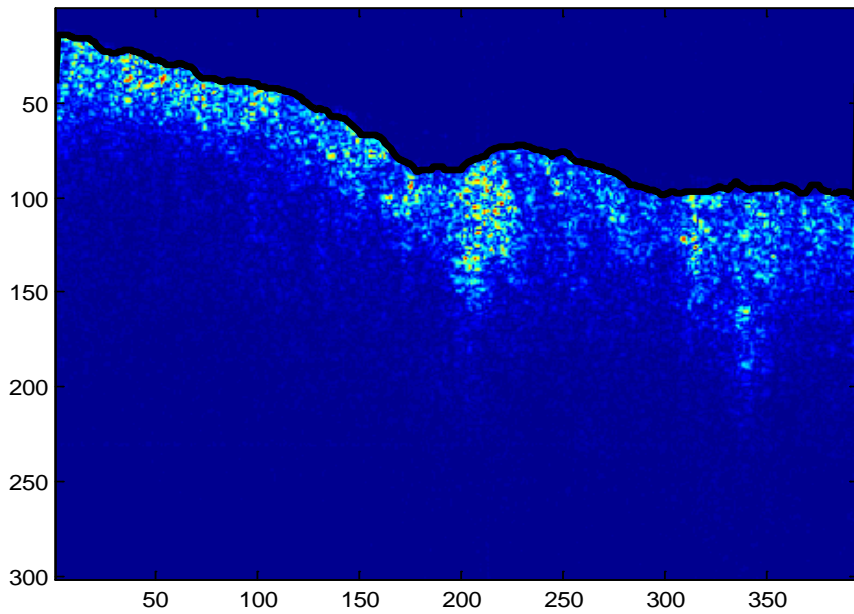
	k	sigma	mu	$(k_s - k_n)/k_n$	$(s_s - s_n)/s_n$	$(m_s - m_n)/m_n$
<i>normal</i>	0.1303	0.4492	0.6768			
<i>ws</i>	0.0786	0.4510	0.7021	-39.71%	0.39%	3.74%
<i>ms</i>	0.1517	0.4515	0.6640	16.37%	0.50%	-1.89%

saturation lines: remove or add

25+8 = 33 over 395

33/395 = 0.083544 8.4%

	k	sigma	mu	$(k_d - k_n)/k_n$	$(s_d - s_n)/s_n$	$(m_d - m_n)/m_n$
<i>normal</i>	0.1303	0.4492	0.6768			
<i>deriv/2</i>	0.1206	0.4499	0.6815	-7.45%	0.16%	0.68%
<i>deriv</i>	0.1230	0.4520	0.6790	-5.65%	0.61%	0.31%



DDLS K35 sheet2 Vol7

	k	sigma	mu	$(k_p - k_n)/k_n$	$(s_p - s_n)/s_n$	$(m_p - m_n)/m_n$
<i>normal</i>	0.1272	0.4484	0.6790			
<i>p+10</i>	0.2252	0.4518	0.6224	76.98%	0.76%	-8.33%
<i>p0</i>	0.2441	0.5111	0.5635	91.82%	13.99%	-17.01%
<i>p-10</i>	0.5147	0.4919	0.4190	304.55%	9.70%	-38.28%

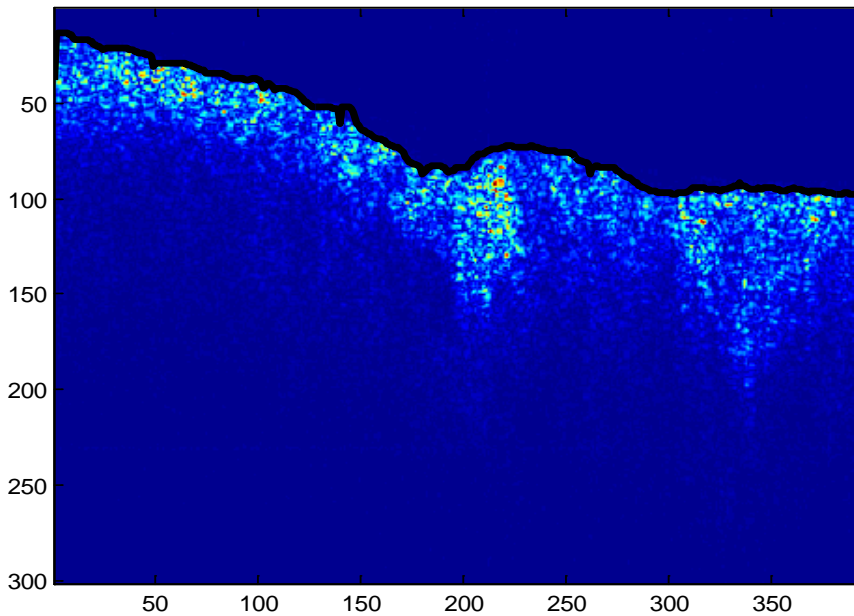
	k	sigma	mu	$(k_s - k_n)/k_n$	$(s_s - s_n)/s_n$	$(m_s - m_n)/m_n$
<i>normal</i>	0.1272	0.4484	0.6790			
<i>ws</i>	0.0752	0.4515	0.7034	-40.92%	0.69%	3.60%
<i>ms</i>	0.1513	0.4491	0.6657	18.94%	0.15%	-1.95%

saturation lines: remove or add

25+16 = 41 over 395

41/395 0.103797 10.4%

	k	sigma	mu	$(k_d - k_n)/k_n$	$(s_d - s_n)/s_n$	$(m_d - m_n)/m_n$
<i>normal</i>	0.1272	0.4484	0.6790			
<i>deriv/2</i>	0.1151	0.4478	0.6858	-9.56%	-0.13%	1.00%
<i>deriv</i>	0.1154	0.4480	0.6855	-9.28%	-0.09%	0.96%



DDLS K35 sheet3 Vol7

	k	sigma	mu	$(k_p - k_n)/k_n (s_p - s_n)/s_n (m_p - m_n)/m_n$		
<i>normal</i>	0.1079	0.4492	0.6886			
<i>p+10</i>	0.2095	0.4532	0.6312	94.11%	0.88%	-8.33%
<i>p0</i>	0.2252	0.5195	0.5697	108.70%	15.65%	-17.26%
<i>p-10</i>	0.4914	0.5020	0.4270	355.38%	11.75%	-37.99%

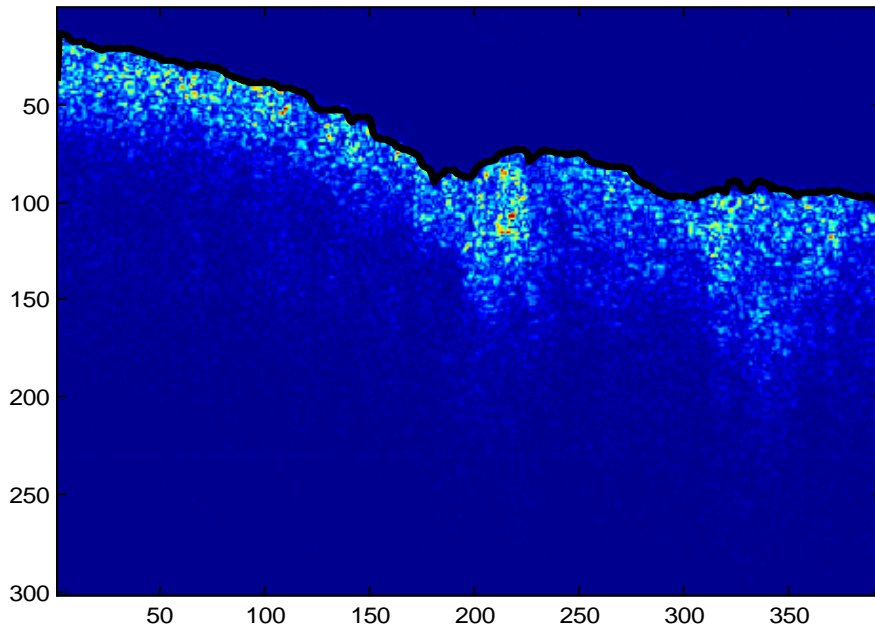
	k	sigma	mu	$(k_s - k_n)/k_n (s_s - s_n)/s_n (m_s - m_n)/m_n$		
<i>normal</i>	0.1079	0.4492	0.6886			
<i>ws</i>	0.0562	0.4515	0.7126	-47.88%	0.50%	3.49%
<i>ms</i>	0.1302	0.4507	0.6761	20.65%	0.34%	-1.81%

saturation lines: remove or add

25+12 = 37 over 395

37/395 = 0.093671 9.4%

	k	sigma	mu	$(k_d - k_n)/k_n (s_d - s_n)/s_n (m_d - m_n)/m_n$		
<i>normal</i>	0.1079	0.4492	0.6886			
<i>deriv/2</i>	0.0942	0.4504	0.6948	-12.69%	0.26%	0.90%
<i>deriv</i>	0.0959	0.4525	0.6925	-11.13%	0.73%	0.57%



DDLS K12 sheet20 Vol1

	k	sigma	mu	$(k_p - k_n)/k_n$	$(s_p - s_n)/s_n$	$(m_p - m_n)/m_n$
<i>normal</i>	0.0863	0.4471	0.7010			
<i>p+10</i>	0.1421	0.4399	0.6771	64.78%	-1.60%	-3.41%
<i>p0</i>	0.2483	0.4502	0.6108	187.88%	0.69%	-12.86%
<i>p-10</i>	0.4372	0.4414	0.5056	406.84%	-1.29%	-27.87%

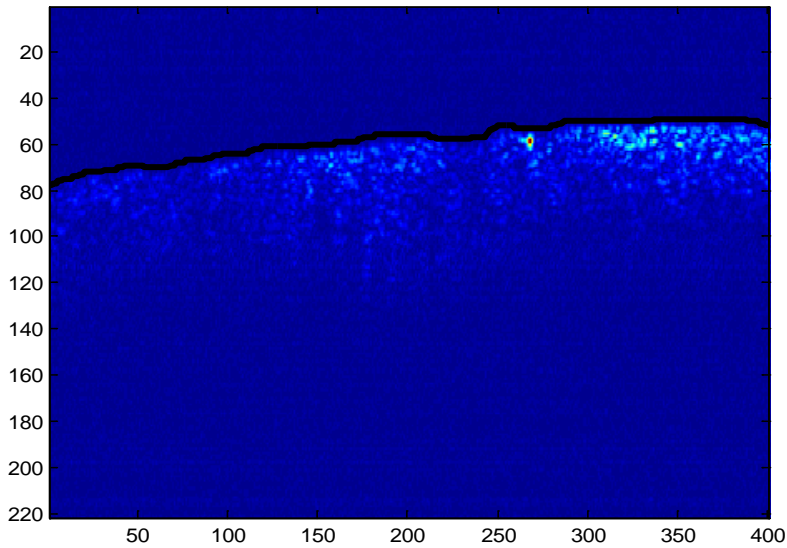
	k	sigma	mu	$(k_s - k_n)/k_n$	$(s_s - s_n)/s_n$	$(m_s - m_n)/m_n$
<i>normal</i>	0.0863	0.4471	0.7010			
<i>ws</i>	0.0742	0.4482	0.7061	-14.00%	0.24%	0.73%
<i>ms</i>	0.0953	0.4465	0.6969	10.54%	-0.13%	-0.59%

saturation lines: remove or add

8 over 401

8/401 = 0.01995 2.0%

	k	sigma	mu	$(k_d - k_n)/k_n$	$(s_d - s_n)/s_n$	$(m_d - m_n)/m_n$
<i>normal</i>	0.0863	0.4471	0.7010			
<i>deriv/2</i>	0.0784	0.4470	0.7049	-9.10%	-0.03%	0.56%
<i>deriv</i>	0.0708	0.4469	0.7087	-17.91%	-0.06%	1.10%



DDLS K12 sheet19 Vol1

	k	sigma	mu	$(k_p - k_n)/k_n$	$(s_p - s_n)/s_n$	$(m_p - m_n)/m_n$
<i>normal</i>	0.1026	0.4464	0.6933			
<i>p+10</i>	0.1531	0.4399	0.6709	49.14%	-1.46%	-3.24%
<i>p0</i>	0.2483	0.4527	0.6079	141.97%	1.42%	-12.32%
<i>p-10</i>	0.4451	0.4414	0.4996	333.73%	-1.10%	-27.94%

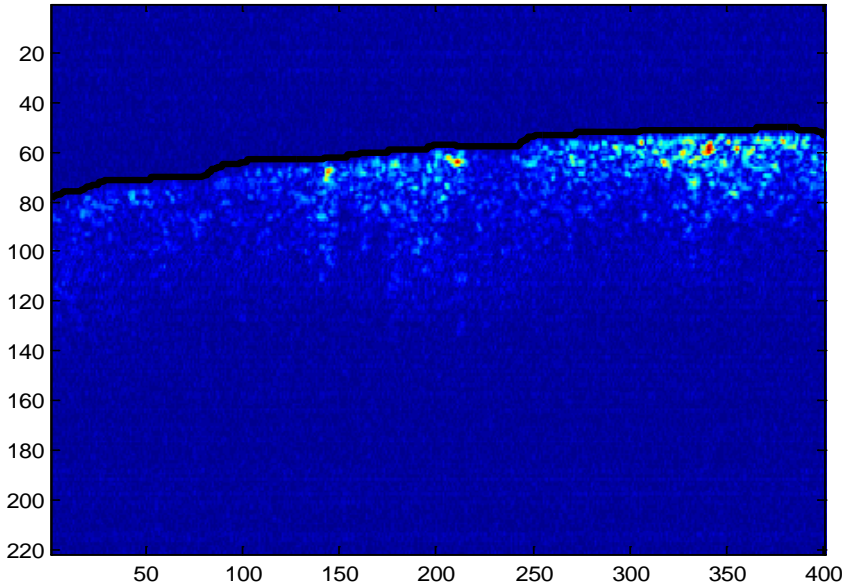
	k	sigma	mu	$(k_s - k_n)/k_n$	$(s_s - s_n)/s_n$	$(m_s - m_n)/m_n$
<i>normal</i>	0.1026	0.4464	0.6933			
<i>ws</i>	0.0904	0.4460	0.6997	-11.93%	-0.08%	0.91%
<i>ms</i>	0.1109	0.4473	0.6885	8.09%	0.21%	-0.69%

saturation lines: remove or add

7+3+4 = 14 over 401

14/401 = 0.034913 3.5%

	k	sigma	mu	$(k_d - k_n)/k_n$	$(s_d - s_n)/s_n$	$(m_d - m_n)/m_n$
<i>normal</i>	0.1026	0.4464	0.6933			
<i>deriv/2</i>	0.0951	0.4462	0.6972	-7.38%	-0.03%	0.56%
<i>deriv</i>	0.0876	0.4461	0.7010	-14.61%	-0.05%	1.10%



DDLS K12 sheet18 Vol1

	k	sigma	mu	$(k_p - k_n)/k_n (s_p - s_n)/s_n (m_p - m_n)/m_n$		
<i>normal</i>	0.0991	0.4412	0.6985			
<i>p+10</i>	0.1455	0.4397	0.6751	46.85%	-0.34%	-3.34%
<i>p0</i>	0.2443	0.4496	0.6120	146.62%	1.91%	-12.38%
<i>p-10</i>	0.4283	0.4418	0.5082	332.33%	0.14%	-27.24%

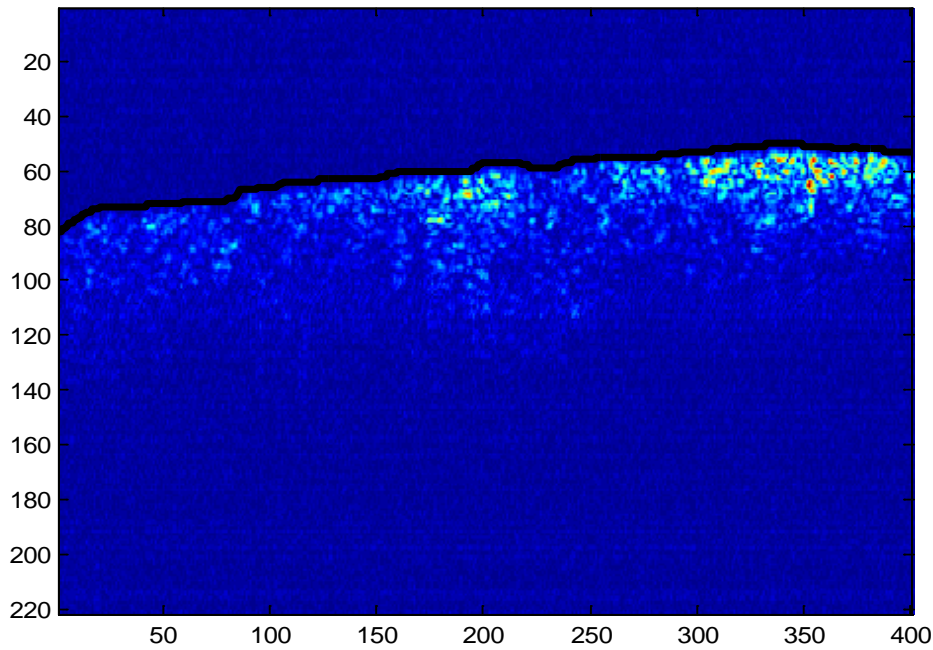
	k	sigma	mu	$(k_s - k_n)/k_n (s_s - s_n)/s_n (m_s - m_n)/m_n$		
<i>normal</i>	0.0991	0.4412	0.6985			
<i>ws</i>	0.0819	0.4430	0.7058	-17.35%	0.40%	1.05%
<i>ms</i>	0.1136	0.4398	0.6919	14.72%	-0.31%	-0.94%

saturation lines: remove or add

8 over 401

8/401 = 0.01995 2.0%

	k	sigma	mu	$(k_d - k_n)/k_n (s_d - s_n)/s_n (m_d - m_n)/m_n$		
<i>normal</i>	0.0991	0.4412	0.6985			
<i>deriv/2</i>	0.0922	0.4412	0.7019	-6.93%	0.01%	0.49%
<i>deriv</i>	0.0855	0.4413	0.7051	-13.67%	0.02%	0.95%



DDLS K33 sheet1 vol1

	k	sigma	mu	$(k_p - k_n)/k_n$	$(s_p - s_n)/s_n$	$(m_p - m_n)/m_n$
<i>normal</i>	0.0277	0.4435	0.7314			
<i>p+10</i>	0.0133	0.4427	0.7383	-52.00%	-0.19%	0.94%
<i>p0</i>	0.0956	0.4505	0.6941	244.78%	1.58%	-5.10%
<i>p-10</i>	0.2028	0.4554	0.6335	631.57%	2.68%	-13.39%

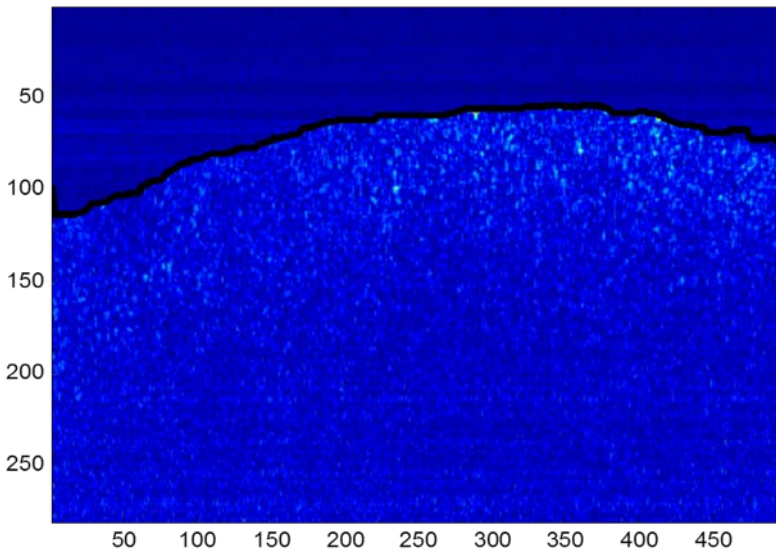
	k	sigma	mu	$(k_s - k_n)/k_n$	$(s_s - s_n)/s_n$	$(m_s - m_n)/m_n$
<i>normal</i>	0.0277	0.4435	0.7314			
<i>ws</i>	-0.0020	0.4469	0.7415	-107.24%	0.77%	1.38%
<i>ms</i>	0.0470	0.4416	0.7240	69.69%	-0.44%	-1.02%

saturation lines: remove or add

3+3+2+2 = 10 over 496

10/496 = **0.020161** 2.0%

	k	sigma	mu	$(k_d - k_n)/k_n$	$(s_d - s_n)/s_n$	$(m_d - m_n)/m_n$
<i>normal</i>	0.0277	0.4435	0.7314			
<i>deriv/2</i>	0.0130	0.4425	0.7387	-53.08%	-0.22%	0.99%
<i>deriv</i>	0.0055	0.4426	0.7417	-80.31%	-0.20%	1.41%



DDLS K33 sheet2 vol1

	k	sigma	mu	$(k_p - k_n)/k_n$	$(s_p - s_n)/s_n$	$(m_p - m_n)/m_n$
<i>normal</i>	0.0330	0.4442	0.7286			
<i>p+10</i>	0.0125	0.4462	0.7363	-62.19%	0.45%	1.06%
<i>p0</i>	0.1034	0.4513	0.6896	213.76%	1.61%	-5.35%
<i>p-10</i>	0.2048	0.4514	0.6349	521.22%	1.62%	-12.85%

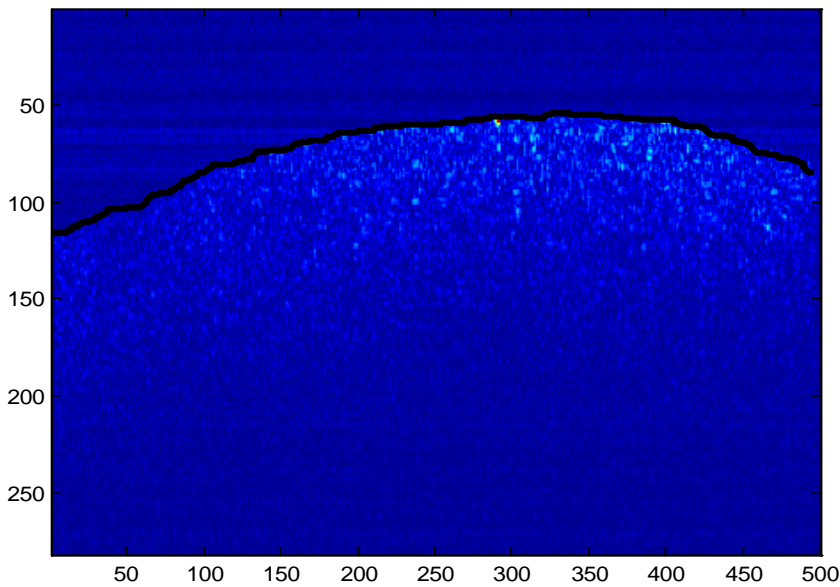
	k	sigma	mu	$(k_s - k_n)/k_n$	$(s_s - s_n)/s_n$	$(m_s - m_n)/m_n$
<i>normal</i>	0.0330	0.4442	0.7286			
<i>ws</i>	0.0133	0.4466	0.7353	-59.64%	0.53%	0.92%
<i>ms</i>	0.0462	0.4428	0.7236	40.22%	-0.32%	-0.69%

saturation lines: remove or add

4 over 496

4/496 = 0.0081 1.0%

	k	sigma	mu	$(k_d - k_n)/k_n$	$(s_d - s_n)/s_n$	$(m_d - m_n)/m_n$
<i>normal</i>	0.0330	0.4442	0.7286			
<i>deriv/2</i>	0.0186	0.4432	0.7358	-43.71%	-0.21%	0.98%
<i>deriv</i>	0.0121	0.4432	0.7385	-63.39%	-0.21%	1.36%



DDLS K33 sheet3 vol1

	k	sigma	mu	$(k_p - k_n)/k_n$	$(s_p - s_n)/s_n$	$(m_p - m_n)/m_n$
<i>normal</i>	0.0160	0.4450	0.7354			
<i>p+10</i>	0.0011	0.4442	0.7422	-93.28%	-0.20%	0.92%
<i>p0</i>	0.0910	0.4526	0.6951	468.92%	1.69%	-5.49%
<i>p-10</i>	0.2044	0.4538	0.6339	1178.62%	1.96%	-13.80%

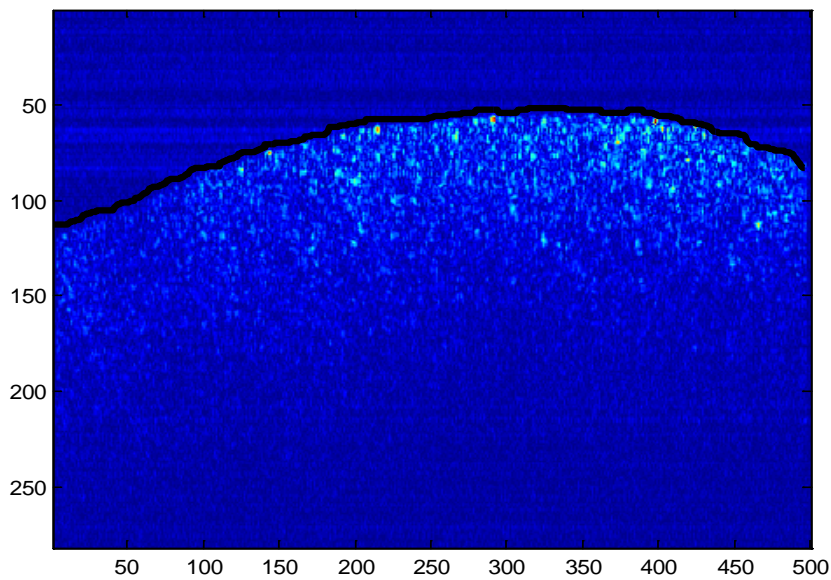
	k	sigma	mu	$(k_s - k_n)/k_n$	$(s_s - s_n)/s_n$	$(m_s - m_n)/m_n$
<i>normal</i>	0.0160	0.4450	0.7354			
<i>ws</i>	0.0160	0.4450	0.7354	0.00%	0.00%	0.00%
<i>ms</i>	0.0464	0.4420	0.7242	190.39%	-0.68%	-1.53%

saturation lines: only added

3+3+2+2 = 10 over 496

10/496 = **0.020161** 2.0%

	k	sigma	mu	$(k_d - k_n)/k_n$	$(s_d - s_n)/s_n$	$(m_d - m_n)/m_n$
<i>normal</i>	0.0160	0.4450	0.7354			
<i>deriv/2</i>	0.0070	0.4438	0.7402	-56.47%	-0.27%	0.65%
<i>deriv</i>	0.0086	0.4434	0.7397	-46.46%	-0.36%	0.58%



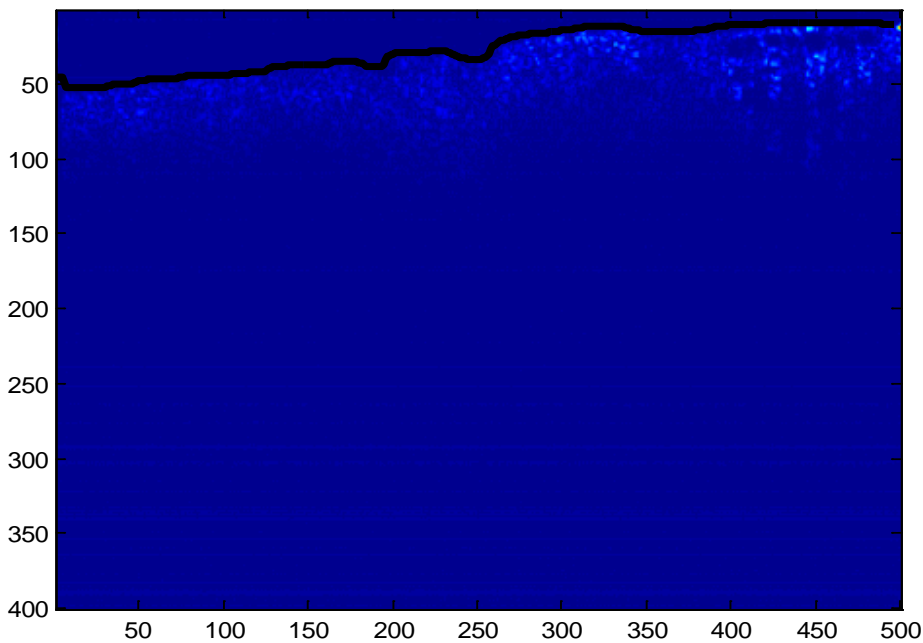
DDLS K26 sheet3 Vol1 originally 2

	k	sigma	mu	$(k_p - k_n)/k_n$	$(s_p - s_n)/s_n$	$(m_p - m_n)/m_n$
<i>normal</i>	0.1346	0.4527	0.6718			
<i>p+10</i>	0.2098	0.4449	0.6349	55.90%	-1.73%	-5.49%
<i>p0</i>	0.3052	0.4520	0.5762	126.84%	-0.17%	-14.23%
<i>p-10</i>	0.3909	0.4641	0.5205	190.50%	2.51%	-22.52%

	k	sigma	mu	$(k_s - k_n)/k_n$	$(s_s - s_n)/s_n$	$(m_s - m_n)/m_n$
<i>normal</i>	0.1346	0.4527	0.6718			
<i>ws</i>				-100.00%	-100.00%	-100.00%
<i>ms</i>	0.1632	0.4477	0.6575	21.31%	-1.12%	-2.13%

saturation lines: only add
 5 rows + 2 cols over 496 cols
 2/496 = **0.004032** 0.4%

	k	sigma	mu	$(k_d - k_n)/k_n$	$(s_d - s_n)/s_n$	$(m_d - m_n)/m_n$
<i>normal</i>	0.1346	0.4527	0.6718			
<i>deriv/2</i>	0.1223	0.4545	0.6773	-9.10%	0.39%	0.81%
<i>deriv</i>	0.1106	0.4563	0.6823	-17.79%	0.80%	1.56%



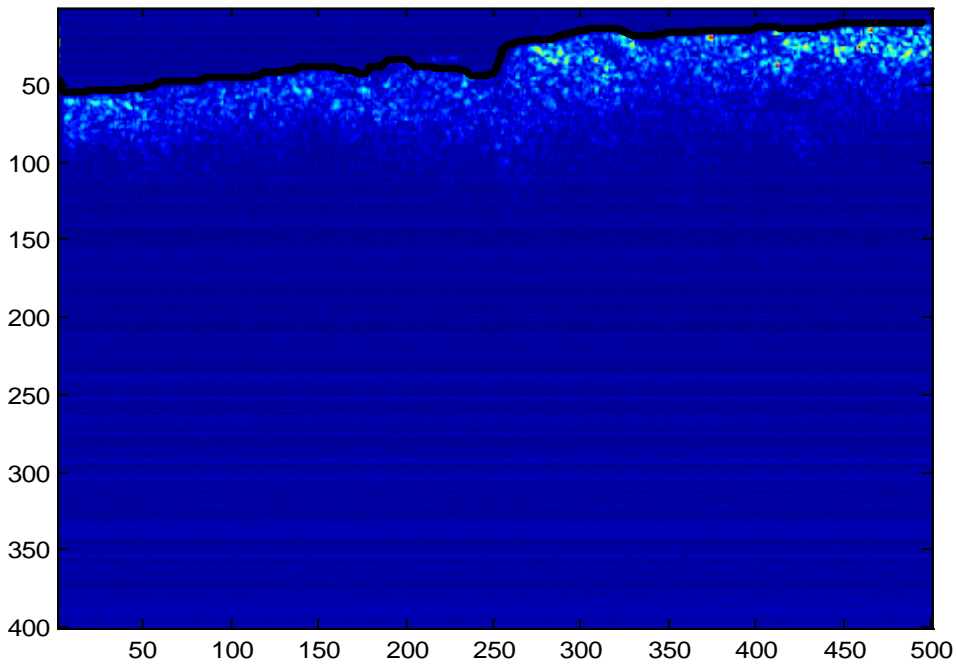
DDLS K26 sheet7 Vol1 originally 2

	k	sigma	mu	$(k_p - k_n)/k_n$	$(s_p - s_n)/s_n$	$(m_p - m_n)/m_n$
<i>normal</i>	0.0701	0.4462	0.7095			
<i>p+10</i>	0.1653	0.4456	0.6614	135.84%	-0.14%	-6.77%
<i>p0</i>	0.2678	0.4598	0.5941	282.01%	3.06%	-16.26%
<i>p-10</i>	0.3934	0.4636	0.5205	461.24%	3.90%	-26.64%

	k	sigma	mu	$(k_s - k_n)/k_n$	$(s_s - s_n)/s_n$	$(m_s - m_n)/m_n$
<i>normal</i>	0.0701	0.4462	0.7095			
<i>ws</i>				-100.00%	-100.00%	-100.00%
<i>ms</i>	0.1082	0.4409	0.6935	54.33%	-1.18%	-2.25%

saturation lines: only add
 5 rows + 2 cols over 496 cols
 $2/496 = 0.004032$ 0.4%

	k	sigma	mu	$(k_d - k_n)/k_n$	$(s_d - s_n)/s_n$	$(m_d - m_n)/m_n$
<i>normal</i>	0.0701	0.4462	0.7095			
<i>deriv/2</i>	0.0608	0.4465	0.7137	-13.29%	0.07%	0.60%
<i>deriv</i>	0.0523	0.4469	0.7174	-25.40%	0.16%	1.12%



DDLS K26 sheet19 Vol1 originally 2

	k	sigma	mu	$(k_p - k_n)/k_n \quad (s_p - s_n)/s_n \quad (m_p - m_n)/m_n$		
<i>normal</i>	0.0263	0.4424	0.7324			
<i>p+10</i>	0.1540	0.4479	0.6660	485.41%	1.23%	-9.07%
<i>p0</i>	0.2524	0.4744	0.5922	859.50%	7.23%	-19.15%
<i>p-10</i>	0.4270	0.4670	0.5012	1522.96%	5.55%	-31.56%

	k	sigma	mu	$(k_s - k_n)/k_n \quad (s_s - s_n)/s_n \quad (m_s - m_n)/m_n$		
<i>normal</i>	0.0263	0.4424	0.7324			
<i>ws</i>				-100.00%	-100.00%	-100.00%
<i>ms</i>	0.0722	0.4374	0.7146	174.47%	-1.14%	-2.42%

saturation lines: only add
 5 rows + 2 cols over 496 cols
2/496 = 0.004032 0.4%

	k	sigma	mu	$(k_d - k_n)/k_n \quad (s_d - s_n)/s_n \quad (m_d - m_n)/m_n$		
<i>normal</i>	0.0263	0.4424	0.7324			
<i>deriv/2</i>	0.0171	0.4423	0.7365	-35.17%	-0.02%	0.57%
<i>deriv</i>	0.0094	0.4423	0.7399	-64.41%	-0.03%	1.03%

